An Investigation of the Difference Between Skin and Bulk Sea Surface Temperatures in the Southern Ocean Between Australia and Antarctica

by

Clive Brent Rapier

(B. Surv., Grad. Dip. (ASOS) Hons.)

University of Tasmania

This thesis is submitted in fulfilment
of the requirements for the degree of

Master of Science

at the Institute of Antarctic and Southern Ocean Studies (IASOS),
University of Tasmania,
Hobart, Australia,

March, 1995

DECLARATION

This thesis contains no material which has been accepted for the award of any other higher degree or graduate diploma in any tertiary institution and, to the best of my knowledge and belief, this thesis contains no material previously published or written by another person, except where due reference is made in the text of this thesis.

Clive Brent Rapier

(DATE 30/11/1995)

Authority of Access

This thesis may be made available for loan and limited copying in accordance with the *Copyright Act 1968*.

C B Rapier

Clive Brent Rapier

(DATE 30 / 11 / 1995)

ACKNOWLEDGMENTS

The work contained in this thesis has been the culmination of many years of work and many thanks must go to the following people.

Firstly to my supervisor Dr. Kelvin Michael. This project simply would not have been possible without his encouragement, patience and persistence. I thank Kelvin for this project as it has given me the opportunity to see the great white continent, Antarctica and much of the Southern Ocean. It has been an experience I will remember for a long time.

Thanks also to Mark Chladil, Dr. Manuel Nunez and Denis Charlesworth (all from the Department of Geography and Environmental Studies) for the loan and use of calibration equipment and laboratory space.

Thanks also to Ian Knott (Antarctic CRC) for his general assistance in setting up the radiometric equipment.

Thanks must also go to Kim Badcock (CSIRO) for the gathering of NOAA-AVHRR imagery.

To relevant staff and students for their general advice and assistance

and to my mother, family and friends for their moral support

THANK YOU ALL !

In memory of the late Terry Rapier

ABSTRACT

Data were collected on board the RSV *Aurora Australis* in order to investigate the difference between the skin sea surface temperature (SST) and the bulk SST in the Southern Ocean. Bulk SST is the traditional sea surface temperature measured *in situ* by ship and buoy based thermometers and is representative of the upper few metres of the ocean. Thermal infrared radiometers will measure the skin SST, the temperature of the upper few microns less than 0.05 mm (Maul 1985), of the ocean surface. Previous research has shown that given typical conditions over tropical and temperate oceans, the skin SST is 0.1 - 0.5 °C cooler on average than the bulk SST (Robinson *et al.* 1984). This temperature difference (ΔT = skin SST - bulk SST) is due mainly to the presence of a thermal boundary layer (less than 1 mm thick) which is a consequence of evaporation from the sea surface and the molecular conductive processes of heat transfer across the air-sea interface (Robinson *et al.* 1984; Hepplewhite 1989).

It was found that the sign and magnitude of ΔT is influenced by the air temperature and the air-bulk temperature difference ΔT_{ab}. An analysis which related ΔT to the air-bulk temperature difference yielded the simple relationship

$$\Delta T = a(\Delta T_{ab}) + b$$

where a is the gradient coefficient and was found to be 0.40 (±0.1) and b is the y-intercept, which varied between -0.2 (at night) and 0.6 (during the day).

The root mean square difference (RMSD) for the regression between ΔT and ΔT_{ab} at night is 0.26 °C. The RMSD value for clear days was 0.63 °C and is affected in part by a 5 % signal contribution from the PVC pipe used to house the radiometers. This error source would be more dominant on clear days. A correction factor was applied to some of the data (see Appendix F).

Cloudy days showed a slightly better performance, with RMSD values of 0.40 °C. The average value of ΔT was +0.17 °C in the day time and -0.48 °C at

night. The average ΔT value for clear nights was -0.67 °C, while for cloudy nights ΔT averaged -0.28 °C, demonstrating the insulating effect of cloud.

It was found that ΔT values were negative (skin less than bulk) for southerly winds and positive (skin greater than bulk) for northerly winds, suggesting a synoptic relationship between ΔT and wind direction. There also appeared to be a relationship between the air-skin temperature difference ΔT_{as} and wind speed. Strong wind speeds (>10 knots) reduced the magnitude of ΔT_{as} whilst light winds (<10 knots) increased the magnitude of ΔT_{as}.

It is concluded that ΔT is influenced by air temperature, the diurnal cycle and the amount of cloud cover. However, the day time data are potentially affected by solar heating of the PVC pipes. If values for air and bulk temperature are known, then the skin SST can be estimated with a standard error of 0.25 °C for night time conditions. Given a satellite measurement of air temperature and skin SST, then estimates of the bulk SST can be obtained.

CONTENTS:

List of Figures

List of Tables

Chapter 1

CHAPTER 1: Introduction

1.1 Location

This study examines the difference between *in situ* thermal infrared radiometric skin sea surface temperature (SST) measurements and the bulk SST measured at 7.5 metres depth in the Southern Ocean. The SST data were collected during two Australian National Antarctic Research Expedition (ANARE) marine science voyages in the 1993/94 season on board the RSV *Aurora Australis*. The first marine science voyage was Voyage 1 (code name THIRST) departed on the 7th of August 1993 and returned on the 9th of October 1993. This voyage started at Hobart (43° S, 146° E) and sailed to Macquarie Island (54° S, 159° E). This was followed by the easterly transect to Heard Island (53° S, 73° E). This was then followed by a 4 week fishing and CTD campaign north of Heard Island. The final leg of the journey was the great circle transect from Heard Island back to Hobart. This voyage lasted for 9 weeks. Figure 1.1 and Table 1.1 summarises the itinerary of voyage 1.

The second marine science voyage was voyage 7 (code name SHAM) which departed Hobart on the 1st of January 1994 and returned on the 1st of March 1994 and extended over a period of 8 weeks. Voyage 7 included the World Ocean Circulation Experiment (WOCE) transect SR3 which runs from Hobart to about 57° S, 137° E, then along a north-south transect between 57° S, 137° E and 65° S, 137° E. Voyage 7 also included a short northerly transect (the Prince Elizabeth Trough Experiment PETE) near the West Ice Shelf from about 67° S, 85° E to 57° S, 82° E. A number of the Australian Antarctic bases were visited including Mawson (68° S, 63° E), Law base (69° S, 76° E), Davis (69° S, 78° E), Casey (66° S, 111° E) and the French station Dumont D'urville (67° S, 140° E). The final leg of voyage 7 was from Dumont D'urville back to Hobart. Figure 1.2 and Table 1.2 summarises the itinerary of voyage 7.

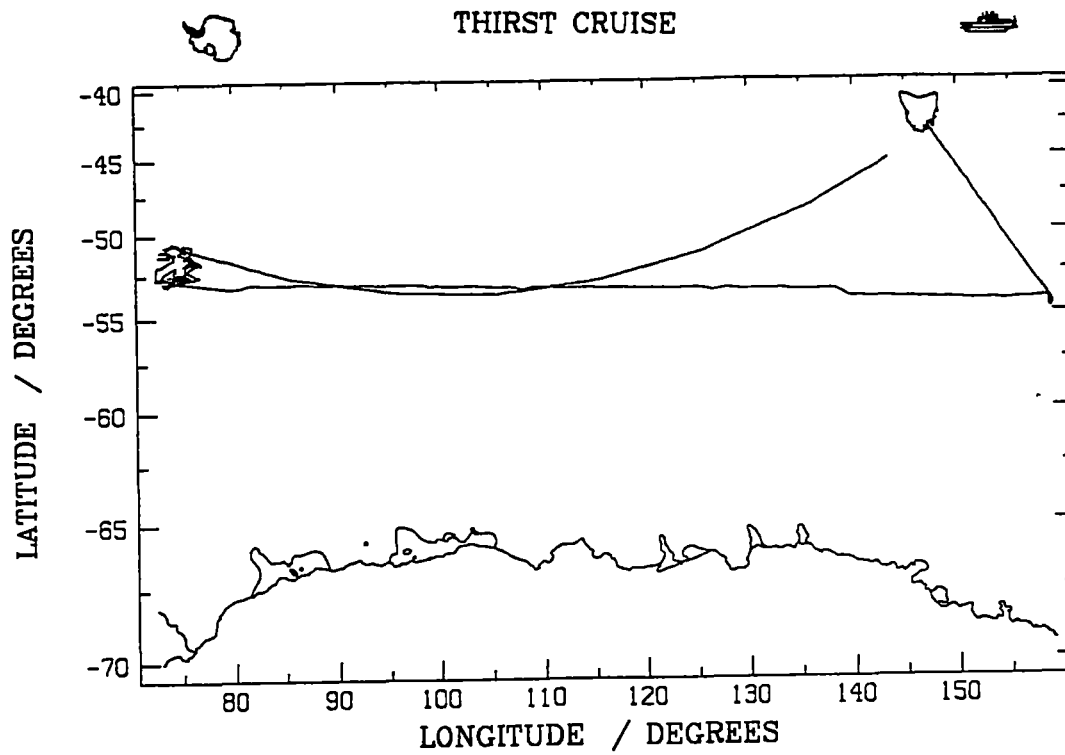

FIGURE 1.1 Voyage 1 (THIRST) transect from August 7 to October 7 (1993).

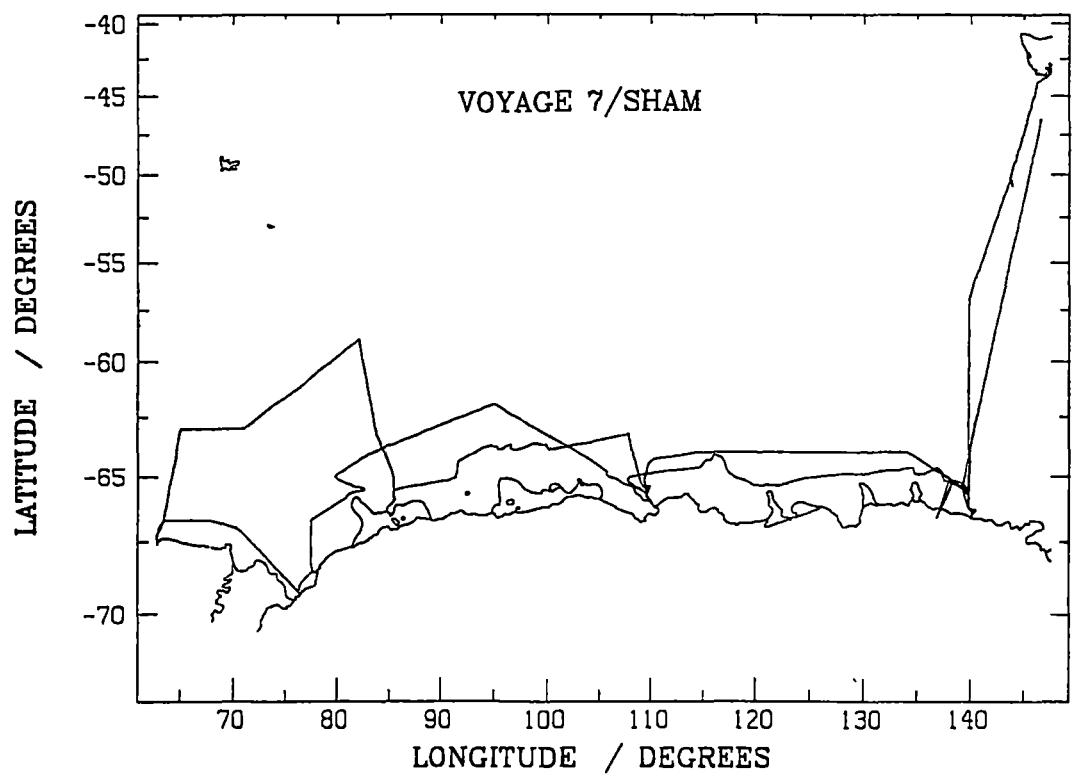

FIGURE 1.2 Voyage 7 (SHAM) transect from January 1 to February 27 (1994).

TABLE 1.1

A summary of the Latitude, Longitude and position description for the THIRST transect.

Date (1993)	Latitude (°S)	Longtitude (°E)	Description
7-Aug	43.3	147.6	departing Hobart
8-Aug	47.2	151.3	
9-Aug	50.1	154.2	
10-Aug	53.2	157.5	
11-Aug	54.2	158.4	arrive/depart Macquarie Island
12-Aug	54.2	153.0	
13-Aug	54.1	146.1	
14-Aug	54.1	140.9	
15-Aug	53.6	136.4	
16-Aug	53.6	132.3	
17-Aug	53.5	127.5	
18-Aug	53.4	123.9	
19-Aug	53.4	118.6	
20-Aug	53.4	113.9	
21-Aug	53.4	108.7	
22-Aug	53.3	102.7	
23-Aug	53.2	97.1	
24-Aug	53.2	93.7	
25-Aug	53.2	89.3	
26-Aug	53.1	83.8	
27-Aug	53.3	79.6	arriving near Heard Island
3-Sep	52.8	74.8	start of marine science at Heard I.
7-Sep	51.4	75.9	
8-Sep	51.2	75.2	
9-Sep	50.7	74.9	
10-Sep	50.7	74.7	
11-Sep	50.6	74.6	most northerly extent of fishing area
12-Sep	51.0	73.5	
13-Sep	51.3	73.5	
14-Sep	51.3	73.6	
15-Sep	51.3	74.3	
16-Sep	52.0	72.7	
17-Sep	52.3	73.4	
18-Sep	52.6	74.3	
19-Sep	52.5	74.9	
22-Sep	52.2	75.5	
23-Sep	51.5	75.8	end of marine science
27-Sep	50.7	76.1	
28-Sep	51.3	77.6	
29-Sep	52.6	84.9	
30-Sep	53.3	92.2	
1-Oct	53.7	100.0	most southerly point on voyage
2-Oct	53.5	107.9	
3-Oct	52.9	115.5	
4-Oct	51.8	122.5	
5-Oct	50.1	129.6	
6-Oct	48.3	136.1	
7-Oct	46.0	141.7	arriving Hobart

TABLE 1.2

A summary of the Latitude, Longitude and position description for the SHAM transect.

Date (1994)	Latitude (°S)	Longtitude (°E)	Description
1-Jan	43.4	147.3	depart Hobart
2-Jan	44.1	146.2	
3-Jan	45.8	145.6	
4-Jan	47.5	144.9	
5-Jan	48.7	144.3	
6-Jan	50.5	143.9	
7-Jan	51.4	143.0	Sub-Antarctic Front
8-Jan	53.1	142.1	Polar Front
9-Jan	55.0	141.0	
10-Jan	56.5	140.1	
11-Jan	58.4	139.9	turning point in SR3 transect
12-Jan	59.9	139.9	
13-Jan	61.8	139.9	
14-Jan	63.4	139.9	
15-Jan	65.2	139.9	end SR3 transect (Dumont D'urville)
22-Jan	64.8	108.7	150 km NW of Casey
23-Jan	63.5	104.9	
24-Jan	63.9	96.0	
25-Jan	65.3	88.5	
26-Jan	65.9	85.4	start of PETE transect
27-Jan	64.6	85.0	
28-Jan	62.8	83.5	
29-Jan	60.4	82.6	
30-Jan	59.9	79.6	finished PETE transect
31-Jan	62.7	71.8	
1-Feb	63.5	64.8	
2-Feb	67.0	63.0	arrive Mawson
5-Feb	67.5	62.9	depart Mawson
6-Feb	67.5	71.6	
7-Feb	68.7	77.1	near Law Base and Davis
8-Feb	66.7	77.5	
9-Feb	65.5	82.6	
10-Feb	64.0	83.9	
11-Feb	62.9	90.0	
12-Feb	63.3	99.7	
13-Feb	65.1	106.1	heading into Casey
19-Feb	64.0	118.3	depart Casey
20-Feb	64.0	130.3	
21-Feb	65.8	139.4	arrive Dumont D'urville
25-Feb	62.4	140.7	depart Dumont D'urville area
26-Feb	56.8	143.0	Polar Front
27-Feb	50.4	145.3	near Hobart

1.2 Motivation

In general, there are two types of sea surface temperature. *Bulk SST* is the traditional sea surface temperature measured *in situ* by ship and buoy based thermometers and is representative of the upper few metres of the ocean. Thermal infrared radiometers measure the temperature of the upper few microns (0.05 mm) of the ocean surface (Maul 1985). The resulting radiometrically-derived temperature is known as the *Skin SST*. Previous research has shown that, given typical conditions over tropical and temperate oceans, the skin SST is 0.1 °C to 0.5 °C cooler on average than the bulk SST. Previous studies have indicated that this temperature difference (ΔT) is due mainly to the presence of a thermal boundary layer, which is a consequence of surface evaporation and the molecular conductive processes of heat transfer across the air-sea interface (Robinson *et al.* 1984; Hepplewhite 1989). This thesis will examine the sign and magnitude of ΔT with respect to skin and bulk temperature measurements taken in the Southern Ocean and will relate ΔT to the overall air-bulk temperature difference (ΔT_{ab}) as well as to diurnal and cloud cover variations.

To date, there has been little examination of ΔT in the Southern Ocean between Australia and Antarctica at high latitudes. Hepplewhite (1989) conducted research from the equator down to high latitude waters in the Southern Atlantic Ocean. Some general comparisons between the Hepplewhite data and the data presented in this thesis will be discussed.

Radiometric skin SST measurements can assist in the interpretation of satellite derived SST. The Advanced Very High Resolution Radiometer (AVHRR) carried by the NOAA series of satellites can currently estimate SST with a standard error of 0.6 °C using conventional bulk SST as ground truth (Robinson *et al.* 1984). If AVHRR is coupled with vertical sounding profile data (TOVS), then it is estimated that the standard error will be about 0.3 °C (Schluessel *et al.* 1987). It is anticipated that by using the latest European Earth Resources Satellite (ERS-1)

Along Track Scanning Radiometer (ATSR) data, a standard error of 0.2 °C can be obtained (Robinson *et al.* 1984; Prata *et al.* 1990).

The problems of the validation of satellite SST measurements relate to the *in situ* data quality and the space and time distribution of the data. There is also the fact that the radiative effects of the atmosphere may not be properly corrected. An investigation into the sign and magnitude of ΔT is a vital first step in solving the satellite SST validation problem. The current *in situ* data quality for SST depends on the quality of data obtained from Voluntary Observing Ships (VOS) or ships of opportunity and the data collected from drifting buoys. These temperatures are not representative of the true skin SST. Ship and/or airborne radiometric measurements of skin SST will provide a more appropriate *in situ* data set on which to base atmospheric correction algorithms.

In situ radiometric measurements can provide SST values with a standard error of 0.1 °C and therefore provide better quality ground truth for the satellite radiometric sensors. It is not always possible to deploy *in situ* radiometers on board ships on a regular basis and so a greater understanding of the factors that influence the skin/bulk temperature difference (ΔT) is needed. This thesis will ultimately examine the possibility of deriving skin SST values from meteorological data (including air temperature, wind speed and direction) and bulk SST based on a simple model of ΔT for the Southern Ocean. The sign and magnitude of ΔT is an important measure of the exchange of heat and water vapour between the ocean and the atmosphere and is therefore relevant to the weather and climate issues associated with global climate prediction and modelling. A further objective would be to provide a means of estimating bulk SST given satellite measurements of air and skin SST temperature. This is important as it allows satellite images such as AVHRR, to be turned into bulk SST maps.

The Antarctic Cooperative Research Centre (Antarctic CRC) is based in Hobart, Tasmania at the University of Tasmania and is divided into a series of sub-programs involving research in the Antarctic and Southern Ocean

environment. One of these sub-programs is Southern Ocean Processes which, amongst other things, studies heat and carbon dioxide transport across the ocean/atmosphere interface and the relationship these have to present and future climates. This sub-program contributes to the international effort in global modelling which includes the World Ocean Circulation Experiment (WOCE); the World Climate Research Program (WCRP) and the Joint Global Ocean Flux Study (JGOFS).

1.3 User Requirements of SST

A number of users have identified particular requirements of SST measurements in relation to a variety of physical and chemical processes in the ocean and atmosphere. The WCRP require global SST fields to determine the lower boundary conditions of the global atmosphere to within 0.5 °C. In tropical regions for SST values greater than 28 °C, the acceptable error is 0.3 °C (Minnett *et al.* 1984; WCRP 1986). These requirements will enable a better understanding of the El Nino Southern Oscillation (ENSO) episodes, in which a cooling of less than 0.5 °C in the Western Pacific is associated with the eastward migration of the West Pacific-Indonesian convection regime (WCRP 1986).

SST values are required to estimate the poleward flux of heat in the North Atlantic Ocean between 20° N and 60° N (CAGE experiment). The desired SST accuracy for the CAGE experiment is 0.25 °C. Large scale SST anomalies can produce significant variations in the circulation of the atmosphere. The Eastern Tropical Pacific and Tropical Atlantic Oceans are the most sensitive regions and an accuracy of 0.5 °C in SST is required for these regions (Robinson *et al.* 1984; WCRP 1986).

It is estimated that volcanic eruptions can change the global temperature by a few tenths of a degree over a 1 to 2 year period. The accuracy needed in the SST measurements in order to detect these changes is 0.1 °C (WCRP 1986). The

measurable effects of CO_2 warming will also require a similar order of accuracy (Robinson *et al.* 1984).

Sea surface temperature influences the rate of evaporation which plays a pivotal role in the formation of cloud and associated weather systems. Anomalies in the SST field may therefore effect the development of local weather patterns (Minnett *et al.* 1984; WCRP 1986).

Deep convection in the ocean is important in the production of bottom water in the ocean. Deep convection has been observed at high latitude in the Weddell Sea, where the process is associated with intense cooling of the surface over a period of a few days. The changes in SST are relatively small, between 0.1 and 0.3 °C, although the cooling is spread through depths of 1 to 4 km. An accuracy of 0.05 °C is thus required and could be obtained using *in situ* radiometry.

A climatological data base of SST can best be achieved from satellite coverage. In the past, SST information was dependent on the measurements taken by merchant ships, often subject to large standard errors of the order of 0.5 °C. The coverage of these so called ships of opportunity is also limited by their respective trade routes (see Figure 1.3). A satellite data base could be achieved providing SST to an accuracy of up to 0.2 °C provided that quality *in situ* radiometric ground truth data is obtained over a large enough area.

Most applications of SST require an accuracy of between 0.1 and 0.5 °C. The ΔT values can have a similar order of magnitude and so a better understanding of the meteorological and oceanographical factors that influence the sign and magnitude of ΔT is thus important to ocean heat flux studies, atmospheric circulation, global climate and weather prediction.

1.4 Objectives

The objectives of this study are summarised as follows:

(a) To deploy simple and economical radiometers (the Everest 4000ALCS™) in the Southern Ocean on board the RSV *Aurora Australis*, to obtain quality *in situ* measurements of skin SST. This follows on from the work done in Australian tropical and subtropical waters by Michael & Skirving (1991) and in the Southern Ocean (Rapier 1992).

(b) To collect supporting meteorological and ship data such as the latitude; longitude; universal time; bulk SST; air temperature; quantum radiation; wind speed and direction.

(c) To ensure that the data collected is calibrated and that erroneous data is removed.

(d) To investigate the difference between skin SST and bulk SST and to relate this difference (ΔT) to other meteorological observations.

In general, *in situ* radiometric skin SST can be used to validate satellite derived SST. A simple model of ΔT will allow for estimates of bulk SST to be made from satellite measurements of skin SST and air temperature.

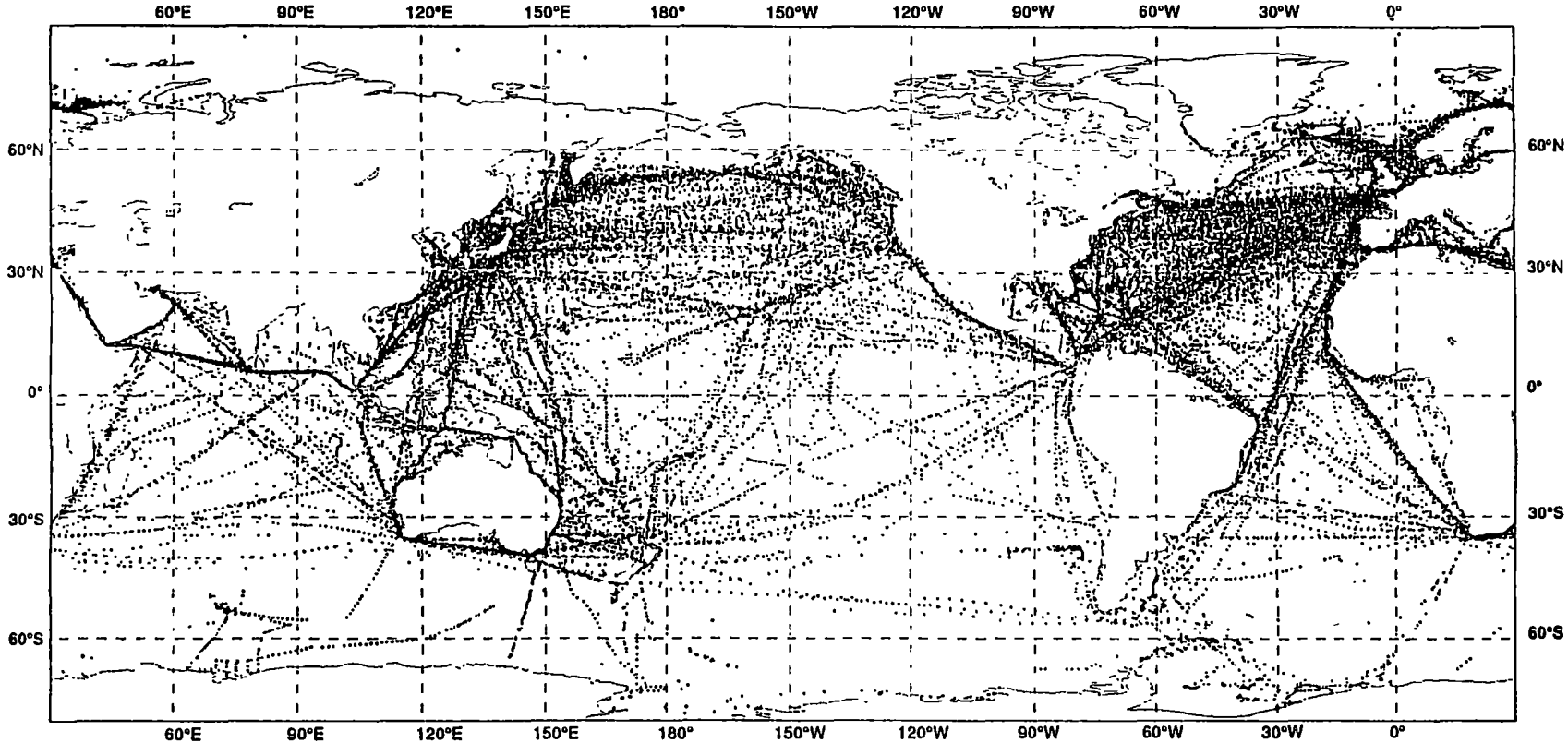

FIGURE 1.3 Global shipping routes received during February 1992 by the French National Meteorological Centre. Note that there were very little shipping movements in the Southern Ocean as compared to the northern hemisphere (from GCOS 1992).

Chapter 2

CHAPTER 2: A Review of Skin and Bulk SST Measurement

2.1 Introduction

This chapter gives a general overview of the physics of infrared radiation associated with the ocean surface. The thermal structure of the upper layers of the oceans will be discussed, including the conductive thermal boundary layer; the convective turbulent layer and the mixed homogeneous layer. The formation of diurnal deck layers will be mentioned along with the various environmental factors that affect the skin-bulk temperature difference ΔT.

A review of laboratory and field work associated with the oceanic thermal boundary layer and the measurement of ΔT is included as well as a description of the Saunders (1967b) model. The observations of ΔT in the Southern Ocean by Hepplewhite (1989) will be discussed along with measurements collected by other researchers mostly in the tropical, sub-tropical and temperate regions of the globe.

A description of some of the different types of radiometers used for both *in situ* and airborne SST measurements will be included as well as a review of satellite radiometric measurements of SST.

2.2 The General Principles of Radiation

All surfaces with a temperature greater than absolute zero (0 kelvin or -273.15 °C) will emit electromagnetic radiation (Lillesand & Kiefer 1987). The amount of energy that an object radiates is a function of the surface temperature of that object and is described by the basic law of blackbody emission, *Planck's Law* which states that

$$M_\lambda^* = \frac{C_1}{\left[\lambda^5\left(\exp\left(C_2 / \lambda T\right)-1\right)\right]} \tag{2.1}$$

where M_λ^* is the spectral radiant exitance ($Wm^{-2}\ \mu m^{-1}$) emitted at wavelength λ (μm) by a body at temperature T in kelvin. Constants C_1 and C_2 have values

$3.74\times 10^{8}\ W\mu m^{-4}m^{2}$ and $1.44x10^{4}\ \mu mK$ respectively (Robinson 1985; Henderson-Sellers & Robinson 1986).

The wavelength of maximum emission for a body at a particular temperature is inversely proportional to the temperature and is expressed by *Wien's Law* which states that

$$\lambda_{max} = \frac{2897(\mu m\, K)}{T(K)} \tag{2.2}$$

This formula is obtained by the differentiation of equation (2.1). If we take the Sun as having a temperature of 5800 K, the associated peak spectral radiant exitance occurs at 0.5 μm, which lies in the visible part of the spectrum. If we take the Earth as having a temperature of 255 K, then the peak spectral radiant exitance occurs at 11.4 μm which is in the thermal infrared part of the spectrum (Henderson-Sellers & Robinson 1986; Lillesand & Kiefer 1987; Harris 1987).

The integration of the Planck's law (2.1) gives the area under each curve as shown in Figure 2.1a, which is the total energy emitted by a body and is expressed by the *Stefan-Boltzmann law*

$$M^{*} = \sigma T^{4} \tag{2.3}$$

where M^{*} is the total radiant exitance in Wm^{-2}. The Stefan-Boltzmann constant (σ) is $5.6697\times10^{-8}\ Wm^{2}\,K^{-4}$ and T is the absolute temperature in kelvin of the emitting material (Robinson 1985; Lillesand & Kiefer 1987; Szekielda 1988).

The above three laws relate to objects that behave as a *blackbody*, which is defined as a perfect radiator that absorbs and re-emits all energy incident upon it (Sabins 1973). Real objects are not blackbodies. The emissivity of a material indicates how efficiently a real object radiates energy as compared to that of a blackbody.

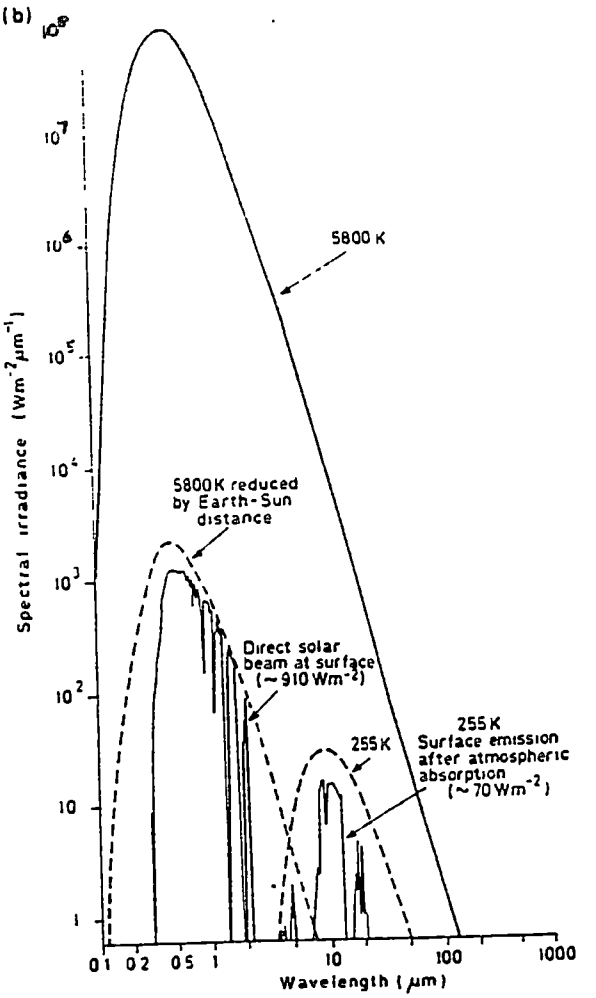

FIGURE 2.1a The distribution of spectral irradiance for bodies radiating at temperatures of 255 K and 5800 K(from Henderson-Sellers & Robinson 1986).

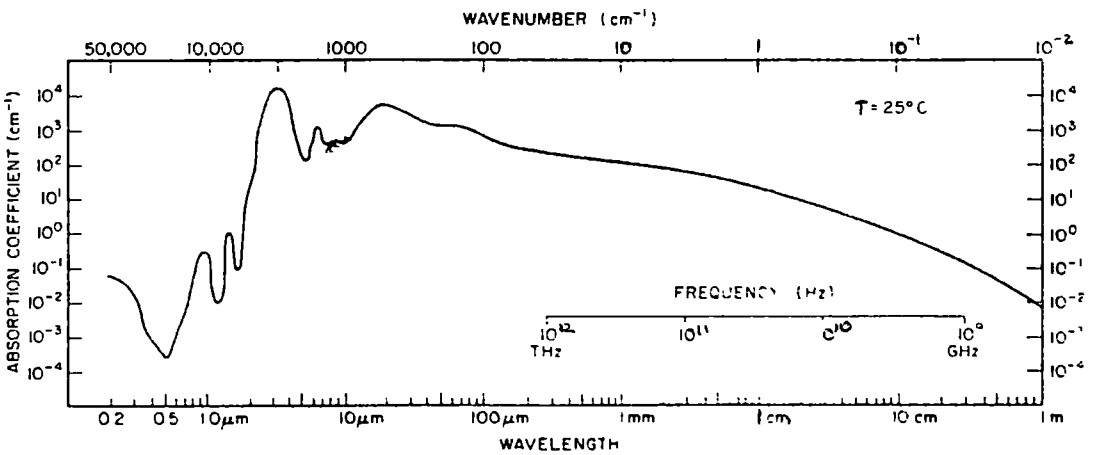

FIGURE 2.1b Absorption Coefficients for pure water. The depth of emission of thermal radiation in the 8-13 μm window is about 0.05 mm (from Maul 1985).

The emissivity ε is hence the simple ratio of the radiant exitance of a real body M_λ to the radiant exitance from a blackbody M_λ^* at a particular wavelength at the same temperature. The emissivity is therefore expressed as

$$\varepsilon = \frac{M_\lambda}{M_\lambda^*} \tag{2.4}$$

The Stefan-Boltzmann Law (2.3) can be modified to include an emissivity term so that

$$M = \varepsilon \sigma T^4 \tag{2.5}$$

The emissivity will vary depending on the nature of the emitting object. Solids and liquids radiate across a continuous spectral interval, with an emissivity which remains relatively constant, usually between 0.9 and 1.0 and are sometimes referred to as *greybodies*. Gases on the other hand radiate only at specific wavelengths and as a result have variable emissivity and are some times referred to as selective radiators (Henderson-Sellers & Robinson 1986; Lillesand & Kiefer 1987). Interpretation of satellite imagery needs to take into account the atmospheric gases that behave as selective radiators and absorbers of radiation. The sea surface however behaves as a greybody whose emissivity ranges between 0.95 and 0.99 assuming a thermal infrared spectral band of 8-14 μm (Sidran 1981). A detailed study of the emissivity of Lake Ontario, Canada (Davies *et al.* 1971) found that the emissivity of the lake water ranged from between 0.952 to 0.989 with an average of 0.972 (±0.021). The spectral behaviour of sea water was examined by Salisbury & D'Aria (1992) and found that for an 8-14 μm window, sea water had a reflectance of 1% or an emissivity of 0.99. The difference between clear sea water and sea water with foam appears to be minimal (Salisbury & D'Aria 1992).

The total radiant exitance (M_{total}) from the sea surface consists of the radiant exitance from the sea surface (M_{sea}) and the reflected radiant exitance

from the sky (M_{sky}). From equation 2.5, the emitted component of radiation from the sea surface can be expressed as

$$M_{sea} = \varepsilon \sigma T_{sea}^4 \tag{2.6}$$

where T_{sea} is the temperature of the sea surface in kelvin. The component of radiant exitance reflected from the sea surface can be expressed as

$$M_{sky} = \alpha \sigma T_{sky}^4 \tag{2.7}$$

where T_{sky} is the temperature of the sky in kelvin and $\alpha = 1 - \varepsilon$. Combining equations 2.6 and 2.7 gives the total radiant exitance from the sea surface

$$M_{total} = \varepsilon \sigma T_{sea}^4 + (1-\varepsilon)\sigma T_{sky}^4 \tag{2.8}$$

Now the radiometer gives us a brightness temperature T_S such that

$$M_{total} = \sigma T_S^4 \tag{2.9}$$

where T_S is the temperature of a blackbody which would produce the amount of radiation as measured by the radiometer. We can then relate the sea surface temperature T_{sea} to the temperature as measured by the radiometer T_S by combining equations 2.8 and 2.9 so that

$$\sigma T_S^4 = \varepsilon \sigma (T_{sea})^4 + (1-\varepsilon)\sigma (T_{sky})^4 \tag{2.10}$$

Re-expressing equation 2.10 in terms of T_{sea}, we get

$$T_{sea} = \left[\frac{(T_S)^4 - (1-\varepsilon)(T_{sky})^4}{\varepsilon} \right]^{\frac{1}{4}} \tag{2.11}$$

The above formula allows for a correction to be applied to the measured sea surface temperatures T_S for the reflected component of down-welling sky radiation T_{sky} given a value for emissivity (ε).

2.3 The Oceanic Skin Effect and ΔT

A radiometer detects thermal infrared radiation emitted from a thin layer of water molecules that lie close to the surface. The thermal radiation between 8 and 13 μm is emitted from the top few microns of the ocean. Figure 2.1b is a plot of the absorption coefficient (e) against the wavelength of emitted radiation. The probability of a photon passing through a unit distance of pure water is 1/e, the e-folding distance. In the thermal infrared window between 8 and 13 μm, the absorption coefficient lies between 10^2 and 10^3 cm^{-1}. The mean reciprocal yields the e-folding distance of about 0.05 mm (Maul 1985) The *skin* SST is therefore defined as the temperature of the top 0.05 mm of the water column.

The *bulk* SST of the ocean can be defined as the temperature of the mixed layer of the sea, usually sampled 1 to 3 metres below the surface on ships via CTD, XBT, bucket thermometers, ship intake water or by drifting meteorological buoys. Many studies have found that on average , the skin SST is of the order of 0.1 to 0.5 °C cooler than the bulk SST. The difference between the skin SST and the bulk SST is sometimes referred to as the *skin effect* or ΔT (Ball 1954; Ewing & McAlister 1960; Saunders 1973; Katsaros 1980; Hepplewhite 1989; Schluessel *et al.* 1990; Coppin *et al.* 1991). The skin effect exists because there is usually a flux of heat between the ocean and the atmosphere over the top few centimetres of the ocean resulting from a combination of conductive and convective heat transfer processes. Figure 2.2 summarises the physical processes which can influence the air-sea interface and therefore the skin effect. A model of the total heat flux Q_N (Wm^{-2}) associated with this interface can be written as

$$Q_N = Q_I + Q_{IR} + Q_G + Q_H + Q_L \qquad (2.12)$$

where $Q_I(\mathrm{Wm}^{-2})$ is the incoming solar radiation. $Q_{IR}(\mathrm{Wm}^{-2})$ is the infrared radiation emitted by the sea surface. $Q_G(\mathrm{Wm}^{-2})$ is the down-welling infrared radiation from the sky, clouds and atmosphere $Q_H(\mathrm{Wm}^{-2})$ is the sensible heat flux and $Q_L(\mathrm{Wm}^{-2})$ is the latent heat flux and are both related to the turbulent transfer of sensible heat and water vapour respectively between atmosphere and ocean. The sensible heat is dependent on the air-sea temperature differences which in turn depend on wind speed, wind direction, solar radiation and the diurnal cycle.

A diurnal thermocline can result from absorbed solar radiation where a warm deck layer may form in the top few metres (see Figure 2.2). The diurnal thermocline will be at its maximum on a calm and sunny afternoon as the lack of wind prevents the sun-warmed water from mixing downward. The warmed water is more stable as it is less dense than the cooler water below. Under conditions of strong winds, there will be greater shear stresses acting on the ocean surface. This in turn generates orbital wave motion and turbulence in the upper layers of the ocean. This will result in a breakdown of the diurnal deck layer as the solar heat becomes more uniformly mixed in the top few metres (Hepplewhite 1989).

The diurnal deck layer, as shown in Figure 2.2, is affected by the amount of incoming solar radiation that is absorbed at depth. If we again consider Figure 2.1b, then the absorption coefficient of pure water at 0.5 μm, is between 10^{-3} and 10^{-4} cm^{-1} (Maul 1985). The mean reciprocal of the absorption coefficient gives an e-folding distance of about 50 metres. The shape of the diurnal deck layer and the diurnal thermocline relates to the probability of a given amount of solar radiation being absorbed at a unit depth in the water column. Most of the solar radiation (about 90%) is absorbed in the top 2 to 3 metres and it is in this layer of the ocean, that diurnal deck layers are most likely to form.

Under most circumstances, the net upwards heat flux Q_N is positive in that the surface loses heat to the atmosphere. This results in a cooler skin layer or thermal boundary layer and it is through this layer that the strongest temperature gradients occur (McAlister & McLeish 1969; Katsaros 1980).

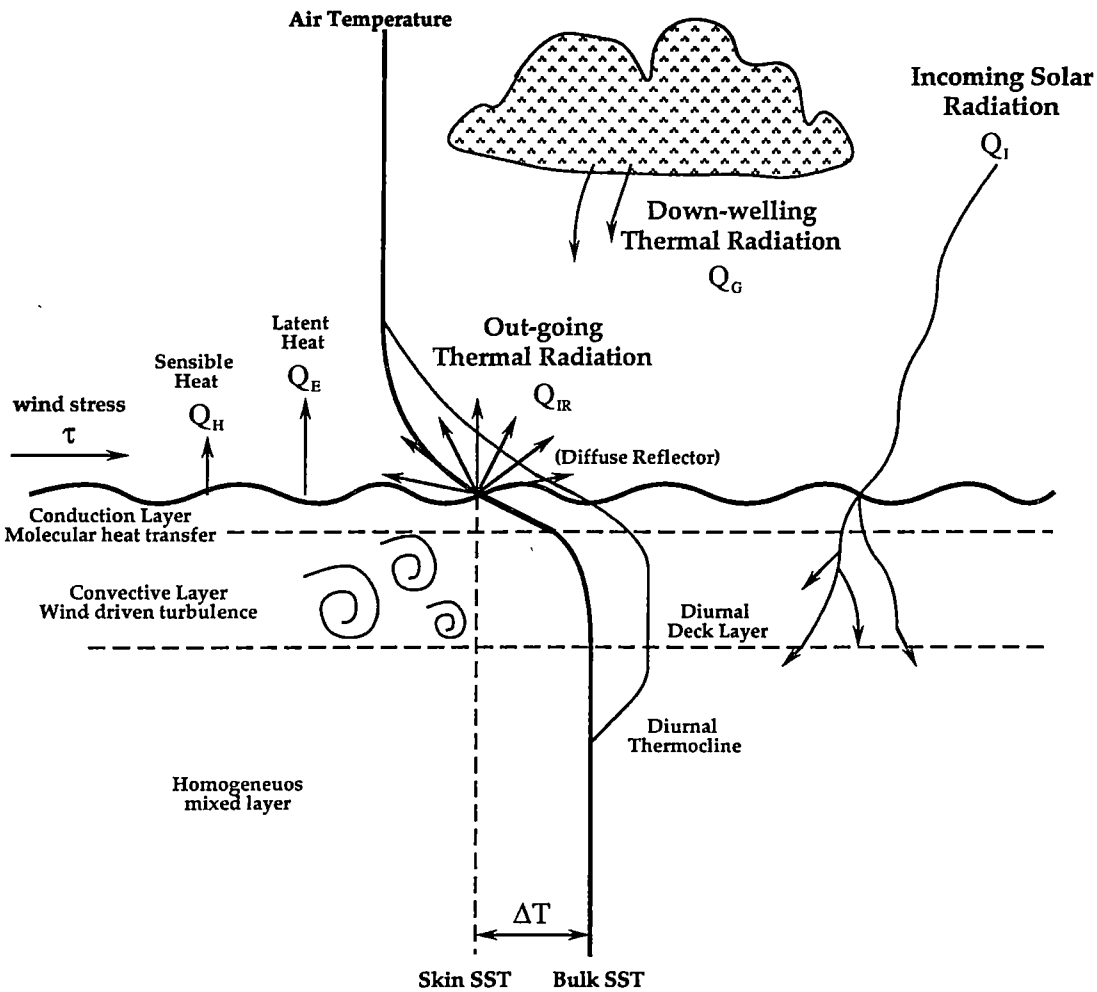

FIGURE 2.2 The factors that influence the sign and magnitude of ΔT.

In general, if the air is dry and cooler than the sea, then there will be an upwards heat flux or a transfer of heat from the sea to the air above. Alternatively, negative or downward heat fluxes can occur when the air is warm and humid which results in warmer skin temperatures. This has been seen to occur in tropical waters (Hepplewhite 1989).

2.4 The Heat Transfer Mechanics Associated with ΔT

Heat transfer across the air-sea interface results from conduction and/or convection processes. Figure 2.3 shows a skin-bulk temperature profile that exists in the upper few centimetres of the ocean when heat is being transferred from the ocean surface to the atmosphere above.

2.4.1 The Conduction layer

The conduction layer is of the order of 0.5 mm in thickness (McAlister & McLeish 1969). Work done by Khundzhua *et al.* (1977) estimated the thickness of the conduction viscous layer to be between 0.2 mm and 0.6 mm. This conduction layer is reported to have a linear temperature profile that decreases with depth (Khundzhua *et al.* 1977). This will only occur if the skin temperature is cooler than the bulk temperature.

The main heat transfer mechanism across the conduction layer is by molecular heat exchange or evaporation. The viscosity of the conduction layer makes it more resistant to wind driven turbulence such that the conduction layer maintains itself for wind speeds up to 10 ms^{-1} (19 knots). For higher wind speeds, the destruction of the viscous conduction layer by white capping or breaking waves becomes more dominant (Grassl 1976). The destruction of the viscous layer will be common in the Southern Ocean as wind speeds exceed 20 knots on a regular basis.

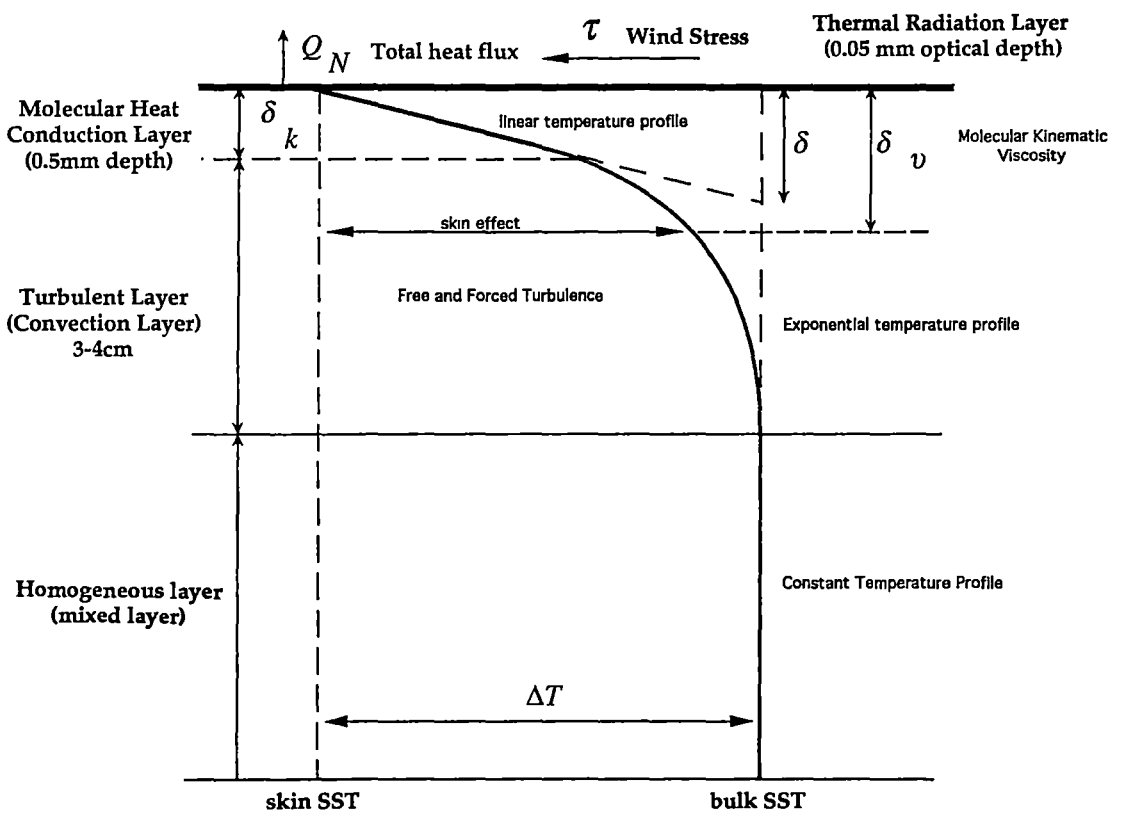

FIGURE 2.3

Schematic diagram defining the upper layers of the ocean (after Robinson *et al.* 1984).

2.4.2 The Turbulent Layer

The turbulent layer or convective layer is immediately below the conduction layer. It consists of water that is mostly in turbulent motion induced either by wind forced turbulence or by gravitational instability (free turbulence) resulting from evaporation and surface cooling (McAlister & McLeish 1969). This transitional turbulent convective layer has a decreasing exponential temperature profile which has been reported to exist to a depth of about 3.5 mm (Khundzhua *et al.* 1977). The precise depth of this turbulent layer is unknown but the thickness of both the conductive and convective layers is dependent on wind speed. For strong winds greater than 10 ms^{-1}, the forced turbulence becomes dominant and heat exchange comes directly from depths lower than the conductive layer. Mechanical heat transfer of this type can occur as a result of the formation of capillary waves. It should be emphasised that for strong winds greater than 10 ms^{-1}, the conduction layer can still exist thus resulting in both conductive and convective heat transfer mechanisms occurring at the same time (McAlister & McLeish 1969; Grassl 1976).

A discussion of the turbulent layer is particularly relevant for Southern Ocean research were wind speeds can exceed 30 ms^{-1} (60 knots). At these wind speeds, heat transfer via forced turbulence is going to be dominant.

2.4.3 Homogeneous Layer

Below the turbulent layer, there is the homogeneous layer otherwise known as the mixed layer of the ocean wherein the temperature remains relatively constant with increasing depth. It is in this homogeneous layer that bulk SST are normally sampled. The homogeneous layer can be affected by the absorption of incoming solar radiation in the top 2 to 3 metres thus forming a diurnal deck layer during clear sunny days. This will only occur for very low wind speeds and is a function of absorbed solar radiation with depth as described in section 2.3.

2.5 The Saunders Theoretical Model

Saunders (1967b) developed a dimensional argument (see Figure 2.3) relating the thickness of the shear layer (δ_υ) to the molecular kinematic viscosity (υ) and the friction velocity in the water U_* is defined as $(\tau/\rho)^{1/2}$ where τ is the surface shear stress and ρ is the water density. Saunders wrote

$$\delta_\upsilon \sim \frac{\upsilon}{U_*} \tag{2.13}$$

The heat transfer through the conduction layer δ_k is by molecular conduction k over a depth z such that

$$k\frac{\partial T}{\partial z} = -Q_N \tag{2.14}$$

Now most of the temperature gradient occurs across the conduction layer δ_k which means that

$$\frac{\partial T}{\partial z} = -\frac{\Delta T}{\delta} \tag{2.15}$$

Now if we assume δ to be approximately equal to δ_υ and on re-arranging equations 2.13, 2.14 and 2.15, we obtain

$$Q_N \sim \frac{k\,\Delta T\,U_*}{\upsilon} \tag{2.16}$$

If we now adopt a dimensionless constant of proportionality λ, we can re-arrange 2.16 to provide an estimate of ΔT such that

$$\Delta T = \frac{\lambda Q_N \upsilon}{k U_*} \tag{2.17}$$

The usefulness of formula 2.17 in the prediction of ΔT is based on the assumption that the heat flux through the sea surface Q_N can be determined

accurately. Another way of looking at the Saunders model (equation 2.17) is to express Q_N as a function of ΔT such that

$$Q_N = \frac{k \Delta T U_*}{\lambda \upsilon} \tag{2.18}$$

If radiometry is used to measure ΔT, then the value of the vertical heat flux Q_N can be determined relatively simply.

There are a number of potential problems with equations 2.17 and 2.18. The main concern is that under the high wind speeds found in the Southern Ocean, the thermal conductive cool-skin layer will be physically disrupted through white capping (Coppin *et al.* 1991). There is also some uncertainty in the shear stress as it has been reported that some of this stress goes into wave generation (Grassl 1976), as opposed to the production of mechanical turbulence.

The friction velocity U_* may become very small at low wind speeds. In this situation, equation 2.17 becomes undefined (Coppin *et al.* 1991). The value of λ is uncertain, having been reported to lie between 2.2 and 15 at an average of about 6.5 (Robinson *et al.* 1984). This variation in λ values could be due to the inclusion by some authors of solar radiation absorbed within the conduction layer. It has been suggested that λ is more likely to be a variable dependent on wind speed, solar radiation, wave action and the surface tension conditions that act on the air-sea interface (Coppin *et al.* 1991).

2.6 A Review of Laboratory and Field Work

The skin effect has been studied by a number of authors over the past 50 years. Woodcock & Stommel (1947) and Ball (1954) were two of the earliest works suggesting that the temperature of the ocean was less than that of the layers beneath. After Saunders (1967b) had developed a theoretical model of the skin effect, there was interest shown by a number of authors through the seventies (eg. Witting 1972; Grassl 1976; Schooley 1977; Katsaros 1977).

Reviews of work done were written in the eighties by Katsaros (1980), Simpson & Paulson (1980), Paulson & Simpson (1981), and Bradley (1982). Recent work has focussed on the validation of satellite derived sea surface temperatures, for example Robinson *et al.* (1984), Bernstein & Chelton (1985), Schluessel *et al.* (1987) and Dalu & Liberti (1988). Some recent studies have dealt with the skin effect and its impact on remote SST observations (Hepplewhite 1989; Schluessel *et al.* 1990; Coppin *et al.* 1991; Michael & Skirving 1991; Rapier 1992).

2.6.1 Laboratory Measurements

The laboratory experiments conducted in order to determine ΔT values were conducted in a controlled environment which allows for optimum accuracy to be obtained. However, some of the physical processes that occur in the field may not be taken into account due to the complexity of the ocean/atmosphere interface. Authors have in general simulated these conditions by introducing artificial wind and waves into their experiments. For example, Miller and Street (1978) made measurements at the Stanford Wind, Water Wave Research Facility, in which waves could be generated mechanically using a wave plate, and air flow generated by an airfoil-bladed centrifugal fan. Chang and Wagner (1975) used the TRW Engineering Science Laboratory wave tank facility, which allowed the frequency and amplitude of the waves to be varied.

The methods commonly adopted for measuring skin SST are by using thermal infrared radiometers. Measurements of the temperature of water below the surface have generally been made using mercury or electric thermometers at varying depths and with varying resolution. Paulson and Parker (1972) used such a method to relate ΔT to the evaporation and heat loss as air was blown over the water surface. Ewing and McAlister (1960), Hill (1972) and Katsaros (1977) all adopted a technique of stirring the surface, thus breaking down the skin layer or the molecular conduction layer. This then allows the surface temperature to be equal to the temperature of the water a few centimetres below. The accuracy of

such a technique is potentially greater as the same instrument is used to measure both the skin temperature and the bulk temperature, removing the chance of instrumental bias. Ewing and McAlister (1960) found that a skin effect of -0.6 °C re-established itself 10 seconds after the effect of wind turbulence was removed.

2.6.2 Field measurements

Katsaros (1977) reports the use of radiometric techniques on board the research vessel *Gauss* in 1973. The radiometer was mounted 4 metres above the water and the skin layer was periodically broken up by throwing buckets of water which had been drawn from 0.5 metres depth. It was found that given low wind speeds and air-sea temperature differences (ΔT_{ab}) of -4.2 °C, that ΔT values were -0.7 °C (±0.1 °C) over 17 observations. Katsaros (1977) plotted a graph of ΔT against ΔT_{ab} shown here as Figure 2.4. This graph is a plot of eight different studies and indicates a possible correlation between ΔT and ΔT_{ab}.

Simpson & Paulson (1980) observed SST and wave heights from the manned spar buoy FLIP about 100 km off the coast of Baja, California. A Barnes PRT-5 radiometer was situated at the end of a boom extended out to the port side of the ship. It was observed, in 1 metre amplitude waves, that there were warm temperature spikes corresponding to a breakdown in the conduction layer as a result of wave action. The ΔT values were estimated to be the difference between the mean and the maximum of a time series plot of the radiometric skin SST. It was found that ΔT was of the order of -0.3 °C.

Hasse (1963) adopted an interesting technique where ΔT was estimated using calibrated platinum resistance thermometers. One thermometer measured the temperature of the water at 0.5 metres depth and the other measured the air temperature profile between 0.8 metres and 13.6 metres above the water. When a uniform potential temperature gradient was observed in the air column above the surface, the skin SST was assumed to equal the air temperature extrapolated to the sea surface. The ΔT values were observed to be -0.2 °C on average.

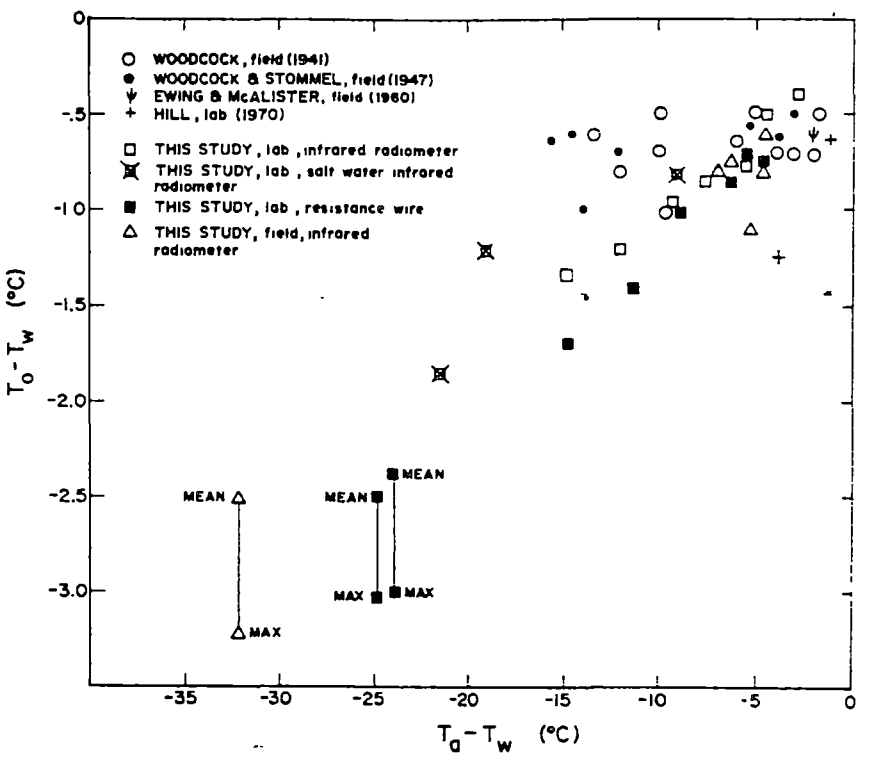

FIGURE 2.4

Scatter plot of skin-bulk (ΔT = To-Tw) against air-bulk (ΔT_{ab} = Ta-Tw) obtained from a number of previous field and laboratory studies. There appears to be a correlation between ΔT and ΔT_{ab} (from Katsaros 1977).

Hasse (1971) derived an expression relating ΔT to incoming short wave radiation Q_I, latent and sensible heat transfer Q_H and wind speed U such that

$$\Delta T = C_1 \cdot \frac{Q_H}{U} + C_2 \cdot \frac{Q_I}{U} \tag{2.19}$$

where C_1 and C_2 are constants. It was found that ΔT ranged between -0.1 and -0.4 °C for wind speeds of 7 ms^{-1} in the Equatorial Atlantic Ocean.

Grassl (1976) used a Barnes PRT-5 radiometer mounted on the side of the German research vessel *Planet* as a part of the GARP Atlantic Tropical Experiment in order to study ΔT. The radiometer measurements were compared to bucket SST measurements. The ΔT values were found to be between -0.17 °C and -0.21 °C. Grassl (1976) makes mention that for high wind velocities (greater than 10 ms^{-1}), the destruction of the conduction layer by white capping or breaking waves is dominant. For speeds less than 10 ms^{-1}, the conduction layer in general remained intact.

The work done by Schluessel *et al.* (1990) in November 1984 examined ΔT in the North Atlantic Ocean by taking radiometric measurements of skin SST and ship bulk temperature measurements over a period of 6 weeks between latitudes of 20° N and 50° N on the German research vessel *Meteor*. Observed ΔT values ranged from -1 °C to +1 °C with a mean of -0.2 °C. The PRT-5 radiometer was oriented at a 53° angle from the downward vertical. This angle corresponds to the Brewster angle and was adopted to minimise the contribution of reflected sky radiation. Corresponding bulk SST measurements were made at depths of 0.1, 2, 4 and 7 metres using platinum resistance thermometers. An Eppley pyrgeometer was used to measure the down-welling longwave radiation. The incoming solar radiation was measured using a Kipp und Zonen pyranometer in order to determine the radiative heat balance. Dry and wet bulb temperatures were taken to estimate the sensible and latent heat fluxes. In addition, the wind speed, wind direction and ship speed were recorded.

A model was derived to estimate ΔT during daytime where ΔT is related to the net solar radiative flux Q_I, the net longwave flux Q_{IR}, the wind velocity U and the water vapour mixing ratios of the sea surface and the atmosphere $q_s - q_a$ so that

$$\Delta T = a_0 + a_1\left(Q_I/U\right) + a_2(q_s - q_a) + a_3 Q_{IR} \tag{2.20}$$

where the (a_i) values are constants. It was found that mean ΔT values of -0.3 °C were observed at night and -0.11 °C during the day with a standard error of ±0.17 °C. It appeared that ΔT had a larger magnitude at night under clear skies. It was recommended by Schluessel *et al.* (1990) that night time comparisons be made between SST derived by satellite and *in situ* skin temperatures so as to avoid the effect of diurnal thermocline formation in the top metres of the ocean.

It was also found by Schluessel *et al.* (1990), that strong winds (>5 ms^{-1}) increased the magnitude of ΔT whereas for light winds (<5 ms^{-1}), the magnitude of ΔT was less. The stronger winds may have increased the amount of sensible and latent heat transfer across the air-sea interface which resulted in an increased temperature difference between skin and bulk SST.

Hepplewhite (1989) investigated the size and variability of ΔT from the equatorial waters in the Atlantic Ocean to the Southern Ocean. A radiometer made by Hepplewhite was mounted on the side of a British Antarctic Survey vessel to measure skin SST. A rubber bucket with a mercury thermometer was used to measure bulk SST. No prior research had made measurements of the skin effect at high latitudes. Hepplewhite concluded that the average ΔT value for the Atlantic Ocean transect was about -0.3 °C with a range of -1.2 °C to +0.3 °C.

Hepplewhite made the point that in the cold Southern Ocean region where the atmosphere bears very little water vapour, the sky appears much colder than the sea surface in the absence of cloud cover. The correction for surface reflection would therefore be larger in the Southern Ocean region as compared to the tropical

oceans. Hepplewhite highlights the fact that on all occasions, the positive ΔT values (skin SST warmer than bulk SST) occurred at night in the tropics. Hepplewhite also mentions that at higher latitudes, there appeared to be no such bias between day and night values. The Hepplewhite data are discussed further in Chapter 7.

Coppin *et al.* (1991) described an experiment conducted over a 13 day period in the Western Equatorial Pacific Ocean on board the research vessel *R.V. Franklin*. Skin SST values were obtained using an infrared radiometer developed by the Commonwealth Scientific and Industrial Research Organisation (CSIRO). The radiometer had an estimated accuracy of ±0.1 °C (Bradley *et al.* 1991). The radiometer had a band pass of 1 μm centred on the 11 μm band (similar to channel 11 of the AVHRR). The radiometric measurements were compared to the bulk sea temperature measurement taken via the engine room intake, 2 metres below the surface and 37 metres aft of the bow. The bulk temperature measurement was taken 1 second after the water entered the ship.

It was found that cool skins (skin SST less than bulk SST) were a near permanent feature in the Western Equatorial Pacific region where ΔT averaged -0.3 °C with a standard error of 0.15 °C, and ranged between -1.5 °C and +1.0 °C. The measured skin/bulk temperature difference were compared to ΔT values estimated by a Saunders (1967b) model. Reasonable agreement was found to occur for wind speeds between 1 and 6 ms^{-1}. Most of the data were collected when seas were smooth and winds very light (Coppin *et al.* 1991).

A general summary of the observed skin effects for field and laboratory experiments can be seen in Table 2.1. It appears from this table that ΔT has an average of -0.6 °C with a range of -1.8 to +1.0 °C. The research shows that on average, the skin SST is less than the bulk SST due to molecular heat transfer across the conduction layer from ocean to atmosphere.

TABLE 2.1

A summary of ΔT values obtained by previous authors. The ΔT values have been obtained using a number of different techniques both in the field and in the laboratory.

Author	ΔT (°C)	Description
Paulson & Parker 1972	-1.14 to -1.81	Lab experiment relating ΔT to wind speed, Barnes PRT radiometer & mercury thermometer used.
Ewing & McAlister 1960	-0.6	200m offshore, calm winds at night, radiometer & thermistor used.
Hill 1972	-0.1 to -2.0	Laboratory wind and wave experiment
Katsaros 1977	-0.4 to -2.4	Lab experiment, no wind, Barnes PRT-5, depth soundings and bulk temperature by water disruption
Kropotkin *et al.* 1978	-1.0 +5.0*	1 μm thick oil slick, with radiometer. open sea with a 1 mm oil slick (calm sunny day)
Schooley 1977	-0.2 0.0	wind 2.5 ms^{-1} at sea. No cloud under cloud shadow, thermopile soundings
Simpson & Paulson 1980	-0.15 to -0.3	At sea (wind 5.5 to 9.2 ms^{-1}) PRT-5 radiometer.
Grassl 1976	-0.17 to -0.21	wind 1 to 10 ms^{-1}, PRT-5 & resistance thermometer
Woodcock & Stommel 1947	-0.5 to -1.0	At night in a calm pond. Mercury thermometer used.
Coppin *et al.* 1991	-0.3	Western Equatorial Pacific. 11 μm radiometer. bulk SST via bow engine intake water.
Hepplewhite 1989	+0.3 to -1.3	Open sea water in Atlantic Ocean, Equator to Antarctic coast. Radiometric and bucket thermometer temperature measurements.
Schluessel *et al.* 1990	+1.0 to -1.0 (-0.2 mean)	PRT-5 radiometer and platinum resistance thermometer used at about 30° N, 20° W in the Indian Ocean
Hasse 1971	-0.4 -0.2	Night time in equatorial Atlantic (wind 7 ms^{-1}) Day time in equatorial Atlantic
Ball 1954	-0.25	Melbourne pier, light winds, clear skies, Feussner actinometer & dip bucket used
Chang & Wagner 1975	-0.2 to -0.3	Thermistor measured profile, Lab experiment
AVERAGE ΔT	-0.6	Range -1.8 to +1.0 (NB * not included)

The magnitude of the ΔT values may vary due to the number of different methods adopted in the measurement of skin and bulk SST, the latter having been measured at different depths.

2.7 Thermal Infrared Radiometers

This section discusses the operating principles of the thermal infrared radiometer and provides examples of the different types of radiometer that have been used in the past for *in situ* and airborne SST measurement.

Figure 2.5 presents a schematic diagram of a Barnes PRT-5 thermal infrared radiometer whose basic function is to detect radiation in the thermal infrared part of the spectrum. The radiometer consists of a filter which typically allows wavelengths of between 8 to 14 μm to pass through to the detector. Radiometers of this type are self calibrating in that a thermistor-controlled, electrically heated cavity provides a calibration source inside the radiometer. The radiation received from the calibration source is compared to that from the target (Sabins 1973; Katsaros 1982). A *chopper* is used to allow for alternate viewing of the target and the internal reference cavity. The chopper is a rotating disk with alternating blades that are plated with gold or other polished metals. When the chopper is in the field of view (in the vertical position as shown in Figure 2.5), the radiation energy from the internal reference cavity is reflected back on to the detector. When the chopper is out of view (in the horizontal position), the thermal radiation from the target is then focused on the detector. The difference between the reference cavity signal and the unknown target signal is converted into a temperature correction and hence into a target surface temperature (Sabins 1973). There are also *un-chopped* radiometers but these instruments are considered to have poor stability with respect to time and their internal ambient temperature (Huband 1985a).

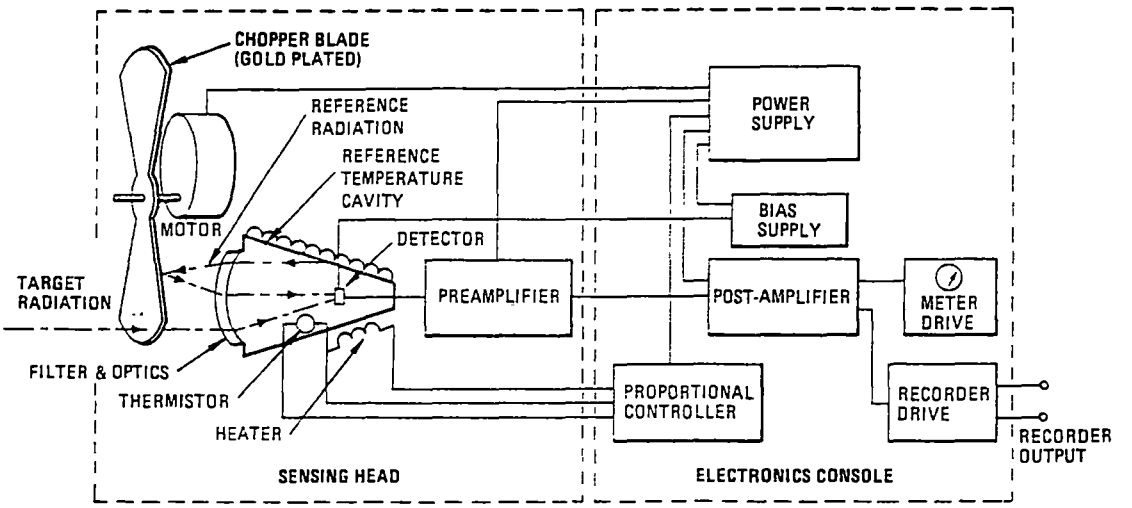

FIGURE 2.5 A schematic illustration of the internal workings of a Barnes PRT-5 infrared radiometer (from Sabins 1973).

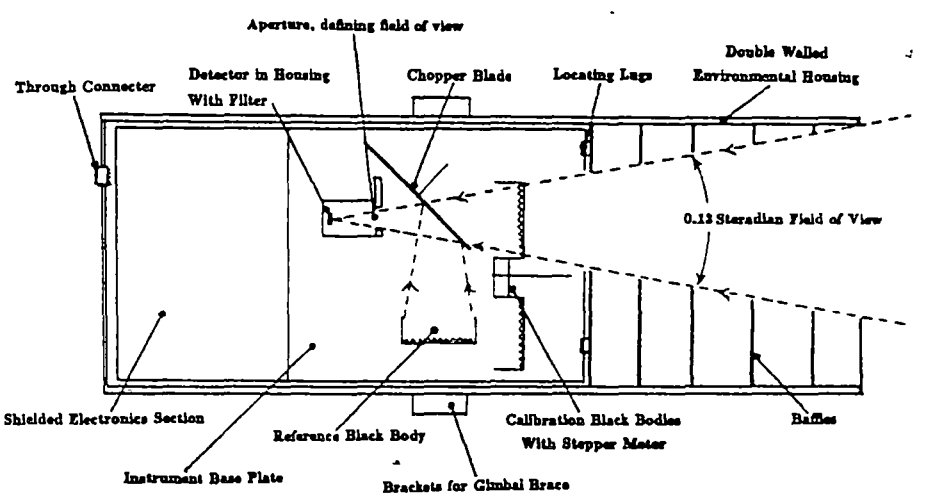

FIGURE 2.6 A schematic diagram of a dual reference cavity, self calibrating radiometer used by Hepplewhite (1989).

Hepplewhite designed and built a radiometer (see Figure 2.6) which included two internal reference blackbodies. One of these reference blackbodies was at a temperature slightly higher than the sea surface and the other slightly cooler, thus allowing for a 2 point internal calibration where the sea surface radiance is obtained by a simple linear interpolation between the two reference temperatures. This type of radiometer would have greater stability as compared to a radiometer that has only one internal reference cavity.

McAlister & McLeish (1970) described a dual wavelength radiometer, as shown in Figure 2.7. The instrument was deployed on board an aircraft to measure SST near Barbados, West Indies. The instrument has an instantaneous field of view of 25° and has two channels: channel 1 operating in the 3.5 - 4.1 μm waveband and channel 2 operating at 4.5 - 5.1 μm. The instrument was reported to be capable of measuring skin SST to ±0.01 °C. It has two reference blackbody cavities in the shape of an 8° wedge to facilitate self internal calibration. The dual radiometer was designed for airborne SST measurements and made use of a rotating spherical mirror which enabled the detector to cycle through views of the thermal radiation from the sky, the two blackbody cavities and the sea surface. Channel 1 detects thermal radiation emitted from the top 0.075 mm and channel 2 detects emittance from the top 0.025 mm. From these two measurements, McAlister and McLeish (1970) were able to estimate the temperature gradient in the top 1 mm of the ocean, being a direct estimate of the total heat flux Q_N.

2.8 Airborne Radiometry

One problem in airborne measurements of radiometric SST is the amount of absorption, scattering and self emission of radiation in the atmospheric path between the aircraft and the ocean. The loss in radiation is a function of the flying altitude of the aircraft. McAlister & McLeish (1970) countered this by running 3 or more flights at different altitudes, and then extrapolating the intensity differences to a zero altitude, corresponding to the ocean surface.

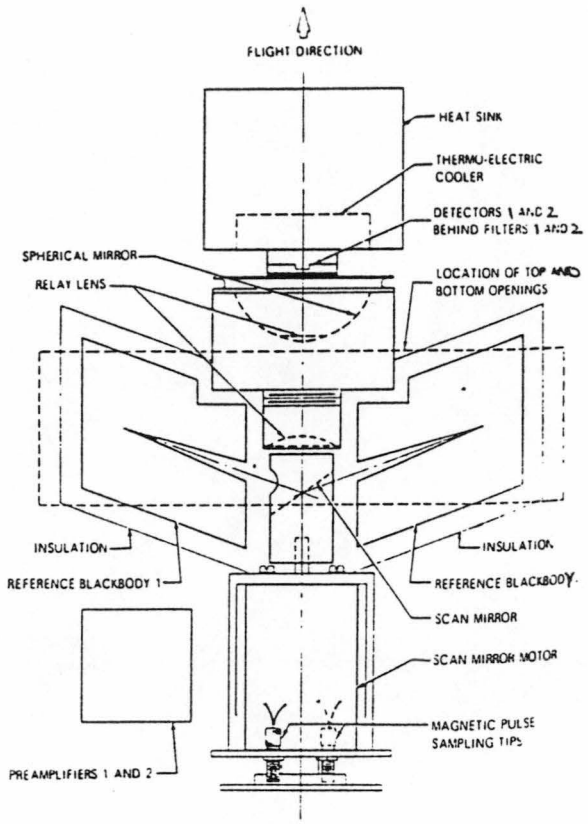

FIGURE 2.7 A dual wavelength radiometer used for airborne measurements of SST (from McAlister & McLeish 1970).

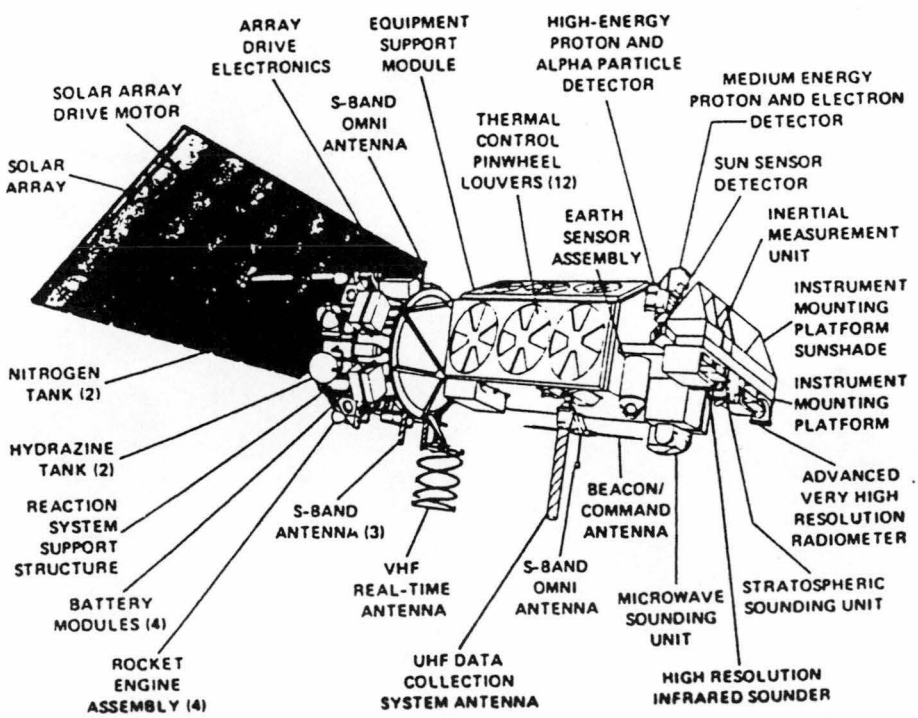

FIGURE 2.8 A TIROS-N satellite including the AVHRR instrument (from Szekielda 1988).

Saunders (1967a) identified the two main problems associated with airborne radiometry. The first problem is the imperfect transparency of the atmosphere between surface and sensor, and the second problem is the non-blackness of the surface itself. Saunders proposed that the correction for these two problems be measured at flight level by observing the sea surface at two angles, the first at the normal or nadir and the second at an oblique angle of near 60°. This has the effect of doubling the absorption-emission correction and also approximately doubles the correction for the non-blackness of the sea surface (Saunders 1967a).

The temperature change resulting from the angle change of viewing is equivalent to the correction to be added to the normal nadir value to obtain a proper estimate of surface temperature. Field tests conducted seemed to suggest that an absolute accuracy of 0.2 °C is achievable in the estimation of surface temperatures. The radiometer data was compared to bulk sea measurements and it was found that ΔT values were of the order of -0.2 °C to -0.3 °C.

Becker *et al.* (1979) reported on the use of infrared scanning sensors in the German Bight. A DO-28 D2 *SkyServant* aircraft was fitted with a Barnes PRT-5 radiometer as well as a Multi-Spectral Scanner (MSS). The German scientific research vessel *Gauss* made measurements of the near surface water temperature with thermistors. Radiosondes were launched to collect data relating to the transmission characteristics of the atmosphere. The transmittance of the atmosphere was also assessed using a numerical atmospheric model, LOWTRAN-3. The mean difference between the radiometrically measured skin temperature and the conventional bulk SST was estimated to be about -0.4 °C.

Spyers-Duran & Winant (1985) described the application of an aircraft-based Barnes PRT-5 radiometer. The radiometer data was compared to aircraft-deployed expendable bathy-thermograph (AXBT) drops. The Barnes PRT-5 operated in the 9.5 to 11.5 μm spectral window. The AXBTs had a quoted accuracy of 0.55 °C, and there were some 125 XBT drops in all. The mean

difference between the PRT-5 (skin) and the AXBT (bulk) measurements was of the order of -0.1 °C with a standard error of 0.57 °C. It was found that the largest temperature differences occurred at low wind speeds typically less than 5 ms^{-1}.

2.9 Satellite Measurement of SST

This section will briefly look at existing satellite radiometer technology and the expected accuracy achievable in satellite measurement of SST.

The National Oceanic and Atmospheric Administration (NOAA) operates the NOAA series of satellites. The third generation in this series include the Television and Infrared Observation Satellite (TIROS-N) and the NOAA-6 through to NOAA-13 satellites. These satellites have a near polar, sun-synchronous orbit at an altitude of 830 km. Each area on the Earth's surface is observed at least four times daily, as there are two satellites in orbit at any one time (Curran 1985). Each of these satellites carries an Advanced Very High Resolution Radiometer (AVHRR) or its derivative, the AVHRR/2 (see Figure 2.8). The spatial resolution of the AVHRR is 1.1 km at nadir and the swath width is 3000 km. The AVHRR/2 is carried on the odd-numbered NOAA satellites and has an extra thermal infrared channel. Channel 1 is in the visible (red) part of the spectrum between 0.58 and 0.68 μm. Channel 2 is in the near infrared between 0.725 and 1.1 μm. Channel 3 is in the middle infrared between 3.55 and 3.93 μm. Channels 4 and 5 are in the thermal infrared part of the spectrum with wavelengths of 10.5 - 11.5 μm and 11.5 - 12.5 μm respectively and are commonly used in SST retrieval algorithms (e.g. Robinson *et al.* 1984; Dalu & Liberti 1988).

The first European Remote Sensing Satellite (ERS-1) was launched in 1991 and housed the Along Track Scanning Radiometer (ATSR). The ATSR has a channel at 1.6 μm and another 3 infrared channels identical to those carried by the AVHRR/2. The spatial resolution at the surface for ATSR is 1.1 km at nadir again similar to AVHRR. The ATSR has been designed for greater accuracy and includes

on board calibration; active cooling of detectors and dual angle viewing of the Earth's surface (Prata *et al.* 1990).

Longwave radiation emitted by the sea surface is partly absorbed by atmospheric constituents such as water vapour and aerosols as well as other gases. The absorption is least in the 'window' regions, occupied by AVHRR channels 3, 4 and 5. It is necessary to correct the brightness temperatures observed in these channels to estimate the radiometric SST. The atmospheric effect has been estimated using a split window technique to yield near true values of SST (e.g. Llewellyn-Jones *et al.* 1984; Robinson *et al.* 1984; McClain *et al.* 1985; Dalu & Liberti 1988; Barton & Cechet 1989; Wick *et al.* 1992; Tabata 1993). Channels 4 and 5 are used for day and night time measurements where algorithms have been determined, for example, NOAA/NESS adopted the following atmospheric correction algorithm in preparation for a SST database (Robinson *et al.* 1984):

$$SST = a_1 T_{11} + a_2 (T_{11} - T_{12}) - a_3 \tag{2.21}$$

where a_i are constants and T_{11} and T_{12} refer to the temperature measured by channels 4 and 5 respectively. A triple window correction formula has been derived in the form

$$SST = b_1 T_{11} + b_2 (T_{3.7} - T_{12}) - b_3 \tag{2.22}$$

as well as a dual window formula

$$SST = c_1 T_{11} + c_2 (T_{3.7} - T_{11}) - c_3 \tag{2.23}$$

where $T_{3.7}$ is the temperature measured by channel 3, which can not be used for day time measurements because of the reflection of solar radiation at this wavelength. The coefficients a_i, b_i and c_i in these cases are derived from comparisons with drifting buoy measurements of bulk SST and do not take the skin effect into account. In general, it was found that the split window method

yielded the least bias of 0.06 °C with a standard deviation of 0.61 °C (Robinson *et al.* 1984).

The above dual window algorithms are generally referred to as Multi-Channel SST or MCSST. There has since been the development of a non linear algorithm called the Cross Product SST or CPSST which takes the form

$$CPSST = \frac{T_i SST - T_j SST_i}{T_i - T_j + SST_j - SST_i} \tag{2.24}$$

were i and j represent 2 separate window channels. This algorithm is considered to account for varying temperature and water vapour conditions in the atmosphere better than the earlier methods (Tabata 1993).

Dalu & Liberti (1988) adopted algorithms using SST values obtained by *in situ* radiometric measurements. When these algorithms were tested in parallel with other algorithms, it was revealed that theirs tended to over estimate the SST by an average 0.3 °C. Dalu & Liberti (1988) make the point that for the large variety of algorithms that are found in the literature, there were differences as large as 2.5 °C when applying the algorithms to the same data set. In general, the coefficients a_i, b_i and c_i are not true constants, but vary with the state of the atmosphere and the degree of contaminants such as aerosols and water vapour.

Schluessel *et al.* (1987) compared satellite derived SST with *in situ* radiometric and ship measurements of SST using 3 split window retrieval methods. The first method used AVHRR data alone, and yielded standard errors of 0.31 °C and 0.51 °C for two different orbits. The second method coupled the AVHRR data with vertical sounding profile data (TOVS) to yield standard errors of 0.24 °C and 0.36 °C with biases of -0.39 °C and 0.71 °C respectively. The third method coupled AVHRR with high resolution infrared sounder data (HIRS) yielding standard errors of 0.32 °C and 0.45 °C with bias errors of 0.22 °C and 0.33 °C respectively. The third method seemed to perform best, particularly in warm moist atmospheric conditions.

The AVHRR/2 data appears to have an uncertainty of ±0.6 °C under MCSST retrieval techniques. Bias errors can be of the order of 0.4 °C between buoy measurements and satellite measurements (Robinson *et al.* 1984). An AVHRR/HIRS method can improve this to about 0.4 °C and with a bias between 0.2 and 0.3 °C (Schluessel *et al.* 1987). It has been suggested that with the ATSR data from the ERS-1 satellite, SST measurements could be attained with a standard error of 0.2 °C.

It has been stated that the best possible uncertainty of AVHRR measurements of SST is 0.31 °C (Robinson *et al.* 1984). The actual uncertainty depends on whether absolute SST or relative SST are required. It also depends on the user requirements for SST measurements from space. The accurate calibration of SST from satellites requires sea temperature truth so as to detect and remove any bias. The two main factors that need to be taken into account are the sign and magnitude of ΔT and the effects of the atmosphere. *In situ* measurements of SST using radiometers at sea become important in the assessment of ΔT, which in turn assists in the interpretation of satellite derived SST. The situation in the past has been that the ship measurements of bulk SST have been used as the ground truth for atmospheric correction algorithms, ignoring the presence of ΔT.

Another source of error in satellite derived SST is the presence of clouds which can affect the SST values averaged over a number of image pixels. There are histogram techniques that effectively remove the cloud-contaminated pixels, although errors of 0.2 °C to 0.5 °C can still occur (Robinson *et al.* 1984). Reflection of solar radiation during day time can cause errors as high as 1 °C due to sky glitter. This is most problematic for channel 3, where errors as high as 15 °C can occur.

Chapter 3

CHAPTER 3 : Data Collection from the RSV *Aurora Australis*

This chapter describes the methods used to collect SST data from the *Aurora Australis* during the two marine science voyages, THIRST (1993) and SHAM (1994). There will be a brief discussion of the method used to collect the data and a brief discussion on how the data was checked for data quality.

3.1 The Collection of Skin SST

Two Everest 4000ALCS™ radiometers were used during the two marine science voyages THIRST and SHAM. The radiometers were fitted with band pass filters admitting thermal infrared radiation between 8 and 13 μm (Everest 1993). The specifications and characteristics of these instruments will be discussed in more detail in Chapter 4. One radiometer was pointed downwards at the ocean surface at 53° to the vertical so that the radiometer viewed the ocean in advance of the ship's wake and sea foam. An angle of 53° is also the Brewster angle, for which the surface reflection from sky radiation is at a minimum (Schluessel *et al.* 1990). The downward-looking radiometer measures the skin SST. The second radiometer was pointed upwards at the sky at a constant angle of 45° from the vertical in order to measure a representative value of the sky brightness temperature.

The radiometers were mounted inside PVC protective shields, (see Figure 3.1) designed to protect the instruments from the natural elements such as salt, sea spray, rain, snow and solar radiation. The PVC shields were mounted on the railings aft of the port side flying bridge (top deck), about 15 metres above normal sea level (see Figure 3.2). The area of sea surface viewed was approximately 1.5 m^2.

The radiometers were connected to a IBM-compatible 286 personal computer (PC) situated in the meteorology laboratory aft of the wheel house. The radiometer cables were wrapped in a protective metal sheath and were connected to the serial input ports of the PC.

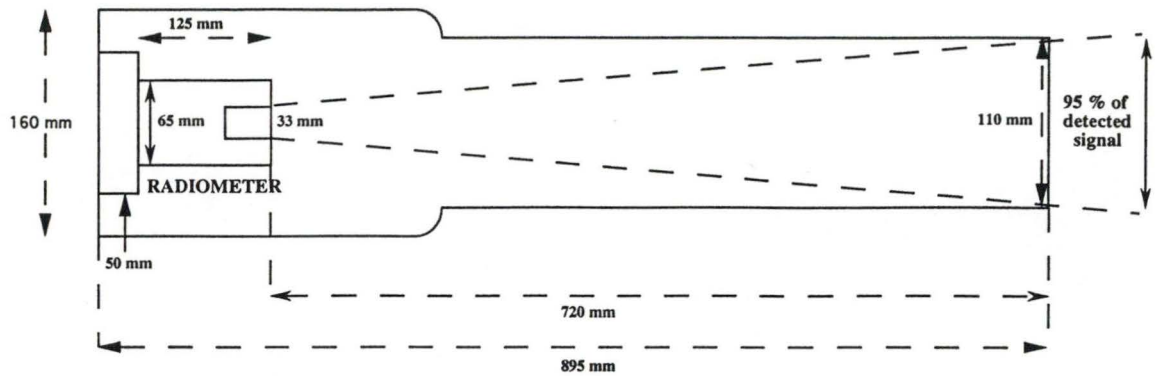

FIGURE 3.1 The dimensions of a PVC pipe protective shield used to house and protect the Everest 4000A radiometers from snow drift, sea spray and reflected solar and thermal radiation.

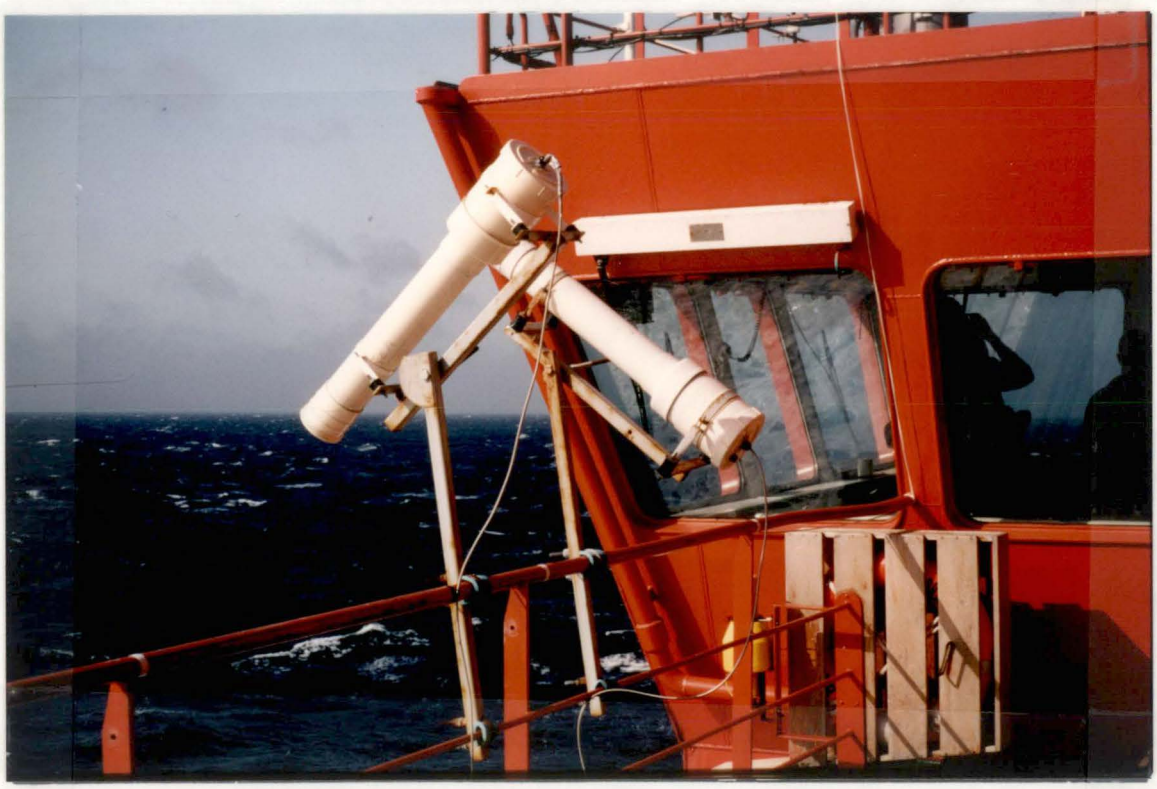

FIGURE 3.2 Photograph of the two PVC protective shields mounted on the railings (port side, aft of the flying bridge) on board the RSV *Aurora Australis*.

The resulting brightness temperatures from both radiometers as well as the internal temperatures of the radiometers were stored on the PC using a program written in Quick-Basic™. The PC time was synchronised with the ships Universal Time. The data were logged every 60 seconds, to be later averaged over a 10 minute interval.

In order to ensure that the radiometers were working correctly throughout the 2 voyages, daily checks were made. Both radiometers were directed at the same angle towards the sky. Typical differences (or offsets) between the radiometer readings ranged from 0 °C in cloudy conditions to 10 °C on cloud free days. The radiometers were calibrated in a laboratory experiment before and after each voyage to assess the changes that might be occurring in the instruments. The calibration methods and results are discussed in Chapter 4.

During each day of the voyage, the operator (author) monitored the equipment as often as was practical, ideally every 2 hours. A log book was maintained and notes were kept describing the time, position and the air, skin and bulk temperature differences as well as humidity and wind speed observations. Other features recorded in the log book included the activity of the ship at the time, and approximate time of passing through various oceanographical features such as the Sub-Tropical Convergence, Sub-Antarctic Front and the Polar Front.

There were times during each voyage when radiometric data were not collected, particularly in the case of bad weather. Under extreme winds and heavy seas for example, if too much sea foam, spray snow and salt was present in the air, then this would increase the uncertainty in the skin temperature measurement.

Some interference was caused by telex and radar transmissions from the adjacent radio office. This however only occurred for up to 1 hour a day at predictable times. When the ship was being held stationary, some irregularities in skin SST may have resulted. This was especially the case at oceanography CTD stations when the forward port side bow thruster operated near the view of the

radiometers. Minimal deviations in the skin temperatures were observed whilst the bow thrusters were in operation. The radiometer data were not logged whilst the ship was at the Antarctic stations, ie. Mawson, Casey and Davis or when the ship was caught in bad weather for a prolonged period of time or when thick pack ice was present.

3.2 The Ships Data Logging System (DLS)

A number of meteorological and ship-related parameters are routinely logged by the DLS on the *Aurora Australis* and stored on the ships main VAX computer system. Data were retrieved from the DLS at 10 minute averages and included latitude, longitude, universal time, sea temperature, air pressure, port and starboard air temperature; port and starboard humidity; ship's heading and speed; pitch and roll; sea water flow; quantum radiation; wind direction; wind speed; wind gust and salinity. In addition to the above, information was collected from the bridge log book including wave height; swell height, visibility and cloud cover in octas. Table 3.1 lists the instrumentation and the expected precision of all of the parameters collected on the *Aurora Australis* .

The ships sea temperature measurements were taken 7.5 metres below sea level, 1 metre inside a feed line under the bow of the *Aurora Australis* . During the SR3 transect on the SHAM voyage between the 1st and the 15th of January, the ship's bulk temperature measurements were compared with the CTD measurements taken at a similar depth at a resolution of 2 metres. Figure 3.3 shows an excellent correlation (R^2 = 0.999) between the CTD measurements and the ship's bulk temperature measurements with a RMSD of 0.09 °C and a y-intercept or offset of 0.03 °C in the temperature range 1 to 14 °C. This compares favourably with the operating precision of the Everest radiometer of 0.1 °C and with the operating precision of the sea temperature measuring probe of 0.07 °C. The sea temperature as measured by the ship was therefore considered to be a good estimate of the true bulk SST.

TABLE 3.1

A summary of the climatological parameters measured on board the RSV *Aurora Australis*.

Parameter name	Units	Make of Instrument	Resolution	Standard Error	Comments
RADIOMETRIC					
Skin and Sky brightness temperature	°C	Everest 4000ALCS	0.01	0.1	
MET SYSTEM					
Wind speed	knots	Belfort Instrument Co.	0.1	10%	corrected for ship's speed & roll
Wind direction	degrees	Aero Vane, Model	0.1	5°	referenced to ship's heading
Wind gust	knots	123 HD	0.1	10%	no correction
Barometric Air Pressure	hPa	Vaisala DPA21	0.1	0.5	18 m above sea level
Port/Stbd Air Temperature.	°C	Platinum Probes	0.1	0.3	weather dependant
Port/Stbd Air Humidity	%	Stevenson Screen electronic probe	1%	10%	1% of Relative Humidity affected by weather
Quantum Radiation	micro mole per second per metre square	Stevenson Screen Li Cor model LI-190SA Quantum Sensor	1	20%	function of ships angle
Sea Temperature		Yokogawa 7563 Digital Thermometer Platinum resistance probe	0.01	0.07	7.5 m below sea level 1m inside front bow (sea water inlet pipe)
NAVIGATION					
Ships Speed	knots	Electromagnetic Log	1	10%	
Ships Heading	degrees	Thomas Walker & Son Gyro Compass	1	2°	
Position (GPS)	degrees Lat. and Long.	Magnovox MX1107 GPS & Transit		300 m	coarse resolution
Pitch/Roll	degrees	Trim Two Axis electrolytic gravity sensor		0.1°	(over a ±30° range)
Time	Hour:Minute:Second	GMT	5 seconds	5 seconds	Universal Time
GENERAL					
Water Flow Rate	litres per minute	Flowmeter	0.1 litre		up to 4-9 litres a minute
Salinity	ppm	Thermo-Salinity Graph (TSG)	0.01		range 32-36 ppm
BRIDGE LOG BOOK					
Wave height & swell	metres	by observation	±1m	1	
Cloud cover	octas	" "	1	1	

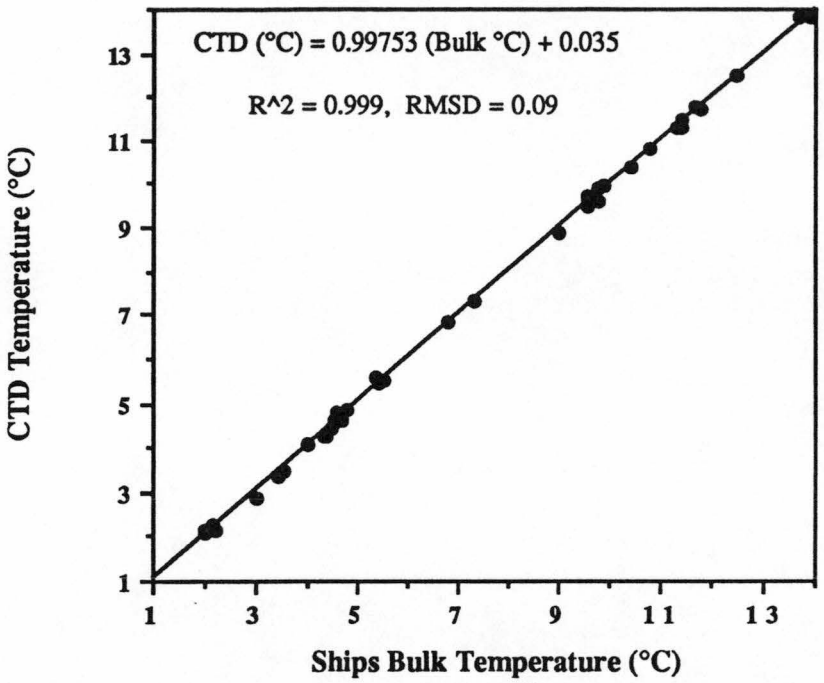

FIGURE 3.3 A scatter plot of the CTD near surface SST measurements against the *Aurora Australis* bow temperature measurements. The difference between the CTD and the ships measurement is negligible.

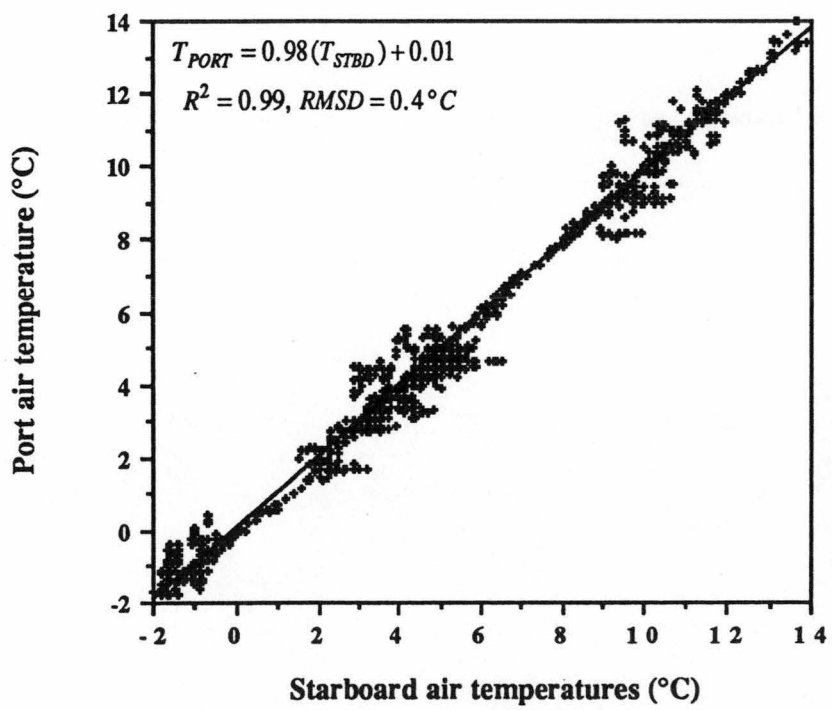

FIGURE 3.4 A scatter plot comparing the port air temperature and the starboard air temperature taken on board the RSV *Aurora Australis*. The bias error is small, but the RMSD is high due to changes in ships heading and wind direction.

The air temperature measurements were made using platinum probes contained in a Stevenson screen located on top of the flying bridge about 20 metres above sea level. The expected standard error of the air temperature measurements was expected to be 0.3 °C. The air temperature adopted was the mean of the port and starboard air temperature measurements. Figure 3.4 show a scatter plot of port against starboard air temperatures which fits near the line of true correlation with a y-intercept of 0.01. It is assumed from this that the air temperatures are not in significant bias error. However, at times, there is a lot of scatter in this plot coinciding with sudden changes in wind direction and ship heading resulting in a RMSD of 0.4 °C.

The wind speed and wind direction data were automatically corrected for the ship's heading and speed. The anemometer used to measure wind speed was located about 25 metres above sea level. The Quantum radiation (μ mole s^{-1} m^{-2}) measurements were obtained using a Li Cor model LI-190SA Quantum sensor. This Quantum radiation sensor was used principally to differentiate between day time and night time.

3.3 Initial Data Sorting

Data were extracted from the ship's DLS at 10 minute averages for both voyages. The data collected from the ship's DLS and the Everest radiometers were stored on floppy disk in a MS-DOS format. On return to the University of Tasmania (Hobart), all of the data were transferred into Excel (Macintosh) spread sheets for preliminary data quality checking and investigation. The Everest data were averaged over 10 minute intervals to correspond to the DLS data.

The first phase of data analysis was to create individual files for each day for both voyages. A number of time series graphs were then plotted including the skin temperature; the ship's bulk temperature; air temperatures; wind speed and direction; humidity, air pressure and quantum radiation. These time series helped to identify any erroneous data points in the data set (including radar and telex

interference), as well as to give a general picture of the data quality. Once all data were filtered and sorted into day files, the radiometric skin temperatures were corrected for calibration (see Chapter 4) and then corrected for the reflected component of downwelling thermal radiation. The data were then arranged into monthly data files for both voyages. The analysis methods and results are presented and discussed in Chapter 6.

Chapter 4

CHAPTER 4: Calibration of the Everest 4000A Radiometers

4.1 Introduction

Rapier (1992) outlined a method for calibrating an Everest 4000A radiometer. This method was originally designed to test the stability of the Everest radiometer over rapidly changing temperatures in the range -20 °C to +40 °C over periods of 30 to 60 minutes. This chapter details an improved set of experiments which gives a more realistic view of the operating precision of the Everest radiometers for ambient temperature settings in the range of -8 °C to +25 °C, which includes the operating temperatures experienced in the Southern Ocean environment.

The Everest 4000 series of radiometers were selected due to their simplicity and economy. The suitability and flexibility of the Everest series has been proven in crop, soil and vegetation research (eg. Nilsson 1991, Kalma *et al.* 1988). The Everest 4000A has also been used successfully in the American desert near Yuma, Arizona (Everest 1990). The Everest 4000A radiometer was designed to work in a temperature range of -10 °C to +50 °C, making it a suitable choice for the harsh conditions of the Southern Ocean. Its durability had been proven in the Southern Ocean during two previous ANARE voyages on board the *Aurora Australis* in October 1991 (Rapier 1992) and in March 1993 as well as the 2 most recent voyages, THIRST (1993) and SHAM (1994). The Everest 4000A has also been used in Australian tropical and sub-tropical waters (Michael & Skirving 1991; Skirving & Michael 1992).

As mentioned in Chapter 1, two Everest 4000A radiometers were used in the Southern Ocean from the 7th of August through to the 9th of October 1993 and from the 1st of January through to the 1st of March 1994. These two voyages lasted for a combined total of 17 weeks. The main objective of the calibrations was to determine if there had been any noticeable change in the characteristics of the radiometers during these voyages. A second objective was to assess the

operating precision of the two instruments under controlled conditions. On occasions during the two voyages, the skin SST was noted to be warmer than both the air temperature and the bulk sea surface temperature, which suggested at the time a bias error in the radiometers. It was also observed that the radiometers were measuring open sea temperatures less than -2 °C, below the freezing point of sea water, again suggesting a bias error. The magnitude of these bias errors were determined in a controlled laboratory calibration.

4.2 Experimental Design

The radiometers were calibrated on 4 separate occasions: pre voyage 1 in June 1993, between voyage 1 and voyage 7 in November 1993, post voyage 7 in March 1994 and post voyage 7 in October 1994. A Thermos™ cooler (60 litre capacity) and a Cool Room were used for the first calibration. A Contherm™ unit (controlled temperature cabinet) was used for the later two calibrations. A description of the apparatus used in the calibration experiments follows.

4.2.1 The Everest 4000A Radiometers

The Everest 4000A radiometers are 12.5 cm long and have a diameter of 6.5 cm (see Figure 4.1 and Figure 4.2). The instrument viewed the target with a beam width diameter of about 4.4 cm over a target distance of 15 cm. The radiometer has a filter window 3.0 cm in diameter, with a filter band pass of 8 to 13 μm (Figure 4.3). The internal detector is a miniature multi-junction dual element DR26 thermopile, made of evaporated bismuth and antimony (Everest 1993). The radiometer uses an optical chopper stabilisation technique which corrects for DC drift. An embedded microcomputer outputs a single composite analog signal from a digital-to-analog converter at the rate of exactly 10 mV per degree Celsius. The radiometer accepts an unregulated input power voltage (anywhere between 4.5 V and 18 V DC) and outputs the resulting temperature signal in degrees Celsius (Everest 1990).

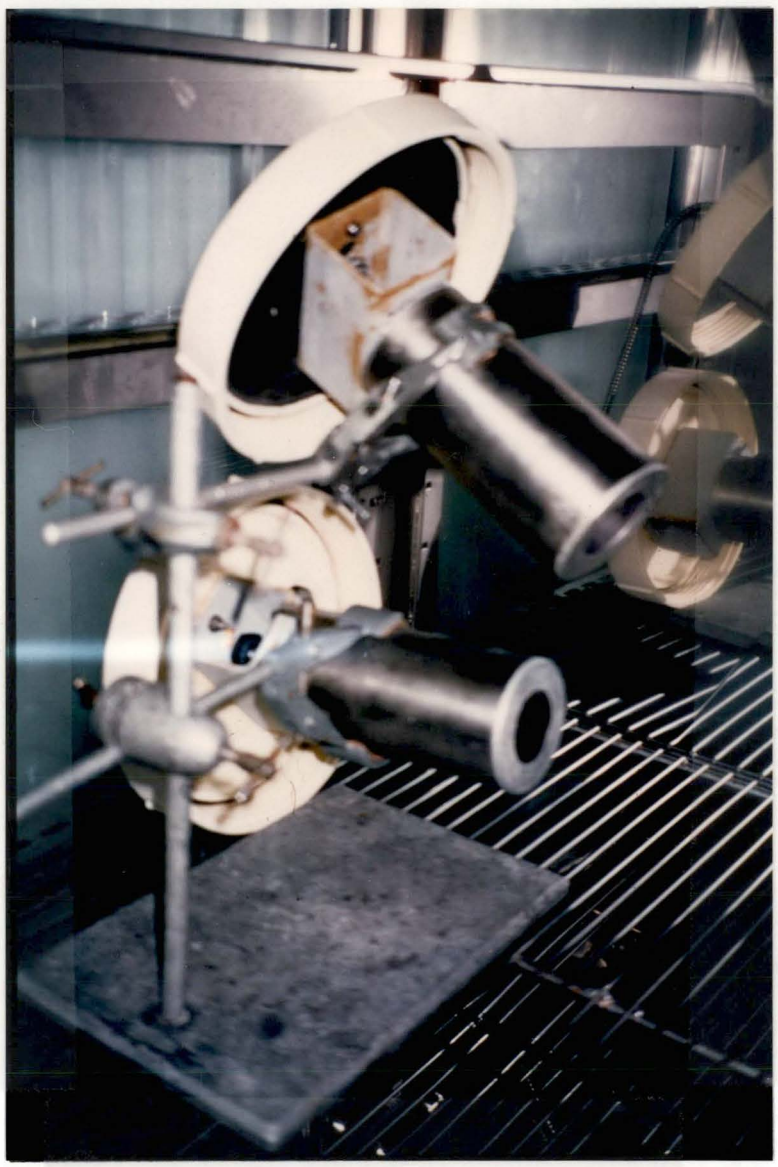

FIGURE 4.1 Photograph of the two Everest 4000A radiometers set up inside the Contherm™ unit.

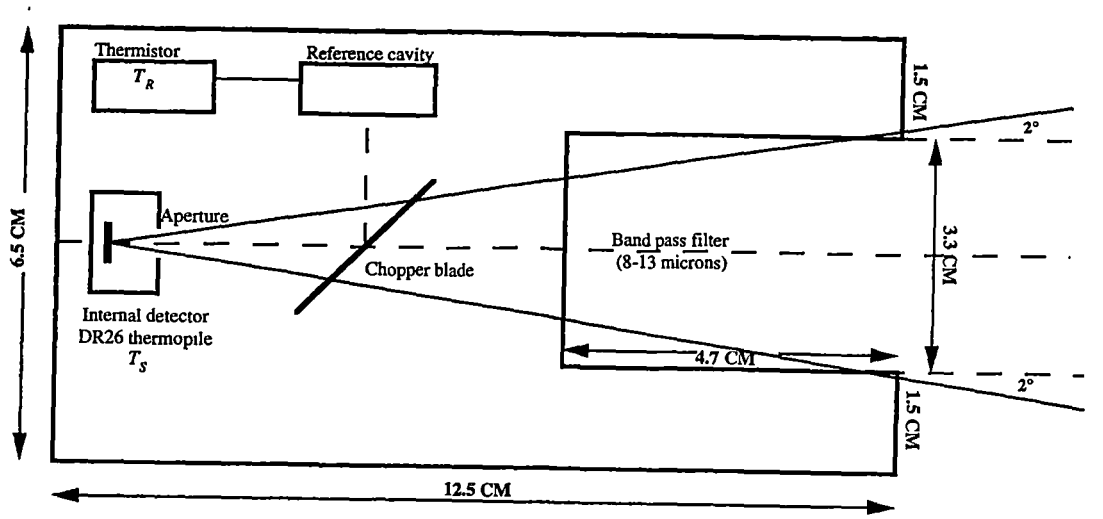

FIGURE 4.2 A schematic diagram of an Everest 4000A radiometer.

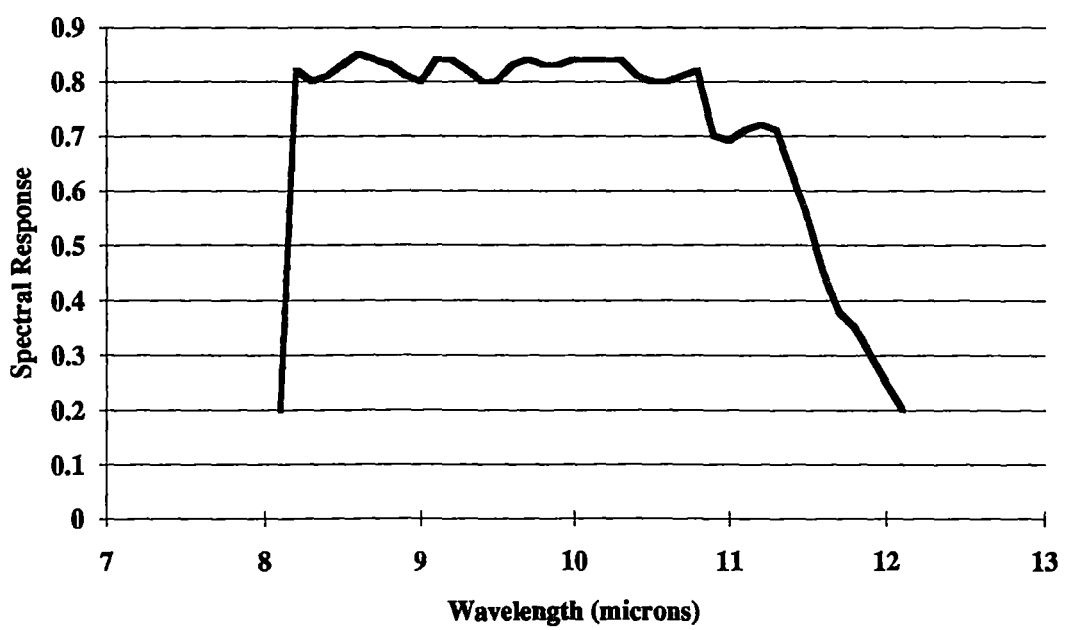

FIGURE 4.3 The spectral response curve for the 8 to 13 μm band pass filter used in the Everest 4000A radiometer.

The radiometer operates by comparing (or chopping) the target temperature T_S against an ambient internal blackbody of temperature T_R. The output of the thermopile provides a temperature difference, which is added to the internal blackbody temperature to provide an estimate of the target temperature. The internal blackbody temperature is monitored by a thermistor, and it is also assumed to equal the ambient temperature of the radiometer, an assumption which can not take into account any thermal gradients within the radiometer itself. It is assumed that the temperature difference between the DR26 thermopile and the thermistor is negligible.

4.2.2 Temperature Control Chambers

The three temperature control chambers used (Thermos, Cool Room and Contherm) were adapted to form a convenient insulated environment guarding against radiative and convective exchange of heat between the radiometer and the out side environment.

The Thermos cooler measured 60 cm long, 35 cm wide and 38 cm high and consisted of a 3 cm layered polystyrene insulation wall. The lid of the thermos cooler was 6 cm thick and was closed during the course of the experiment. The thermos cooler included a 2 cm diameter drainage hole, used to pass any necessary cables into and out off the chamber. The hole was sealed to avoid heat loss or gain in or out of the thermos cooler and was used for room temperature calibration experiments at about 15 °C.

The Cool Room measured 2.7 metres wide, 2.0 metres deep and 2.4 metres high and was located on the 4^{th} floor of the IASOS building (University of Tasmania). While the room temperature was set at a desired temperature of -5 °C, the actual temperature varied between 0 °C and -6 °C, due to limitations in the mechanics of the freezing elements. The cool room was well insulated from the outside environment.

The Contherm unit (see Figure 4.4), which is a precision humidity and light simulator principally used for plant growth experiments, allowed the ambient temperatures to be set anywhere in the range -5 °C to +30 °C. The relative humidity could also be controlled, and was set at about 30% for the duration of the experiments. The Contherm unit was located in the Department of Geography and Environmental Studies, University of Tasmania.

Both the Contherm and the Cool room had outlets which allowed cables to pass into the chambers. These outlets were sealed off using insulation pads.

4.2.3 The Calibration Target

In all experiments, the target was an Everest Model 1000™ calibration target consisting of a high emissivity, black aluminium oxide plate coated with Epply Parsons optical black lacquer (see Figure 4.5 and Figure 4.6). The plate is 10 cm in diameter, with a surface machined into concentric grooves to increase the effective surface area of the plate and to further reduce reflection of infrared radiation from the surface of the plate. The emissivity of the plate is quoted as being 0.98 (±0.01) (Everest Operating Manual).

4.2.4 Thermocouple Measurements

Although the calibration unit featured its own thermistor and digital temperature display, a thermocouple was attached to the centre of the target to allow its temperature (T_C) to be measured remotely and more accurately. A very small diameter T-type copper/constantan thermocouple was glued with epoxy resin to the centre front surface of the calibration plate to ensure a good thermal contact and to minimise any thermal gradients across the front surface of the calibration plate. A second thermocouple measuring the chamber wall temperature (T_W) was attached to the wall surface using tape. The radiometers were positioned inside the chambers using clamps and a burette stand and were aligned (over a 15 cm distance) to the centre of the plate near the thermocouple.

FIGURE 4.4

Photograph of the Contherm™ unit used as a controlled temperature environment for the calibration of the Everest radiometers. The Campbell CR21 Micrologger, tape recorder and ice/water reference bath are located at the lower right hand corner of the photograph.

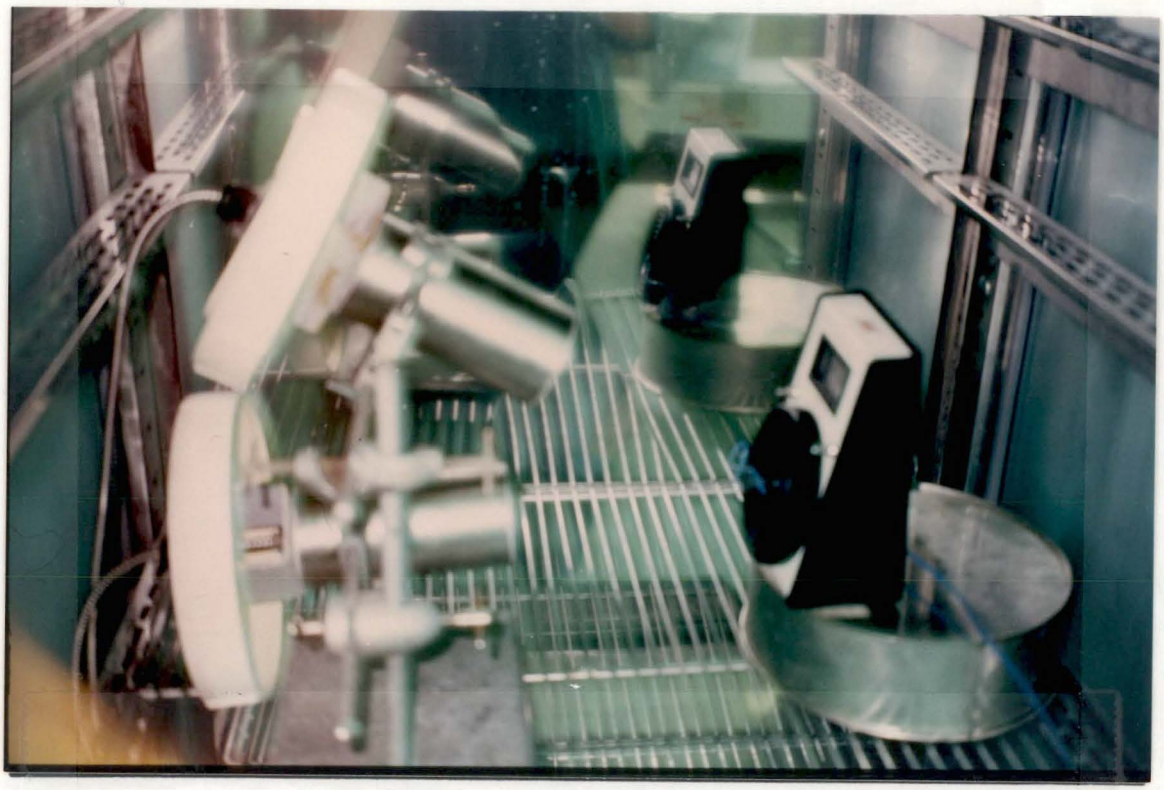

FIGURE 4.5 Photograph of the two Everest radiometers set up inside the Contherm™ unit and pointed at the centre of the Model 1000™ calibration target. The distance between the radiometers and the target is 15 cm.

FIGURE 4.6 An illustration of the Model 1000™ calibration target used as a reference temperature for the calibration experiments.

For each of the experiments conducted, a correction was made for the small reflection of infrared radiation by the calibration plate, assuming a plate emissivity ε = 0.98. The corrected target temperature T_{SO} is given by equation 2.11 re-expressed as

$$T_{SO} = \left[\frac{(T_S)^4 - (1-\varepsilon)(T_W)^4}{\varepsilon} \right]^{\frac{1}{4}} \tag{4.1}$$

where T_S is the observed radiometric temperature for the target. This above formula converts T_S to T_{SO} by taking account of the small flux of radiation emanating from the walls of the chamber and being reflected from the calibration unit towards the radiometer. Equation 4.1 is of little consequence when T_S and T_W are near the same as is the case for ambient temperature settings.

4.2.5 The Campbell CR21 Micrologger

The thermocouple wires were connected to a Campbell (Scientific Inc.) CR21 Micrologger which logged the target temperature (T_C) and the wall temperature (T_W) at one minute intervals. The data were stored on a cassette tape, and later down-loaded to a MS-DOS floppy disk using software provided by Campbell Scientific Inc. The data were transferred into an Excel spread sheet on an Apple Macintosh computer for further analysis.

A Thermos flask held a water-ice mixture at 0 °C which provided a reference for the thermocouple junctions (see Figure 4.4 lower right hand corner and Figure 4.7). The Campbell CR21 Micrologger recorded the thermocouple measurements in millivolts (mV). The values of T_W and T_C were subsequently calculated using the following mV to °C conversion formula

$$Temp(^\circ C) = -0.78116(mV)^2 + 26.069(mV) - 0.0053423 \tag{4.2}$$

This is based on a temperature range of +40 °C to -30 °C for a T-type thermocouple (Jones 1969).

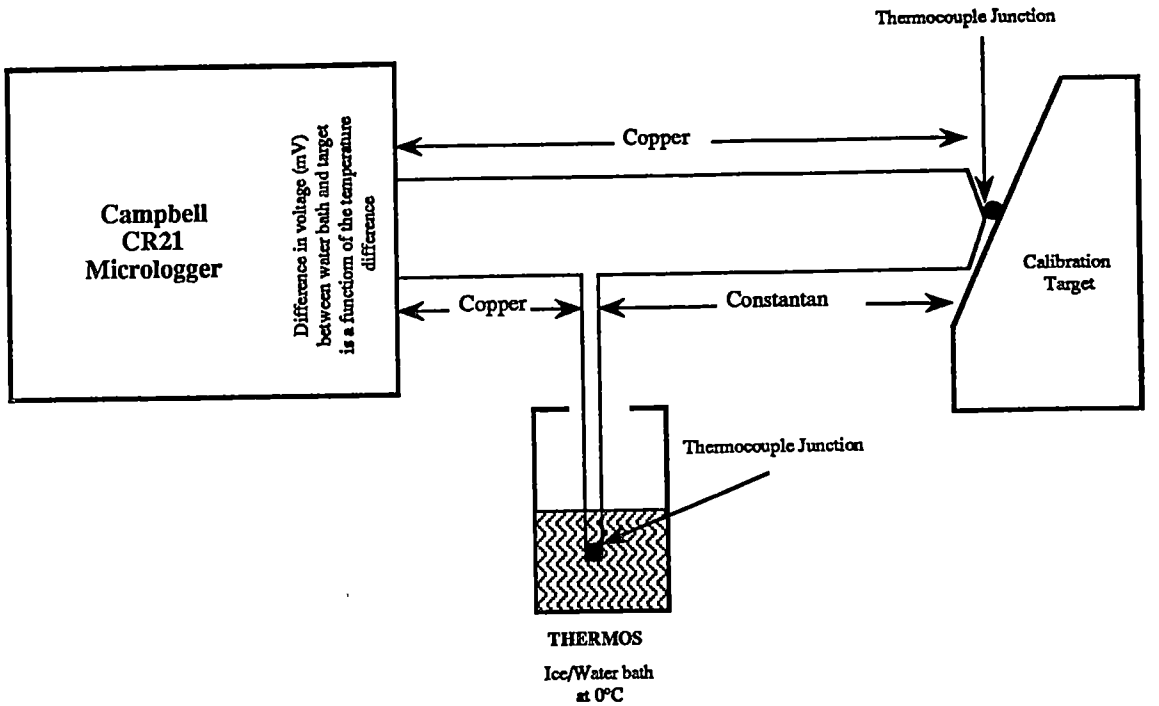

FIGURE 4.7 A dual T-type thermocouple junction wire connecting the Campbell CR21™ Micrologger to the calibration target and the thermos ice/water reference bath.

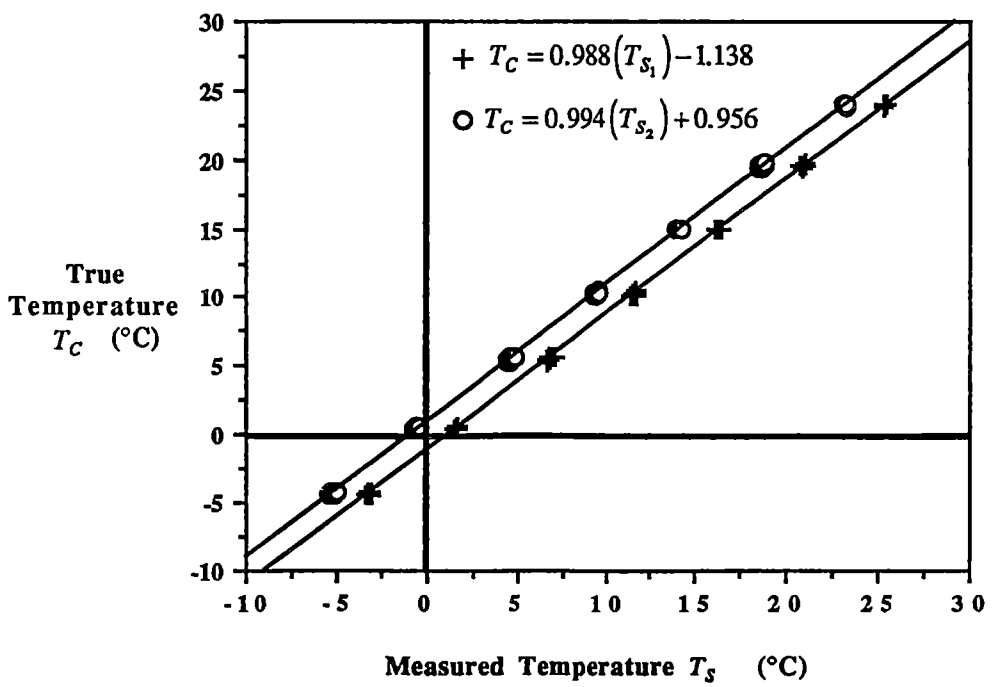

FIGURE 4.8 An example scatter plot of the near perfect correlation between the true thermocouple temperature measurement (T_C) and the radiometric temperature measurement (T_S).

4.3 The Methods

This next section outlines the method used in the cool room, thermos and contherm calibration experiments

4.3.1 The Cool Room and Thermos Method (June 1993)

In this experiment, the radiometer temperature (T_R) was held near constant whilst the calibration target temperature (T_C) was allowed to vary over a range from -8 °C to +30 °C. Graphs of T_S against T_C were plotted and a simple correction function was assumed, *ie*

$$T_C = aT_S + b \tag{4.3}$$

Cool Room Method

The first phase of the experiment was conducted in a cool room that was set at about -3 °C, although in practise the room temperature varied between -6 °C and 0 °C. The Everest 4000A radiometer was placed inside the cool room and allowed to equilibrate for about 2 hours. The calibration target was kept at standard room temperature at about 15 °C and then placed in front of the radiometer in the cool room. Measurements were collected as the target cooled towards the cool room temperature at about -3 °C. The process was then repeated.

In the next phase of the experiment, the calibration target was first chilled to about -10 °C in a chest freezer. The cold target was then placed in front of the radiometer. Measurements were collected as the target warmed to the cool room temperature of about -3 °C.

This experiment allowed the behaviour of the radiometer to be investigated for a target temperature range of -8 °C to +10 °C. The time taken to set up the target in front of the radiometer resulted in a large heat loss or gain by the target

before the start of measurements, and prevented the full range of target temperatures being attained.

Thermos Method

The second phase of this experiment was conducted with the radiometer placed inside a Thermos cooler. The thermos cooler was allowed to settle at a near ambient room temperature of about 15 °C. On two separate occasions, the calibration target was placed in front of a small bar heater in another room and gently warmed to about +30 °C. The target was then placed in front of the radiometer and allowed to cool to the ambient 15 °C. On two further occasions, the calibration target was chilled to about 0 °C in the cool room, then placed in front of the radiometer and allowed to warm to the ambient room temperature. This procedure provided an overall target temperature range of +3 °C to +27 °C. Once again the effective temperature range was contracted slightly due to delays in arranging the target in front of the radiometer.

The overall temperature range for the cool room experiment and the Thermos cooler experiment combined was -8° C to +27 °C. The result of the regression analysis between T_S against T_C are shown in Table 4.1.

4.3.2 The Contherm Method (November 1993; March/November 1994)

The main aim of the 3 ambient Contherm calibrations was to stabilise both the radiometers and the calibration unit at a number of ambient temperatures. On 8 separate occasions, the radiometers and calibration unit were allowed to stabilise at the following ambient temperatures which were set on the Contherm control panel ie. -5 °C, 0 °C, +5 °C, +10 °C, +15 °C, +20 °C, +25 °C and +30 °C. It took about 2 hours in each case to settle at the nominated ambient temperature. Once ambience had occurred, values of T_S, T_C T_W and T_R were logged over a 30 minute period. Regression analysis results of the T_S against T_C plots can be seen in Table 4.1.

TABLE 4.1 : A summary of the calibration results for the Everest-1 and Everest- 2 radiometers.

Regression Analysis for Everest-1							
Time	**Description**	**Temperature Range (°C)**	**Data Points**	**Gradient**	**Y-Intercept**	**RMSD**	**Correlation Coefficient**
June/1993 (Pre V1)	Cool Room &Thermos	-8 to +30	311	0.965	-0.60	0.30	0.999
Nov/1993 (Post V1)	Non-Ambient Contherm	-5 to +25	580	0.980	-1.05	0.60	0.993
Nov/1993 (Post V1)	Ambient Contherm	-5 to +30	264	0.960	-0.39	0.10	0.999
Mar/1994 (Post V7)	Ambient Contherm	-5 to +25	223	0.988	-1.14	0.10	0.999
Nov/1994 (Post V7)	Ambient Contherm	-5 to +25	210	0.972	-0.53	0.09	1.000
Regression Analysis for Everest-2							
Nov/1993 (Post V1)	Non-Ambient Contherm	-5 to +25	580	0.993	1.25	0.40	0.998
Nov/1993 (Post V1)	Ambient Contherm	-5 to +30	264	0.977	1.34	0.10	0.999
Mar/1994 (Post V7)	Ambient Contherm	-5 to +25	223	0.994	0.96	0.10	0.999
Nov/1994 (Post V7)	Ambient Contherm	-5 to +25	210	0.983	1.25	0.09	1.000

A non-ambient method was also conducted where the radiometers and target were forced through large temperature gradients in the range -5 °C to +25 °C. This was done to test the performance of the Everest instruments under regimes of rapidly changing temperature.

4.4 Results and Discussion

Table 4.1 summarises the results of the calibration experiments. This table describes the time and nature of the calibration method; the temperature range for each experiment; the gradient coefficient (a); the y-axis intercept (b); the RMSD values and the correlation coefficient (R^2).

The R^2 values for all of the experiments demonstrate a very good correlation between the radiometric measured temperature T_S and the true thermocouple target temperature T_C (see for example, Figure 4.8).

The gradients for the Everest-1 calibrations average 0.97 (±0.01) and the gradients for Everest-2 calibrations average 0.99 (±0.01). The gradients in each case are consistent but take a value slightly less than 1.0 indicating that the line of regression deviates from the line of 1:1 correspondence.

The cool room and thermos calibration method (June 1993) for the Everest-1 yielded a RMSD of 0.3 °C. For the November 1993 calibration, the non-ambient Contherm method yielded a RMSD of 0.6 °C. The larger RMSD results from forcing the radiometer through a rapidly changing temperature gradient. A similar result can be seen for Everest-2 for the same November (1993) calibration were it returned a RMSD of 0.4 °C. The ambient Contherm calibrations for both Everest-1 and Everest-2 yielded a RMSD of 0.1 °C which is in agreement with the manufacturers estimation of the operating precision of the Everest radiometers (Everest Operating Manual).

The y-intercepts are representative of the bias error or offset associated with Everest-1 and Everest-2. The magnitude of these y-intercepts have varied for

each radiometers over the course of the calibration experiments, indicating that a drift has occurred in the instruments. The change in the y-intercept or bias error for the Everest-1 radiometer between the November 1993 and the March 1994 calibrations was observed to have changed from -0.4 °C to -1.1 °C, a shift of 0.7 °C. Over the same period, the Everest-2 radiometer had drifted from 1.3 °C to 0.95 °C, a shift of 0.35 °C.

Between the March (1994) calibration and the November (1994) calibration, Everest-1 had a shift in the y-intercept from -1.1 °C back to -0.5 °C, a value similar to that obtained in the November 1993 calibration some 12 months earlier. The y-intercept values for the Everest-2 radiometer had drifted from 0.95 °C back to 1.25 °C which again is similar to the y-intercept obtained for the November 1993 calibration. The drift in the Everest radiometers appears to be cyclic rather than divergent. The exact reason for the change in bias error is unknown.

4.5 A Summary of the Calibration Results

(a) The Ambient Contherm method reports the lowest standard errors achievable by both radiometers at 0.1 °C. This occurs when the radiometer and the target are at the same ambient temperature and are not forced through large temperature gradients.

(b) When the Everest-1 radiometer was held at a constant temperature and when the calibration target is subjected to temperature gradients (as experienced in the cool room and thermos experiment), the observed RMSD was 0.3 °C.

(c) When both the Everest radiometers and the calibration target are subjected to large temperature gradients, then the RMSD increases to about 0.5 °C. This suggests that the Everest 4000A series do not have the capacity to deal with rapidly changing temperature regimes.

(d) The drift in Everest-1 over the course of voyage 7 (SHAM) was 0.7 °C and the drift in Everest-2 over the same period was 0.5 °C. The reason for these drifts is unknown but illustrates the need to calibrate these instruments on a regular basis.

It is concluded that the relative offset between the Everest-1 and the Everest-2, should be monitored throughout an extended marine science voyage, in order to determine whether the change in offset in the radiometers occur gradually, or whether they are subject to sudden jumps.

Chapter 5

CHAPTER 5: Analysis of Skin SST

5.1 Introduction

This chapter outlines the errors associated with the radiometric measurement of SST. It will discuss the sensitivity of the skin SST to error with respect to sky temperature, emissivity, the angle of incidence of the radiometer and the temperature difference between the radiometer and the sea surface.

5.2 Error Analysis

The first step in the data analysis process was to apply the calibration functions as outlined in Chapter 4 (Table 4.1) and to then correct for long wave reflection from the ocean surface.

The sensitivity to error of formula 2.11, re-expressed below as formula 5.1, must first be considered, *ie*

$$T_{skin} = \left[\frac{(T_{rad})^4 - (1-\varepsilon)(T_{sky})^4}{\varepsilon} \right]^{\frac{1}{4}} \tag{5.1}$$

where T_{skin} is the skin SST corrected for reflected down-welling thermal radiation, ε is the emissivity of sea water and T_{rad} is the sea surface temperature as read by the radiometer after a correction has been applied for the calibration function. T_{sky} is the temperature of the sky as read by the upward pointing radiometer. Table 5.1 is a summary of correction factors ΔT_{CF} calculated from equation 5.1, that need to be added to T_{rad} in order to obtain an estimate of the corrected value of skin SST T_{skin}. Table 5.1 shows that the greater the difference between T_{rad} and T_{sky}, the larger the correction factor becomes. A decrease in the emissivity from 0.98 to 0.97 for example, will have the effect of increasing the correction factor by 0.34 °C when the T_{rad} - T_{sky} difference is 40 °C. Even a small change in emissivity can affect the precision with which T_{skin} can be determined.

TABLE 5.1 A summary of the correction factors (ΔT_{CF}) needed to be added to the radiometric SST measurements (T_{rad}), in order to get the true skin SST, (T_{skin}). All values are in °C.

emissivity ε			0.96	0.97	0.98	0.99
T_{sky}	T_{rad}	$T_{rad}-T_{sky}$	Correction Factor ΔT_{CF}			
0	0	0	0.00	0.00	0.00	0.00
0	5	5	0.20	0.15	0.10	0.05
0	10	10	0.39	0.29	0.19	0.10
0	15	15	0.58	0.43	0.28	0.14
-15	0	15	0.57	0.43	0.28	0.14
-15	5	20	0.74	0.55	0.37	0.18
-15	10	25	0.91	0.67	0.45	0.22
-15	15	30	1.06	0.79	0.52	0.26
-35	0	35	1.19	0.89	0.59	0.29
-35	5	40	1.33	0.99	0.65	0.32
-35	10	45	1.46	1.09	0.72	0.36
-35	15	50	1.59	1.18	0.78	0.39

TABLE 5.2 A summary of the predicted standard errors in T_{skin} ($\sigma_{T_{skin}}$) as estimated from a propagation of variance analysis. All values are in °C.

emissivity ε			0.96	0.97	0.98	0.99
T_{sky}	T_{rad}	$T_{rad}-T_{sky}$	Standard error $\sigma_{T_{skin}}$			
0	0	0	0.11	0.11	0.10	0.10
0	5	5	0.12	0.12	0.12	0.11
0	10	10	0.15	0.15	0.14	0.14
0	15	15	0.19	0.18	0.18	0.17
-15	0	15	0.19	0.18	0.18	0.17
-15	5	20	0.22	0.22	0.21	0.21
-15	10	25	0.26	0.26	0.25	0.25
-15	15	30	0.30	0.29	0.29	0.28
-35	0	35	0.33	0.32	0.32	0.31
-35	5	40	0.37	0.36	0.35	0.34
-35	10	45	0.40	0.39	0.38	0.38
-35	15	50	0.43	0.42	0.41	0.41

The sensitivity to error of formula 5.1 can be examined assuming a propagation of variance analysis (Mikhail & Gracie 1981), re-expressed as

$$\sigma_{T_{skin}}^2 = \left(\frac{\partial T_{skin}}{\partial T_{rad}}\right)^2 \sigma_{T_{rad}}^2 + \left(\frac{\partial T_{skin}}{\partial T_{sky}}\right)^2 \sigma_{T_{sky}}^2 + \left(\frac{\partial T_{skin}}{\partial \varepsilon}\right)^2 \sigma_{\varepsilon}^2 \tag{5.2}$$

where $\sigma_{T_{rad}}$, $\sigma_{T_{sky}}$ and σ_{T_ε} are the estimated standard errors in the variables T_{rad}, T_{sky} and ε respectively. $\sigma_{T_{skin}}$ is therefore the standard error in T_{skin}. The partial derivatives of T_{skin} with respect to the 3 independent variables control the sensitivity of $\sigma_{T_{skin}}$.

The partial derivatives of T_{rad}, T_{sky} and ε with respect to T_{skin} are as follows:

$$\frac{\partial T_{skin}}{\partial T_{rad}} = \frac{1}{\varepsilon}\left(\frac{T_{rad}}{T_{skin}}\right)^3 \tag{5.3}$$

$$\frac{\partial T_{skin}}{\partial T_{sky}} = \frac{\varepsilon - 1}{\varepsilon}\left(\frac{T_{sky}}{T_{skin}}\right)^3 \tag{5.4}$$

$$\frac{\partial T_{skin}}{\partial \varepsilon} = \frac{T_{sky}^4 - T_{rad}^4}{4\,T_{skin}^3\,\varepsilon^2} \tag{5.5}$$

Table 5.2 presents some typical standard errors as estimated from equation 5.2, for various values of T_{rad}, T_{sky} and ε. It is assumed that the standard deviation in the radiometric measurements $\sigma_{T_{rad}}$ is 0.1 °C as discussed in Chapter 4. It is also assumed that the standard deviation in the value of emissivity σ_ε is 0.01 as it has been shown by research that the emissivity values for sea water ranges from between 0.96 to 0.99 (eg. Davis *et al.* 1971; Sabins 1973; Sidran 1981; Salisbury & D'Aria 1992).

There are a number of problems with T_{sky} measurements that effect the value of $\sigma_{T_{sky}}$ and are summarised as follows:

(1) It is not possible to calibrate the radiometer down to temperatures of -30 °C which would be desirable if accurate values of T_{sky} are sought.

(2) The radiometer measures only a relatively small portion of the sky which may present itself as a problem given variable and patchy cloud cover.

(3) The atmosphere between the upward looking radiometer and the sky will result in specular and diffuse reflection of radiation in the atmospheric column and will thus affect $\sigma_{T_{sky}}$.

From this, it is assumed that $\sigma_{T_{sky}}$ is greater than $\sigma_{T_{rad}}$ for which, a value of 1.0 °C will be adopted. From equation 5.1, an error in T_{sky} of 5 °C for example, will result in an error in T_{skin} of 0.1 °C for an emissivity of 0.98.

The other assumption made in Table 5.2 is that T_{rad} and T_{skin} are approximately the same when calculating $\sigma_{T_{skin}}$ values. It is for this reason, that $\sigma_{T_{skin}}$ values appear to be unaffected by changes in emissivity. Table 5.2 shows the change in the value of $\sigma_{T_{skin}}$ as a function of the sea-sky temperature difference.

It is concluded from Table 5.2 that the largest standard errors are likely to occur on cloud free days at high latitudes, given the clear atmosphere that is found there. The main reason for the increase in standard error lies in the sensitivity of the partial derivative of ε with respect to T_{skin} (see Equation 5.5). When T_{sky} and T_{rad} are approximately the same (as they would be on an overcast day), equation 5.5 takes a value close to 0 thus resulting in standard errors of 0.1 °C. When T_{sky} and T_{rad} differ by as much as 50 °C (as is the case on a very clear day), equation 5.5 takes a value of about -40 resulting in larger standard errors of about 0.4 °C.

Equation 5.1 assumes that the radiance is a function of temperature to the power 4. Singh (1985) indicated that the power variable (b) ranged between 4.3 and 5.0 for the 8-13 μm spectral window, *ie*

$$T_{skin} = \left[\frac{(T_{rad})^b - (1-\varepsilon)(T_{sky})^b}{\varepsilon} \right]^{\frac{1}{b}} \qquad (5.6)$$

Consider a typical high latitude situation where T_{rad} is 0 °C (273 kelvin), T_{sky} is -30 °C (243 kelvin) and we let ε equal 0.96, then T_{skin} is equal to 1.053 °C for a value b equal to 4. Now if b was equal to 5, then T_{skin} becomes equal to 0.997 °C. The resulting difference is only 0.06 °C which is well within the operating precision of the Everest radiometer and suggests that a variation in the value of b from 4 to 5 is insignificant to this study. It should however be considered for targets which have much lower emissivity.

Another property of the Everest radiometer is that the greater the difference between the ambient temperature of the radiometer T_R and the surface temperature as read by the radiometer T_S, the larger its error becomes. Figure 5.1 is a plot of the thermal stress $\Delta T_{stress} = T_R - T_S$ against the temperature difference between T_S and the true calibration temperature T_C ($\Delta T_{error} = T_S - T_C$). The graph in Figure 5.1 is based on calibration data collected by Rapier (1992) for the Everest-1 radiometer (June 1992) in order to investigate the performance of the radiometer under extreme temperature gradients. If ΔT_{stress} has a value of 10 °C, then the error (ΔT_{error}) is of the order of 1 °C. The larger the magnitude of ΔT_{stress}, the larger the error becomes. Typical field situations result in ΔT_{stress} values ranging from between 0 to 6 °C of ambient. On clear sunny days, the radiometer and the radiation shield were noted to warm by as much as 10 °C above ambient. This would lead to a maximum possible error of 1 °C during clear sunny days. Figure 5.2 is an example of what happened during the SR3 WOCE transect between the 1st and 15th of January. The day time peaks in the T_{skin} values correspond with the peaks in the $T_R - T_{skin}$ values.

This implied bias error has not been taken into account, as the number 2 radiometer (Everest-2) was not calibrated in the same way as Everest-1 had been back in 1992. The Everest-2 was used to measure T_{skin} much of the time on Voyage 7 (SHAM) and as a result, it is not possible to justify applying a correction for thermal stress to these data. The best results will be obtained when the radiometer is operated at a temperature similar to that of the sea water.

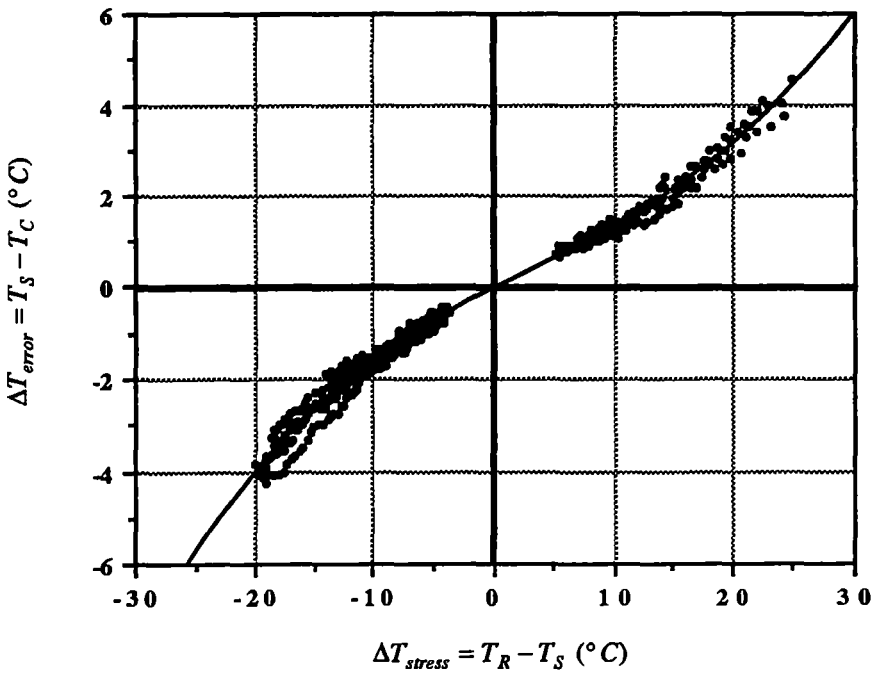

FIGURE 5.1 A scatter plot of the error in radiometric measurement (ΔT_{error}) as a function of the temperature difference between the radiometer and the target (ΔT_{stress}).

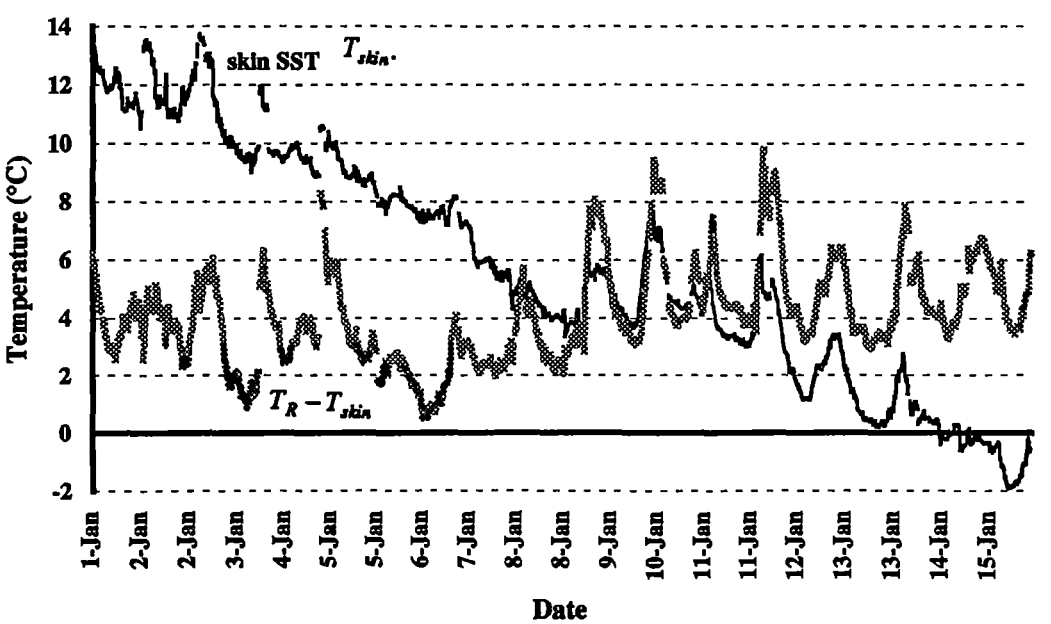

FIGURE 5.2 A time series plot showing the diurnal peaks in T_{skin}, and the temperature difference between the internal temperature of the radiometer T_R and T_{skin}.

Figure 5.1 also indicates that on clear days, ΔT_{stress} will be as much as 30 °C for the sky temperature measurements. The sky temperature could therefore be in error by as much as 5 °C under clear skies which only represents 0.1 °C error in T_{skin}.

A less significant source of error is that associated with the angle from the downward vertical of the radiometer. Figure 5.3a and Figure 5.3b show examples of angular tests conducted on board the *Aurora Australis*. It can be seen that the difference between a 45° angle and a 60° angle is 0.14 °C. This difference would be due mainly to the depth from which the detected thermal radiation is emitted (see Figure 5.4). At an angle of 60°, the detected thermal radiation comes from a shallower depth and hence will appear to have a lower temperature. If the angle of incidence was 45°, then the detected emitted thermal radiation will come from slightly deeper and hence the temperature would appear slightly greater, assuming a normal air less than bulk temperature profile. It may also be that the emissivity decreases with shallower angles of incidence (60°) which has the affect of increasing the amount of reflected sky radiation and again lowering the observed skin temperature. Another point is that for the shallower angle of 60°, there exists a slightly longer path through the atmosphere. This would result in a greater amount of absorbed thermal radiation and hence, the skin temperature may appear slightly cooler.

The majority of measurements were taken with the downward looking radiometer set between 45° and 53° from the vertical. The ship itself was prone to pitch and roll motion. If the ship was to roll by 15°, then the uncertainty associated with the change in angle of incidence will be 0.14 °C. The effect of waves may come into play as the local tilt of the sea surface would alter the angle of incidence at which the radiometer is detecting the emitted radiation. The errors associated with waves would be very difficult to determine but it is suspected that the rolling motion will be the main contributor to the change in angle of incidence.

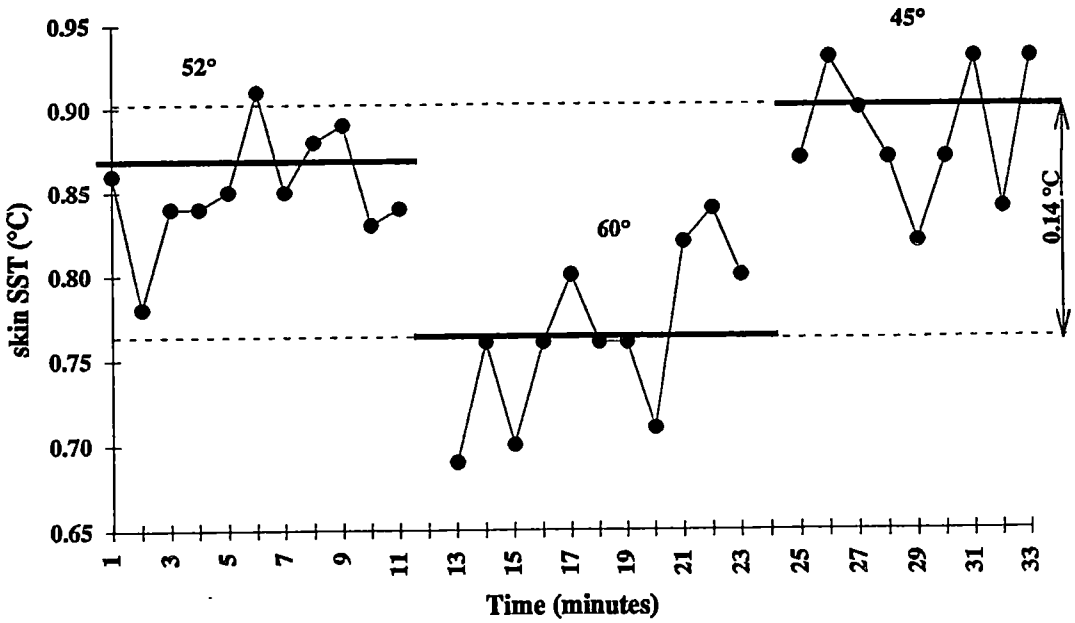

FIGURE 5.3a Time series plots showing the change in skin SST with a change in angle of incidence for the angles 60°, 52° and 45° from the downward vertical.

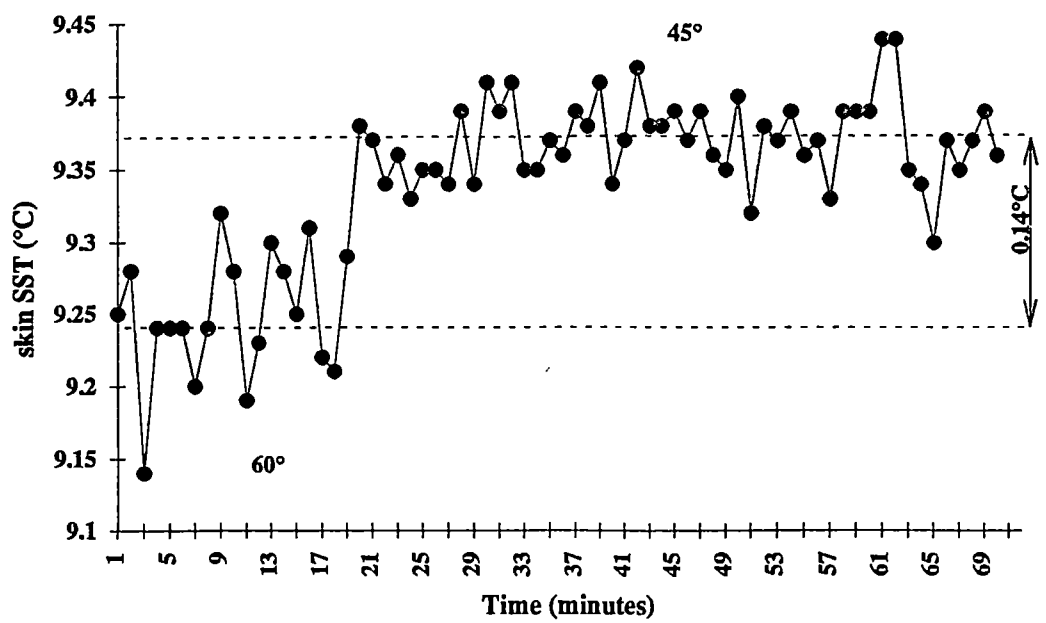

FIGURE 5.3b Time series plots showing the change in skin SST with a change in angle of incidence for the angles 60° and 45° from the downward vertical.

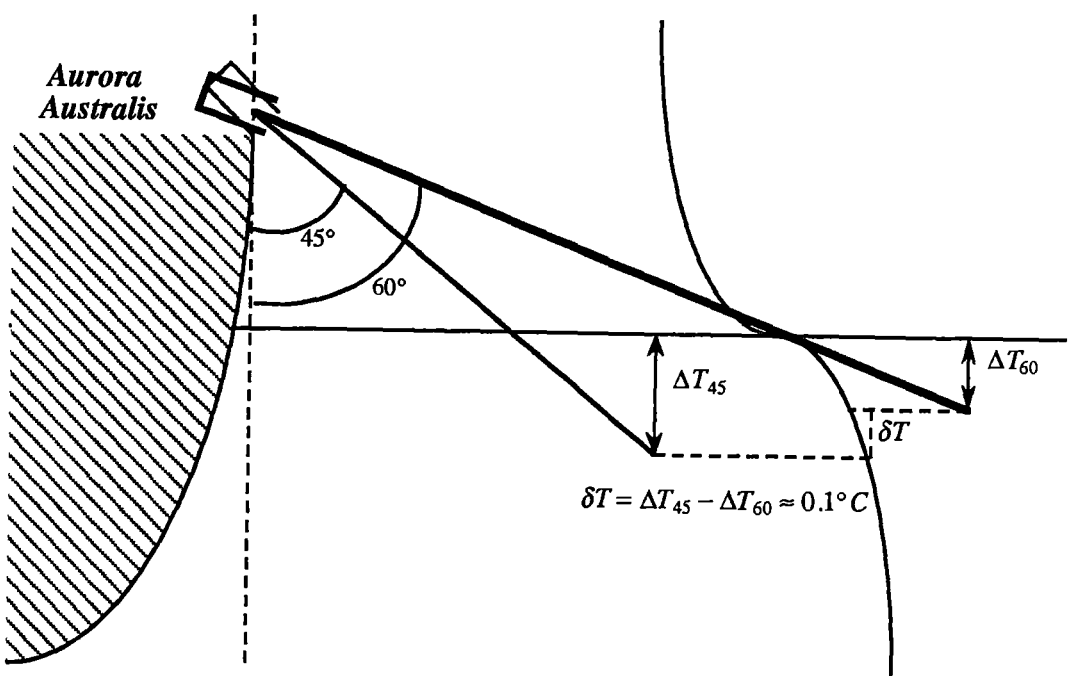

FIGURE 5.4 An illustration of how the skin SST changes with the angle of incidence. A change in optical depth and/or a change in surface emissivity may account for a small temperature change of 0.1 °C.

The roll of the ship would need to be greater than 20° (*ie.* in rough seas) if the error is to exceed 0.2 °C which in itself, is the largest acceptable error needed for this ground truth study.

5.3 LOWTRAN-7 Analysis

The transmittance of radiation through an 8-13 μm filter over a 20 metre atmospheric path between the Everest 4000A radiometer and the sea surface was briefly examined using LOWTRAN-7 software. As mentioned in Chapter 3, the downward looking radiometer was pointed mostly at 45°, a distance of 21 metres from the sea surface.

A standard atmosphere for a high latitude winter was chosen. The sea surface temperature was set at 280 kelvin or 7 °C. The radiance transmitted through a zero metre filtered atmosphere was adopted as a reference at 19.08 $Wm^{-2}sr^{-1}$. This was converted to a radiant exitance, and a factor was calculated to increase this radiant exitance to that produced by a 280 kelvin blackbody. The process was repeated for a 20 metre passage through the atmosphere, giving a radiance of 19.06 $Wm^{-2}sr^{-1}$. This was converted to an effective blackbody temperature, found to be 279.92 kelvin.

It is concluded that a 20 metre standard atmosphere (high latitude in winter) results in a maximum temperature difference of 0.1 °C. This temperature difference lies within the operating precision of the Everest 4000A radiometer and does not significantly affect the results of this study.

Chapter 6

CHAPTER 6: Results and Discussion

This chapter will first describe how the data was sorted and analysed. The results will be presented as time series plots; histograms and scatter plots. The data will also be summarised in tabular form. The influences that effect the sign and magnitude of ΔT are discussed and the final section in this chapter compares *in situ* measurements of skin and bulk SST with measurements derived from NOAA-AVHRR imagery.

6.1 Data Analysis Method

Voyage 7, the summer voyage (SHAM), was considered in 3 parts. The period from the 1st of January to the 15th of January 1994 (code name Jan SR3) represents the WOCE SR3 transect starting at Hobart (43° S, 147° E) and finishing just north of Dumont D'urville (65 °S, 140° E). The second set of data was from the 22nd of January through to the 31st of January (code name Jan B) which starts at about 150 km NW of Casey (65° S, 109° E) and concluded prior to the arrival at Mawson (67° S, 63° E). The gap between the 15th of January and the 22nd of January was due to a hardware failure in the data logging PC. The third part of voyage 7 contains the data collected during the month of February from the 1st to the 27th (code name Feb) and contains the data collected from Mawson back to Hobart, via Law Base, Davis, Casey and Dumont D'urville.

Voyage 1, the winter voyage (THIRST), was also considered in 3 parts. The period from the 7th to the 27th of August (code name Aug) was from Hobart to Heard Island (53° S, 75° E) via Macquarie Island (54° S, 158° E). During the period from the 3rd to the 30th of September (code name Sep), the ship was involved in fishing operations in an area north of Heard Island. The final set of data was the first week on October from the 1st to the 7th (code name Oct) and includes an easterly transect from Heard Island back to Hobart.

The first phase of the data analysis was to correct the radiometric sea surface brightness temperature T_S to T_{rad} using the calibration function as outlined

in Chapter 4. The T_{rad} values were then corrected for the reflected component of sky radiation using equation 5.1 (see Chapter 5) where an emissivity value of 0.98 was adopted.

The next step was to further separate the 6 data files, as mentioned above, into day and night files assuming that quantum radiation values of less than 30 μ moles s^{-1} m^{-2} represents the boundary between night time and day time. The data were then further divided depending on the estimated amount of cloud cover, according to the radiometric sky temperature measurements. Sky temperatures lower than -10 °C (in the range -10 to -40 °C) were assumed to represent relatively clear skies (0-2 octas). Sky temperatures warmer than -10 °C (in the range -10 °C to +5 °C) were assumed to represent heavy cloud cover (3-8 octas). Additional cloud cover observations were obtained from the *Aurora Australis* bridge log book. It was found that there was a consistent relationship between the observed cloud cover (in octas) and the radiometric sky temperature measurements. A regression analysis was then performed between the skin-bulk temperature difference ΔT and the air-bulk temperature difference ΔT_{ab} as a function of time of day and cloud cover.

The relationship between wind speed and ΔT was examined independently of the diurnal and cloud cover effects. Three wind classifications were chosen: low wind speeds less than 10 knots (light air to gentle breeze); intermediate wind speeds between 15 and 20 knots, and strong wind speeds greater than 22 knots (strong breeze to storm). These wind classification groups were selected from the Beaufort scale (Walton-Smith 1973).

A second wind speed analysis examined the relationship between wind speed and ΔT was examined as a function of the diurnal and cloud cover effects. The data was stratified into 2 categories of wind speed: strong winds (>10 knots) and light winds (<10 knots). The 10 knot wind speed cut off was chosen because the conduction layer remains intact for wind speeds less than 10 knots, or 5 ms^{-1} (Grassl 1976).

6.2 Results

For ease of reference, some of the results are presented in Appendices A through to E. Appendix A contains the time series plots of selected radiometric and meteorological data. Appendix B shows the histogram plots of ΔT. Appendix C contains the scatter plots and regression of ΔT against ΔT_{ab}. Appendix D summarises the monthly averages of the data in tabular form and Appendix E shows histograms and scatter plots relating wind speed to ΔT. It is advised that some of the day time data may have been affected by solar heating of the PVC pipes used to contain the radiometers as it was discovered that there is a 5 % signal contribution from the PVC pipes themselves (see Appendix F).

6.2.1 The Time Series Plots

Appendix A shows time series plots for the 6 monthly data files as defined in section 6.1. These include time series plots of skin, bulk and air temperatures; ΔT and ΔT_{ab} temperature differences; quantum radiation; sky temperature, wind direction, wind speed and wind gust.

The January - SR3 Transect (SHAM)

Between the 5th and the 7th of January (see Appendix A1-A6), it can be seen that the differences between the air, skin and bulk temperatures are quite large. On around the 6th and 7th of January, the value of ΔT_{ab} was as much as -6 °C. A ΔT value of about -2 °C occurred at the same time suggesting that the air temperature in some way is related to the magnitude of ΔT. It can also be seen during the same period that the quantum radiation values peak at about 800 μ mole s^{-1} m^{-2} and the sky temperature values are of the order of 0 °C representing extensive cloud cover. The wind direction turned from a westerly direction (270°) to a more southerly direction (180°) during the period from the 5th to the 7th of January. This is significant because it is this southerly air flow which is bringing the colder air from higher latitude and confirms that the synoptic situation can influence the magnitude and sign of ΔT. On the 6th of January, the wind speed

reached a maximum of 40 knots, with gusts up to 45 knots. It is not immediately clear from the time series plots (see A2 and A6) if there is any significant correlation between wind speed and ΔT.

The time series for the SR3 transect shows some strong diurnal cycles in the skin SST and ΔT values. The peaks in the skin SST values correspond with the peaks in the quantum radiation, which had values ranging up to 1400 μ mole s^{-1} m^{-2}. The observed diurnal peaks may be due to the solar heating of the PVC pipes. It was indicated in Chapter 5 that the peaks in skin SST may in part be due to the warming of the radiometer and radiation shield, leading to increases of up to 1 °C. This does not account however for the 2 to 3 °C diurnal amplitude as seen in the time series plot (see A1 and A2). The indications are that there are still diurnal and insolation effects at higher latitudes on cloud free days.

The January B Time Series (SHAM)

The data collected during this period were gathered south of 60° S (see Appendix A7-A12). Low air temperatures were the order of the day, reaching minima of -4 °C. The bulk SST values remain fairly constant, whilst the air temperatures were much more variable in response to fluctuations in the wind direction and associated weather patterns. The skin SST values seem to fluctuate in response to the changes in air temperature. There are again peaks in the skin SST and ΔT values corresponding to peaks in quantum radiation again indicating the affects of solar radiation.

On the 25th of January (at about 66° S, 85° E), an unusual peak was noted in the ΔT values, corresponding to a trough in the ΔT_{ab} values (see A8). The peak in ΔT may have resulted from absorbed solar radiation at the sea surface and by the PVC pipes. At the same time, SE winds were bringing cold air from the Antarctic continent which resulted in a rapid lowering of air temperatures.

On the 30th of January, the sky temperature values (about 0 °C) indicates the presence of extensive cloud cover (see A10). The winds were quite strong

reaching up to 30 knots (see A12). These conditions correspond to minimal temperature differences between measurements of air, skin and bulk temperatures (see A7).

The Month of February (SHAM)

The data collected between the 1st and the 25th of February originated south of 64° S (see Appendix A13-A18). On occasions, the air temperatures dropped to -4 °C, resulting in large negative ΔT_{ab} values (air cooler than bulk) (see A14). Again diurnal peaks in skin and ΔT temperatures were observed corresponding to the peaks in quantum radiation. The highest latitude reached by the vessel was in Prydz Bay near Law Base (69° S, 83° E) and it was during this time (7th of February) that large negative values of ΔT were observed due mainly to the cold air flowing off the Lambert Glacier/Amery Ice Shelf region.

On the 27th of February, large temperature gradients in ΔT and ΔT_{ab} were observed and seemed to coincide with the Sub-Antarctic and Polar Frontal region (see A13). It is in this region that warm air and water from the north mix with the cold air and water from the south thus resulting in greater magnitudes of ΔT and ΔT_{ab}.

The Month of August (THIRST)

The winter voyage started with a SE transect from Hobart to Macquarie Island from the 7th to the 11th of August (see Appendix A19-A24). There appears to be a diurnal cycle in the skin SST values particularly on the 12th and 13th of August and again on the 17th of August. Diurnal peaks in the skin SST are less pronounced at other times due to patchy cloud cover and shorter periods of day light (see A19).

There appears to be large amplitudes in the ΔT and ΔT_{ab} values on the 17th of August and it is suspected that this was due to the ship passing through a

meander in the polar frontal zone. There also appears overall to be a good correlation between ΔT and ΔT_{ab} during the month of August (see A20).

From the 13th to the 24th of August, the wind was mainly from the west but varied between NW (315°) to SW (225°) winds for much of the time. The SW winds on the 16th and on the 25th, for example, brought cooler air from the south. A series of weather fronts is evidenced by a cycle of peaks and troughs in the wind speed data where the wind speeds varied between 0 and 60 knots (see A24).

The Month of September (THIRST)

The month of September was spent in the waters north of Heard Island (see Appendix A25-A30). The time series plots show the diurnal variations much more clearly during this period (see A25). On the 9th, 12th and 16th of September, the wind direction was north to NW (315° to 360°) bringing warmer air temperatures reaching a maximum of 3.5 °C. The bulk sea temperatures remained fairly constant through out this period and ranged between 1 to 1.5 °C between the 3rd and the 28th of September. The skin SST values peak in response to the warmer air temperatures. On the 10th, 14th and 23rd of September, the wind direction was more from the SW (225°) and brought cooler air temperatures of -2 °C resulting in negative ΔT values. The September data set shows a clear relationship between ΔT, ΔT_{ab} and wind direction.

Peaks in quantum radiation appear to have been dampened on some days due to extensive cloud cover although there are still some instances where peak quantum radiation correspond to peaks in the skin and ΔT temperatures.

The First Week of October (THIRST)

The most interesting period in the October data set is the period from the 4th to the 5th of October (see Appendix A31-A36) during which time, the

magnitude of ΔT and ΔT_{ab} are greatest (see A32). This time seems to be coincident with the crossing of the Sub-Antarctic and Polar Frontal zone.

On the 4th of October, the wind direction starts from the north then rapidly swings around to the south bringing a sudden flow of cooler air. At the same time, the bulk SST values increase as the ship passes over the Sub-Antarctic Front resulting in large ΔT values.

In the remaining sections of this chapter, the effects of the day/night diurnal cycle and the amount of cloud cover will be examined in more detail. There will also be a discussion of the regression analysis between ΔT and ΔT_{ab}. The relationship between ΔT and wind speed will be discussed separately. A comparison between the *in situ* skin and bulk SST data and the NOAA-AVHRR SST data are discussed in the final section of this chapter.

6.2.2 Frequency Histograms

Appendix B1 shows frequency histograms of ΔT for each of the 3 summer voyage data files January (SR3), January (B) and February. The ΔT values for the period January SR3 average -0.43 °C and range from -2.5 to +2.5 °C. The histogram has a near normal distribution. The wide range in ΔT values is due to large spatial, temporal and diurnal variations. The January B file has a smaller range of ΔT values from -1.5 to +1.5 °C and is centred at -0.33 °C. This may be due to the fact that it is a comparatively small data file and consists of data collected south of 60° south only. The month of February has a more classic normal distribution frequency centred at -0.26 °C and ranges from -2.25 to +1.75 °C.

Appendix B1 also shows frequency histograms for the winter voyage for the months of August, September and October. A normal distribution can be seen for August where ΔT values range from -3.0 to +2.0 °C and average -0.40 °C. The month of September appears to depart from a classic normal distribution, and ΔT ranges from -1.25 to +3.0 °C with an average of +0.37 °C. This is due in part to the

frequent occurrence of warm air temperatures, as a result of northerly winds. The first 7 days in October display a very large range of ΔT values from -2.75 to +2.75 °C and averages +0.14 °C. These measurements were collected in the region of the Sub-Antarctic and Polar Fronts, where the warm and cool air and sea temperatures are in close proximity.

The next phase of the data analysis was to relate ΔT to the time of day and to the amount of cloud cover. The data from the summer voyage (SHAM) and the winter voyage (THIRST) were split into the following 4 categories:

(a) cloudy days,
(b) clear days,
(c) cloudy nights and
(d) clear nights.

A day or night was defined as *clear* where the radiometer sky temperature measurements (T_{sky}) are less than -10 °C. Clear sky conditions range from -10 °C to -35 °C and imply that the sky is relatively free of cloud cover. The term *Cloudy* applies when T_{sky} is greater than -10 °C. The temperature of cloudy skies range from -10 °C up to +5 °C and imply that the sky contains extensive cloud cover. The distinction between *Day* time and *Night* time was taken as a quantum radiation value of 30 μ mole s^{-1} m^{-2}. If the quantum radiation is in the range 0 to 30, then the data were assumed to be at night. For quantum radiation values greater than 30, the data were then assumed to be representative of day time. A small correction was applied to the ΔT values to account for a 5 % signal contribution from the PVC pipes assuming that the air temperature is representative of the pipe temperature (see Appendix F).

Appendix B2 shows histograms of ΔT for voyage 7 (SHAM). It can be seen that there are distinct differences between the 4 categories. On cloudy days in summer (B 2.1), the histograms show a normal distribution with ΔT values ranging from -2.25 °C to +1.75 °C and averaging -0.09 °C. On clear days in summer (B 2.2), the average is +0.10 °C with a range from -2.0 to +2.5 °C. The frequency

distribution for clear days seems to bias towards positive ΔT values and is likely to be due to absorbed solar radiation at the surface and by solar heating of the PVC pipes resulting in an increased skin SST.

On cloudy nights in summer (B 2.3), ΔT tends to be biased towards negative values with a range -2.5 to +1.0 °C at an average -0.44 °C. On clear nights (B 2.4), the ΔT values are almost all negative and range from -2.25 to 0.0 °C at an average -0.94 °C. During clear nights, there is heat loss from the ocean surface to the atmosphere resulting in cooler skin temperatures. Cloud cover at night acts as an insulator maintaining air temperatures and impeding heat loss from the sea surface to the atmosphere.

Appendix B3 shows histograms of ΔT for voyage 1 (THIRST). The ΔT values for cloudy days (B 3.1) appear as a normal distribution with values ranging from -2.0 to +2.5 °C at an average of +0.29 °C. On clear days in winter (B 3.2), a large range of ΔT values exist from -2.5 °C to +3.0 °C at an average of +0.36 °C. This is due in part to warm air temperature fluxes from the north but again may be due to solar heating of the pipes, but is less likely due to the higher wind speeds.

The cloudy night histogram for winter (B 3.3) is centred at -0.12 °C and ranges from -2.75 to +1.75 °C whilst for clear nights (B 3.4), the average ΔT is -0.39 °C and ranges from -3 °C to +1.25 °C. The effect of cloud cover at night is similar for both the summer and winter voyages in that the cloud cover at night reduces heat loss from the ocean surface.

Table 6.1 summarises ΔT values for the SHAM and THIRST voyages. The overall average for cloudy days is +0.10 °C and the overall average for clear days is +0.23 °C. A reverse situation is seen at night where the average ΔT for cloudy nights is -0.28 °C and for clear nights, averages -0.66 °C. On clear nights, all heat exchange is likely to be upwards from the ocean to the atmosphere which results in cooler skins.

TABLE 6.1

A summary of the average ΔT values given the time of year, cloud cover and the time of day.

Month	Day		Night		Monthly Mean
	Cloud	Clear	Cloud	Clear	
Jan (SR3)	-0.31	0.45	-0.94	-0.92	-0.43
Jan (B)	-0.05	-0.16	-0.22	-0.90	-0.33
Feb	0.10	0.01	-0.15	-1.00	-0.26
Mean (SHAM)	-0.09	0.10	-0.44	-0.94	-0.34
Aug	-0.13	-0.47	-0.13	-0.86	-0.40
Sep	0.61	0.77	0.26	-0.16	0.37
Oct	0.38	0.79	-0.49	-0.14	0.14
Mean (THIRST)	0.29	0.36	-0.12	-0.39	0.04
Mean (Cloud/Clear)	0.10	0.23	-0.28	-0.66	
Mean (Day/Night)	0.17		-0.47		
Total Mean	-0.15				

The diurnal cycle varies dependant on cloud cover. If for example, there is a transition from a clear day to a clear night, then the average amplitude in the diurnal temperature cycle is 0.89 °C and is again influenced by solar heating of the pipes. If there is a transition from a cloudy day to a cloudy night, then the diurnal cycle is less, at about 0.38 °C. The ΔT for the total daytime data set is +0.17 °C and is in part, influenced by absorbed solar radiation.

At night time, the ΔT values average -0.47 °C as a direct result of heat loss from the sea surface to the atmosphere. The average diurnal cycle for the complete data set is 0.64 °C. The average ΔT for the two combined voyages is -0.15 °C thus suggesting that in general, the skin temperatures are slightly less than the bulk SST.

The average ΔT value for the summer voyage is -0.40 °C and the average ΔT for winter is +0.04 °C. The winter average of ΔT is greater than the summer average which can be explained in two ways. Firstly, there are many occurrences of warm air masses brought by northerly winds which are more likely to occur at a mid latitudes of 53° south. The second reason is that the stronger winds experienced in winter may act to break down the conduction layer via turbulent mixing, resulting in skin and bulk temperatures being nearly the same.

6.2.3 Regression Analysis

From the discussion so far, there appears to be a relationship between ΔT, wind speed, wind direction and air temperature. This next section looks more closely at how well ΔT and ΔT_{ab} correlate given the time of day and the amount of cloud cover. Appendix C contains scatter plots of ΔT against ΔT_{ab} and Appendix D summarises the data in tabular form. Table 6.2 summarises the correlation coefficients associated with the regression between ΔT and ΔT_{ab}. It was found that on clear days during the summer voyage, poor correlations existed between ΔT and ΔT_{ab}, with an average correlation coefficient (R^2) of 0.11 (see for example, Appendix C2 and C6).

TABLE 6.2

Summary of the correlation coefficients associated with the regression analysis between ΔT and ΔT_{ab}.

Month	Day		Night	
	Cloud	Clear	Cloud	Clear
Jan (SR3)	0.68	0.21	0.77	0.81
Jan (B)	0.31	0.00	0.70	0.45
Feb	0.46	0.12	0.68	0.63
Mean (SHAM)	0.48	0.11	0.72	0.63
Aug	0.93	0.87	0.85	0.78
Sep	0.68	0.45	0.90	0.78
Oct	0.77	0.78	0.90	0.92
Mean (THIRST)	0.79	0.70	0.88	0.83
Total mean	0.64	0.41	0.80	0.73

TABLE 6.3

Summary of the gradient coefficients associated with the regression analysis between ΔT and ΔT_{ab}.

Month	Day		Night	
	Cloud	Clear	Cloud	Clear
Jan (SR3)	0.49	0.47	0.34	0.35
Jan (B)	0.34	-0.03	0.33	0.41
Feb	0.38	0.25	0.42	0.48
Mean (SHAM)	0.40	0.23	0.36	0.41
Aug	0.42	0.48	0.40	0.37
Sep	0.41	0.58	0.42	0.34
Oct	0.46	0.52	0.38	0.43
Mean (THIRST)	0.43	0.53	0.40	0.38
Total mean	0.42	0.38	0.38	0.40
Average Gradient	0.40 (±0.1)			

The solar heating of the PVC pipes and the 5% signal contribution is one explanation for the poor correlation. The R^2 values for cloudy days in summer is 0.48, an improvement on clear days in summer although this might suggest that there are still some solar radiation effects.

The R^2 values for cloudy night time conditions in general are quite good and average 0.72 for the summer voyage and 0.88 for the winter voyage (see for example, Appendix C19). During clear nights, the R^2 values are 0.63 for summer and 0.83 for winter.

Day time R^2 values for the winter voyage still rate quite high and indicates that there is less solar radiation incident on the ocean surface and on the PVC pipes due to the low angle of the sun and shorter day length from August to October.

Figure 6.1 is a plot of the correlation coefficients for the summer and winter voyages. The first thing to note is that the R^2 values for the winter voyage in general are larger than the R^2 values in summer. For both voyages, night time correlations are better than day time correlations due to solar radiation. The order of rank from good correlations to poor correlations are summarised as follows:

(a)	cloudy nights	(R^2 = 0.80)
(b)	clear nights	(R^2 = 0.73)
(c)	cloudy days	(R^2 = 0.64)
(d)	clear days	(R^2 = 0.41)

Table 6.3 summarises the gradient coefficients associated with the regression between ΔT and ΔT_{ab} and are consistent with an average value of 0.40 (±0.1). The gradients are not consistent for the clear day data set for both the summer and winter voyages due to the poor correlation between ΔT and ΔT_{ab}.

The y-intercepts shown in Table 6.4 tend to vary much more so than the gradient coefficients. The y-intercepts for day time values tend to be higher (averaging 0.48) again due to solar warming of the shields.

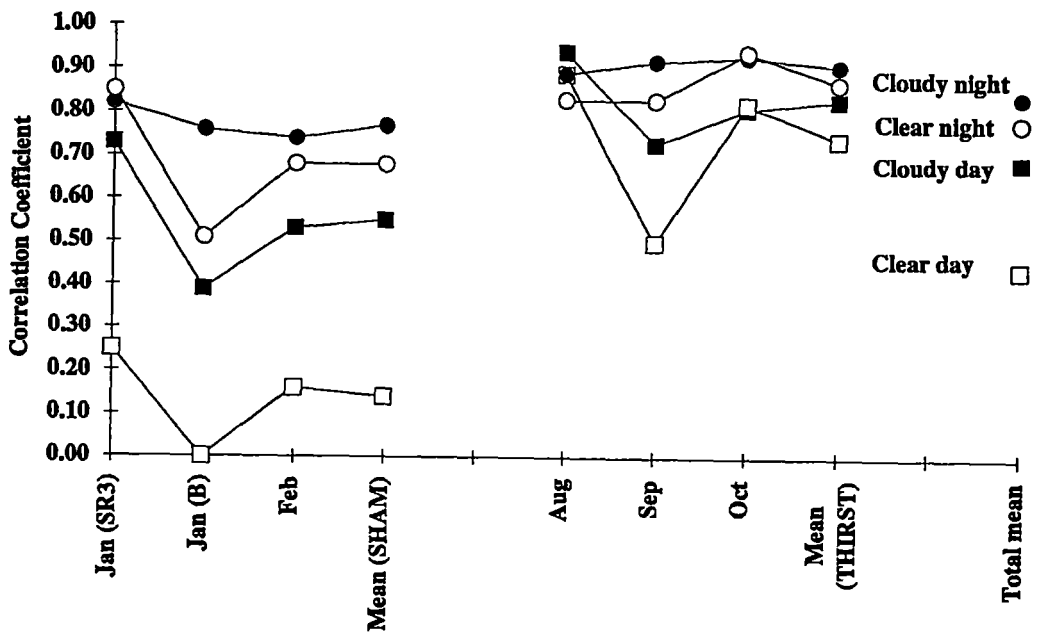

FIGURE 6.1 A graphical representation of the correlation coefficients associated with the regression between ΔT and ΔT_{ab}. The correlation coefficients vary with the time of day and cloud cover.

TABLE 6.4

Summary of the y-intercepts associated with the regression analysis between ΔT and ΔT_{ab}.

Month	Day		Night	
	Cloud	Clear	Cloud	Clear
Jan (SR3)	0.41	0.84	-0.42	-0.54
Jan (B)	0.23	-0.19	0.02	-0.25
Feb	0.45	0.52	0.26	0.01
Mean (SHAM)	0.36	0.39	-0.05	-0.26
Aug	0.31	0.36	0.17	-0.05
Sep	0.59	0.87	0.33	0.16
Oct	0.56	0.71	0.14	0.16
Mean (THIRST)	0.49	0.65	0.21	0.09
Total mean	**0.43**	**0.52**	**0.08**	**-0.09**
Day/Night mean	**0.48**		**-0.01**	

TABLE 6.5

Summary of the RMSD values associated with the regression analysis between ΔT and ΔT_{ab}.

Month	Day		Night	
	Cloud	Clear	Cloud	Clear
Jan (SR3)	0.52	0.91	0.27	0.22
Jan (B)	0.42	0.65	0.18	0.26
Feb	0.48	0.77	0.34	0.37
Mean (SHAM)	0.47	0.78	0.26	0.28
Aug	0.20	0.35	0.27	0.34
Sep	0.34	0.66	0.20	0.20
Oct	0.41	0.40	0.25	0.21
Mean (THIRST)	0.32	0.47	0.24	0.25
Total mean	**0.40**	**0.63**	**0.25**	**0.27**
Day/Night mean	**0.52**		**0.26**	

At night, the y-intercepts average 0.0 °C. It would be expected that if air and bulk sea temperatures were the same, then ΔT would be equal to zero resulting in a regression passing through the origin. However, if a diurnal deck layer was allowed to form under clear sky conditions, then a slightly higher value in the skin SST value would result leading to positive y-intercepts for a ΔT versus ΔT_{ab} scatter plot. The average y-intercept for the entire SHAM voyage is 0.11 °C and the average y-intercept for the THIRST voyage is 0.36 °C, both values suggesting a bias offset in both sets of data. This might be explained in three ways.

The bias could be due to an offset error in the air temperature values as they have not been calibrated. The bias could also be explained by the influence of absorbed solar radiation, elevating the skin temperature measurements which in turn, would result in positive y-intercept values. The elevated skin temperatures are also influenced by solar heating of the pipes on clear days.

It is interesting to note that for clear days, the average y-intercept is at its largest at +0.52 °C. For cloudy days, the y-intercepts are slightly less averaging +0.43 °C. The average y-intercepts for cloudy nights are +0.08 °C and for clear nights, average -0.09 °C. The insulating effect of cloud cover at night is again apparent. The cloudy day time y-intercepts on average also tends to be less than the y-intercepts for the clear days again confirming that day time cloud cover is reducing the amount of absorbed solar radiation at the sea surface.

It appears in general that the y-intercepts for the day time data are 0.09 °C lower on average under cloudy conditions as compared to clear sky conditions. This situation is reversed at night where the y-intercepts are 0.17 °C higher on average under cloudy sky cover. It may be concluded that as far as the data from SHAM and THIRST voyages are concerned, skin SSTs are of the order of 0.1 °C cooler on average under a cloud during day time and 0.2 °C warmer on average under cloud during night time.

Table 6.5 summarises the RMSD values for the regression between ΔT and ΔT_{ab}. The RMSD for the clear day time data in summer is 0.78 °C and is consistent with the poor correlation for this set of values. RMSD values for night time data for both clear and cloudy conditions, averages 0.26 °C. The average RMSD for cloudy days is 0.40 °C. The larger RMSD values for the day time data are again effected by solar radiation. It could also be due to the sensitivity to error of equation 5.1 given a large temperature difference between the sea and the sky.

The average RMSD of 0.26 °C for the night time data is potentially very useful as it enables ΔT to be estimated to within ±0.26 °C provided that an air and bulk temperature and time of day are known. A simple algorithm can therefore be derived for the estimation of ΔT based on the regression analysis between ΔT and ΔT_{ab}. This will be discussed later in Chapter 7.

6.3 Wind Speed Analysis

This next section will assess the significance of the relationship between wind speed and ΔT. The wind speed is measured about 20 metres above sea level which may result in misleading information. The ship's speed and direction may affect the way in which the air mass passes around and over the ship. The wind speeds ideally should be measured closer to the sea surface, but this may not be possible in heavy seas. An alternate way of looking at wind speed is to use a log function to estimate what the wind speed will be at a height closer to the sea surface.

It was generally found that there is no direct correlation between wind speed and ΔT. Figure 6.2 is a time series plot of ΔT and wind speed from the 1st of October to the 7th of October. It appears that the wind speed and ΔT are in phase for some parts of this graph but are out of phase for other parts of the graph. The net result is a poor correlation coefficient of 0.05.

The wind direction, as mentioned in the previous sections of this chapter, does appear to exert some control over the ΔT values. Figure 6.3 is a scatter plot

of ΔT against wind direction for the first week in October. This figure shows that north westerly winds were generating positive ΔT values as a result of higher air temperatures whilst south westerly winds generated negative ΔT values as a result of lower air temperatures.

6.3.1 Method 1

A simple wind speed analysis was performed independent of diurnal and cloud cover effects where 3 distinct wind speed classifications were selected, ie light (<10 knots), intermediate (15-20 knots) and strong (>22 knots).

The ΔT values for each of the above wind speed classifications have been plotted as histograms and can be seen in Appendix E1. The histogram for calm winds in summer (E 1.1) have ΔT values ranging from -2.0 to +2.5 °C with an average ΔT of +0.07 °C. The shape of the histogram tends to be biased towards warm skin temperatures or positive ΔT values and is consistent with solar heating of the PVC pipes during the summer voyage, particularly under light winds. On investigating the intermediate wind histogram for summer (E 1.2), we note a shift back towards negative ΔT values. The average ΔT is -0.54 °C with a range of -2.5 to +1.75 °C. As the wind speed increases, it becomes less likely that diurnal deck layers will form due to additional wind driven turbulence in the upper water column. It is also less likely that the temperature of the PVC pipes is going to be significantly different from the air temperature which means that the 5% signal contribution has a minimal affect under stronger winds. The histogram for strong winds in summer (E 1.3) shows a similar picture to that of the intermediate winds where the average ΔT is -0.43 °C and ranges between -2.5 to +2.0 °C.

The situation for the winter voyage seems to give the opposite picture. The histogram for calm winds in winter (E 1.4) has an average ΔT of -0.36 °C with a range of -2.25 to +1.25 °C. This suggests that the effect of solar radiation has less effect in winter due to the shorter day time period.

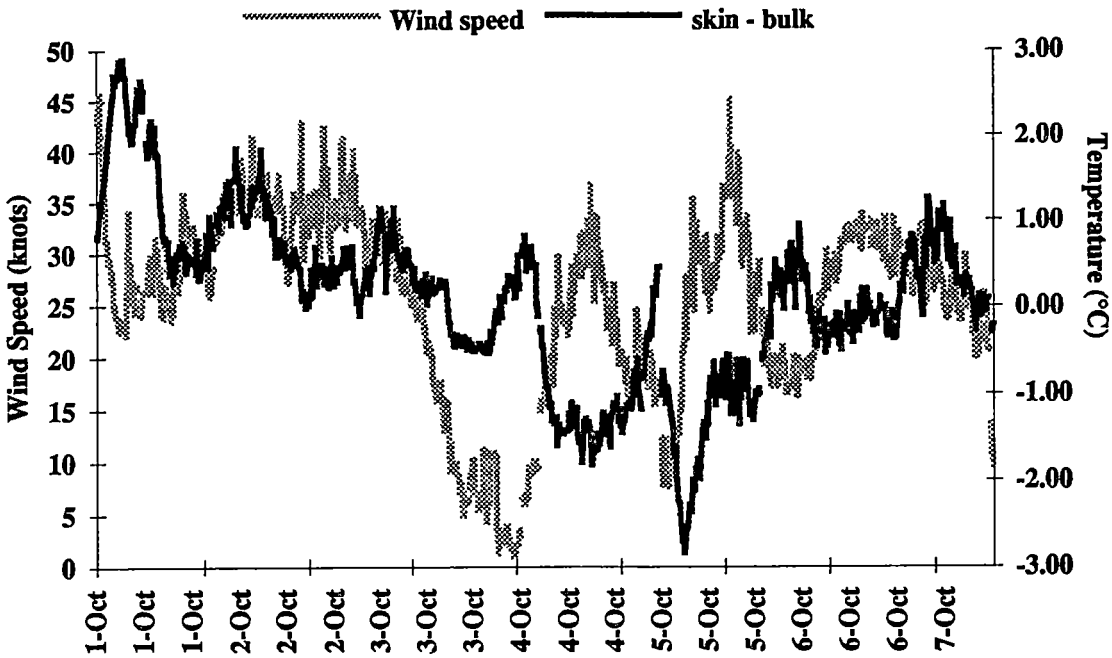

FIGURE 6.2 Time series plot showing the poor correlation between wind speed and ΔT for the first week in October.

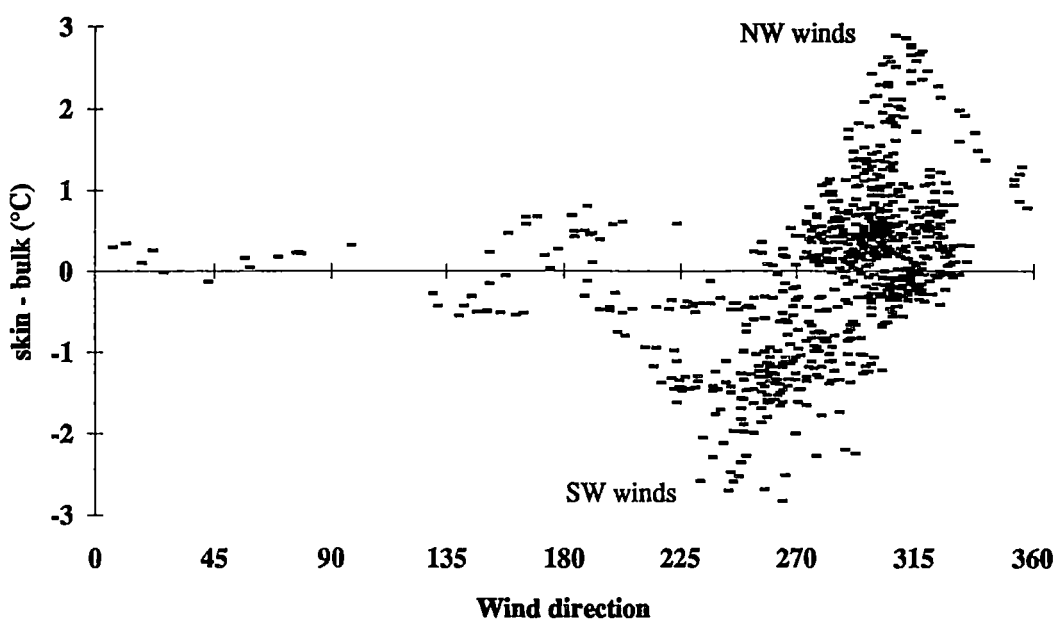

FIGURE 6.3 A scatter plot of ΔT against wind direction for the first week in October. Positive ΔT values occur for NW winds and negative ΔT values occur for SW winds.

For intermediate and strong winds in winter (E 1.5 and E 1.6) have average ΔT values of about 0 °C with a typical range of -2.75 to +2.0 °C. A skin-bulk temperature difference of 0 °C suggests that there might be a break down of the conduction layer which can occur under strong winds.

Appendix E2 shows scatter plots and regression of ΔT against ΔT_{ab} for each of the 3 wind categories for both the summer and winter voyages. Each graph shows a line of regression, the gradient coefficient, the y-intercept and the correlation coefficient. These results are summarised in Table 6.6 and reveals some interesting results.

If we first compare the ΔT values to the ΔT_{ab} values as shown in Figure 6.4, then we can see that the shape of the ΔT curve is similar to that of ΔT_{ab} thus suggesting that the relationship between ΔT and ΔT_{ab} is not strongly dependent on wind speed.

The R^2 values for light winds in summer average 0.30. Again the low correlation is presumably caused by absorbed solar radiation during the day time. The average R^2 for summer is 0.46 which is much less than the average R^2 for the winter voyage of 0.82.

The y-intercepts present an interesting picture (see Figure 6.5). It appears that the y-intercepts are greatest for low wind speeds (ie 0.5 for the summer voyage and 0.57 for the winter voyage). This again is due to elevated skin SST as a result of the PVC pipe warming during the day. The y-intercepts for intermediate wind speeds are 0.10 for summer and 0.40 for winter. The y-intercepts for stronger winds are 0.07 for summer and 0.26 for winter. The stronger winds for both voyages appear to promote air/sea temperature mixing resulting in the y-intercepts being closer to zero. It seems likely that the y-intercepts associated with the regression between ΔT and ΔT_{ab} are a function of wind speed.

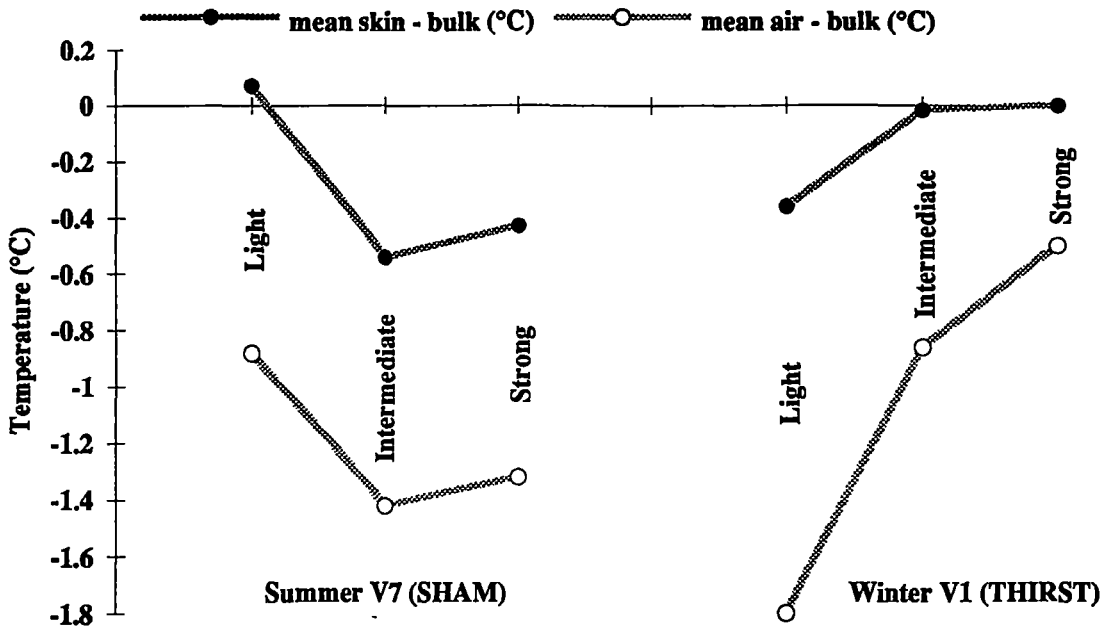

FIGURE 6.4 An averaged plot relating ΔT, ΔT_{ab} and wind speed.

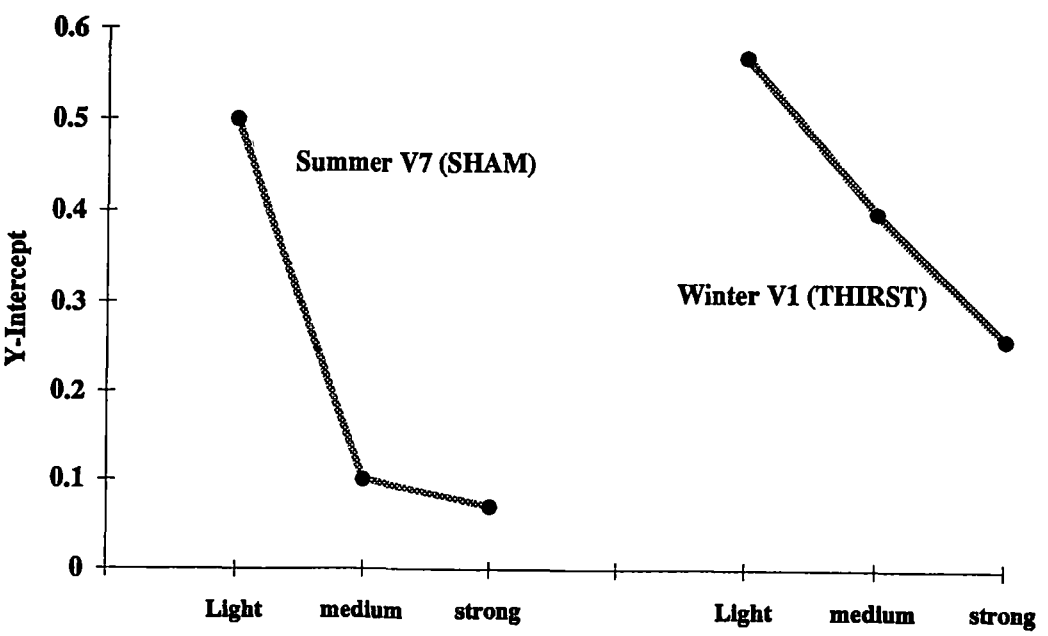

FIGURE 6.5 A graphical representation of the average y-intercepts associated with the regression between ΔT and ΔT_{ab} for light, intermediate and strong wind speeds.

TABLE 6.6

A summary of the relationship between wind speed and ΔT.

	SUMMER V7 (SHAM) JAN-FEB 1994			WINTER V1 (THIRST) AUG-OCT 1993		
	Light U<10 knots light air - gentle breeze	**Intermediate** 15<U<20 knots moderate - fresh breeze	**Strong** U>22 knots strong breeze - storm	**Light** U<10 knots light air - gentle breeze	**Intermediate** 15<U<20 knots moderate - fresh breeze	**Strong** U>30 knots moderate gale - storm
no. data points	819	819	1312	469	486	1214
% of total data	19.1	19.1	30.6	11.2	11.5	28.9
mean skin - bulk (°C)	0.07	-0.54	-0.43	-0.36	-0.02	0.00
standard deviation	0.84	0.78	0.74	0.69	0.92	0.83
mean air - bulk (°C)	-0.88	-1.42	-1.32	-1.80	-0.86	-0.50
% of cool skins	56.9	74.0	75.6	71.6	51.0	49.4
gradient coefficient	0.48	0.45	0.37	0.52	0.49	0.48
y-intercept	0.50	0.10	0.07	0.57	0.40	0.26
correlation coeff.	0.30	0.65	0.43	0.82	0.73	0.91
RMSD	0.71	0.46	0.56	0.29	0.48	0.25
mean wind direction	204.4	183.4	163.6	193.4	241.9	271.4

6.3.2 Method 2

In section 6.2.2, the data was split into day and night time classifications and further split into clear and cloudy sky conditions. The data was subdivided again into strong winds (>10 knots) and light winds (<10 knots) to determine the relationship between wind speed, ΔT, ΔT_{ab} and the air-skin temperature difference ΔT_{as}. Table 6.7 summarises the number of data points and percentages associated with the 8 classification groups:

strong winds on a cloudy day;
light winds on a cloudy day;
strong winds on a clear day;
light winds on a clear day;
strong winds on a cloudy night;
light winds on a cloudy night;
strong winds on a clear night and
light winds on a clear night.

It can be seen that wind speeds exceed 10 knots for 85% of the time whilst for 15% of the time, winds speeds are less than 10 knots. Extensive cloud cover occurs for 66% of the time and that strong winds under cloudy conditions are the most dominant and account for 57% of the total data set. Light winds on clear days account for only 5.4% of the summer voyage data and the overall effects of solar radiation are going to be minimal.

Table 6.8 summarises ΔT which includes the division between strong and light winds. The ΔT averages for the summer voyage (SHAM) are summarised as follows:

	strong winds	light winds
cloudy day	-0.18	+0.27
clear day	-0.03	+0.30
cloudy night	-0.42	-0.12
clear night	-0.99	-0.79

It appears from the above that in summer, the ΔT values are lower for strong winds as compared to the ΔT values associated with light winds, a fact already confirmed and discussed in section 6.3.1 (see Figure 6.4). This finding is also consistent with the results from Schluessel *et al.* (1990) as set out below. Schluessel *et al.* also applied a 10 knot wind speed cut off between light and strong winds.

	strong winds	light winds
cloudy day	-0.16	+0.07
clear day	-0.23	-0.17
cloudy night	-0.28	-0.22
clear night	-0.33	-0.18

Despite the fact that the Schluessel *et al.* (1990) data was collected in the north Atlantic Ocean at mid-latitudes, the above two sets of data are remarkably similar. It seems that the stronger winds enhance latent and sensible heat transfer from the ocean to the air above and in doing so, increases the difference between the skin and bulk SST.

The ΔT averages for the winter voyage (THIRST) present a different picture and are summarised as follows:

	strong winds	light winds
cloudy day	+0.32	-0.05
clear day	+0.34	+0.60
cloudy night	-0.10	-0.31
clear night	-0.36	-0.70

For cloudy days, cloudy nights and clear nights, ΔT values are larger for strong winds than for light winds. This fact is consistent with the findings discussed in section 6.3.1 (see Figure 6.4). It appears that the stronger winds in winter (>10 knots) tend to destroy or reduce the thickness of the conduction viscous layer which in turn means that the skin and bulk temperatures are forced closer together.

TABLE 6.7

A summary of the number of data points in each monthly data set and there relative percentages.

Month	Day				Night			
	Cloud		Clear		Cloud		Clear	
	strong	light	strong	light	strong	light	strong	light
JAN SR3	490	164	228	122	500	31	189	23
JAN B	295	129	131	89	128	107	51	57
FEB	679	23	191	17	464	52	95	0
Total	1464	316	550	228	1092	190	335	80
%	34.4	7.4	12.9	5.4	25.7	4.5	7.9	1.9
AUG	321	20	197	15	710	73	355	79
SEP	428	34	270	24	470	58	277	42
OCT	133	44	196	0	198	35	215	0
Total	882	98	663	39	1378	166	847	121
%	21.0	2.3	15.8	0.9	32.9	4.0	20.2	2.9
TOTAL	2346	414	1213	267	2470	356	1182	201
%	27.8	4.9	14.4	3.2	29.2	4.2	14.0	2.4

TABLE 6.8

A summary of ΔT as a function of wind speed.

Month	Day				Night			
	Cloud		Clear		Cloud		Clear	
	strong	light	strong	light	strong	light	strong	light
JAN SR3	-0.55	0.44	0.20	0.93	-0.98	-0.20	-0.93	-0.80
JAN B	-0.09	0.06	-0.28	-0.02	-0.10	-0.36	-1.03	-0.78
FEB	0.09	0.30	0.00	-0.01	-0.19	0.20	-1.00	no data
Mean (SHAM)	-0.18	0.27	-0.03	0.30	-0.42	-0.12	-0.99	-0.79
AUG	-0.08	-0.88	-0.55	0.61	-0.08	-0.66	-0.81	-1.10
SEP	0.62	0.50	0.79	0.59	0.28	0.10	-0.14	-0.30
OCT	0.43	0.23	0.79	no data	-0.51	-0.36	-0.14	no data
Mean (THIRST)	0.32	-0.05	0.34	0.60	-0.10	-0.31	-0.36	-0.70
TOTAL Mean	0.07	0.11	0.16	0.45	-0.26	-0.21	-0.68	-0.75

The summer and winter voyages combined can be summarised as follows:

	strong winds	light winds
cloudy day	+0.07	+0.11
clear day	+0.16	+0.45
cloudy night	-0.26	-0.21
clear night	-0.68	-0.75

It appears from the above, that there is little difference in ΔT between strong and light winds for cloudy days, cloudy nights and clear nights. This points to the existence of a seasonal and/or spatial variation in ΔT, as the two voyages represent different times of the year and different locations. It also seems that on clear days with light winds, the absorption of solar radiation in the upper few metres of the ocean may force the skin SST to be warmer than the bulk temperature. The average ΔT for light winds on clear days is greater than the average ΔT for strong winds on clear days. The main reason for this is again the affect of solar heating of the PVC pipes (see appendix F). In general, it does appear that the time of day and the amount of cloud cover remain the dominant influence on the sign and magnitude of ΔT.

Table 6.9 is a summary of the relationship between the air-skin temperature difference (ΔT_{as}) and the division between strong and light wind conditions. The ΔT_{as} values for the summer voyage are summarised as follows:

	strong winds	light winds
cloudy day	-0.90	-1.12
clear day	-1.32	-1.69
cloudy night	-0.53	-0.53
clear night	-0.62	-0.10

and the ΔT_{as} values for the winter voyage are summarised as follows:

	strong winds	light winds
cloudy day	-0.58	-1.61
clear day	-0.89	-1.14
cloudy night	-0.62	-1.29
clear night	-0.76	-1.50

It appears that there is a more significant relationship between wind speed and the air-skin temperature difference. Under most conditions, the stronger wind speeds bring the air temperature and the skin SST closer together. The ΔT_{as} values under strong winds are greater than the ΔT_{as} values associated with light winds. This finding seems to suggest that the strong winds either mix the upper ocean, thus reducing the amount of absorbed solar heat, or they actively cool the skin layer so that it is closer to the ambient air temperature.

The situation for night time during the summer voyage appears to be reversed. This suggests that the temperature difference between air and skin SST is increased (particularly on a clear night in summer) due to heat loss from the sea surface to the atmosphere. It may also be due to the fact that the air temperature will cool more rapidly than the skin SST at night time.

On combining the two voyages, the ΔT_{as} values are summarised as follows:

	strong winds	light winds
cloudy day	-0.74	-1.37
clear day	-1.11	-1.42
cloudy night	-0.58	-0.91
clear night	-0.69	-0.80

The above shows a clear trend as it can be seen that on average, stronger winds (>10 knots) reduce the magnitude of the air-skin temperature difference. Light winds have the opposite effect in that the temperature difference between the air temperature and the skin temperature is increased. This could be due to solar heating (during the day) of the ocean surface and of the PVC pipes thus increasing the skin SST much higher than that of the air temperature.

TABLE 6.9

A summary of ΔT_{sa} as a function of wind speed.

Month	Day				Night			
	Cloud		Clear		Cloud		Clear	
	strong	light	strong	light	strong	light	strong	light
JAN SR3	-1.20	-0.75	-1.15	-1.32	-0.60	0.31	-0.23	0.46
JAN B	-0.55	-1.11	-0.90	-1.27	-0.25	-0.72	-0.61	-0.66
FEB	-0.95	-1.50	-1.90	-2.47	-0.75	-1.17	-1.02	no data
Mean (SHAM)	-0.90	-1.12	-1.32	-1.69	-0.53	-0.53	-0.62	-0.10
AUG	-0.80	-2.06	-1.22	-0.86	-0.48	-1.65	-1.09	-1.95
SEP	-0.45	-1.29	-0.85	-1.41	-0.35	-0.76	-0.69	-1.05
OCT	-0.50	-1.47	-0.59	no data	-1.03	-1.47	-0.51	no data
Mean (THIRST)	-0.58	-1.61	-0.89	-1.14	-0.62	-1.29	-0.76	-1.50
TOTAL Mean	-0.74	-1.37	-1.11	-1.42	-0.58	-0.91	-0.69	-0.80

The opposite might occur at night as the air temperature will cool more rapidly than the skin SST under stronger wind conditions.

In general, the relationship between wind speed and ΔT is not a straight forward one but it is clear that air temperature, cloud cover and incoming solar radiation are the dominant influences on ΔT. It appears that wind speed has a greater effects on the magnitude of ΔT_{as}. The wind speed does not appear to effect the sign and magnitude of ΔT to the same extent.

6.4 NOAA-11 AVHRR Data

A comparison was made between the *in situ* measurements of skin and bulk SST and the SST derived from NOAA-11 AVHRR images. The period chosen was from the 2nd to the 14th of January, 1994 (SHAM) along the SR3 transect, as it appeared relatively clear of cloud. Printed black and white visible images were first examined at the CSIRO Marine Laboratories remote sensing facility in Hobart, in order to identify candidate cloud free images. In all, only 25 images were found to be cloud free corresponding to the location of the RSV *Aurora Australis* on the SHAM voyage.

Each digital image was displayed on an image processing work station and examined separately by first plotting the position of the vessel on the image. A value of SST corresponding to the ship's location was obtained as the mean of the temperatures around the location of the ship. The cursor was used to interrogate the grey level values near the ships location, in both AVHRR thermal infrared channels 4 (10.5-11.5 μm) and 5 (11.5-12.5 μm). Each pixel had a grey level ranging from 0 (-5 °C) to 255 (46.1 °C), and with a temperature resolution of 0.2 °C. The brightness temperatures in channel 4 and 5 were converted to an estimate of the SST via a standard split window algorithm.

6.4.1 Results and Discussion of NOAA

From each of the 25 images gathered, a sample of between 10 and 20 SST measurements (T_{NOAA}) were taken. The average standard error in T_{NOAA} is 0.84 °C which resulted from variable cloud cover as well as other atmospheric effects. It was noted in some of the images, that there was a warming affect along the edges of some of the clouds.

The corresponding Everest radiometer skin SST values (T_{skin}) and the ships bulk SST (T_{bulk}), were plotted against T_{NOAA}. Figure 6.6 illustrates the regression between T_{skin} and T_{NOAA} (dark circles) and the regression between T_{bulk} and T_{NOAA} (light circles). The RMSD for the regression between T_{skin} and T_{NOAA} is 1.13 °C which is slightly larger than the RMSD associated with the regression between T_{bulk} and T_{NOAA} of 0.95 °C. The reason for the large RMSD values is due mainly to the uncertainty in T_{NOAA} of 0.84 °C but is also due to atmospheric and cloud effects. The RMSD for the skin SST regression is larger than the bulk SST regression due to the greater sensitivity in the T_{skin} measurements.

The correlation coefficients for both regressions are reasonable given that there are only 25 data points in the plot. The R^2 for the T_{skin} against T_{NOAA} regression was 0.91, slightly less than the R^2 for the T_{bulk} and T_{NOAA} regression of 0.95.

Figure 6.6 indicates that for the temperature range 7 °C to 14 °C, that T_{skin} is less than T_{bulk} on average which is to be expected. The temperature range 0 °C to 5 °C shows a slightly more variable picture where T_{skin} is greater than T_{bulk} on average and would be due to absorbed solar radiation in the upper ocean during this time period. It should also be noted that at higher latitudes, it becomes difficult to distinguish between cloud, ice and water as all of these can have similar brightness temperatures.

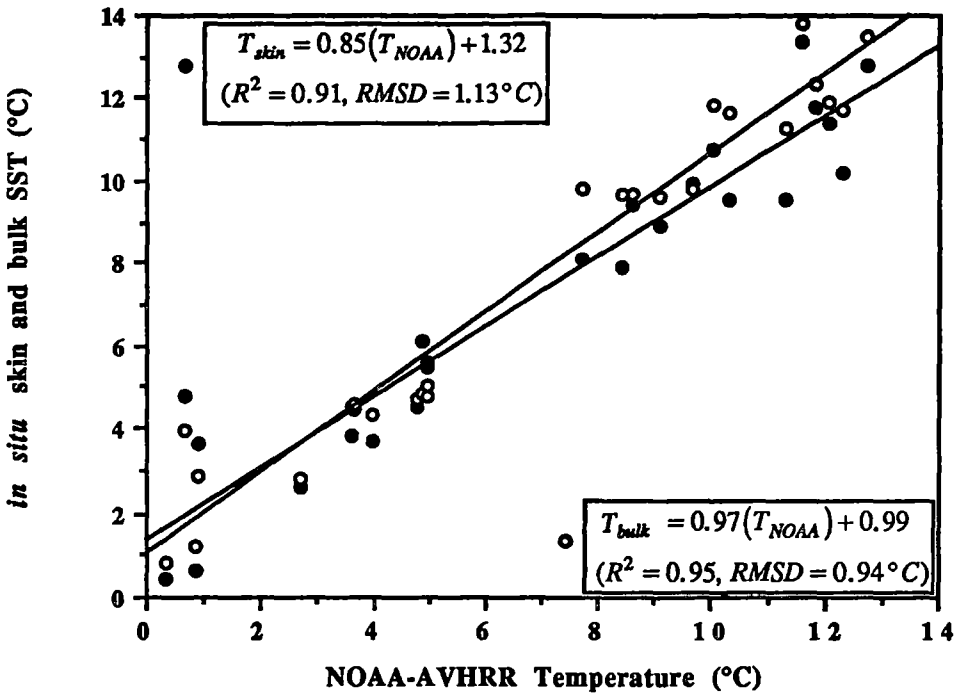

FIGURE 6.6 A scatter plot and regression of the *in situ* skin and bulk SST measurements taken from the *Aurora Australis,* and the NOAA-AVHRR MCSST measurements.

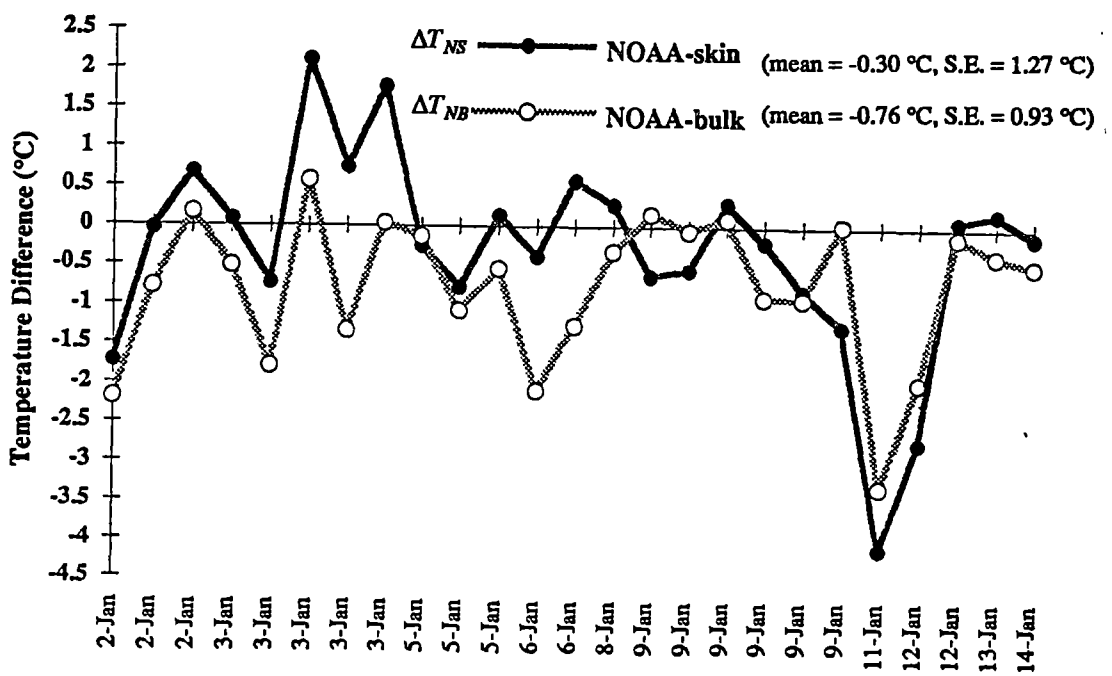

FIGURE 6.7 A time series plot of the temperature differences, ΔT_{NS} and ΔT_{NB}. The bias is 0.46 °C in favour of T_{skin}.

Figure 6.7 is an image sequence time series plot of the temperature difference between T_{NOAA} and T_{skin} (ΔT_{NS}) and the temperature difference between T_{NOAA} and T_{bulk} (ΔT_{NB}). The time series again shows the variability in the data where ΔT_{NS} ranges from +2.0 °C and -4.0 °C and where ΔT_{NB} has a smaller range between +0.5 °C and -3.5 °C.

The standard errors in ΔT_{NS} and ΔT_{NB} are 1.27 °C and 0.93 °C respectively. The largest differences occurred on the 3rd, 11th and 12th of January and maybe a result of cloud cover. The average values for ΔT_{NS} and ΔT_{NB} are -0.3 °C and -0.76 °C respectively. This suggests that T_{NOAA} is less than T_{skin} and T_{bulk} on average. It can also be seen from Figure 6.7, that T_{NOAA} is more likely to be greater than T_{skin} at night time.

It is interesting to note that ΔT_{NB} is larger in magnitude than ΔT_{NS} by an average of 0.46 °C which represents a significant bias error. This suggests that the *in situ* radiometric skin SST measurements are a more accurate source of ground truth for the NOAA-11 AVHRR. In general, the T_{skin} measurements are on average closer to T_{NOAA} but are more scattered.

Chapter 7

CHAPTER 7: General Discussion

7.1 A General Summary

The sign and magnitude of ΔT is influenced by the following primary influences

(a) The air temperature and the overall air-bulk temperature difference ΔT_{ab}.

(b) The diurnal cycle. During the day there is absorbed solar radiation whilst at night, there is heat loss from the ocean surface back to the atmosphere. The clear day time data may have been affected by solar heating of the PVC pipes used to house the radiometers

(c) The amount of cloud cover is also important. Cloud cover during the day lessens the amount of incoming solar radiation and cloud cover at night reduces radiative heat loss from the ocean surface to the atmosphere.

There are also secondary influences governing ΔT such as wind direction and wind speed. The wind direction is important as it tends to control the temperature of the air. A northerly wind brings warmer air from the north whilst a southerly wind will bring cooler air from the south. The wind speed did appear to influence the y-intercepts associated with the regression analysis of ΔT against ΔT_{ab}. This observation might suggest that the greater the wind speed, the smaller the magnitude of ΔT. This is consistent with a breakdown in the conduction layer caused by strong winds. It was found that wind speed has an effect on the air-skin temperature difference in that the magnitude of ΔT_{as} decreases with stronger wind speeds as a result of air-sea mixing. Light winds result in an increase in the magnitude of ΔT_{as} either through the agency of increased effect of insolation during the day or by rapid night time cooling of the air temperature.

7.2 Insolation and the Formation of a Diurnal Deck Layer

The average wavelength of solar radiation incident on the earth surface (ocean surface) is about 0.5 μm. At these wavelengths, incident radiation

penetrates into pure water to a maximum depth of about 50 metres (Maul 1985). As discussed in section 2.3 (chapter 2), 90% or so of the incident solar radiation is most likely to be absorbed in the top 2 or 3 metres of the water column and relates to the absorption coefficient. On a cloud free day with calm seas and low winds, this absorbed solar radiation may course a diurnal deck layer to form over the top few metres of the ocean surface (Hepplewhite 1989; Schluessel *et al.* 1990). Strong wind speeds on the other hand promote turbulent mixing in the upper few metres of the ocean preventing the formation of a deck layers. With the advent of night, a diurnal deck layer will dissipate as the lack of solar radiation means that the shallow warm layer can not be sustained. Figure 7.1 shows how a diurnal deck layer can result in an increase in skin SST to a point where the skin temperature is greater than both the air and the bulk temperatures. If a diurnal deck layer is allowed to form during the day, there is a corresponding artificial increase in skin SST. At night time or when there is cloud cover during the day, a more normal air-bulk temperature profile exits in which the skin temperature lies between the air and the bulk temperatures.

The regression analysis results for ΔT against ΔT_{ab} reveal that poor correlations exist for the clear day data, particularly for the summer voyage (SHAM) (see for example, Appendix C6). The main reason for this poor correlation is that ΔT may take positive values due to a diurnal deck layer or solar heating of the surface, whilst ΔT_{ab} may still have negative values (see Figure 7.1). This apparent anomaly however, could also be explained by solar heating of the PVC pipes which would result in a skin temperature measurement being greater than air and bulk temperature. At night time where the temperature profile across the air/sea interface is better behaved, the correlations for the night time data set are very good. It would be advisable to model the diurnal deck layer formation on clear sunny days, as it is important to relate the surface skin SST to the maximum bulk temperature that exists somewhere in the top few metres of the ocean.

7.2.1 CTD Temperature Profiles

A short investigation was conducted to confirm the existence of diurnal deck layer formation in the upper few metres of the water column. During voyage 7 (SHAM), a series of CTD casts were deployed from the *Aurora Australis* between the 2nd and the 15th of January (1994) along the WOCE-SR3 transect. Five CTD casts were selected at random and the change in temperature with depth was plotted (see Figure 7.1a). The depth scale (y-axis) is in deci Bars (dB), approximately equal to metres. The temperature difference along the x-axis, is the change in temperature with depth such that the minimum temperature in the 23 metre profile is set to 0 °C.

The five CTD casts selected, occurred at different times of the day under different wind speed conditions. CTD cast number 21 (CTD-21) was taken at 8 am (local time) in the morning. The sky was overcast and the wind speed was 21.5 knots. Under these conditions, the temperature profile is likely to be homogeneous which is confirmed in Figure 7.1a (light circles).

CTD cast number 39 (CTD-39) was taken at 11:40 am (local time), around midday. The sky temperature was -30 °C indicating very clear sky conditions, and the wind speed was 9 knots. Figure 7.1a (dark circles) shows that there is a 0.65 °C temperature gradient over the top 15 metres. The maximum temperature occurs at about 4 metres depth. CTD cast number 49 (CTD-49) was taken at 5:30 pm (local time) in the afternoon under relatively clear skies where the wind speed was 6.5 knots. There is a temperature gradient of 0.4 °C over the top 20 metres with a maximum temperature occurring at about 7 metres depth.

CTD casts 39 and 49 (Figure 7.1a) have temperature profiles that are consistent with the idea of the formation of a diurnal deck layer and diurnal thermocline, during clear day time conditions under light winds less than 10 knots.

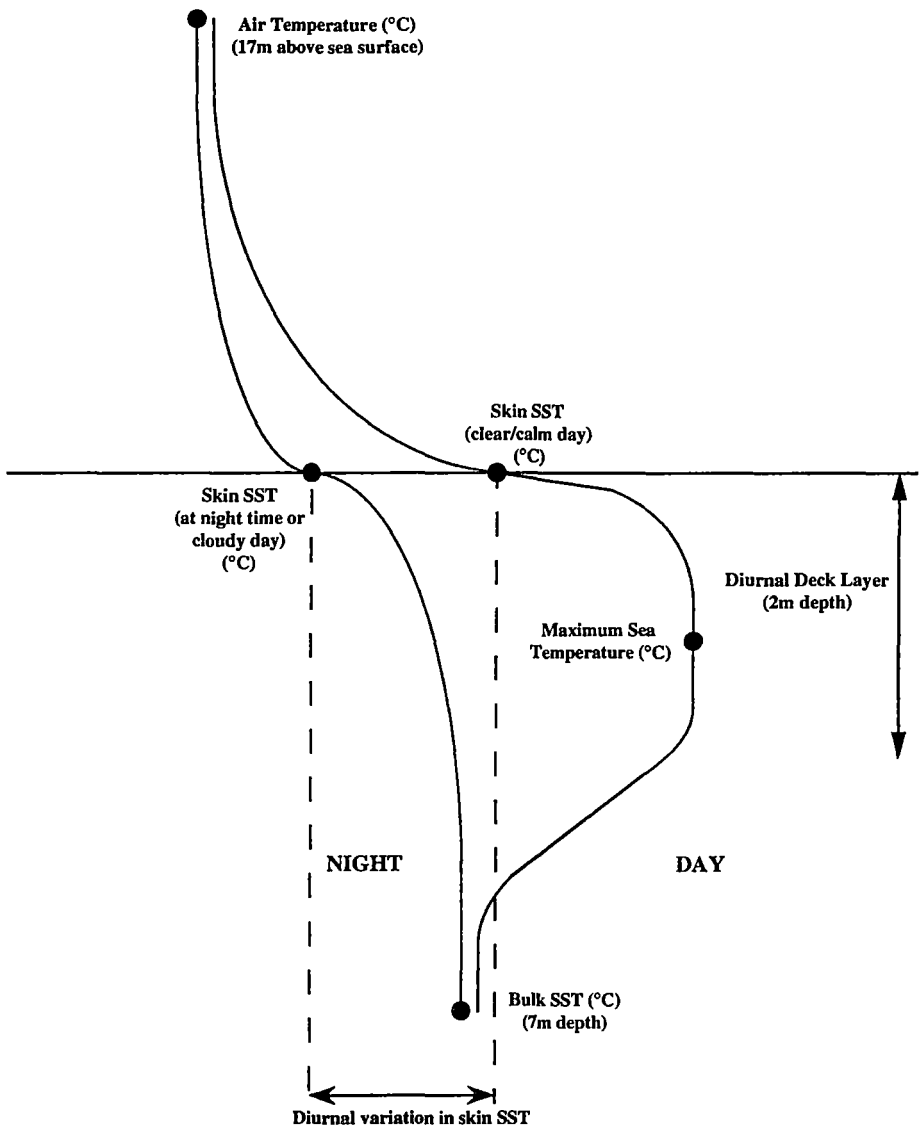

FIGURE 7.1 An illustration of the difference between day time and night time air-sea temperature profiles. A diurnal deck layer is more likely to form on clear calm days.

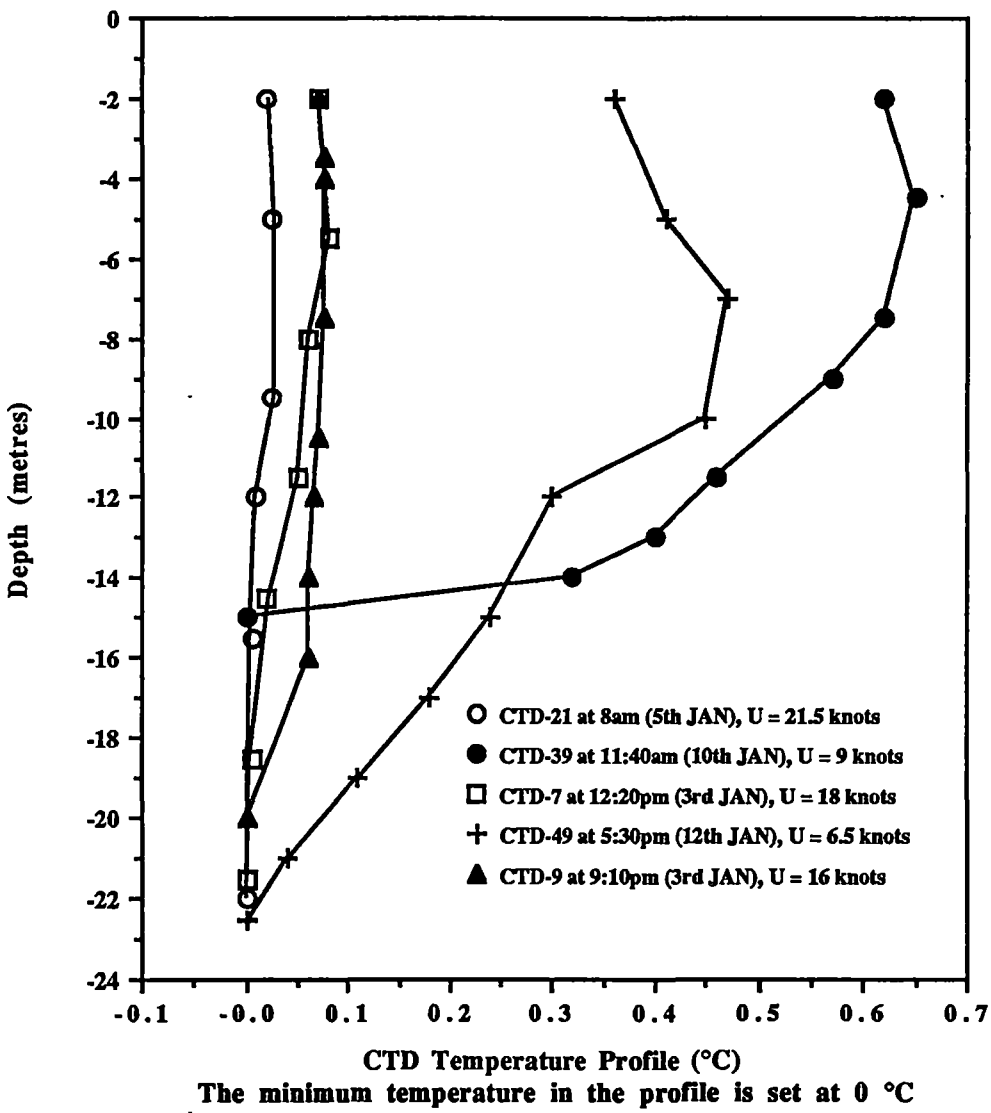

FIGURE 7.1a CTD temperature profiles. A diurnal deck layer and diurnal thermocline are evident in CTD-39 and CTD-49.

CTD cast number 7 (CTD-7) was taken at 12:20 pm (midday) under patchy cloud cover with wind speeds of about 18 knots. In this case, there is a very small temperature change in the top 15 metres of 0.05 °C. The cloud cover and higher winds in this case, are sufficient to stop the formation of a diurnal deck layer through wind driven turbulent mixing.

7.3 An Algorithm for the Estimation of ΔT

The following algorithm allows for the estimation of ΔT and the skin SST given a value of air temperature, bulk sea temperature; the rough amount of cloud cover and the time of day (i.e. day or night). It should be noted that the following algorithm is based on data collected on board the *Aurora Australis* only and does not include the effect of wind speed. The day time algorithms should be treated with some caution as the this data may be subject to error as a result of the 5% signal contribution from the PVC pipes.

The regression analysis of ΔT against ΔT_{ab} for the winter voyage (August to October) provides the following 4 relationships:

(a) cloudy days in winter

$$\Delta T = 0.43\,(\Delta T_{ab}) + 0.49 \qquad \text{(RMSD = 0.32)}$$

(b) clear days in winter

$$\Delta T = 0.53\,(\Delta T_{ab}) + 0.65 \qquad \text{(RMSD = 0.47)}$$

(c) cloudy nights in winter

$$\Delta T = 0.40\,(\Delta T_{ab}) + 0.21 \qquad \text{(RMSD = 0.24)}$$

(d) clear nights in winter

$$\Delta T = 0.38\,(\Delta T_{ab}) + 0.09 \qquad \text{(RMSD = 0.25)}$$

The average y-intercept for winter is 0.36 and suggests that there might be a bias error which maybe linked to the additional solar warming of the PVC pipes.

The regression analysis for the summer voyage (January to February) provides the following relationships:

(a) cloudy days in summer

$$\Delta T = 0.40\,(\Delta T_{ab}) + 0.36 \qquad \text{(RMSD = 0.47)}$$

(b) clear days in summer

$$\Delta T = 0.23\,(\Delta T_{ab}) + 0.39 \qquad \text{(RMSD = 0.78)}$$

(c) cloudy nights in summer

$$\Delta T = 0.36\,(\Delta T_{ab}) - 0.05 \qquad \text{(RMSD = 0.26)}$$

(d) clear nights in summer

$$\Delta T = 0.41\,(\Delta T_{ab}) - 0.26 \qquad \text{(RMSD = 0.28)}$$

The average y-intercept for summer is 0.11 and again indicates a small bias error.

The 2 above mentioned bias errors are influenced by other factors such as a bias error in air temperature measurements or could be due to elevated skin SST values associated with absorbed solar radiation at the sea surface or by the PVC pipes.

If a correction is made for the bias error and if the two voyage data sets are combined, then the algorithm reduces to:

(a) cloudy days

$$\Delta T = 0.42\,(\Delta T_{ab}) + 0.07 \qquad \text{(RMSD = 0.5)}$$

(b) clear days

$$\Delta T = 0.38\,(\Delta T_{ab}) + 0.16 \qquad \text{(RMSD = 0.7)}$$

(c) cloudy nights

$$\Delta T = 0.38\,(\Delta T_{ab}) - 0.03 \qquad \text{(RMSD = 0.25)}$$

(d) clear nights

$$\Delta T = 0.40\,(\Delta T_{ab}) - 0.20 \qquad \text{(RMSD = 0.25)}$$

The total average formula would take the form:

$$\Delta T = 0.40\,(\Delta T_{ab}) \qquad \text{(RMSD = 0.7)}$$

implying that the ΔT value can be estimated as 40% of the overall air-bulk temperature difference on average.

The RMSD for the clear day data (particularly in summer), has the highest value at 0.7. If precise determinations of ΔT and skin SST are required, then the night time formulas should be used as the RMSD values are 0.25 which lie within

the standards set out by the WCRP (1986). One problem with this is that it is difficult to distinguish between cloud, sea and ice in AVHRR imagery at night.

The above algorithm can be expressed in terms of T_{skin}, T_{bulk} and T_{air} such that T_{skin} can be calculated from the following equation:

$$T_{skin} = a(T_{air} - T_{bulk}) + b + T_{bulk} \tag{7.1}$$

Equation 7.1 can be used in the validation of satellite MCSST data. Ultimately, T_{bulk} can be estimated from satellite imagery, given a value of T_{air} and T_{skin} such that

$$T_{bulk} = \frac{aT_{air} - T_{skin} + b}{a - 1} \tag{7.2}$$

It should be noted that the above algorithms do not contain a wind speed dependence. In chapter 6, it was suggested that there might be a relationship between wind speed and the y-intercept such that the average y-intercept had values of around 0.5 for light winds and values of about 0.1 for stronger winds. However, an algorithm that is not a function of wind speed is useful given that a RMSD of 0.25 °C is obtainable for ΔT at night.

Another point to consider is that the y-intercepts are going to be near zero or slightly negative in value at night due to heat loss to the atmosphere. The y-intercepts for the day time data are more likely to be positive in sign due to elevated skin SST values that result from absorbed solar radiation.

The main problem in deriving a day time algorithm for the prediction of ΔT and skin SST is the influence of absorbed solar radiation in the top few metres of the ocean. If the temperature difference between T_{skin} and $T_{\max}$ (see Figure 7.1) could be modelled under clear calm day time conditions, then the RMSD might improve thus allowing for the better use of day time satellite imagery.

7.4 A Comparison with the Hepplewhite (1989) Data

Figure 7.2 is a scatter plot of the data collected by Hepplewhite (1989) along a transect from the tropical Atlantic Ocean to the Southern Ocean off the Antarctic continent during a British Antarctic Survey (ROSSA) project. This graph is a plot of the bulk-skin temperature difference ($-\Delta T$ according to our notation) against bulk temperature. The bulk sea temperature in Hepplewhite's case was measured using a rubber bucket and thermometer. The cross symbols in Figure 7.2 represent night time values and the circle symbols represent day time values. Hepplewhite observed that in the tropical to temperate regions (30 °C to 14 °C), that there was a clear distinction between night time and day time ΔT values where warm skin effects (skin warmer than bulk) occurred at night in the tropics. In the mid to high latitudes (14 °C to -2 °C), it appeared that there was little distinction between day and night time ΔT values.

Figure 7.3 is a scatter plot of the bulk - skin temperature difference against bulk SST for the data collected along the WOCE-SR3 transect during voyage 7 between the 1st and the 15th of January. This graph only covers a sea temperature range of 14 °C to -2 °C. It can be seen from Figure 7.3 that from mid latitude waters (14 °C) down to about the Sub-Antarctic and Polar Frontal region (5 °C), that there is little distinction between day time and night time values. The ΔT values south of the polar front (5 °C to -2 °C) appear to vary greatly between day and night time. Very warm skin effects (skin warmer than bulk) occur at high latitude during the day time and can only be due to absorbed solar radiation. The warmer skin SST measurements may be subject to an error resulting from day time heating of the radiation shields and radiometers, the maximum error being about 1 °C. There is clear evidence of very strong diurnal cycles occurring at high latitudes between 53° S to 65° S where at times the difference in ΔT from night to day time can be as much as 3 °C.

The average diurnal cycle for the entire data set collected on the *Aurora Australis* is 0.65 °C which is similar to the maximum amplitude in the deviation of

skin SST from the daily mean as quoted by Hepplewhite (1989). The large diurnal cycles observed by Hepplewhite and the author are related to absorbed solar radiation during the day time. In the case of this study, solar heating of the PVC pipes is also a contributing factor.

Figure 7.3 also shows that cool skins (skin less than bulk) occur more at night. There were virtually no warm skins at night along the SR3 transect, due to rapid heat loss from the ocean to the cold dry air mass.

Hepplewhite's mean ΔT value is -0.3 °C and ranged between 0.3 and -1.2 °C. The mean ΔT value along the SR3 transect was +0.45 °C for clear days and -0.92 °C for clear nights with a total range of +2.5 °C to -3.0 °C. The maximum diurnal cycle observed along the SR3 transect in January is of the order of 1.4 °C which has been affected by day time solar heating of the PVC pipes, although there are still good indications that a strong diurnal cycle exists in the Southern Ocean.

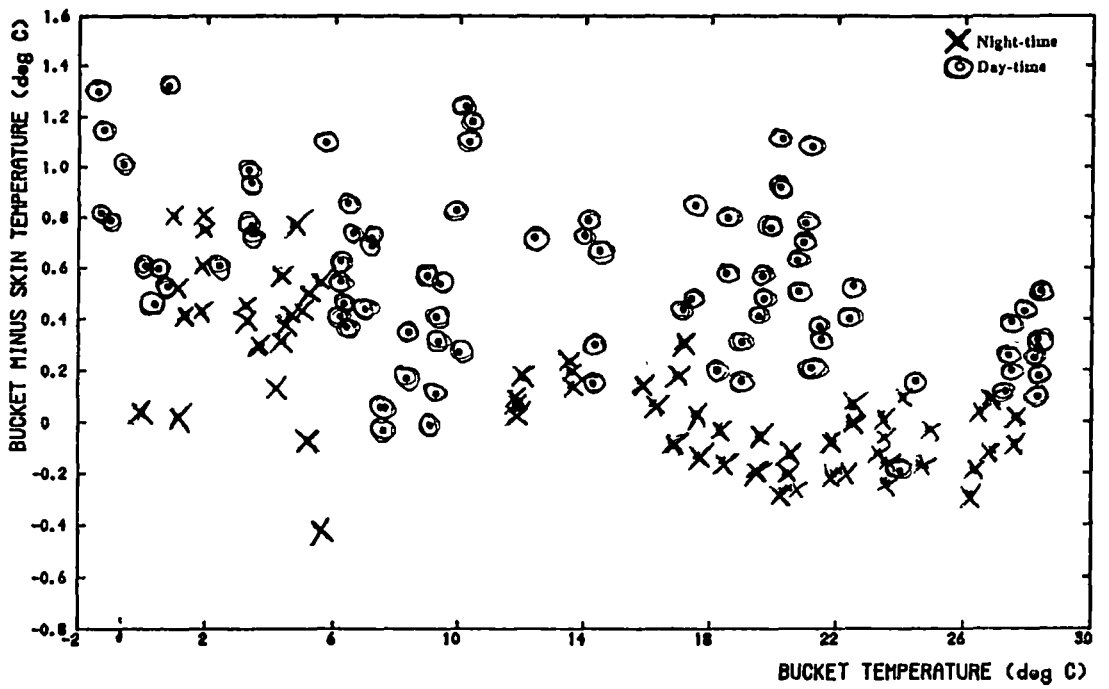

FIGURE 7.2 A scatter plot of the Hepplewhite (1989) data. The bulk-skin temperature differences are plotted against the bulk SST (from Hepplewhite 1989).

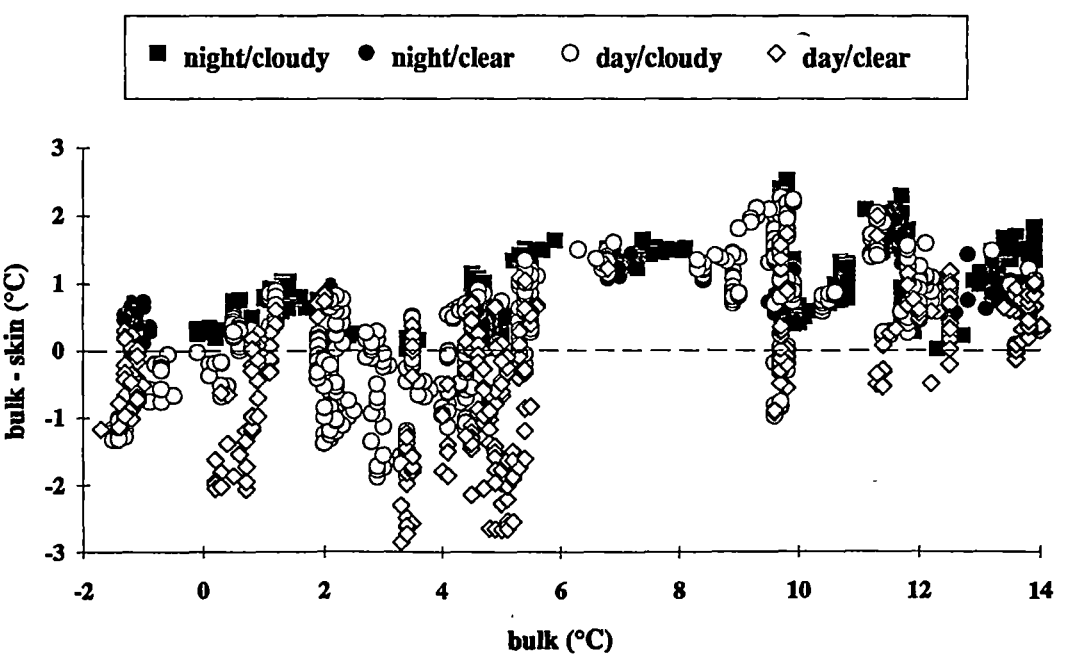

FIGURE 7.3 A scatter plot of the data collected along the WOCE-SR3 transect in January, 1994. The bulk-skin temperature differences are plotted against the bulk SST for a direct comparison with the Hepplewhite (1989) data.

7.5 A General Comparison with other Data

Now consider examples of formulas proposed by 3 authors to estimate the value of ΔT. They are the Saunders (1967b) theoretical model:

$$\Delta T = \frac{\lambda Q_N \upsilon}{\kappa U_*}$$

The mathematical expression derived by Hasse (1971):

$$\Delta T = C_1 \frac{Q_H}{U} + C_2 \frac{Q_I}{U}$$

and the model derived by Schluessel *et al.* (1990):

$$\Delta T = a_0 + a_1 \left(Q_I / U \right) + a_2 \left(q_s - q_a \right) + a_3 Q_{IR}$$

These 3 formulae relate ΔT to the total heat flux Q_N and to wind speed U. The value of Q_N is determined by the sum of incoming solar radiation Q_I; the longwave radiation emitted by the sea or water surface Q_{IR}; the downwelling longwave radiation from the sky, clouds and atmosphere Q_G; the sensible heat flux Q_H and the latent heat flux Q_L. The solar radiation (Q_I) is going to be affected by the day/night cycle. The net longwave radiation (Q_{IR} + Q_G) will be affected by the amount of cloud cover. The sensible and latent heat fluxes (Q_H + Q_L) will be affected by the air-sea temperature difference.

The basis for the analysis contained in this thesis was to first subdivide the data broadly between day time (incoming solar radiation) and night time (no solar radiation). This was done to assess the major differences in solar radiation effects that influence the relationship between ΔT and ΔT_{ab}.

The data was further subdivided between clear sky conditions and cloudy sky conditions. This was done to account in a basic manner for the effects of cloud on the longwave and shortwave radiation budgets. A similar type of data subdivision was also performed by Schluessel *et al.* (1990) whose results were not dis-similar to those results found in this study (refer section 6.3.2).

In general, if we can eliminate solar and longwave radiation effects, then we can show that ΔT is proportional to ΔT_{ab} which in theory, should follow from the Saunders model. In reality, we can not do this, but by adopting a broad subdivision of the data, we can still detect relationships between ΔT and ΔT_{ab}.

It should be noted further that the broad subdivision of the data may have the effect of masking any wind speed influences on ΔT. A further subdivision of the data between strong winds (>10 knots) and light winds (<10 knots) did reveal some interesting relationships between ΔT and wind speed, but no definite relationships could be determined. A complete assessment of the relationship between ΔT and wind speed can only be done using a fine resolution time series analysis.

There have been few researchers who have examined the direct relationship between the skin-bulk temperature difference (ΔT) and the air-bulk temperature difference. There are only two graphs which are vaguely comparable to this study and are compiled by Hasse 1963 (Figure 7.4) and Katsaros 1977 (Figure 7.5). In both of these figures, an area is drawn which corresponds to the relative position of the data as found by this study with an average line of correlation of $\Delta T = 0.4(\Delta T_{ab})$. It can be seen that there are some dis-similarities between this study and previous studies. However, there are some data points that are similar for example, Hasse 1963 (Figure 7.4) and Hill in Katsaros 1977 (Figure 7.5).

The humidity profile data (Hasse 1963) illustrated as dark squares in Figure 7.4, run parallel to the results found in this thesis. The method reported by Hasse (1963) involved the measurement of temperature profiles from a floating buoy in the Baltic Sea. Dry and wet bulb temperatures were measured with platinum resistance thermometers at 4 to 5 different heights between 0.8 and 13.6 m above the sea level. The sea temperature was also measured using a platinum thermometer at 0.5 m depth.

Under conditions where the potential temperature was uniform in the first 10 metres of the atmospheric boundary, the temperature at the sea surface was extrapolated from measurements above and was assumed to be equal to the sea surface skin temperature.

In Figure 7.4, T_0 denotes the sea surface skin temperature. T_W denotes the bulk sea temperature and T_A is the air temperature. The method reported by Hasse (1963) is compatible to the methods adopted in this investigation where the results of both methods follow a similar gradient (see Figure 7.4).

The temperature gradients for the values of ΔT and ΔT_{ab} by this study are relatively small (see Appendix C). It maybe the case that if the ΔT_{ab} values in this study were to take values as low as -20 °C, then we may see different results.

The results shown in Figure 7.4 do seem to indicate that there is a bi-linear or non-linear relationship between ΔT and ΔT_{ab}. This apparent bi-linear relationship should be investigated further over a large range of ΔT and ΔT_{ab} temperature values.

The implication of the Woodcock & Stommel 1947 data (seen in Figure 7.4) is that there was a 'lower limit' in ΔT of about -1.0 °C. This finding has since been disproved by Katsaros 1977 (see Figure 7.5) where ΔT values of between -2 and -3 °C were found to occur for air-water temperature differences of between -20 to -30 °C which represents a gradient of about 1 in 10 (or 0.1). The average gradient for the correlation between ΔT and ΔT_{ab} by this study is about 0.4 which is significantly different to that gradient seen in Figure 7.5.

In general, further investigation would need to take place in order to get a better understanding of the possible bi-linear relationship between ΔT and ΔT_{ab}.

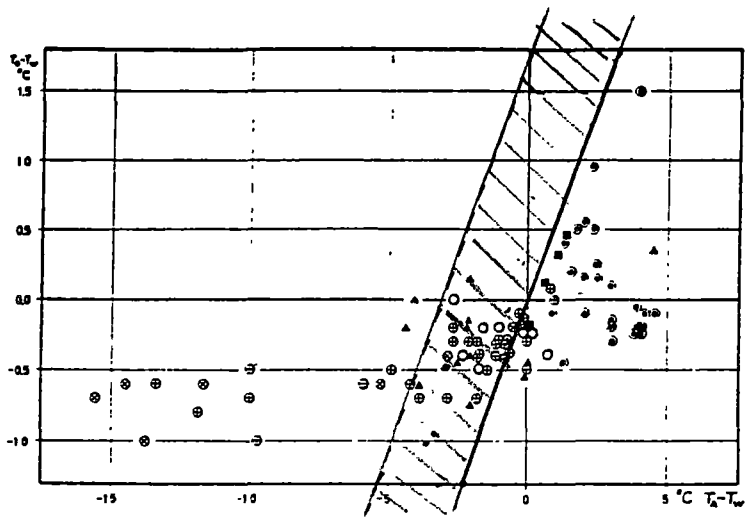

Difference between surface and subsurface temperature versus temperature difference air–sea from different authors: ⊕, Woodcock; ⊗, Woodcock and Stommel; ⊙, Bruch; ○, Roll; ▲, Ball, ■, from humidity profiles.

FIGURE 7.4

Scatter plot of ΔT $(T_0 - T_W)$ against ΔT_{ab} $(T_A - T_W)$ (from Hasse 1963).

The shaded area corresponds to the data collected in this study.

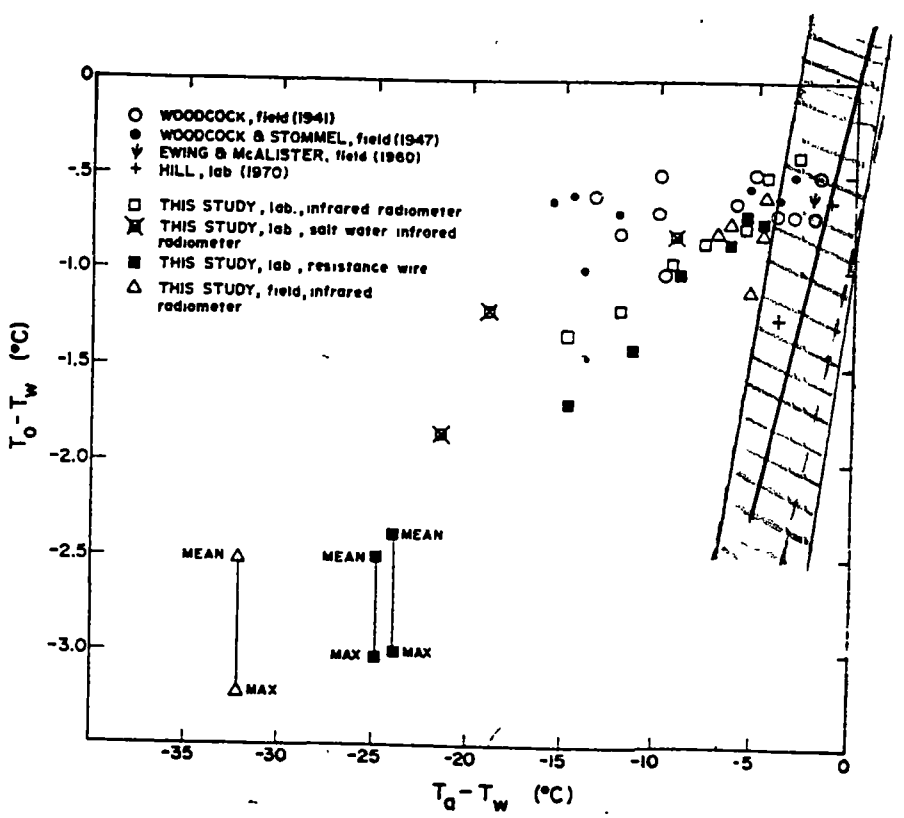

FIGURE 7.5

Scatter plot of ΔT $(T_0 - T_W)$ against ΔT_{ab} $(T_A - T_W)$ (from Katsaros 1977).

The shaded area corresponds to the data collected in this study.

Chapter 8

CHAPTER 8: Conclusions and Recommendations

8.1 The Objectives

Radiometric measurements of skin SST have been taken in the Southern Ocean region on board the RSV *Aurora Australis*. These radiometric measurements have been directly compared to bulk SST measurements taken at 7.5 metre depth below the sea surface, 1 metre inside the front bow of the vessel. The difference between skin SST and bulk SST (ΔT) have thus been obtained with the following 3 objectives in mind.

(a) To obtain radiometric ground truth data for satellite based radiometers such as the NOAA-AVHRR and the ERS-ATSR.

(b) To determine those factors that influence the sign and magnitude of ΔT.

(c) To provide a simple algorithm of ΔT so that values of skin SST and bulk SST can be obtained given values of air temperature, time of day and the amount of cloud cover.

8.2 A General Summary

The Calibration of the Everest 4000A Radiometers

The two radiometers used on the *Aurora Australis* on voyage 1 (THIRST) and voyage 7 (SHAM) were calibrated before and after each voyage. It was found that both of the Everest 4000A radiometers have an operating precision of ±0.1 °C under controlled ambient conditions. The radiometers were found to have an operating precision of ±0.5 °C when exposed to rapidly changing temperature gradients of 20 °C over 45 minutes.

The two radiometers were found to have drifted by an average of 0.6 °C during voyage 7, highlighting the need for regular on board, calibrations of the Everest radiometers.

The Error Analysis

Following a propagation of errors analysis on equation 5.1 (See Chapter 5), it was found that the predicted standard errors in the determination of skin SST (assuming non-blackness of sea water) increased for larger temperature differences between the sky temperature and the sea surface temperature. If the sky-sea temperature difference is 0 °C (under cloud cover), then the expected standard error in skin SST is 0.1 °C for an emissivity of 0.98. If the sky-sea temperature difference is 35 °C (typical of cloud free conditions), then this will result in a standard error of 0.4 °C. If the angle of incidence of the radiometer changes by 15°, then the resulting change in the skin SST measurement is 0.14 °C.

The other main sensitivity associated with the radiometry is related to the temperature difference between the sea surface and the internal temperature of the radiometer. It has been found that a 10 °C temperature difference between the radiometer and the surface could result in a 1 °C error in the measured skin SST (Rapier 1992). This error is most likely to occur as a result of day time solar heating of the PVC pipe radiation shields.

It has since been discovered that there is also a 5.4 % signal contribution from the PVC pipe itself. A simple correction function was applied to the ΔT data set (see Appendix F). It was assumed in this correction that the pipes were at air temperature, which does not fully take into account any potential day time heating of the pipes.

A Summary of ΔT

The data was first separated into 4 categories: cloudy days; clear days; cloudy nights and clear nights. These 4 categories were further subdivided into strong and light wind categories. The resulting ΔT averages over the two voyages THIRST and SHAM are summarised in Table 8.1.

Positive ΔT values (skin greater then bulk) tended to occur during the day time as a result of absorbed solar radiation at the sea surface and by the PVC pipes. Negative ΔT values (skin less than bulk) occurred at night time as a result of heat loss back to the atmosphere. Cloud cover during the day reduced incoming solar radiation resulting in ΔT being 0.1 °C lower on average as compared to clear days. Cloud cover at night reduced the heat loss back to the atmosphere resulting in the ΔT values being 0.4 °C greater on average as compared to clear nights. From Table 8.1, there appears to be little difference in the ΔT values associated with strong and light wind speeds.

The average amplitude in the diurnal cycle from day to night is 0.64 °C and is in agreement with a similar finding by Hepplewhite (1989). The larger amplitudes in the diurnal cycle occurred under cloud free skies averaging 0.89 °C and at times, reaching a maximum diurnal cycle of 3 °C (see Figure 7.3). The average amplitude in the diurnal cycle under cloudy conditions is 0.38 °C. The magnitude and sign of ΔT is primarily affected by incoming solar radiation and cloud cover.

TABLE 8.1 The average ΔT values for THIRST and SHAM combined (all values are in °C).

Time of Day	Day / Night	Wind Speed	
		Strong (>10 knots)	Light (<10 knots)
cloudy days	+0.10	+0.07	+0.11
clear days	+0.23	+0.16	+0.45
Day Mean	**+0.17**		
cloudy nights	-0.28	-0.26	-0.21
clear nights	-0.66	-0.68	-0.75
Night Mean	**-0.47**		

The Regression Analysis

The best correlations between ΔT and ΔT_{ab} occur at night where correlation coefficients average 0.77. The average R^2 value for cloudy days is 0.64. The worst correlation during clear days with an average R^2 of 0.41. The relatively poor correlation between ΔT and ΔT_{ab} during clear days is a result of incoming solar radiation warming the PVC pipes and the sea surface which in turn results in skin SST values being greater than both air and bulk temperatures.

These results are also reflected in the y-intercept values derived from the regression analysis of ΔT against ΔT_{ab}. The average y-intercept for day time data is 0.48 °C whilst the average y-intercept at night is -0.01 °C. A positive y-intercept for a ΔT and ΔT_{ab} regression implies elevated skin SST values.

The RMSD values are summarised as follows:

Cloudy day	0.40 (°C)
Clear day	0.63 (°C)
Cloudy night	0.25 (°C)
Clear night	0.27 (°C)

The larger RMSD values occur during clear days again indicating the effects of solar heating. The RMSD for the night time data set (irrespective of cloud cover) is 0.26 °C. This value allows for ΔT to be estimated within ±0.26 °C, provided that values of air and bulk temperature are known and calibrated. This precision lies within the standards set by the WCRP (1986). This result means that *in situ* radiometry need not be used all the time to provide ground truth to satellite radiometric SST.

Wind Speed, Wind Direction and ΔT

The wind direction was a significant factor. Northerly winds brought warmer air temperatures which resulted in positive ΔT values (skin higher than bulk). Southerly winds on the other hand brought cooler air resulting in negative ΔT values (skin less than bulk).

It was found that ΔT_{ab} was the main influence on the magnitude and sign of ΔT, largely independent of wind speed. The regression analysis of ΔT against ΔT_{ab} for light, intermediate and strong winds revealed a possible relationship between the y-intercept and wind speed. It was found that light winds (0-10 knots) result in positive y-intercepts of about 0.5 °C, implying that solar heating of the pipes is more likely to occur under light wind conditions, leading to positive ΔT values. It was also observed that under strong wind conditions (22-30 knots), the y-intercepts were much lower on average at about 0.1 °C. It would appear that stronger wind speeds act to suppress any solar heating affects wether it be at the sea surface or of the PVC pipes themselves. stronger winds will also act to destroys the conductive viscous layer through turbulent mixing.

The relationship between wind speed and ΔT_{as} also appears significant, in that the stronger wind speeds (>10 knots) forces the air temperature and the skin SST closer together through turbulent mixing whilst light winds (<10 knots) encourage solar heating of the skin layer and the PVC pipes during the day.

AVHRR-11 Comparisons

The mean difference (along the SR3 transect) between T_{NOAA} and T_{skin} was -0.3 °C which is less than the mean difference between T_{NOAA} and T_{bulk} of -0.76 °C. This bias is 0.46 °C in favour of the skin SST measurements and therefore, provide the more accurate ground truth, but with a greater standard error.

8.3 Recommendations for Future Work

There are plans for further work to be conducted on future voyages of the *Aurora Australis*. The following list of recommendations is by no means exhaustive, but should be considered if future work of this type is to be repeated.

(1) There is a need to include measurements and empirical calculations of the various fluxes including solar radiation, latent heat, sensible heat and wind stress if ΔT is to be modelled in full. Some of these measurements may be difficult in heavy seas but should be measured under calm conditions, particularly on clear sunny days when diurnal deck layers are most likely to occur.

(2) The Everest 4000A series of radiometers operate best when the internal temperature of the radiometer is within 5 °C of the sea temperature. The radiometers should therefore be well ventilated so as to avoid over heating during the day.

(3) It has been discovered through calibration that the Everest radiometers used in this investigation are prone to a drifting bias error. It is advised that on-ship calibrations of the radiometers be performed to keep a track of any instability in the instrument. This can be done by simply pointing the two radiometers periodically towards the sea so as to monitor any change in the offset between the two instruments. It would be preferable to use a self calibrating radiometer that contains 2 internal blackbody reference cavities such as the radiometer used by Hepplewhite (1989) and the RAL radiometer described in Coppin *et al.* (1991). The draw back of using a more sophisticated radiometer is that it is more expensive and moves away from the original intention of using a simple and economical radiometer. However, the improvement in precision would be worthwhile.

(4) It is recommended (given calm weather conditions e.g. Derwent River) that air/sea temperature profiles be measured across the air/sea interface. This could be done by using a thermocouple or thermistor probe, that is lowered gradually

through the air/sea interface. At the same time, 2 radiometers would measure values of T_{sky} and T_{rad}. This experiment could be conducted under varying amounts of cloud cover and at different times of the day. This experiment would confirm the shape of the air/water temperature profile under varying conditions which could then be mathematically modelled.

The above experiment would also be useful in providing an estimate of the value of emissivity of sea water under different circumstances. Equation 5.1 (Chapter 5) re-expressed in terms of emissivity gives

$$\varepsilon = \frac{T_{rad}^4 - T_{sky}^4}{T_{skin}^4 - T_{sky}^4} \tag{8.1}$$

where T_{rad} is the radiometric measurement of skin sea temperature. T_{sky} is the radiometric measurement of sky temperature and T_{skin} is the thermistor probe measurement taken at the surface or a temperature extrapolated to zero. Equation 8.1 should be subjected to a propagation of error analysis and the radiometers should be calibrated on a regular basis.

The benefit of doing this type of experiment is that it provides more accurate information about the air-sea viscous layer as well as investigating the formation of diurnal deck layers on clear calm days.

(5) Another source of information that may be useful in the interpretation and modelling of ΔT is information that can be gathered from synoptic weather charts from the Bureau of Meteorology. It might be useful to compare a synoptic weather chart to a chart of the anomalies in the ΔT values. Other sources of data that might prove useful are drifting buoy and ship data other than the *Aurora Australis.*

(6) A more detailed cloud classification scheme could be adopted where ΔT can be related to a number of different cloud types and cloud heights. The work done in this thesis has only considered a simple case of the sky either being cloudy or not cloudy.

(7) The next step in the analysis process would be to use the *in situ* skin SST data as the basis for an atmospheric correction algorithm for the Southern Ocean region.

(8) The PVC pipes themselves should be shortened to get rid of the 5.4% signal contribution that comes from the end 220 mm of the pipes (refer to appendix F for a clarification of the error source).

8.4 A Final Statement

The sign and magnitude of the skin-bulk temperature difference ΔT vary over a wide range of values from -3 °C to +3 °C. The average ΔT for the 2 voyages combined is -0.15 °C indicating that on average, the skin temperature is slightly cooler than the bulk temperature. The sign and magnitude of ΔT is the result of conductive and convective heat transfer processes that are influenced by:

- Absorbed solar radiation at the sea surface
- Day time solar heating of the PVC pipes
- Time of day
- Cloud cover
- Air temperature
- Wind speed and direction

The simple algorithm for the prediction of ΔT presented in this thesis will allow us to determine skin SST given time of day, cloud cover, air temperature and bulk SST, to about 0.26 °C at night, and is based on the data collected on board the *Aurora Australis*. The skin SST data can be used to provide direct ground truth for satellite radiometry such as the AVHRR and ATSR instruments and can assist in the development of atmospheric correction algorithms for the Southern Ocean region.

It is also possible that given an air temperature and a skin SST from a satellite, the bulk SST can then be estimated which is of interest to oceanographers and climate modellers alike. One disadvantage of night time AVHRR imagery is that cloud cover, ice and sea water are not as easily separated. A preferable outcome is to improve day time standard errors in the estimation of ΔT by modelling the diurnal deck layer. This would make better use of day time AVHRR satellite imagery, and also take advantage of the improved cloud/sea/ice discrimination in day light hours.

BIBLIOGRAPHY :

American Society of Photogrammetry [ASP]. 1983, *Manual of Remote Sensing*, **1**: 320-323, **2**: 1091-1097.

Amiro B. D., Thurtell G. W. and Gillespie T. J. 1983. A Small Infrared Thermometer for Measuring Leaf Temperature in Leaf Chambers, *J. Experimental Botony* **34** (148): 1569-1576.

Ball F.K. 1954. Short Communications: Sea Surface Temperatures, *Aust. J. Phys.* **7**: 649-652.

Barton I.J. 1992. Satellite-derived Sea Surface Temperatures: A Comparison between Operational, Theoretical, and Experimental Algorithms, *J. Appl. Meteor.* **31**: 433-442.

Barton I.J. and Cechet R.P. 1989. Comparison and Optimization of AVHRR Sea Surface Temperature Algorithms, *J. Atmos. and Oceanic Tech.* **6**: 1083-1089.

Becker G.A., Huber K. and Krause H. 1979. Infra-red Radiometry in the German Bight, *Dt. hydrogr.* **Z32**: 19-26.

Bernstein R.L. 1984. Satellite Sea Surface Temperature determination from Microwave and infrared Radiometry, In: Gautier, C. and Fieux, M. (editors) *Large-Scale Oceanographic Experiments and Satellites* Nato ASI series, D. Reidel publishing company. Dordrecht Holland: 87-98.

Bernstein R.L. and Chelton D.B. 1985. Large-Scale Sea Surface Temperature Variability From Satellite and Shipboard Measurements, *J. Geophys. Res.* **90**(C6): 11619-11630.

Bradley E. F., Coppin P. A. and Godfrey J. S. 1991. Measurements of Sensible and Latent Heat Flux in the Western Equatorial Pacific Ocean, *J. Geophys. Res.* **96**: 3375-3389.

Bradley S.G. 1982. Transient Radiative Influences of Cumulus Clouds on Surface Temperature and Fluxes, *J. Geophys. Res.* **87**(C4): 3135-3142.

Brown O.B., Brown J.W. and Evans R.H. 1985. Calibration of Advanced Very High Resolution Radiometer Infrared Observations, *J. Geophys. Res.* **90**(C6): 11667-11677.

Campbell Scientific Inc. 1990. *The CR21 Campbell Scientific Operations Manual.*

Chahine M.T. 1980. Infrared Remote Sensing of Sea Surface Temperatures, *Remote Sensing of Atmospheres and Oceans.* Jet Propulsion laboratory, Pasadena, California: 411-434.

Chang J.H. and Wagner R.N. 1975. Laboratory Measurement of Surface Temperature Fluctuations Induced by Small Amplitude Surface Waves, *J. Geophys. Res.* **80** (18): 2677-2687.

Cogan J.L. 1976. Interpretation of 8-13 μm measurements of sea-surface temperature, *Quart. J. R. Met. Soc.* **102**: 771-774.

Coppin P.A., Bradley E.F., Barton I.J. and Godfrey J.S. 1991. Simultaneous Observations of Sea Surface Temperature in the Western Equatorial Pacific Ocean by Bulk, Radiative and Satellite Methods, *J. Geophys. Res.* **96**: 3401-3409.

Curran P.J. 1985. Principles of Remote Sensing, *Longman Group,* UK Limited, London: 164-166.

Dalu G. and Liberti G.L. 1988. Validation Problems for Remotely Sensed Sea Surface Temperatures. *IL Nuovo Cimento* **11C**(5-6): 589-607.

Davies J.A., Robinson P.J. and Nunez M. 1971. Field Determinations of Surface Emissivity and Temperature for Lake Ontario. *J. Applied Meteorology* **10**(4): 811-819.

Deacon E.L. 1982. Slow-Response Temperature Sensors. In: Dobson, F., Hasse, L. and Davis, R. (editors) *Air-Sea Interaction: Instruments and Methods.* Plenum Press: 255-267.

Emery W.J., Kantha L., Wick G.A. and Schluessel P. 1993. The Relationship Between Skin and Bulk Sea Surface Temperature. In: Jones, I.S.F., Sugimori, Y. and Stewart, R.W. (editors) *Satellite Remote Sensing of the Oceanic Environment.* Seibutsu Kenkyusha Co. Ltd.: 25-40.

Everest C.E. (President of Everest Interscience Inc.). 1990, 1992 and 1993. *Personal Communications.* Fullerton, California, USA.

Everest Interscience Inc. *Model 4000A Infrared Temperature Transducer Operating Manual.* Fullerton, California, USA.

Ewing G. and McAlister E.D. 1960. On the Thermal Boundary Layer of the Ocean. *Science* **131**: 1374-1376.

Global Climate Observing System (GCOS) 1992. *Report of the Joint Scientific and Technical Committee,* (first session), Geneva 13-15 April, 1992.

Grassl H. 1976. The Dependence of the Measured Cool Skin of the Ocean on Wind Stress and Total Heat Flux. *Boundary-Layer Meteorology* **10**: 465-474.

Harris R. 1987. Satellite Remote Sensing: An Introduction. Routledge & Kegan Paul: Geography, Environment & Planning, London :12-17, 58-60, 170-172.

Hasse L. 1963. On the cooling of the sea surface by evaporation and heat exchange. *Tellus* **15**(4): 363-366.

Hasse L. 1971. The Sea Surface Temperature Deviation and the Heat Flow at the Sea-Air Interface. *Boundary-Layer Meteorology* **1**: 368-379.

Henderson-Sellers A. and Robinson P.J. 1986. *Contemporary Climatology,* Longman Group, U.K. Limited: 29-80.

Hepplewhite C.L. 1989. Remote observation of the sea surface and atmosphere: The oceanic skin effect. *Int. J. Remote Sensing* **10**(4-5): 801-810.

Hicks B.B. and Hess G.D. 1977. On the Bowen Ratio and Surface Temperature at Sea. *J. Phys Oceanog.* **7**: 141-145.

Hill R.H. 1972. Laboratory Measurement of Heat Transfer and Thermal Structure Near an Air-Water interface. J. *Phys. Oceanog.* **2**: 190-198.

Hinzpeter H. 1982. Atmospheric Radiation Instruments. In: Dobson, F., Hasse, L. and Davis, R (editors) *Air-Sea Interaction: Instruments and Methods,* Plenum Press: 491-507.

Huband N.D.S. 1985(a). An Infra-red Radiometer for Measuring Surface Temperature in the Field: Part I. Design and construction. *Agric. For. Meteorol.* **34**: 215-226.

Huband N.D.S. 1985(b). An Infra-red Radiometer for Measuring Surface Temperature in the Field: Part II. Calibration and performance. *Agric. For. Meteorol.* **34**: 227-233.

Jones T. P. 1969. Reference Tables for Thermocouples. *National Standards Laboratory Technical Paper No. 26,* Commonwealth Scientific Industrial Research Organisation (CSIRO).

Kalma J.D. and Alksins, H. 1988. Calibration of Small Infra-Red Surface Temperature Transducers. *Agric. For. Meteorol.* **43**: 83-98.

Katsaros K.B. 1977. The sea surface temperature deviation at very low wind speeds; is there a limit ? *Tellus* **29**: 229-239.

Katsaros K.B. 1980. The Aqueous Thermal Boundary Later. *Boundary-Layer Meteorology* **18**: 107-127.

Katsaros K.B. 1982. Radiative Sensing of Sea Surface Temperature. In: Dobson, F., Hasse, L., and Davis, R. (editors), *Air-Sea Interaction: Instruments and Methods,* Plenum Press: 293-317.

Khundzhua G.G., Gusev A.M., Andreyev Y.G., Gurov V.V. and Skorokhvatov N.A. 1977. Structure of the Cold Surface Film of the Ocean and Heat Transfer between the Ocean and the Atmosphere. *Izvestiya Atmospheric and Oceanic Physics* **13**(7): 506-509.

Kondo J., Sasano Y. and Ishii T. 1979. On Wind-Driven Current and Temperature Profiles with Diurnal Period in the Oceanic Planetary Boundary Layer. *J. Phys. Oceanog.* **9**: 360-372.

Kropotkin M.A., Verbitskiy V.A., Sheveleva T.Y. and Tarashkevich V.N. 1978. Radiation Temperature of a Water Surface with an Oil Slick. *Oceanology* **18**(6): 730-731.

Larsen S.E., Hojstrup J. and Gibson C.H. 1982. Fast-Response Temperature Sensors. In: Dobson F., Hasse L. and Davis R (editors) *Air-Sea Interaction: Instruments and Methods.* Plenum Press: 269-291.

Lillesand T.M. and Kiefer R.W. 1987. *Remote Sensing and Image Interpre*tation, Wiley: (2nd ed.), New York: 7-15, 396-412.

Liu W.T., Katsaros K.B., and Businger J.A. 1979. Bulk Parameterization of Air-Sea Exchanges of Heat and Water Vapour Including the Molecular Constraints at the Interface. *J. Atmospheric Sciences* **36**: 1722-1735.

Llewellyn-Jones D.T., Minnett P.J., Saunders R.W. and Zavody A.M. 1984. Satellite multichannel infrared measurements of sea surface temperature of the N.E. Atlantic Ocean using AVHRR/2. *Quart. J. R. Met. Soc.* **110**: 613-631.

McAlister E.D. and McLeish W. 1969. Heat Transfer in the Top Millimeter of the Ocean. *J. Geophys. Res.* **74**(13): 3408-3414.

McAlister E.D. and McLeish W. 1970. A Radiometric System for Airborne Measurement of the Total Heat Flow from the Sea. *Applied Optics* **9**(12): 2697-2705.

McClain E.P., Pichel W.G. and Walton C.C. 1985. Comparative Performance of AVHRR-Based Multichannel Sea Surface Temperatures. *J. Geophys. Res.* **90**(C6): 11587-11601.

McLeish W. 1968. On the mechanisms of wind-slick generation. *Deep-Sea Research* **15**: 461-469.

Maul G.A. 1985. Introduction to Satellite Oceaonography. Martinus Nijhoff Publisher: Dordrecht: 71-245.

Michael K.J. 1988. A Satellite-Based Study of Ocean-Atmosphere Heat Fluxes in the Vicinity of John Brewer Reef, Queensland. *unpublished PhD thesis Department of Geography.* University of Tasmania.

Michael K.J. and Skirving W.J. 1991. An investigation of differences of skin and bulk sea surface temperatures. presented at *Australian Physical Oceanography Conference,* Canberra, ACT, 28-31 January 1991.

Mikhail E.M. and Gracie G. 1981. *Analysis and Adjustment of Survey Measurements.* Von Nostrand Reinhold Company, New York.

Miller A.W. and Street R.L. 1978. On the Existence of Temperature Waves at a Wavy Air-Water Interface. *J. Geophys. Res.* **83**(C3): 1353-1365.

Minnett P.J., Zavody A.M. and Llewellyn-Jones D.T. 1984. Satellite Measurements of Sea-Surface Temperature for Climate Research. In: Gautier, C. and Fieux, M. (editors) *Large-Scale Oceanographic Experiments and Satellites.* Nato ASI series, D. Reidel publishing company. Dordrecht Holland: 57-85.

Nilsson H. E. 1991. Hand-held radiometry and IR-thermography of plant diseases in field plot experiments. *Int. J. Remote. Sensing* **12**(3): 545-557.

Njoku E.G. 1985. Satellite-Derived Sea Surface Temperature: Workshop Comparisons. *Bull. Amer. Meteor. Soc.* **66**(3): 274-281.

Njoku E.G., Barnett T.P., Laurs R.M. and Vastano A.C. 1985. Advances in Satellite Sea Surface Temperature Measurement and Oceanographic Applications. *J. Geophys. Res.* **90**(C6): 11573-11586.

Open University. 1989. *Ocean Circulation.* Prepared by an Open University Course Team, Pergamon Press: 159-167.

Paulson C.A. and Parker T.W. 1972. Cooling of a Water Surface by Evaporation, Radiation, and Heat Transfer. *J. Geophys. Res.* **77**(3): 491-495.

Paulson C.A. and Simpson J.J. 1981. The Temperature Difference Across the Cool Skin of the Ocean. *J. Geophys. Res.* **86**(C11): 11044-11054.

Pearce A.F., Prata A.J. and Manning C.R. 1989. Comparison of NOAA/AVHRR-2 sea surface temperatures with surface measurements in coastal waters. *Int. J. Remote Sensing* **10**(1): 37-52.

Pickard G.L. and Emery W.J. 1990. *Descriptive Physical Oceanography: An Introduction.* Pergamon Press (5th edition): 37-49 and 69-91.

Prata A.J.F, Cechet R.P, Barton I.J. and Llewellyn-Jones D.T. 1990. The Along Track Scanning Radiometer for ERS-1 Scan Geometry and Data Simulation. *IEEE Trans. on Geoscience and Rem. Sens.* **28**(1): 3-12.

Rapier C. B. 1992. Radiometric Measurements of Sea Surface Temperatures (SST) in the Assessment of the Skin Effect in the Southern Ocean. *Unpublished Thesis, Institute of Antarctic and Southern Ocean Studies,* University of Tasmania.

Robertson J.E. and Watson A.J. 1992. Thermal skin effect of the surface ocean and its implications for CO_2 uptake. *Nature* **358**: 738-740.

Robinson I.S. 1985. *Satellite Oceanography: An Introduction for Oceanographers and Remote Sensing Scientists.* E.Horwood, Chichester: 141-149, 194-229.

Robinson I.S., Wells N.C. and Charnock H. 1984. Review Article: The sea surface thermal boundary layer and its relevance to the measurement of sea surface temperature by airborne and spaceborne radiometers. *Int. J. Remote Sensing* **5**(1): 19-45.

Sabins F.F. 1973. *Remote Sensing: Principles and Interpretation.* W.H.Freeman, San Francisco: 119-130.

Salisbury J.W. and D'Aria D.M. 1992. Emissivity of Terrestrial Materials in the 8-14 μm Atmospheric Window, *Remote. Sens. Environ.* **42**: 83-106.

Saunders P.M. 1967(a). Aerial Measurement of Sea Surface Temperature in the Infrared. *J. Geophys. Res.* **72**(16): 4109-4117.

Saunders P.M. 1967(b). The Temperature at the Ocean-Air Interface. *J. Atmospheric Sciences* **24**: 269-273.

Saunders P.M. 1973. The Skin Temperature of the Ocean: A Review. *Memoires Societe Royale des Sciences de Liege* **6**: 93-98.

Schluessel P., Emery W.J., Grassl H. and Mammen T. 1990. On the Bulk-Skin Temperature Difference and Its Impact on Satellite Remote Sensing of Sea Surface Temperature. *J. Geophys. Res.* **95**(C8): 13341-13356.

Schluessel P. and Grassl H. 1990. SST in polynias: A case study. *Int. J. Remote Sensing* **11**(6): 933-945.

Schluessel P., Shin H.Y., Emery W.J. and Grassl H. 1987. Comparison of Satellite-Derived Sea Surface Temperatures With in Situ Skin Measurements. *J. Geophys. Res.* **92**(C3): 2859-2874.

Schooley A.H. 1977. Temperature of Ocean Skin Related to Cloud Shadows. *J. Phys. Oceanog.* **7**: 486-488.

Sidran M. 1981. Broadband reflectance and emissivity of specular and rough water surface. *Applied Optics* **20**(18): 3176-3183.

Simpson J.J. and Paulson C.A. 1980. Small-Scale Sea Surface Temperature Structure. *J. Phys. Oceanogr.* **10**: 399-410.

Singh S.M. 1985. Remarks on the use of a Stefan-Boltzmann-type relation for estimating surface temperatures. *Int. J. Remote Sensing* **6**(5): 741-747.

Skirving W.J. and Michael K.J. 1992. A robust ship-board radiometer system for monitoring sea surface temperature, Presented at *Australian Institute of Physics Tenth National Congress*, Melbourne, 10-14 February, 1992.

Spyers-Duran P.A. and Winant C.D. 1985. Comparison of Sea Surface Temperatures Obtained from an Aircraft Using Remote and Direct Sensing Techniques. *J. Atmos. and Oceanic Tech.* **2**: 667-671.

Stigter C. J., Jiwaji N. T. and Makonda M. M. 1982. A Calibration Plate to Determine the Performance of Infrared Thermometers in Field Use. *Agricultural Meterology* **26**: 279-283.

Strong A.E. and McClain E.P. 1984. Improved Ocean Surface Temperatures From Space: Comparisons With Drifting Buoys. *Bull. Am. Meteor. Soc.* **65**(2): 138-142.

Szekielda K.H. 1988. *Satellite Monitoring of the Earth.* Wiley, New York: 2-7, 13, 34-38.

Tabata S. 1993. Visible Band Radiometers. In: Jones, I.S.F., Sugimori, Y. and Stewart, R.W. (editors) *Satellite Remote Sensing of the Oceanic Environment.* Seibutsu Kenkyusha Co. Ltd.: 17-24.

Walton-Smith F.G. 1973. *The seas in Motion.* Thomas Y. Crowell Company: 34-57

Weinreb M.P., Hamilton G., Brown S. and Koczor R.J. 1990. Nonlinearity Corrections in Calibration of Advanced Very High Resolution Radiometer Infrared Channels. *J. Geophys. Res.* **95**(C5): 7381-7388.

Wesely M.L. 1979. Heat Transfer Through the Thermal Skin of a Cooling Pond With Waves. *J. Geophys. Res.* **84**(C7): 3696-3700.

Whitworth T. 1988. The Antarctic Circumpolar Current. *Oceanus* **31**(2): 53-58.

Wick G.A., Emery W.J. and Schluessel P. 1992. A Comprehensive Comparison Between Satellite-Measured Skin and Multichannel Sea Surface Temperature. *J. Geophys Res.* **97**(C4): 5569-5595.

Witting J. 1972. Brief Reports: Temperature Fluctuations at an Air-Water Interface Caused by Surface Waves. *J. Geophys. Res.* **77**(18): 3265-3269.

Woodcock A.H. and Stommel H. 1947. Temperature Observations near the Surface of a Fresh Water Pond at Night. *J. Meterol.* **4**: 102-103.

World Climate Research Programme (WCRP), 1986. *Report of the COSPAR International Workshop on: Satellite-Derived Sea Surface Temperatures for Global Climate Applications*, Camp Springs, Maryland, USA, 28-31 May, 1985.

APPENDIX A: The Monthly Time Series Plots.

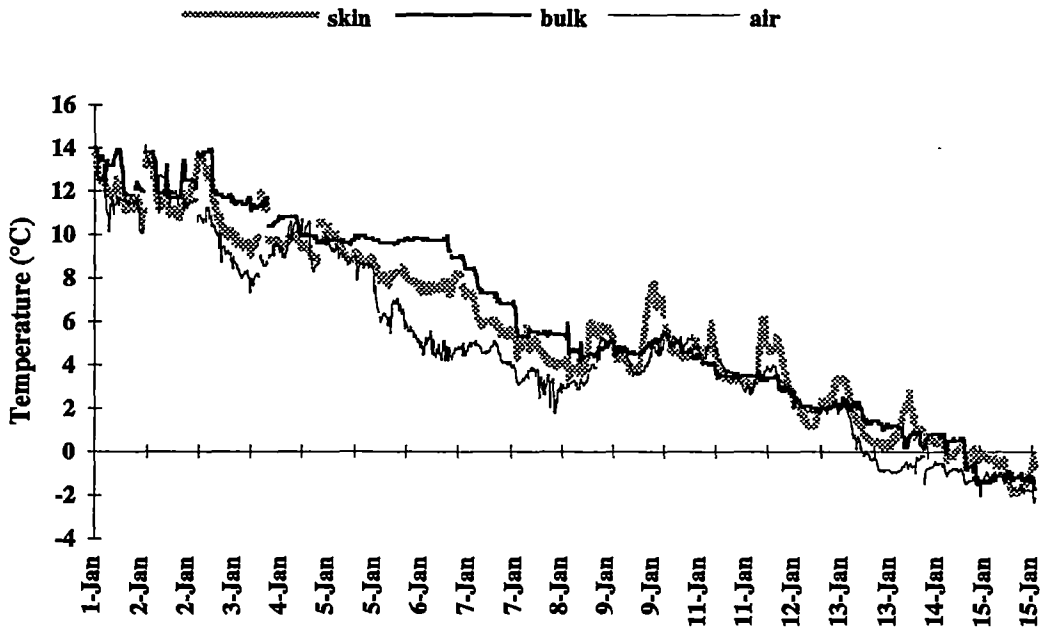

A1

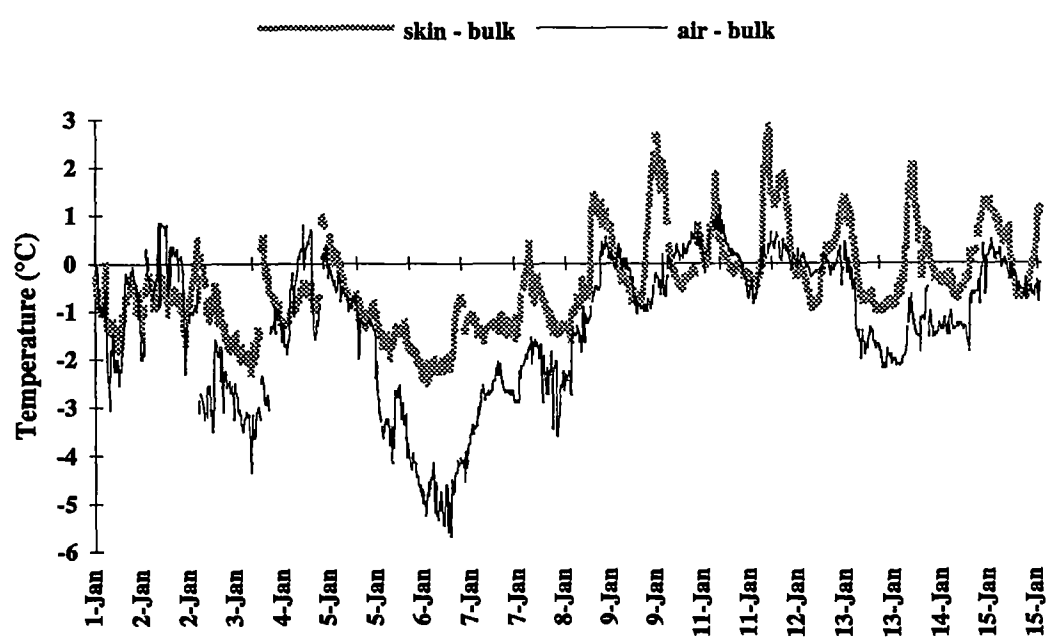

A2

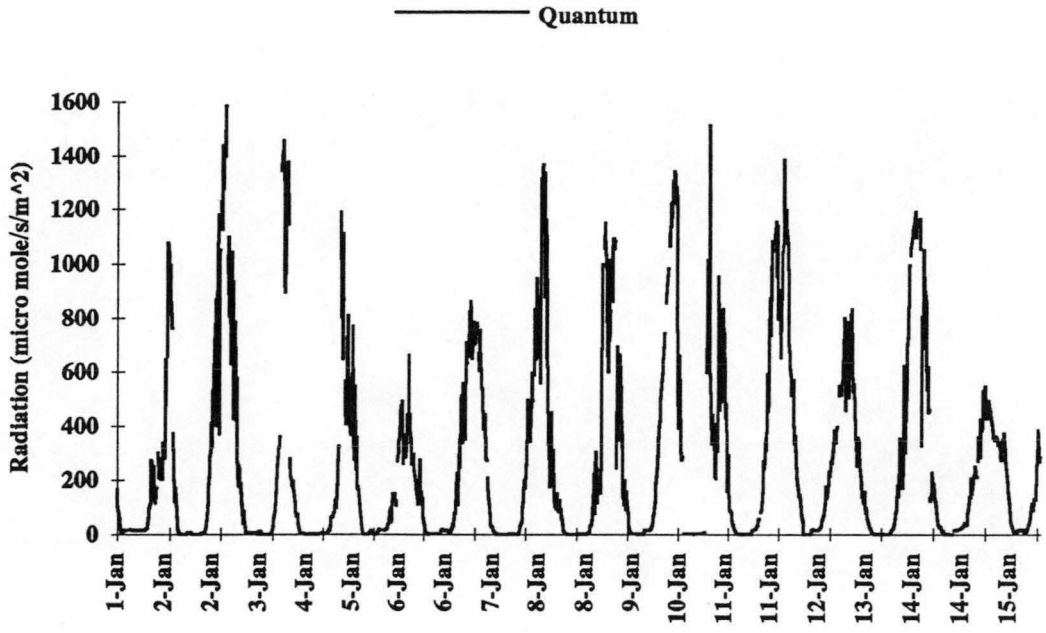
Quantum
Radiation (micro mole/s/m^2)
1600
1400
1200
1000
800
600
400
200
0
1-Jan
2-Jan
2-Jan
3-Jan
4-Jan
5-Jan
6-Jan
6-Jan
7-Jan
8-Jan
8-Jan
9-Jan
10-Jan
11-Jan
11-Jan
12-Jan
13-Jan
14-Jan
14-Jan
15-Jan

A3

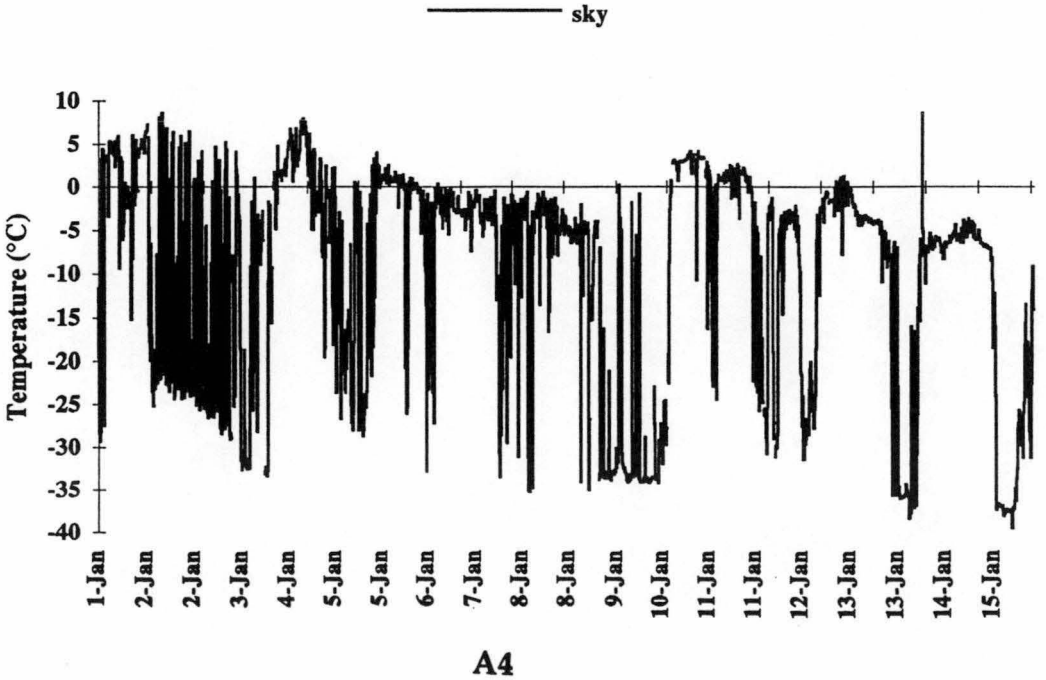
sky
Temperature (°C)
10
5
0
-5
-10
-15
-20
-25
-30
-35
-40
1-Jan
2-Jan
2-Jan
3-Jan
4-Jan
5-Jan
5-Jan
6-Jan
7-Jan
8-Jan
8-Jan
9-Jan
10-Jan
11-Jan
11-Jan
12-Jan
13-Jan
13-Jan
14-Jan
15-Jan

A4

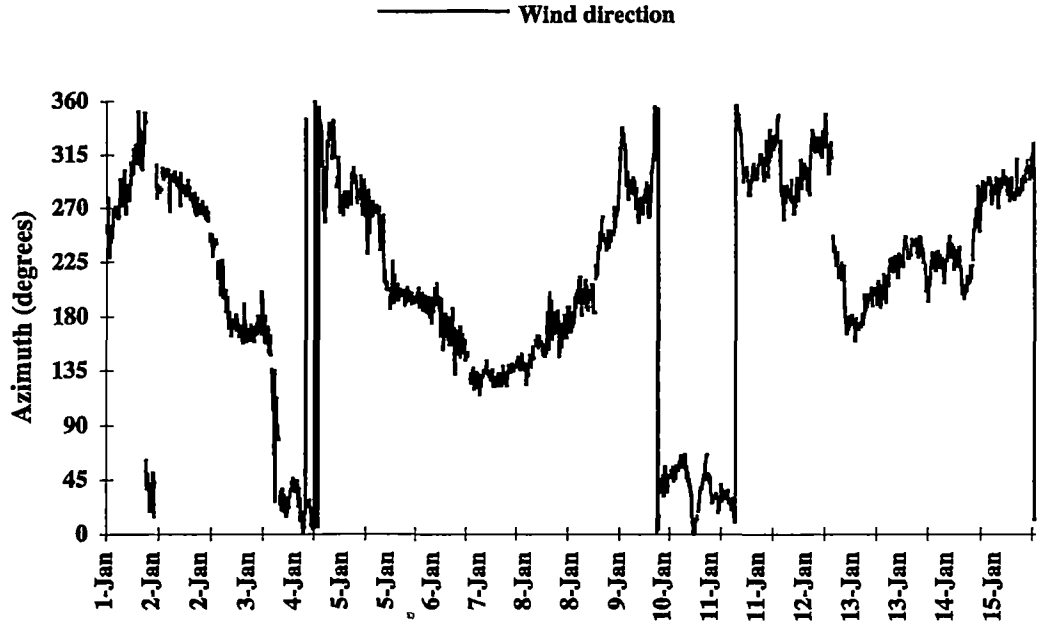
Wind direction
Azimuth (degrees)
360
315
270
225
180
135
90
45
0
1-Jan
2-Jan
2-Jan
3-Jan
4-Jan
5-Jan
5-Jan
6-Jan
7-Jan
8-Jan
8-Jan
9-Jan
10-Jan
11-Jan
11-Jan
12-Jan
13-Jan
13-Jan
14-Jan
15-Jan

A5

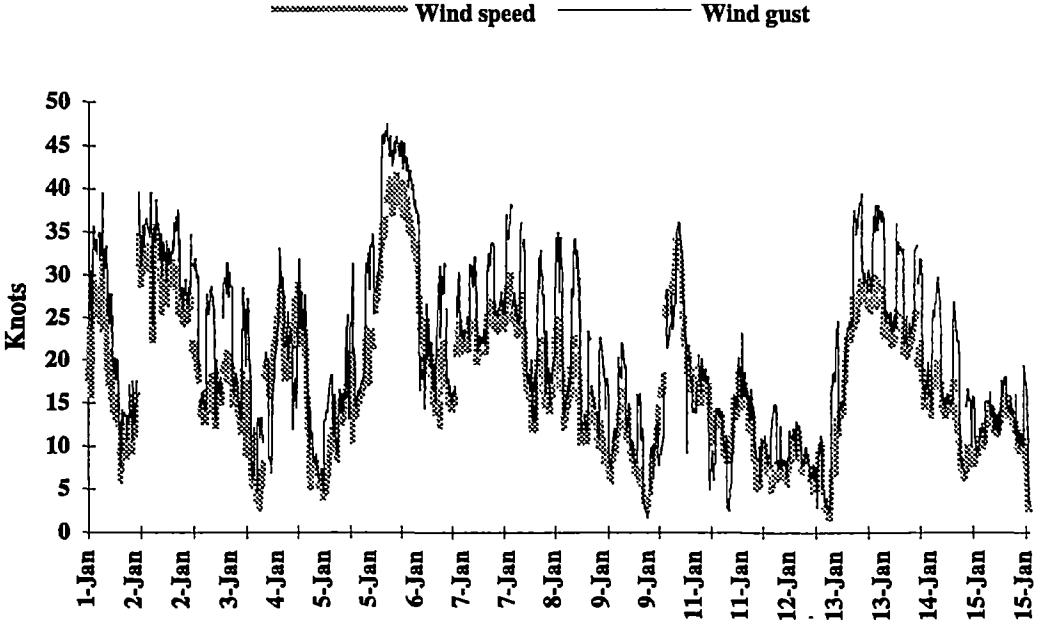
Wind speed
Wind gust
Knots
50
45
40
35
30
25
20
15
10
5
0
1-Jan
2-Jan
2-Jan
3-Jan
4-Jan
5-Jan
5-Jan
6-Jan
7-Jan
7-Jan
8-Jan
9-Jan
9-Jan
11-Jan
11-Jan
12-Jan
13-Jan
13-Jan
14-Jan
15-Jan
15-Jan

A6

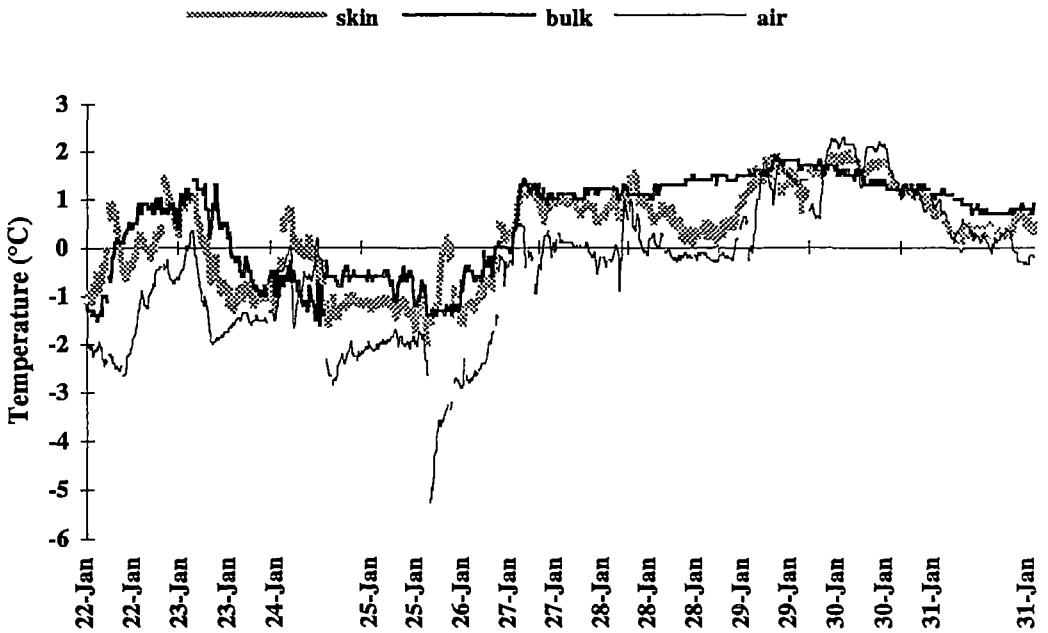
skin
bulk
air
Temperature (°C)
3
2
1
0
-1
-2
-3
-4
-5
-6
22-Jan
22-Jan
23-Jan
23-Jan
24-Jan
25-Jan
25-Jan
26-Jan
27-Jan
27-Jan
28-Jan
28-Jan
28-Jan
29-Jan
29-Jan
30-Jan
30-Jan
31-Jan
31-Jan

A7

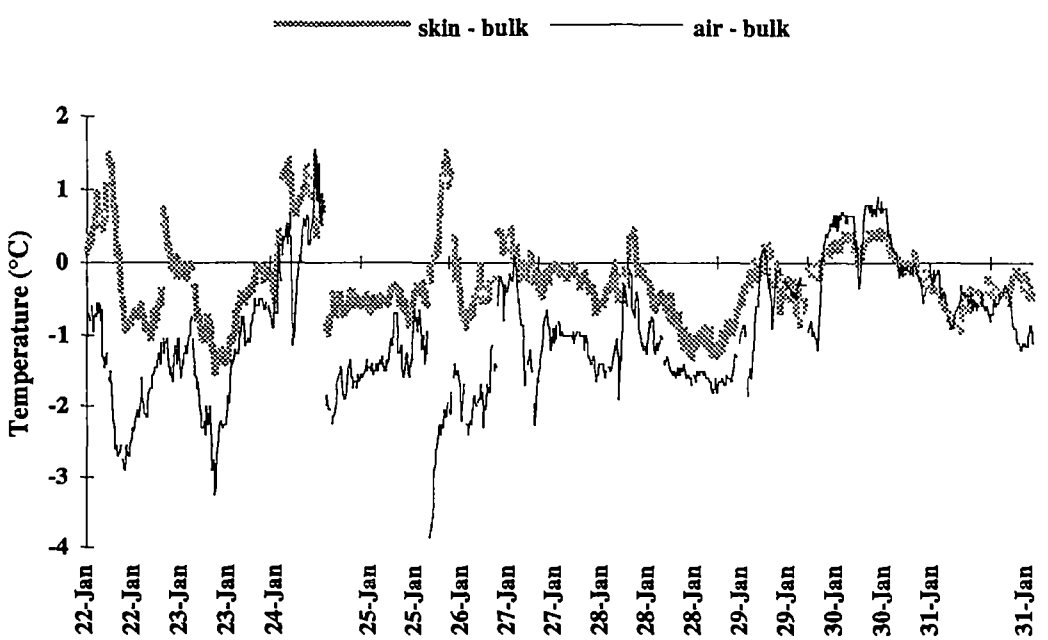
skin - bulk
air - bulk
Temperature (°C)
2
1
0
-1
-2
-3
-4
22-Jan
22-Jan
23-Jan
23-Jan
24-Jan
25-Jan
25-Jan
26-Jan
27-Jan
27-Jan
28-Jan
28-Jan
28-Jan
29-Jan
29-Jan
30-Jan
30-Jan
31-Jan
31-Jan

A8

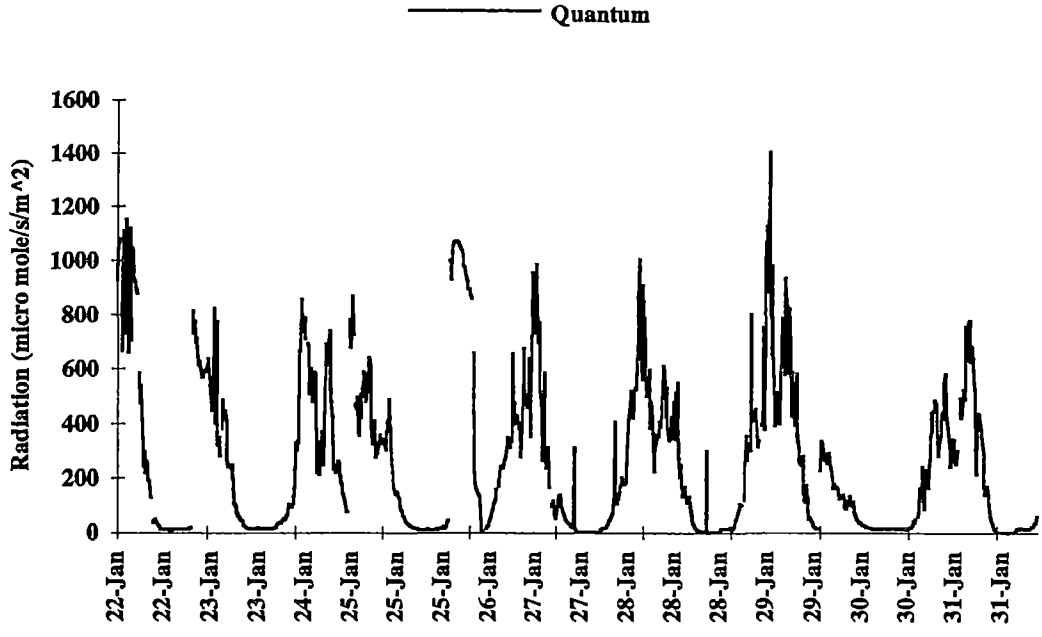
Quantum
Radiation (micro mole/s/m^2)
1600
1400
1200
1000
800
600
400
200
0
22-Jan
22-Jan
23-Jan
23-Jan
24-Jan
25-Jan
25-Jan
25-Jan
26-Jan
27-Jan
27-Jan
28-Jan
28-Jan
28-Jan
29-Jan
29-Jan
30-Jan
30-Jan
31-Jan
31-Jan

A9

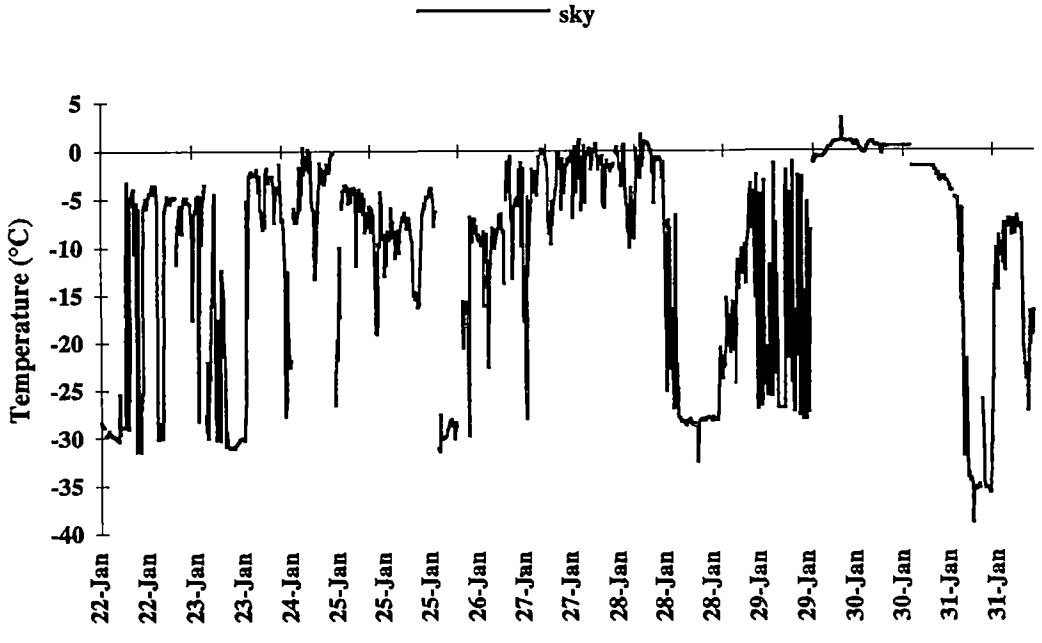
sky
Temperature (°C)
5
0
-5
-10
-15
-20
-25
-30
-35
-40
22-Jan
22-Jan
23-Jan
23-Jan
24-Jan
25-Jan
25-Jan
25-Jan
26-Jan
27-Jan
27-Jan
28-Jan
28-Jan
28-Jan
29-Jan
29-Jan
30-Jan
30-Jan
31-Jan
31-Jan

A10

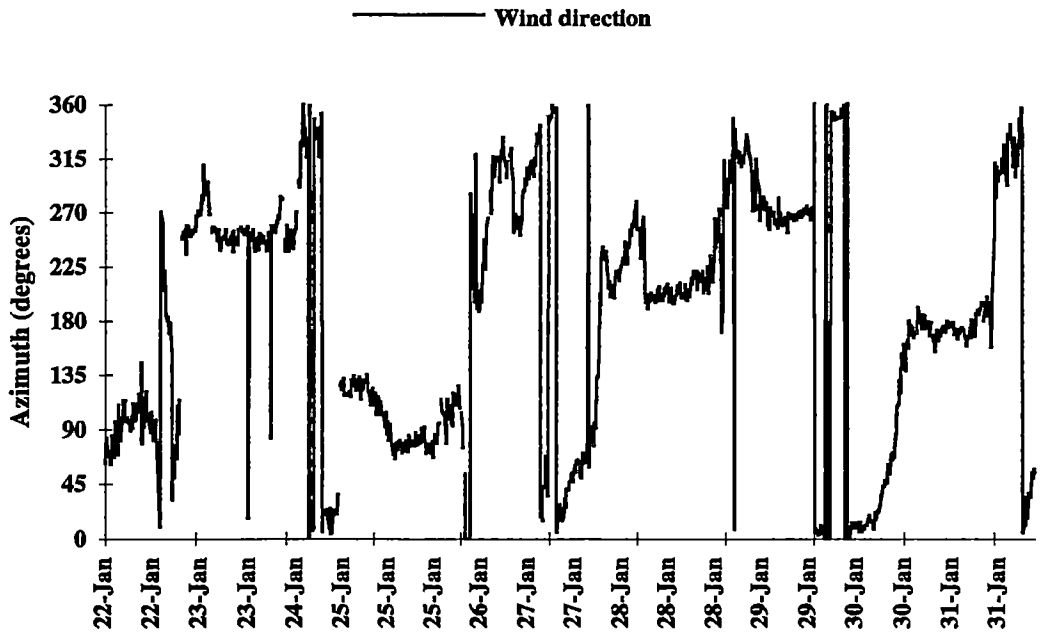
Wind direction
Azimuth (degrees)
360
315
270
225
180
135
90
45
0
22-Jan
22-Jan
23-Jan
23-Jan
24-Jan
25-Jan
25-Jan
25-Jan
26-Jan
27-Jan
27-Jan
28-Jan
28-Jan
28-Jan
29-Jan
29-Jan
30-Jan
30-Jan
31-Jan
31-Jan

A11

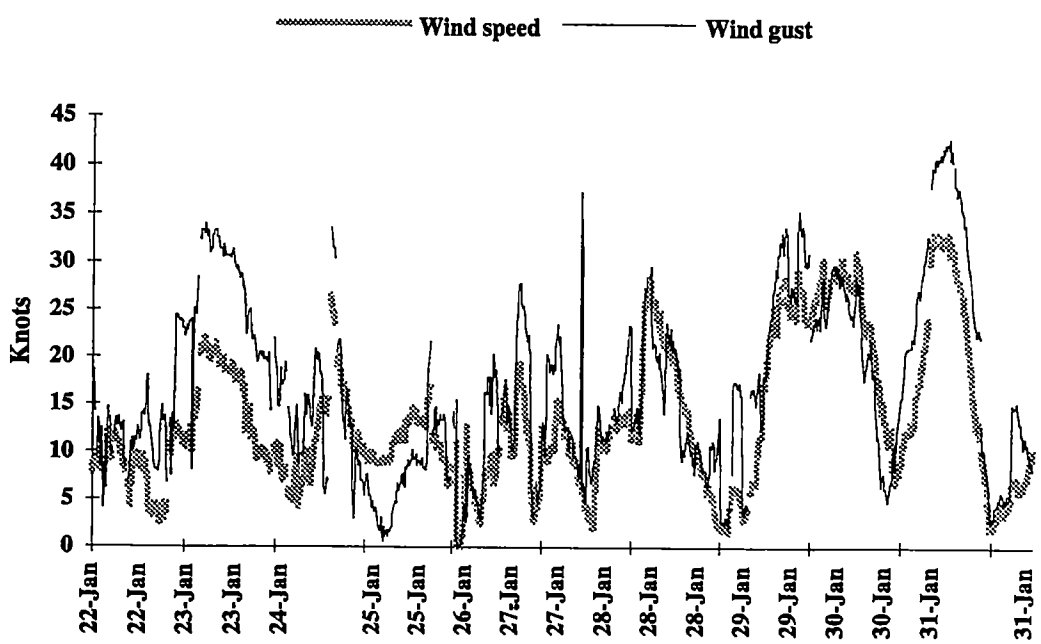
Wind speed
Wind gust
Knots
45
40
35
30
25
20
15
10
5
0
22-Jan
22-Jan
23-Jan
23-Jan
24-Jan
25-Jan
25-Jan
26-Jan
27-Jan
27-Jan
28-Jan
28-Jan
28-Jan
29-Jan
29-Jan
30-Jan
30-Jan
31-Jan
31-Jan

A12

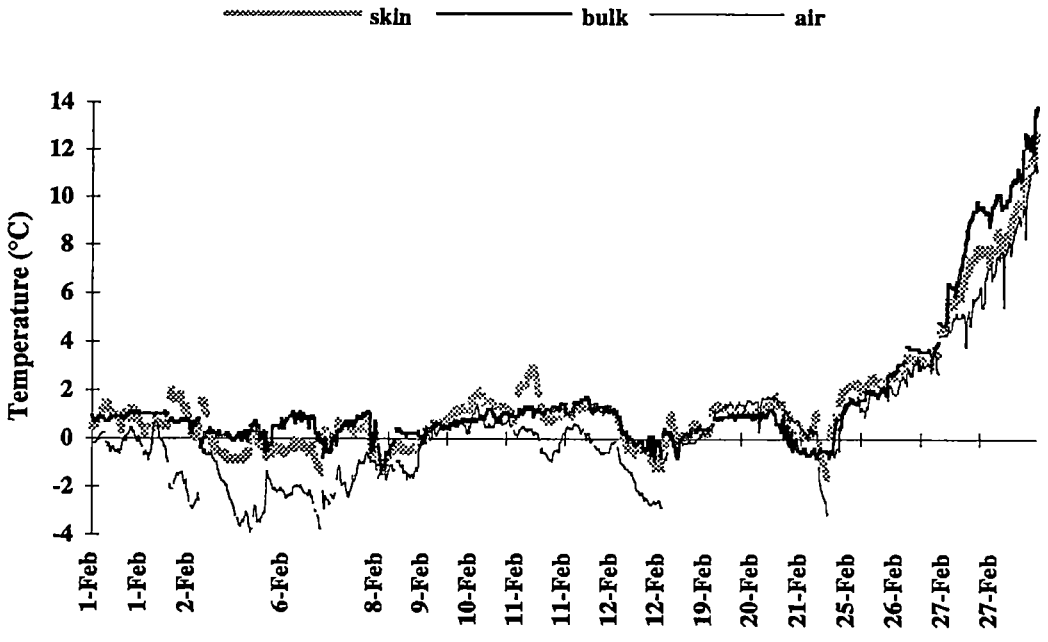
skin
bulk
air
Temperature (°C)
14
12
10
8
6
4
2
0
-2
-4
1-Feb
1-Feb
2-Feb
6-Feb
8-Feb
9-Feb
10-Feb
11-Feb
11-Feb
12-Feb
12-Feb
19-Feb
20-Feb
21-Feb
25-Feb
26-Feb
27-Feb
27-Feb

A13

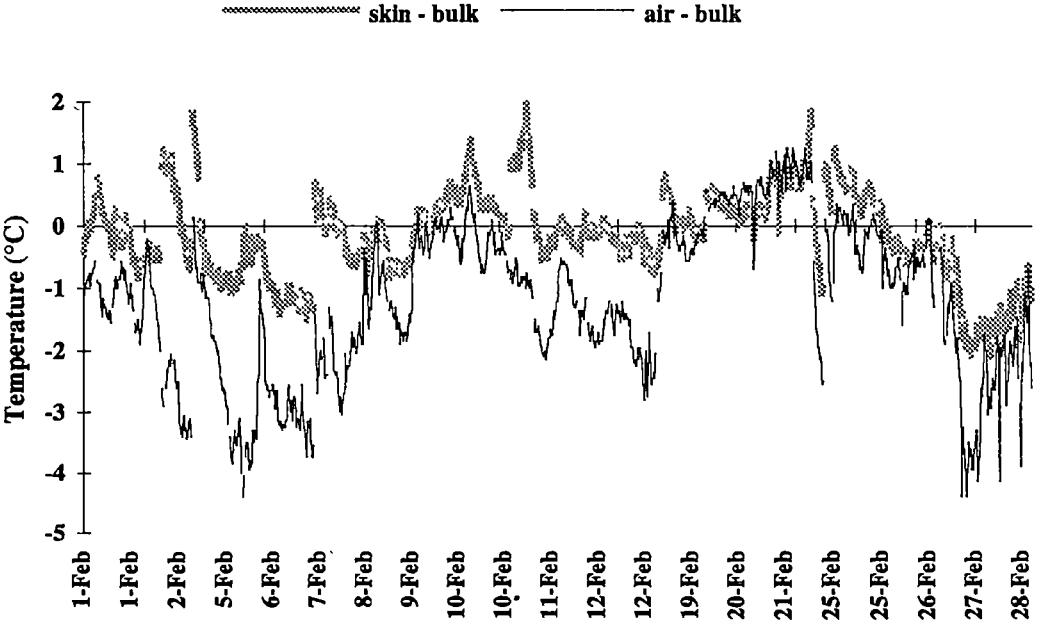
skin - bulk
air - bulk
Temperature (°C)
2
1
0
-1
-2
-3
-4
-5
1-Feb
1-Feb
2-Feb
5-Feb
6-Feb
7-Feb
8-Feb
9-Feb
10-Feb
10-Feb
11-Feb
12-Feb
12-Feb
19-Feb
20-Feb
21-Feb
25-Feb
25-Feb
26-Feb
27-Feb
28-Feb

A14

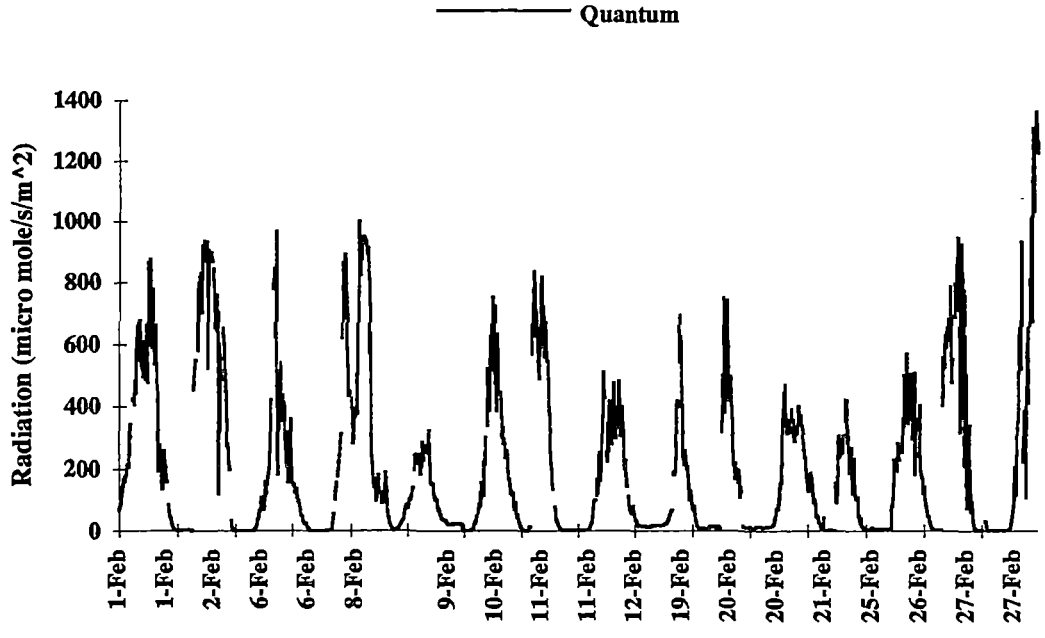
Quantum
Radiation (micro mole/s/m^2)
1400
1200
1000
800
600
400
200
0
1-Feb
1-Feb
2-Feb
6-Feb
6-Feb
8-Feb
9-Feb
10-Feb
11-Feb
11-Feb
12-Feb
19-Feb
20-Feb
20-Feb
21-Feb
25-Feb
26-Feb
27-Feb
27-Feb

A15

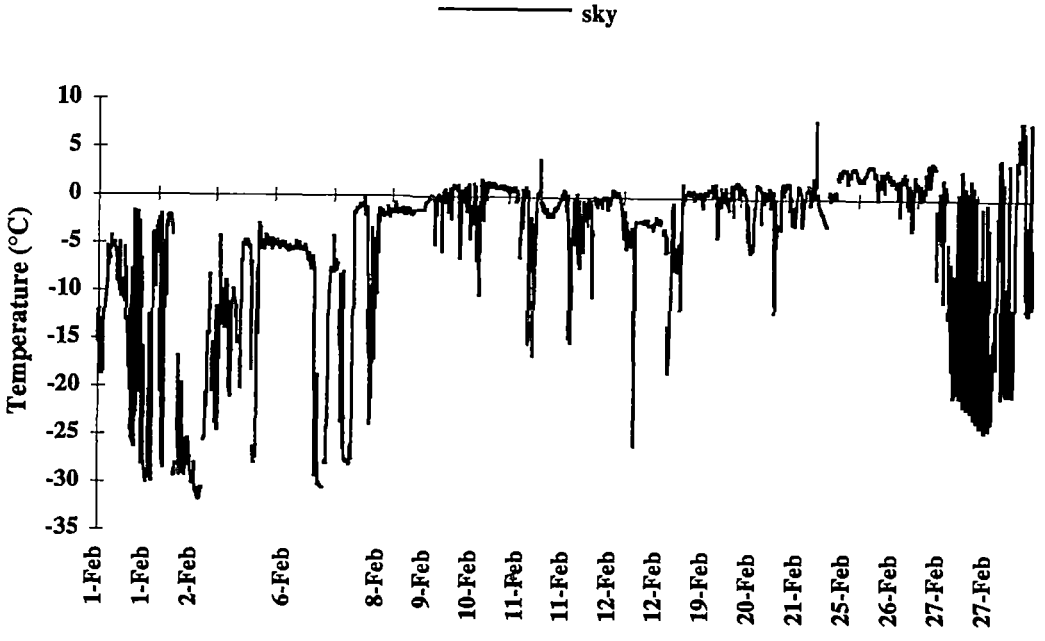
sky
Temperature (°C)
10
5
0
-5
-10
-15
-20
-25
-30
-35
1-Feb
1-Feb
2-Feb
6-Feb
8-Feb
9-Feb
10-Feb
11-Feb
11-Feb
12-Feb
12-Feb
19-Feb
20-Feb
21-Feb
25-Feb
26-Feb
27-Feb
27-Feb

A16

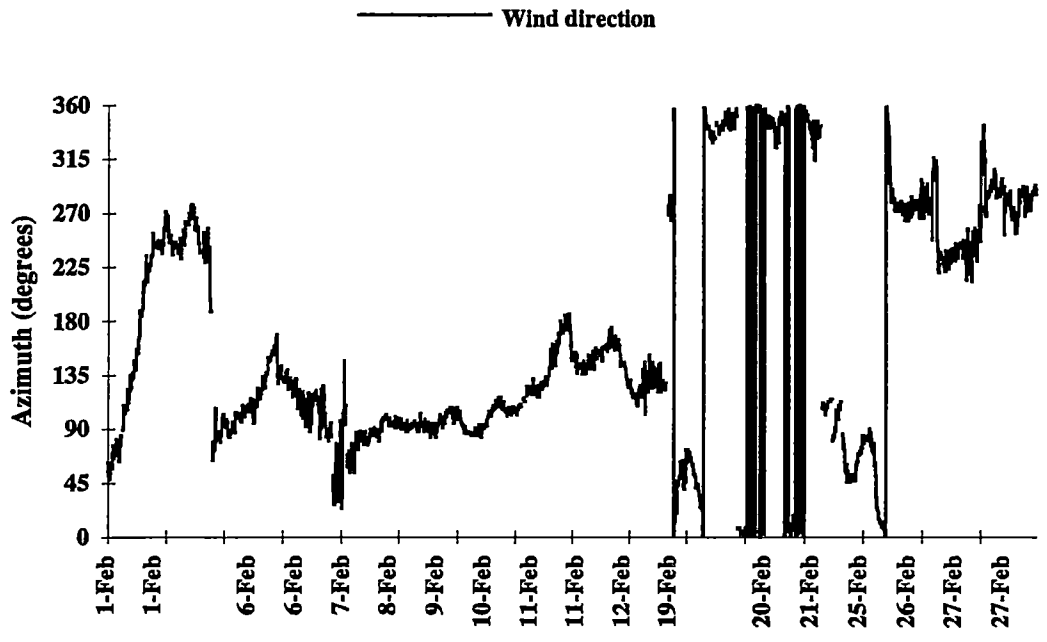
Wind direction
Azimuth (degrees)
360
315
270
225
180
135
90
45
0
1-Feb
1-Feb
6-Feb
6-Feb
7-Feb
8-Feb
9-Feb
10-Feb
11-Feb
11-Feb
12-Feb
19-Feb
20-Feb
21-Feb
25-Feb
26-Feb
27-Feb
27-Feb

A17

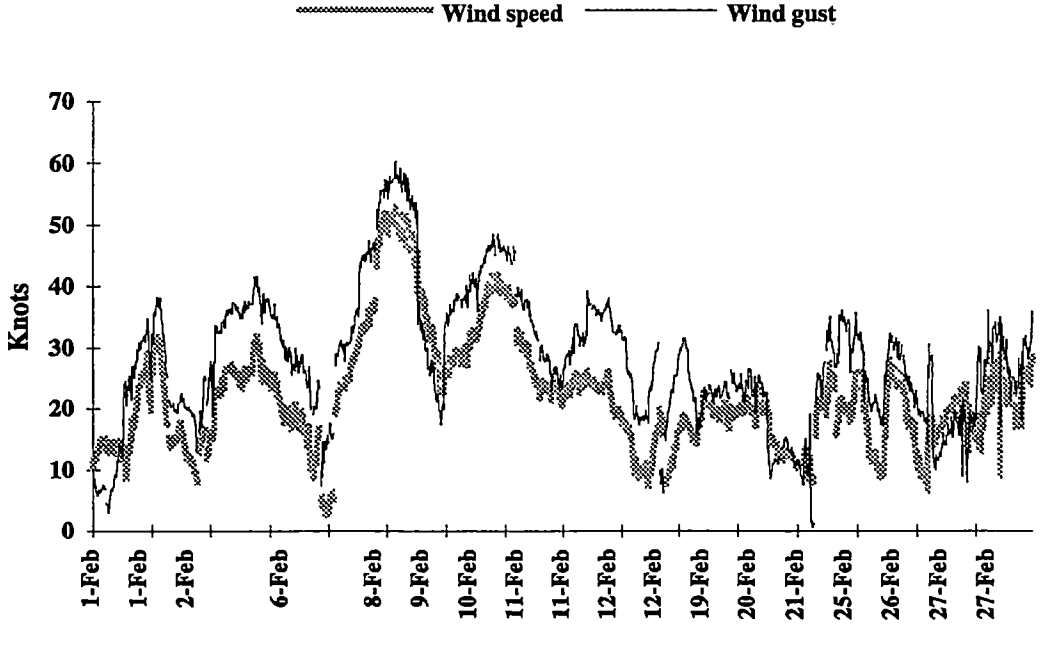
Wind speed
Wind gust
Knots
70
60
50
40
30
20
10
0
1-Feb
1-Feb
2-Feb
6-Feb
8-Feb
9-Feb
10-Feb
11-Feb
11-Feb
12-Feb
12-Feb
19-Feb
20-Feb
21-Feb
25-Feb
26-Feb
27-Feb
27-Feb

A18

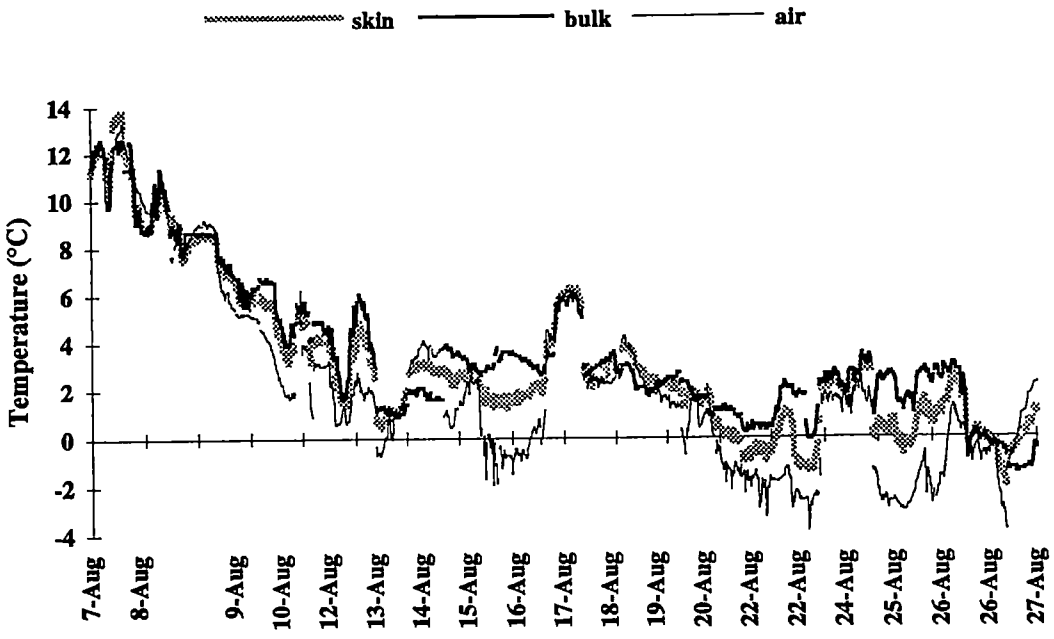
skin
bulk
air
Temperature (°C)
14
12
10
8
6
4
2
0
-2
-4
7-Aug
8-Aug
9-Aug
10-Aug
12-Aug
13-Aug
14-Aug
15-Aug
16-Aug
17-Aug
18-Aug
19-Aug
20-Aug
22-Aug
22-Aug
24-Aug
25-Aug
26-Aug
26-Aug
27-Aug

A19

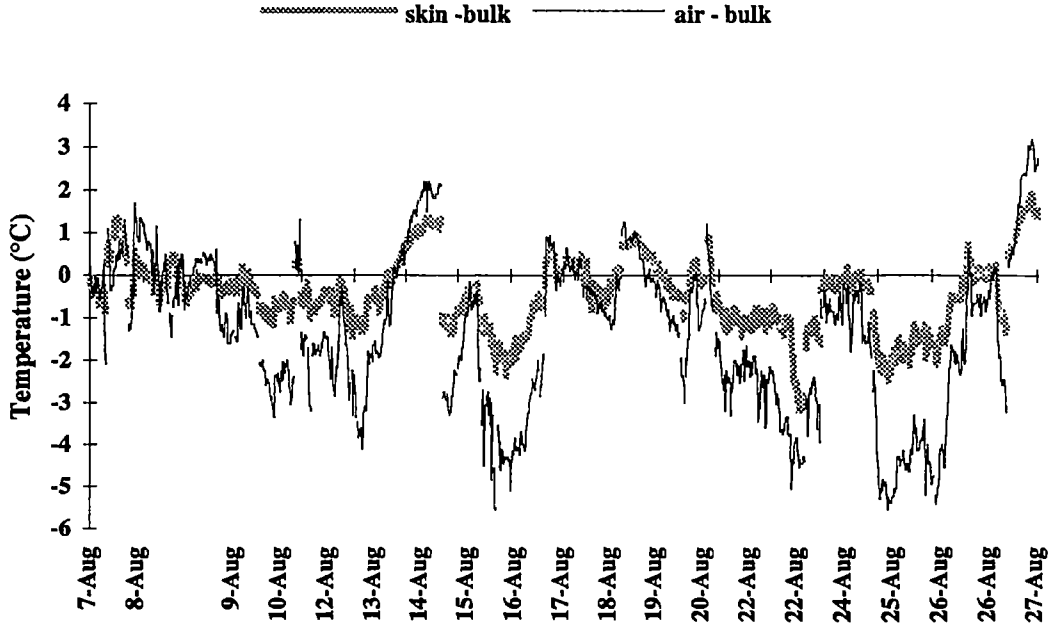
skin -bulk
air - bulk
Temperature (°C)
4
3
2
1
0
-1
-2
-3
-4
-5
-6
7-Aug
8-Aug
9-Aug
10-Aug
12-Aug
13-Aug
14-Aug
15-Aug
16-Aug
17-Aug
18-Aug
19-Aug
20-Aug
22-Aug
22-Aug
24-Aug
25-Aug
26-Aug
26-Aug
27-Aug

A20

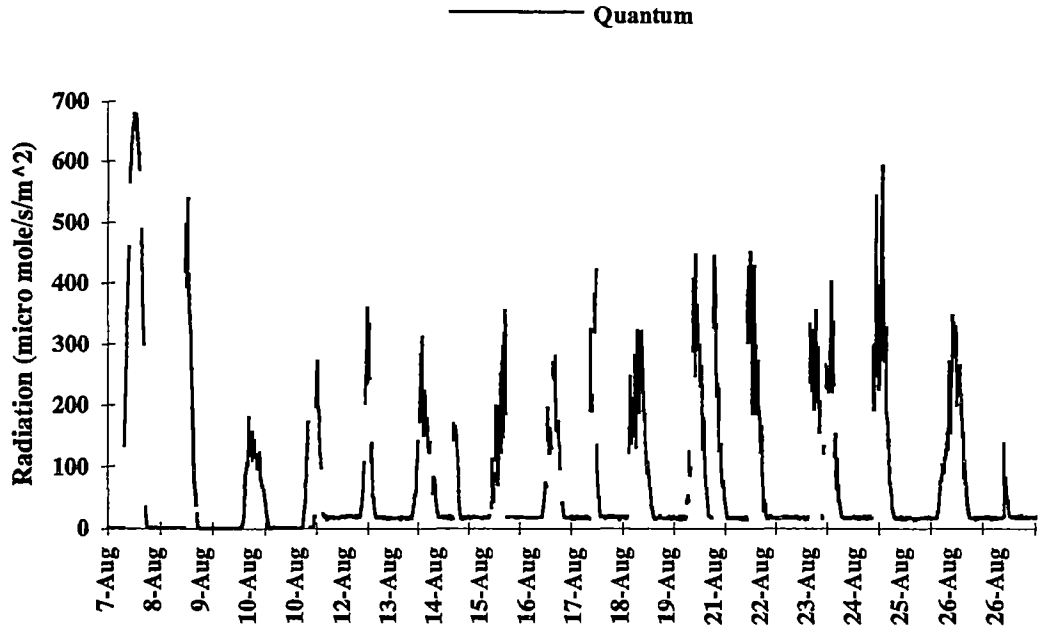
Quantum
Radiation (micro mole/s/m^2)
700
600
500
400
300
200
100
0
7-Aug
8-Aug
9-Aug
10-Aug
10-Aug
12-Aug
13-Aug
14-Aug
15-Aug
16-Aug
17-Aug
18-Aug
19-Aug
21-Aug
22-Aug
23-Aug
24-Aug
25-Aug
26-Aug
26-Aug

A21

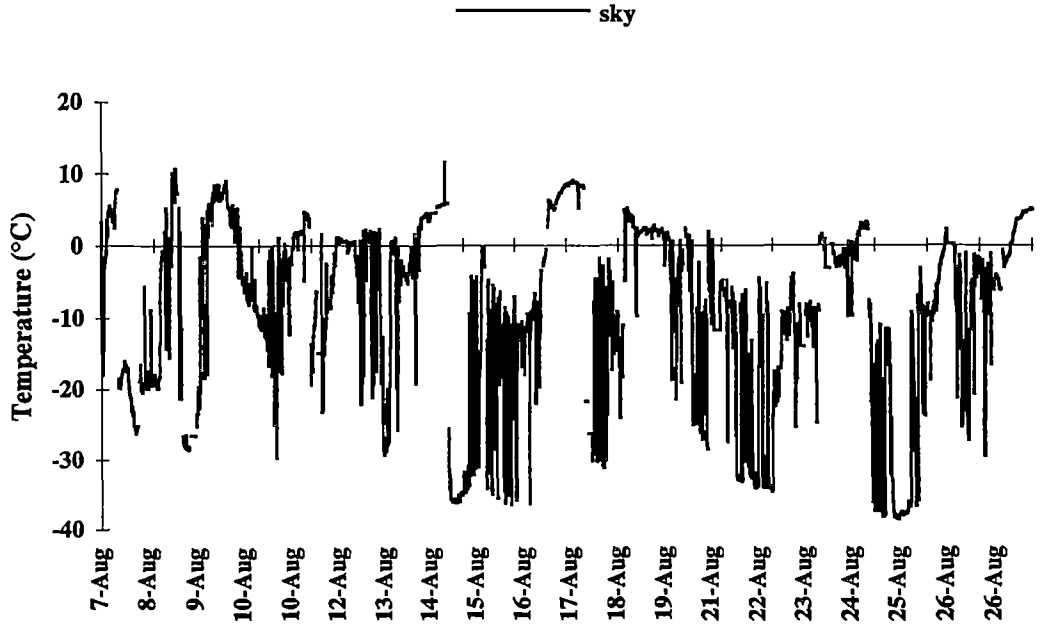
sky
Temperature (°C)
20
10
0
-10
-20
-30
-40
7-Aug
8-Aug
9-Aug
10-Aug
10-Aug
12-Aug
13-Aug
14-Aug
15-Aug
16-Aug
17-Aug
18-Aug
19-Aug
21-Aug
22-Aug
23-Aug
24-Aug
25-Aug
26-Aug
26-Aug

A22

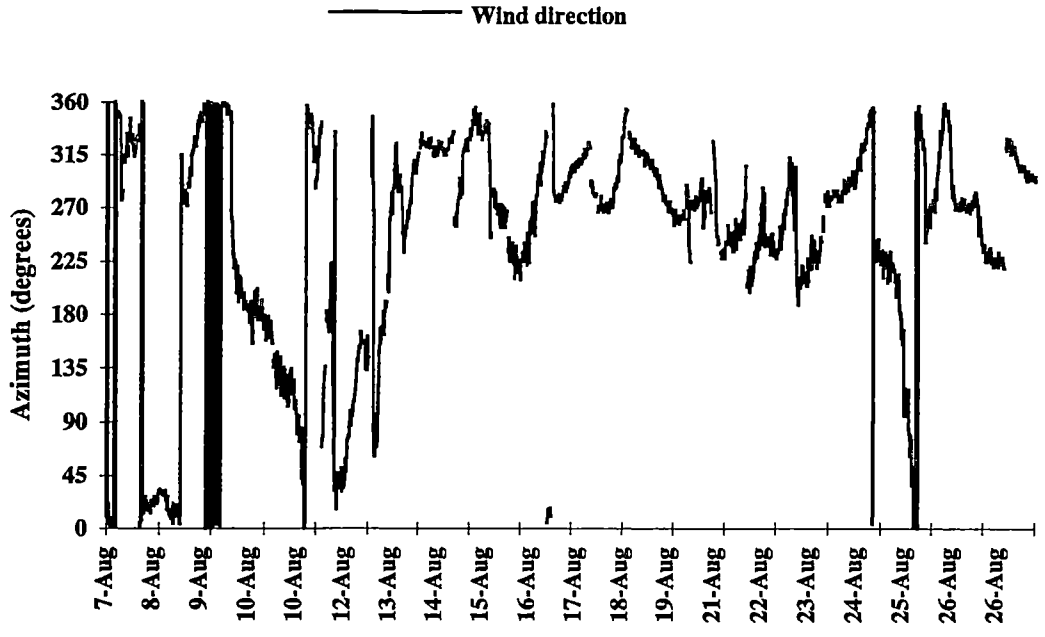
Wind direction
Azimuth (degrees)
360
315
270
225
180
135
90
45
0
7-Aug
8-Aug
9-Aug
10-Aug
10-Aug
12-Aug
13-Aug
14-Aug
15-Aug
16-Aug
17-Aug
18-Aug
19-Aug
21-Aug
22-Aug
23-Aug
24-Aug
25-Aug
26-Aug
26-Aug

A23

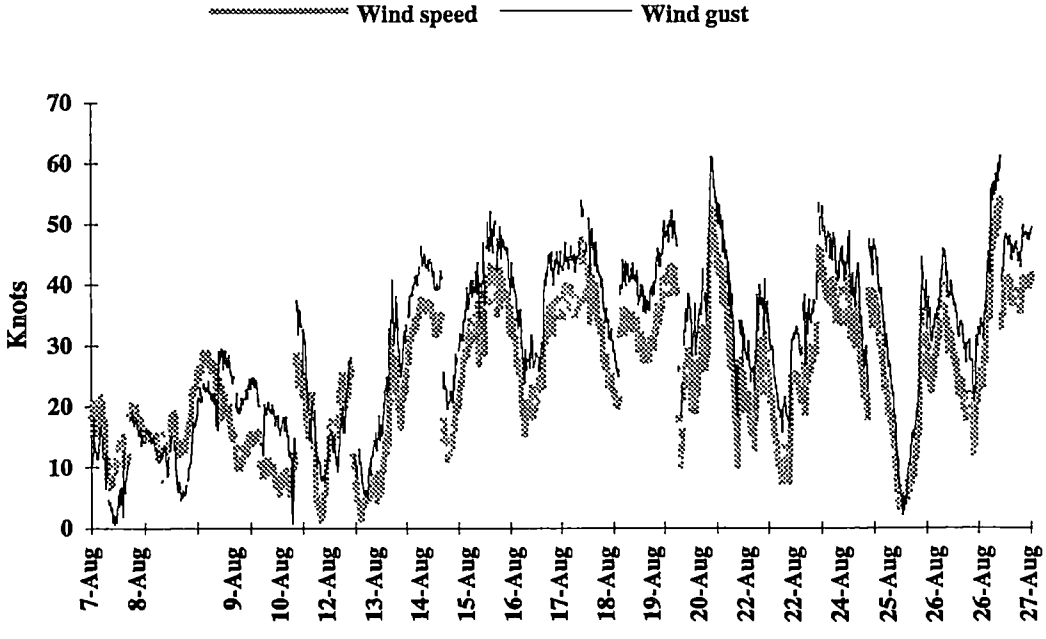
Wind speed
Wind gust
Knots
70
60
50
40
30
20
10
0
7-Aug
8-Aug
9-Aug
10-Aug
12-Aug
13-Aug
14-Aug
15-Aug
16-Aug
17-Aug
18-Aug
19-Aug
20-Aug
22-Aug
22-Aug
24-Aug
25-Aug
26-Aug
26-Aug
27-Aug

A24

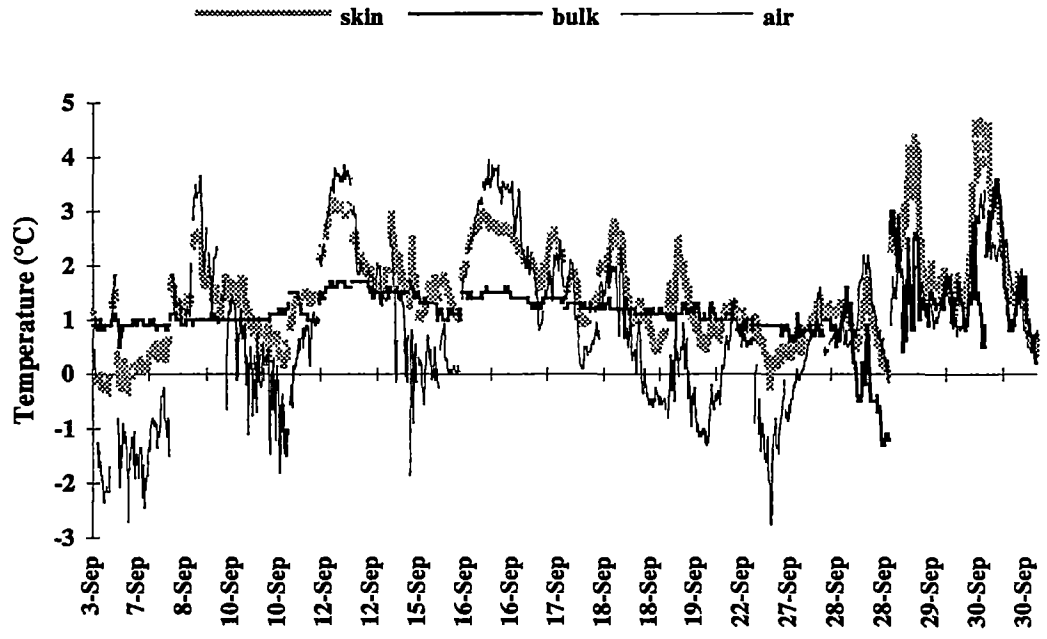
skin
bulk
air
Temperature (°C)
5
4
3
2
1
0
-1
-2
-3
3-Sep
7-Sep
8-Sep
10-Sep
10-Sep
12-Sep
12-Sep
15-Sep
16-Sep
16-Sep
17-Sep
18-Sep
18-Sep
19-Sep
22-Sep
27-Sep
28-Sep
28-Sep
29-Sep
30-Sep
30-Sep

A25

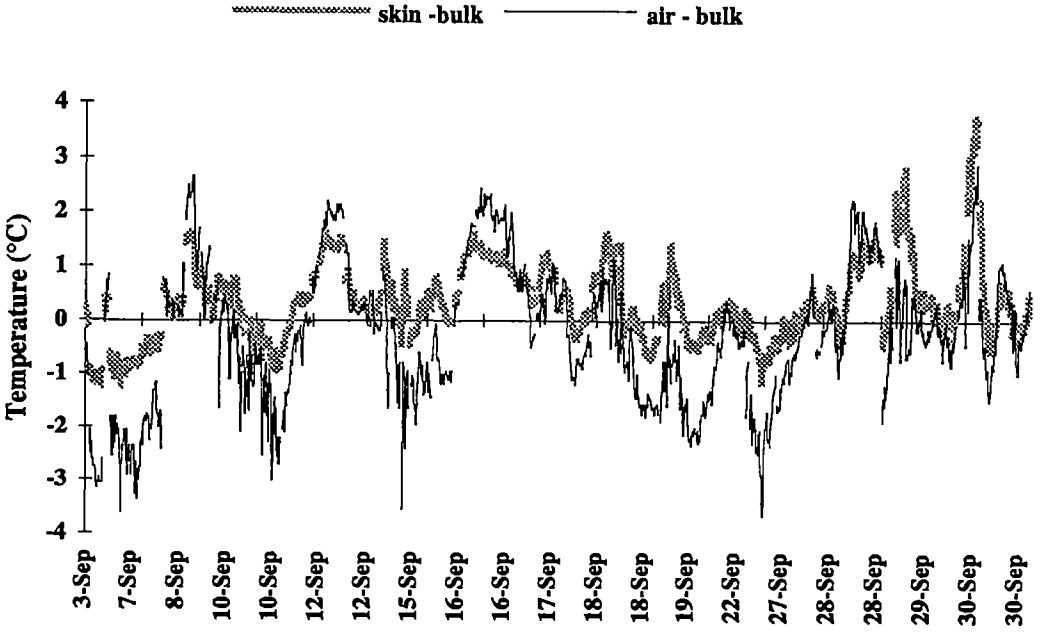
skin -bulk
air - bulk
Temperature (°C)
4
3
2
1
0
-1
-2
-3
-4
3-Sep
7-Sep
8-Sep
10-Sep
10-Sep
12-Sep
12-Sep
15-Sep
16-Sep
16-Sep
17-Sep
18-Sep
18-Sep
19-Sep
22-Sep
27-Sep
28-Sep
28-Sep
29-Sep
30-Sep
30-Sep

A26

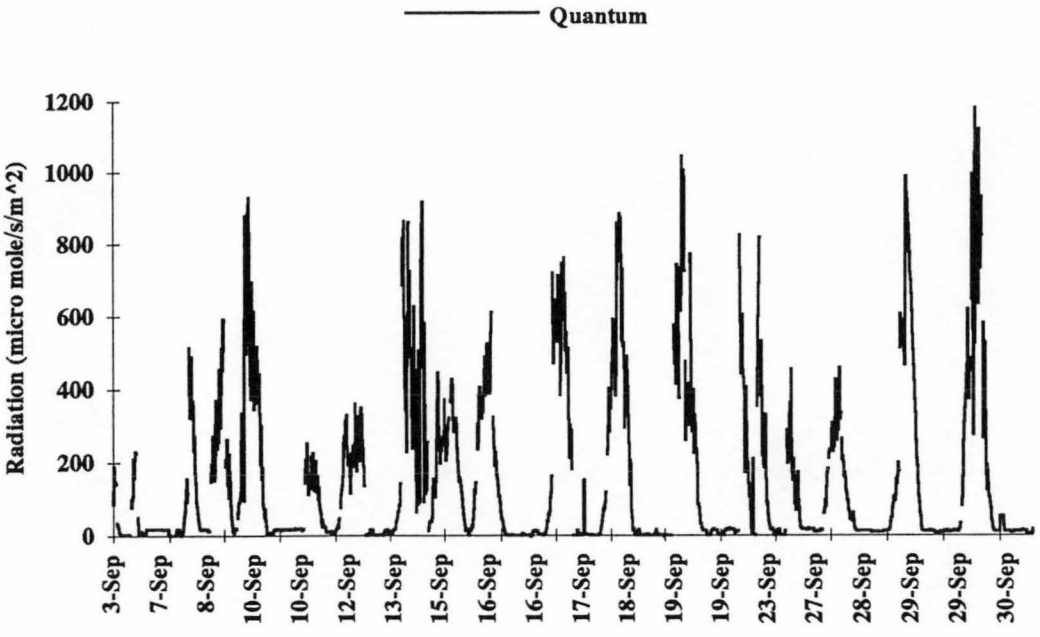
Quantum
Radiation (micro mole/s/m^2)
1200
1000
800
600
400
200
0
3-Sep
7-Sep
8-Sep
10-Sep
10-Sep
12-Sep
13-Sep
15-Sep
16-Sep
16-Sep
17-Sep
18-Sep
19-Sep
19-Sep
23-Sep
27-Sep
28-Sep
29-Sep
29-Sep
30-Sep

A27

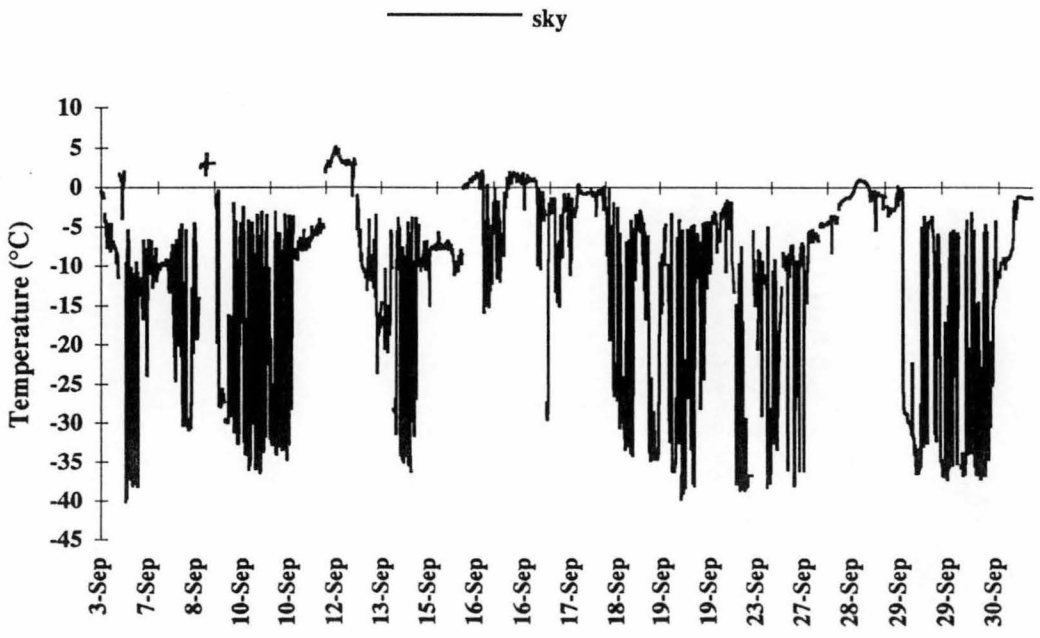
sky
Temperature (°C)
10
5
0
-5
-10
-15
-20
-25
-30
-35
-40
-45
3-Sep
7-Sep
8-Sep
10-Sep
10-Sep
12-Sep
13-Sep
15-Sep
16-Sep
16-Sep
17-Sep
18-Sep
19-Sep
19-Sep
23-Sep
27-Sep
28-Sep
29-Sep
29-Sep
30-Sep

A28

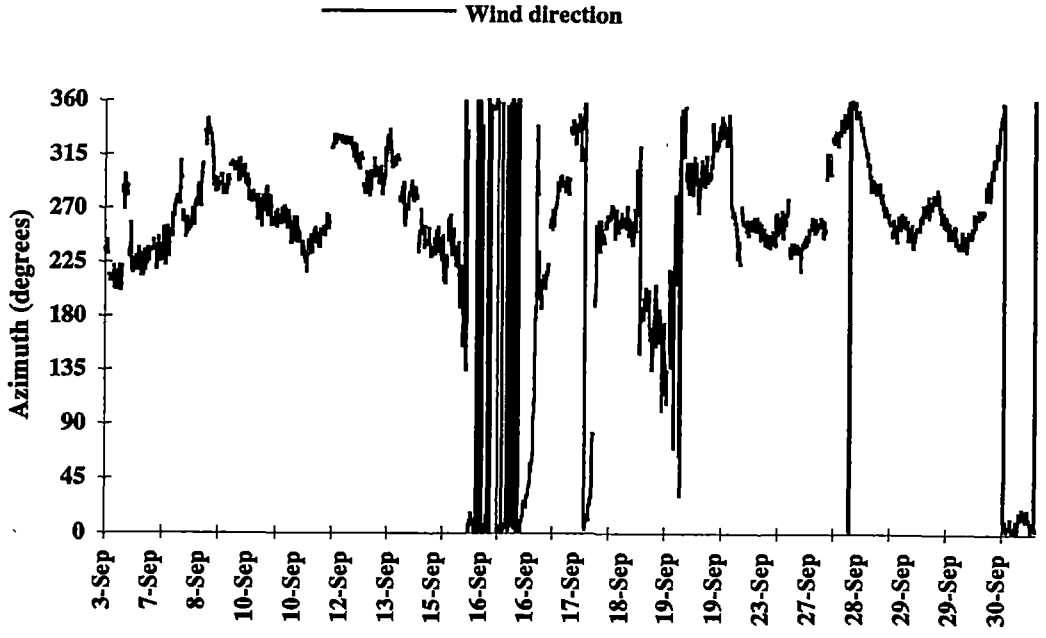
Wind direction
Azimuth (degrees)
360
315
270
225
180
135
90
45
0
3-Sep
7-Sep
8-Sep
10-Sep
10-Sep
12-Sep
13-Sep
15-Sep
16-Sep
16-Sep
17-Sep
18-Sep
19-Sep
19-Sep
23-Sep
27-Sep
28-Sep
29-Sep
29-Sep
30-Sep

A29

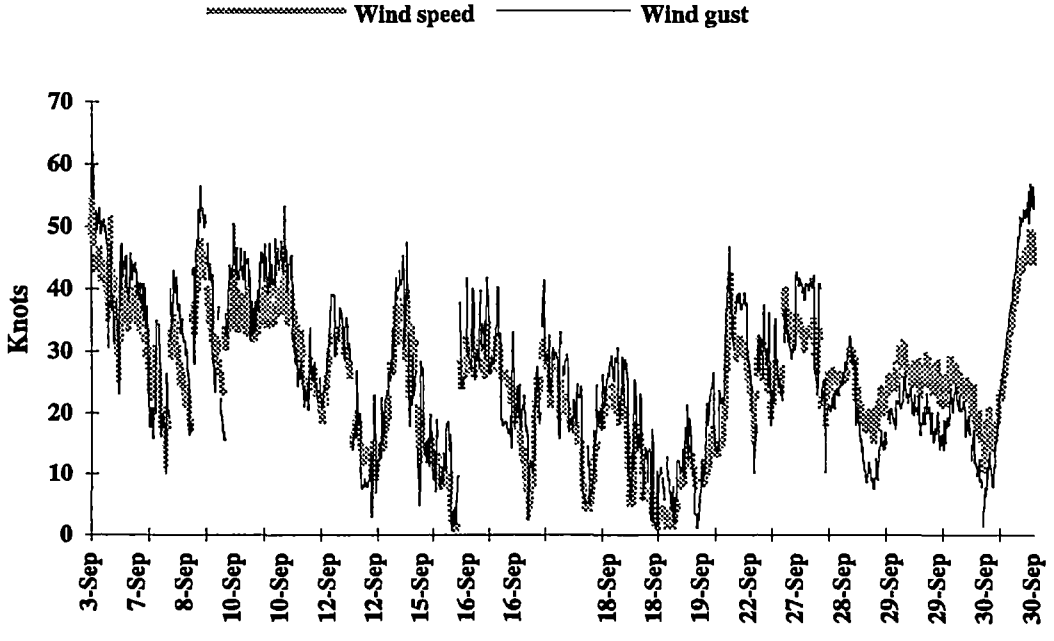
Wind speed
Wind gust
Knots
70
60
50
40
30
20
10
0
3-Sep
7-Sep
8-Sep
10-Sep
10-Sep
12-Sep
12-Sep
15-Sep
16-Sep
16-Sep
18-Sep
18-Sep
19-Sep
22-Sep
27-Sep
28-Sep
29-Sep
29-Sep
30-Sep
30-Sep

A30

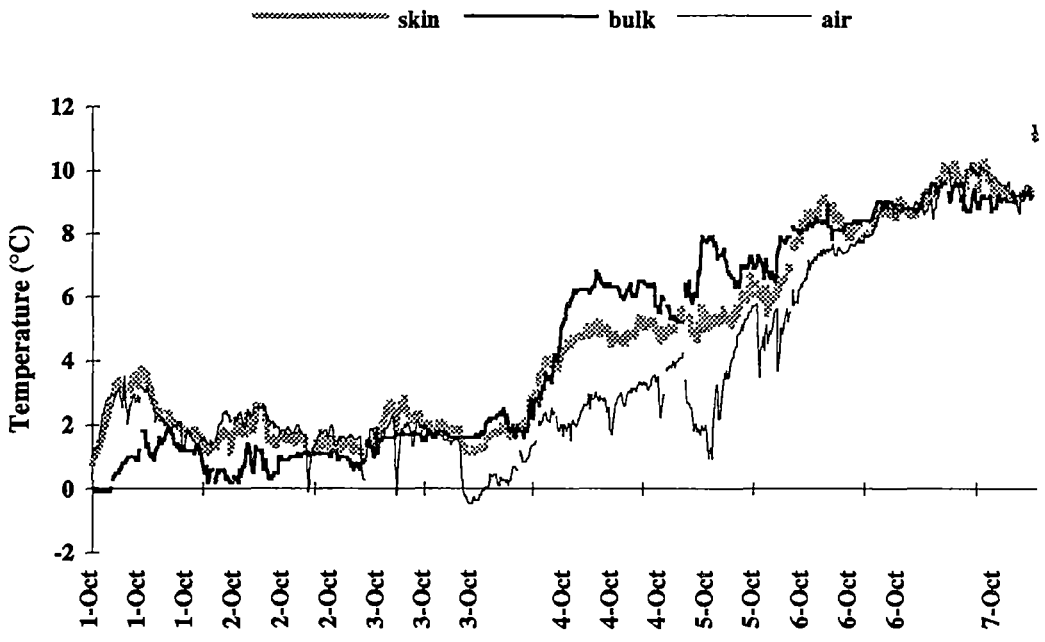
skin
bulk
air
Temperature (°C)
12
10
8
6
4
2
0
-2
1-Oct
1-Oct
1-Oct
2-Oct
2-Oct
2-Oct
3-Oct
3-Oct
3-Oct
4-Oct
4-Oct
4-Oct
5-Oct
5-Oct
6-Oct
6-Oct
6-Oct
7-Oct

A31

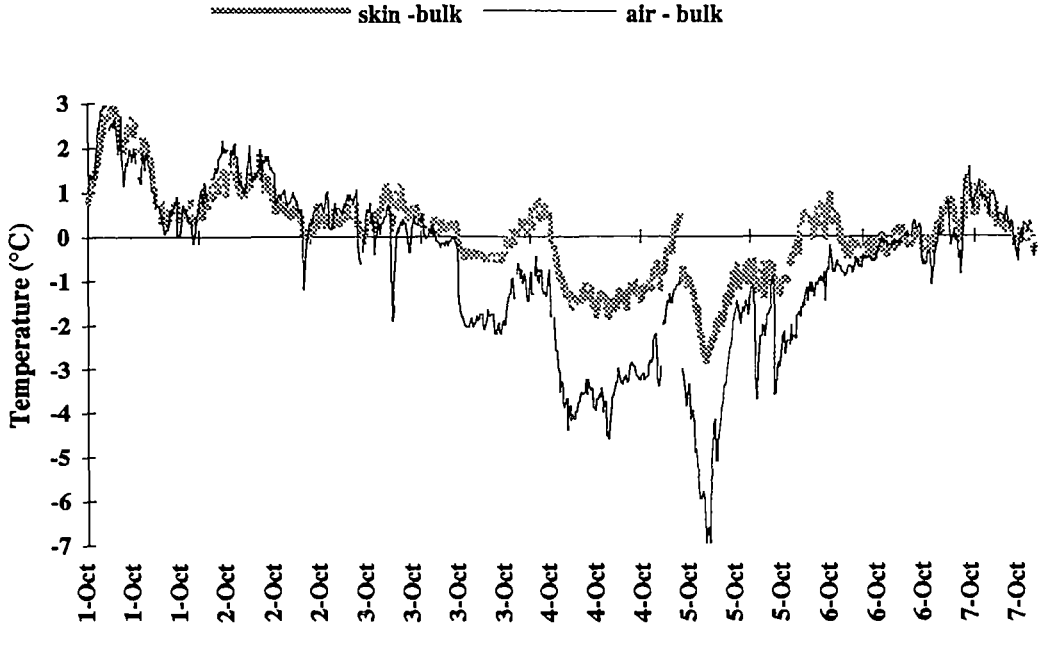
skin -bulk
air - bulk
Temperature (°C)
3
2
1
0
-1
-2
-3
-4
-5
-6
-7
1-Oct
1-Oct
1-Oct
2-Oct
2-Oct
2-Oct
3-Oct
3-Oct
3-Oct
3-Oct
4-Oct
4-Oct
4-Oct
5-Oct
5-Oct
5-Oct
6-Oct
6-Oct
6-Oct
7-Oct
7-Oct

A32

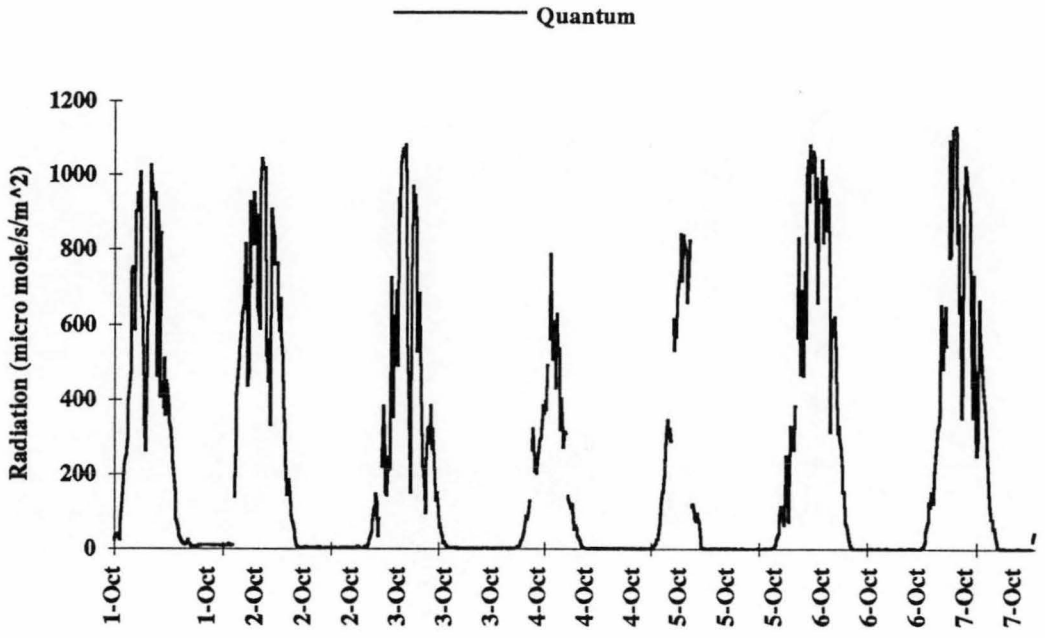
Quantum
Radiation (micro mole/s/m^2)
1200
1000
800
600
400
200
0
1-Oct
1-Oct
2-Oct
2-Oct
2-Oct
3-Oct
3-Oct
3-Oct
4-Oct
4-Oct
4-Oct
5-Oct
5-Oct
5-Oct
6-Oct
6-Oct
6-Oct
7-Oct
7-Oct

A33

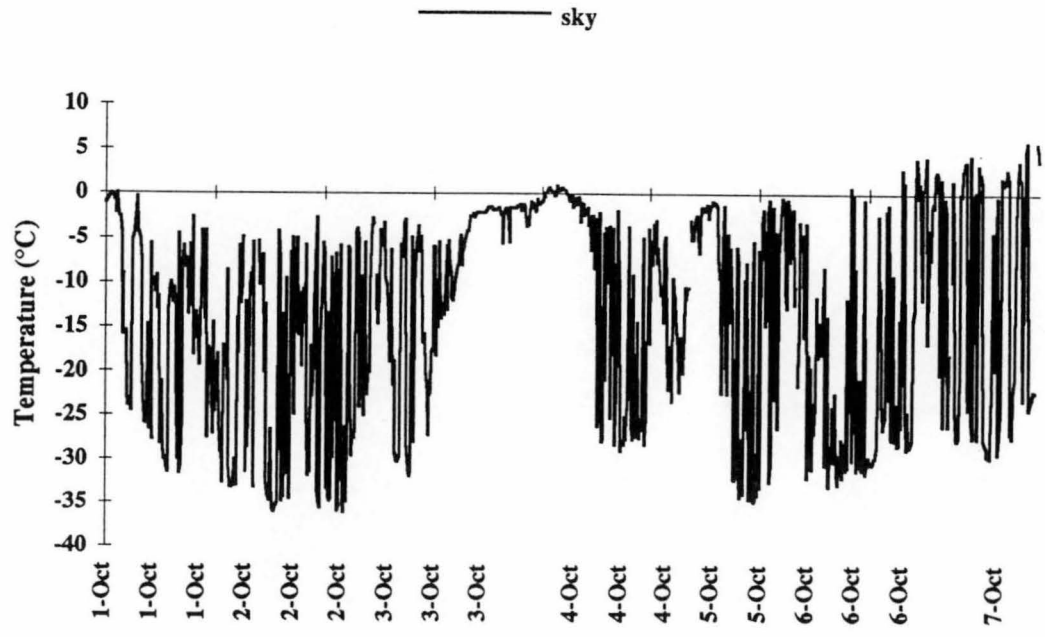
sky
Temperature (°C)
10
5
0
-5
-10
-15
-20
-25
-30
-35
-40
1-Oct
1-Oct
1-Oct
2-Oct
2-Oct
2-Oct
3-Oct
3-Oct
3-Oct
4-Oct
4-Oct
4-Oct
5-Oct
5-Oct
6-Oct
6-Oct
6-Oct
7-Oct

A34

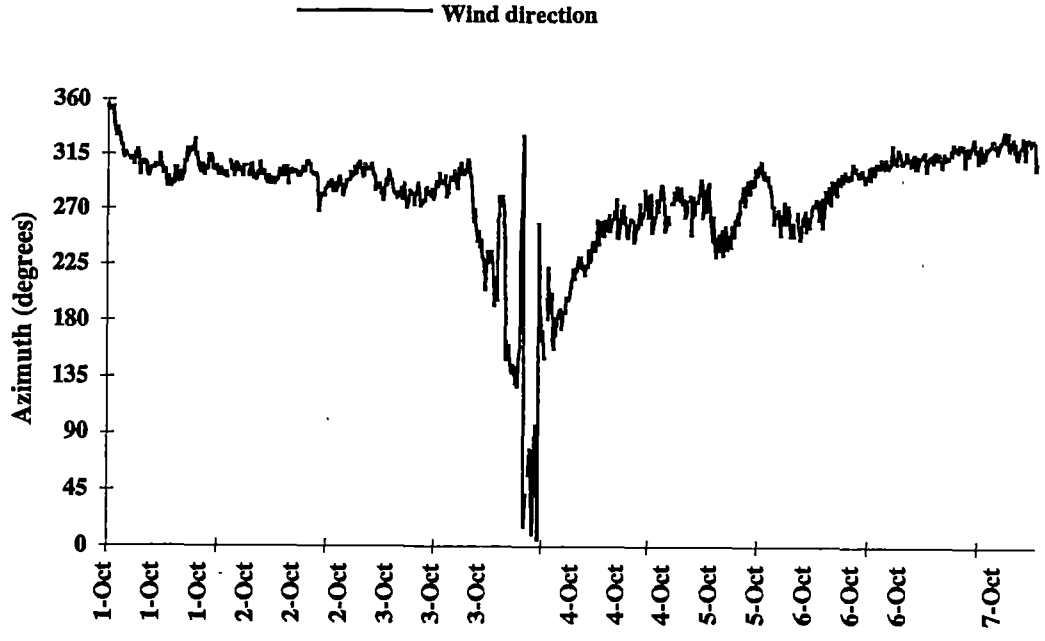
Wind direction
Azimuth (degrees)
360
315
270
225
180
135
90
45
0
1-Oct
1-Oct
1-Oct
2-Oct
2-Oct
2-Oct
3-Oct
3-Oct
3-Oct
4-Oct
4-Oct
4-Oct
5-Oct
5-Oct
6-Oct
6-Oct
6-Oct
7-Oct

A35

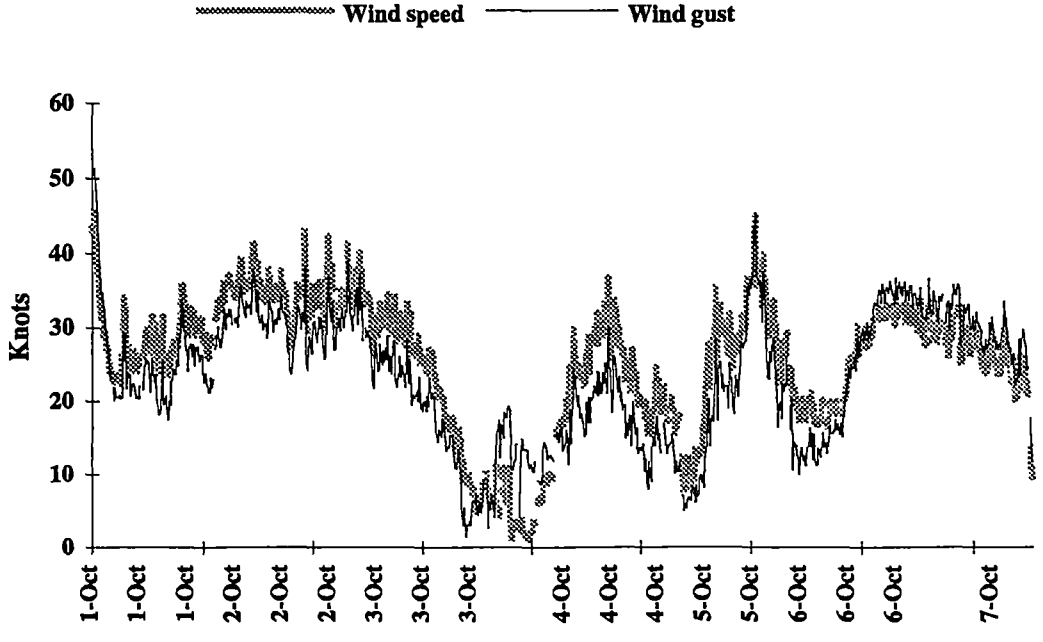
Wind speed
Wind gust
Knots
60
50
40
30
20
10
0
1-Oct
1-Oct
1-Oct
2-Oct
2-Oct
2-Oct
3-Oct
3-Oct
3-Oct
4-Oct
4-Oct
4-Oct
5-Oct
5-Oct
6-Oct
6-Oct
6-Oct
7-Oct

A36

APPENDIX B1: The Monthly Histograms of ΔT.

JAN 1-15

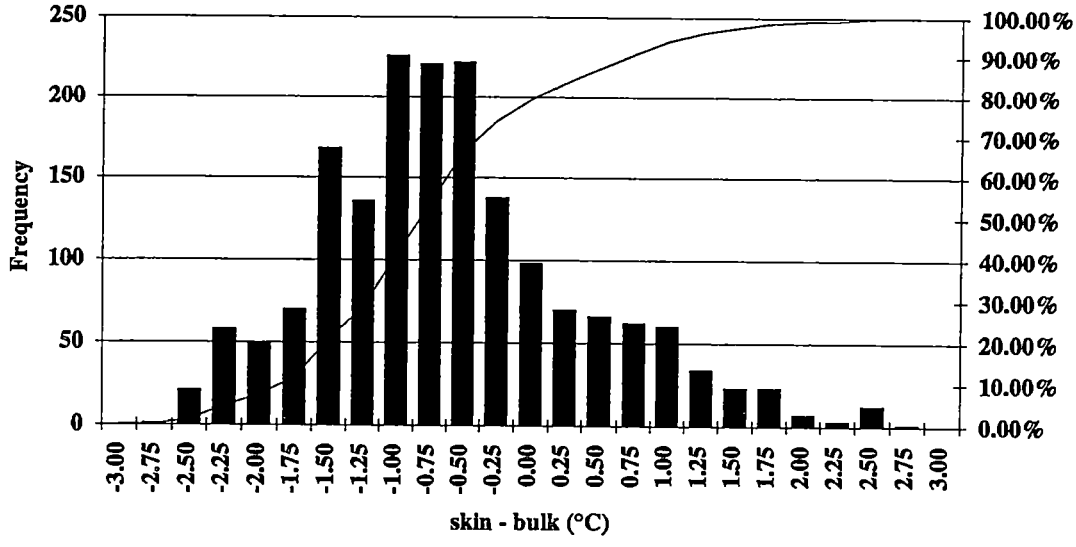

B1.1

JAN 22-29

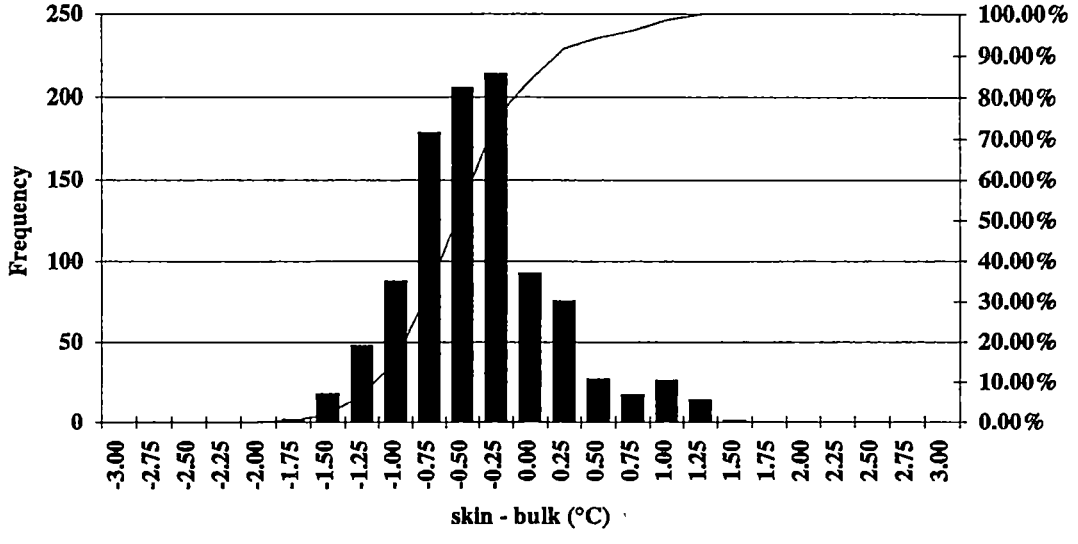

B1.2

FEB

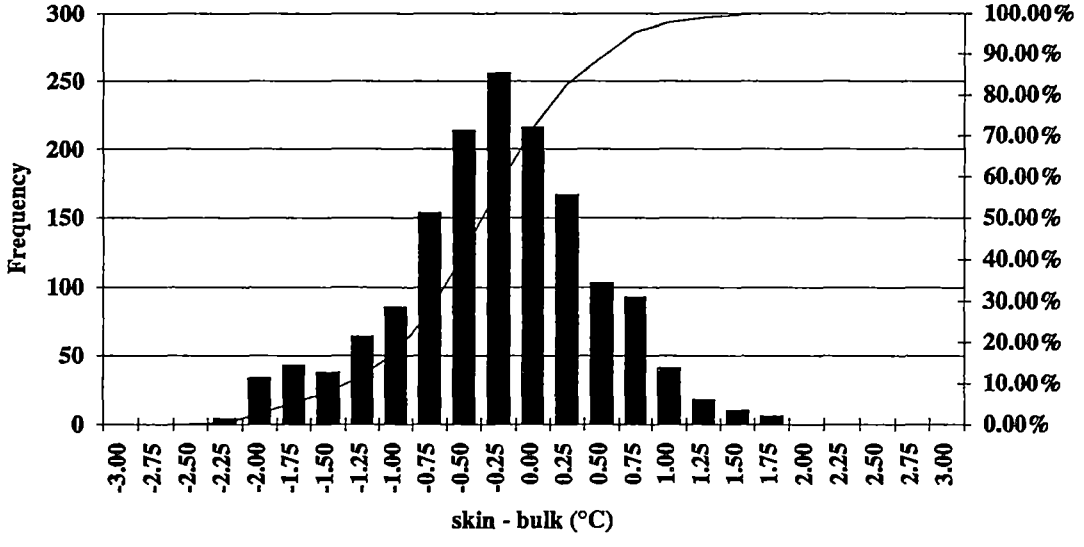

B1.3

AUG

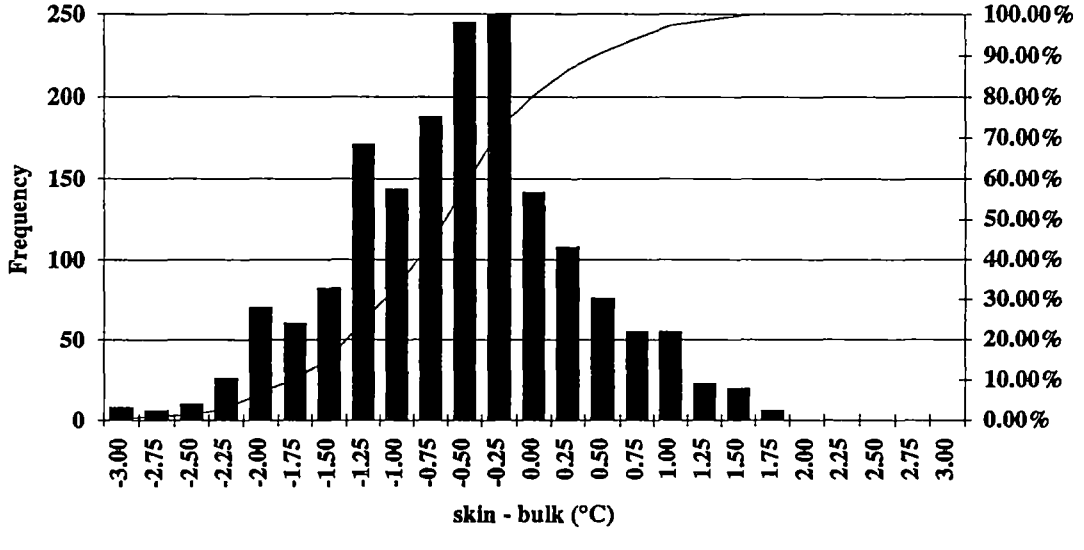

B1.4

SEP

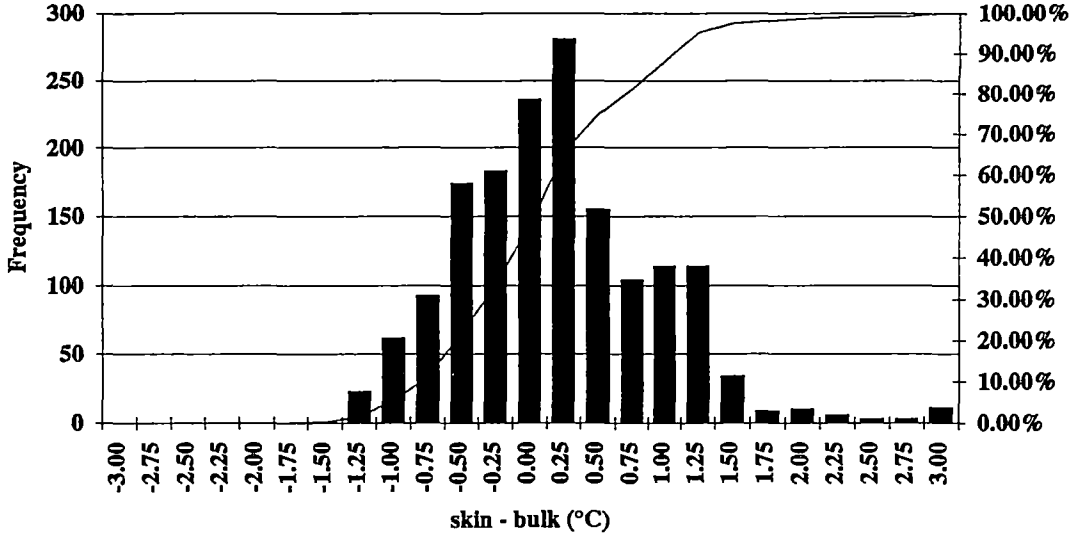

B1.5

OCT 1-7

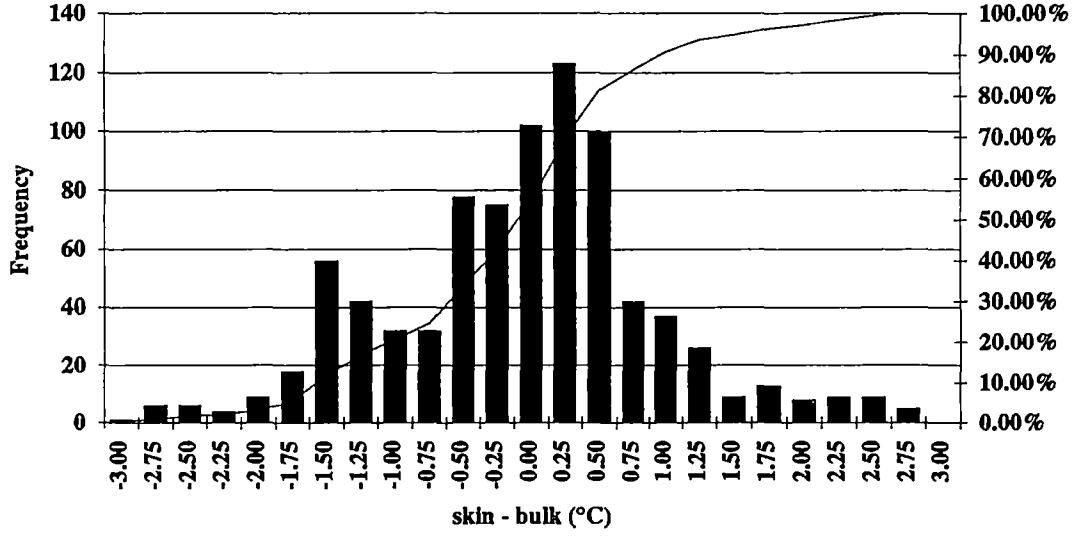

B1.6

APPENDIX B2: The Histograms for Voyage 7 (SHAM).

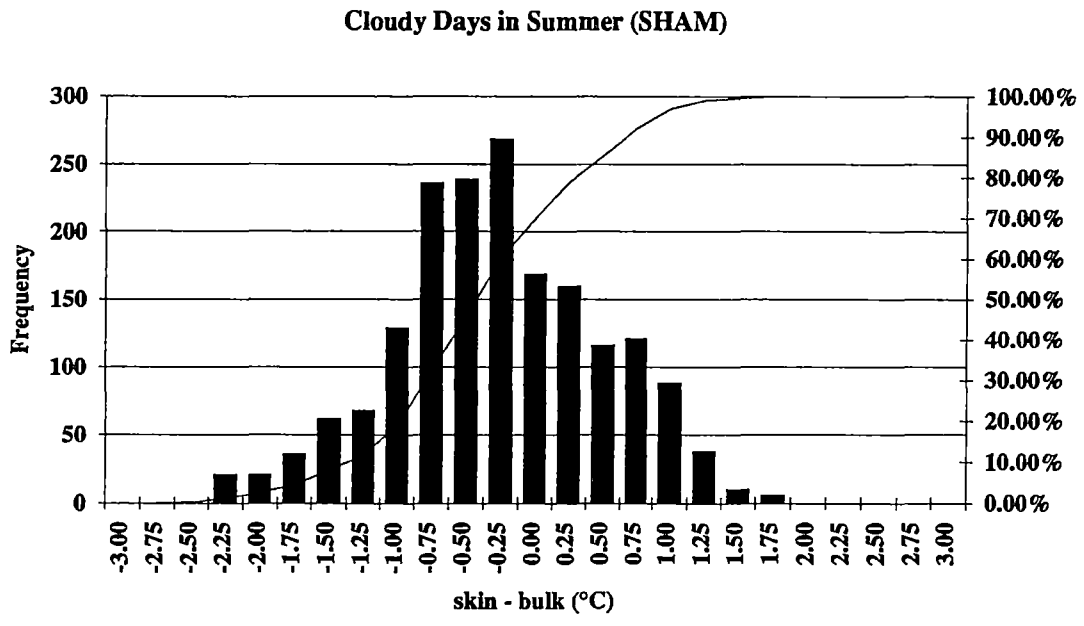

B2.1

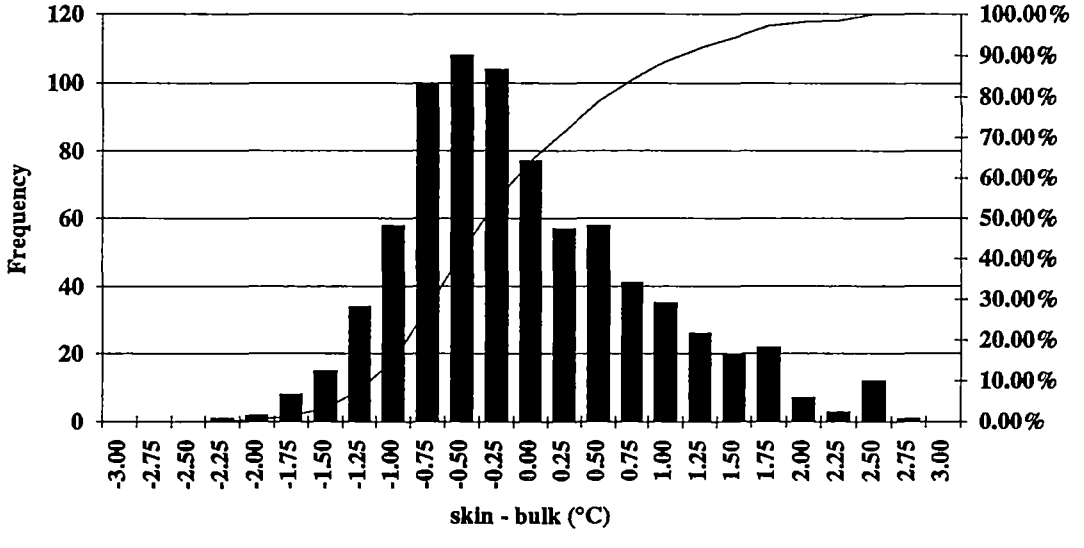

B2.2

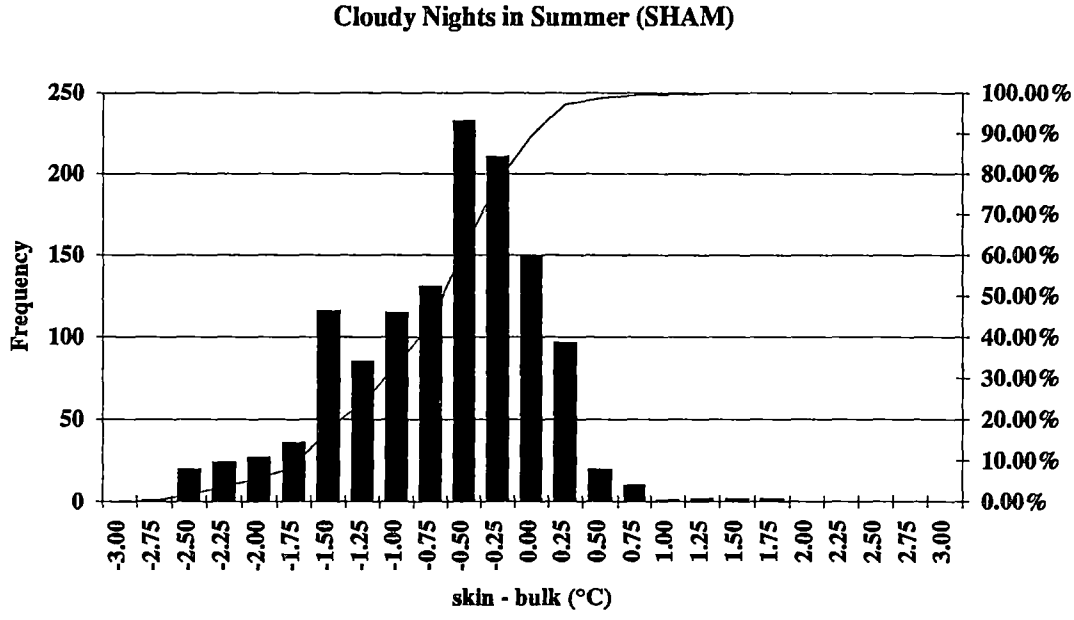
Cloudy Nights in Summer (SHAM)
Frequency
250
200
150
100
50
0
100.00%
90.00%
80.00%
70.00%
60.00%
50.00%
40.00%
30.00%
20.00%
10.00%
0.00%
-3.00
-2.75
-2.50
-2.25
-2.00
-1.75
-1.50
-1.25
-1.00
-0.75
-0.50
-0.25
0.00
0.25
0.50
0.75
1.00
1.25
1.50
1.75
2.00
2.25
2.50
2.75
3.00
skin - bulk (°C)

B2.3

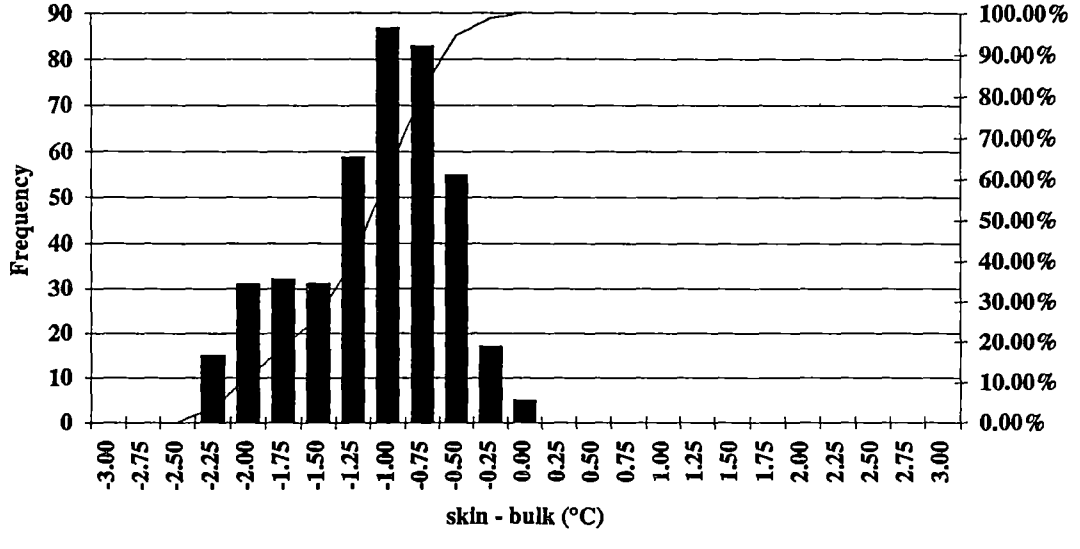
Clear Nights in Summer (SHAM)
Frequency
90
80
70
60
50
40
30
20
10
0
100.00%
90.00%
80.00%
70.00%
60.00%
50.00%
40.00%
30.00%
20.00%
10.00%
0.00%
-3.00
-2.75
-2.50
-2.25
-2.00
-1.75
-1.50
-1.25
-1.00
-0.75
-0.50
-0.25
0.00
0.25
0.50
0.75
1.00
1.25
1.50
1.75
2.00
2.25
2.50
2.75
3.00
skin - bulk (°C)

B2.4

APPENDIX B3: The Histograms for Voyage 1 (THIRST).

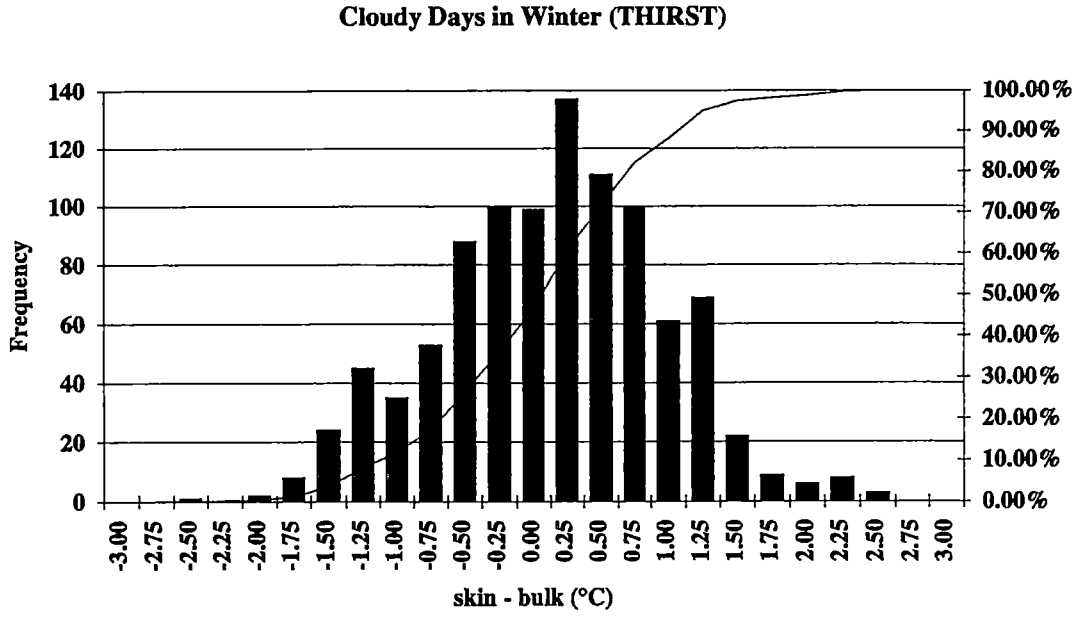

B3.1

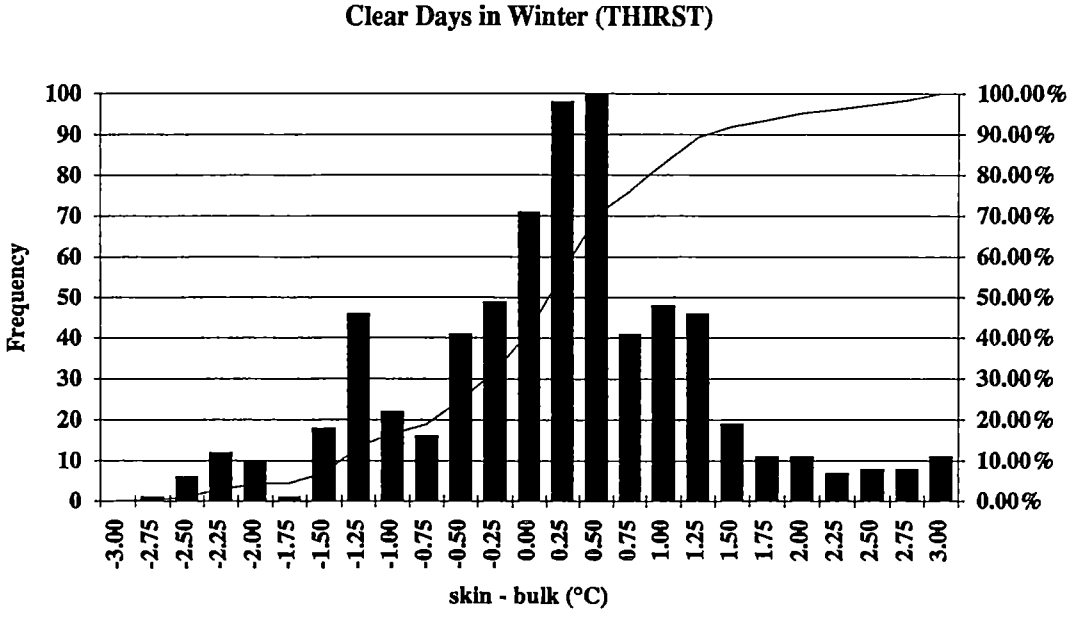

B3.2

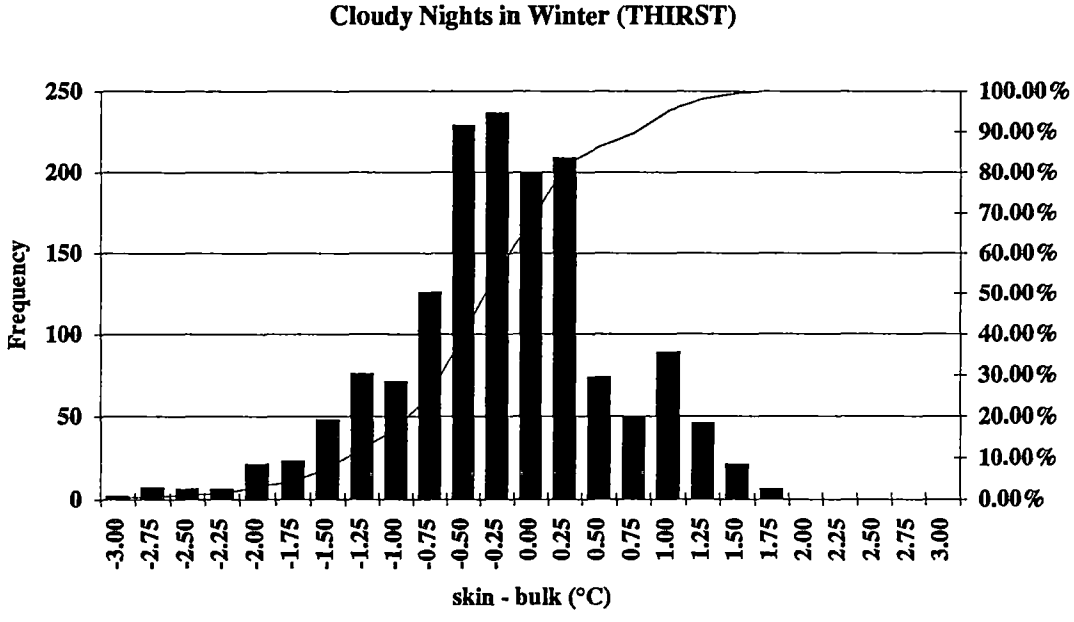
Cloudy Nights in Winter (THIRST)
Frequency
250
200
150
100
50
0
100.00%
90.00%
80.00%
70.00%
60.00%
50.00%
40.00%
30.00%
20.00%
10.00%
0.00%
-3.00
-2.75
-2.50
-2.25
-2.00
-1.75
-1.50
-1.25
-1.00
-0.75
-0.50
-0.25
0.00
0.25
0.50
0.75
1.00
1.25
1.50
1.75
2.00
2.25
2.50
2.75
3.00
skin - bulk (°C)

B3.3

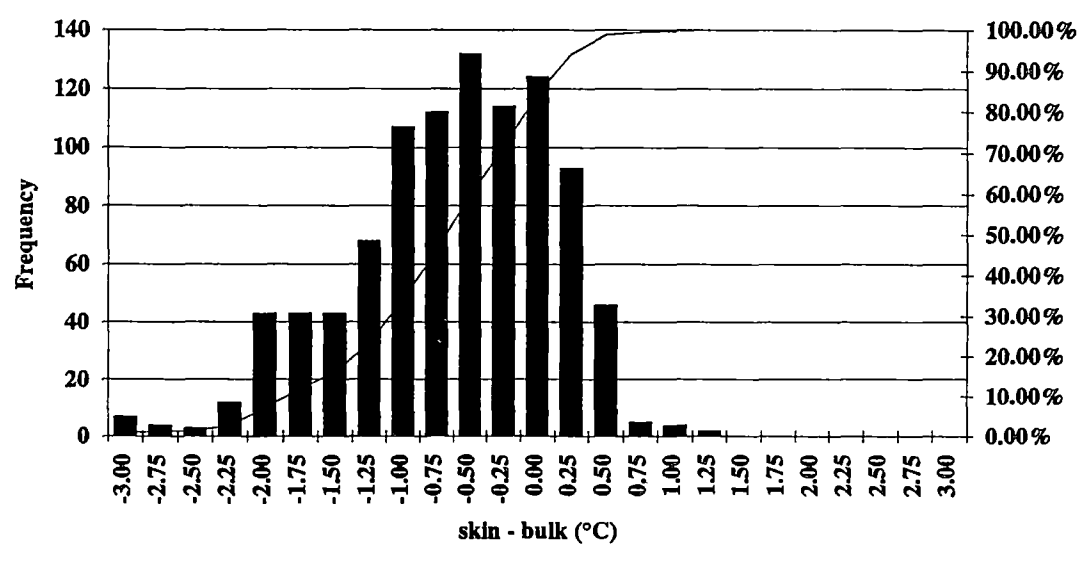
Clear Nights in Winter (THIRST)
Frequency
140
120
100
80
60
40
20
0
100.00%
90.00%
80.00%
70.00%
60.00%
50.00%
40.00%
30.00%
20.00%
10.00%
0.00%
-3.00
-2.75
-2.50
-2.25
-2.00
-1.75
-1.50
-1.25
-1.00
-0.75
-0.50
-0.25
0.00
0.25
0.50
0.75
1.00
1.25
1.50
1.75
2.00
2.25
2.50
2.75
3.00
skin - bulk (°C)

B3.4

APPENDIX C: The Scatter plots and Regression between ΔT and ΔT_{ab} for SHAM and THIRST.

Cloudy Days (JAN 1-15)

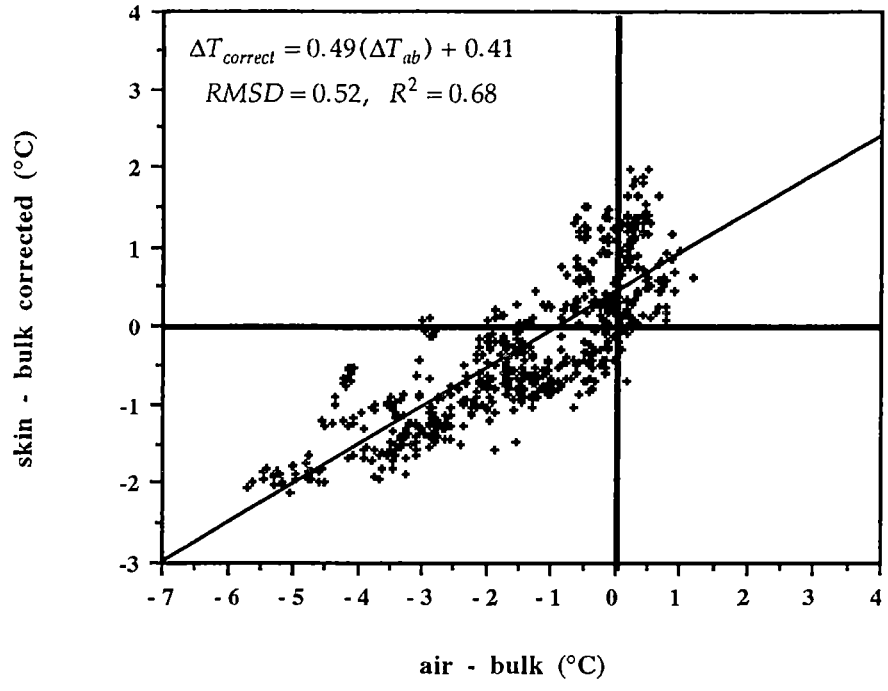

C1

Clear Days (JAN 1-15)

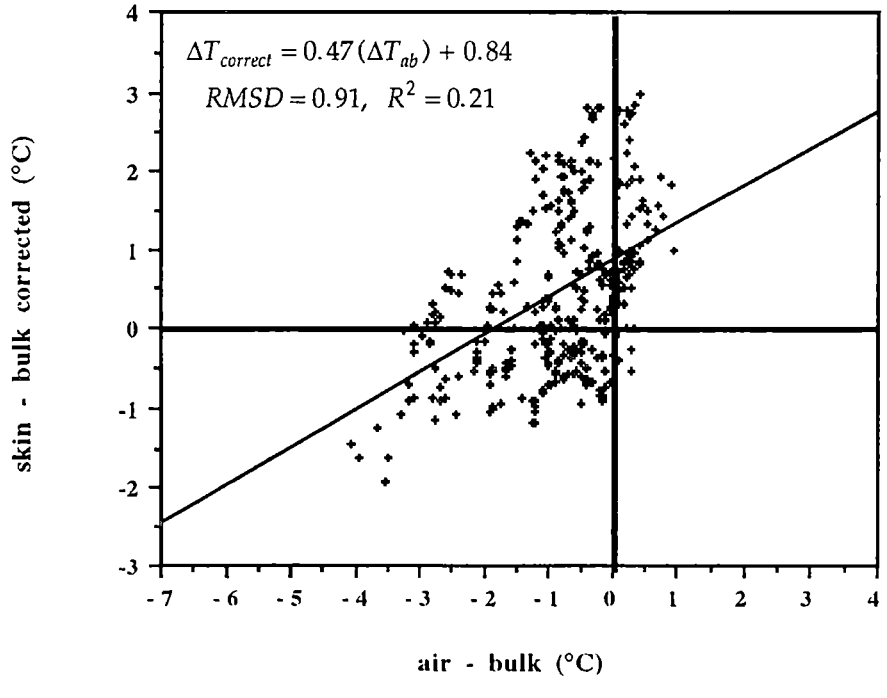

C2

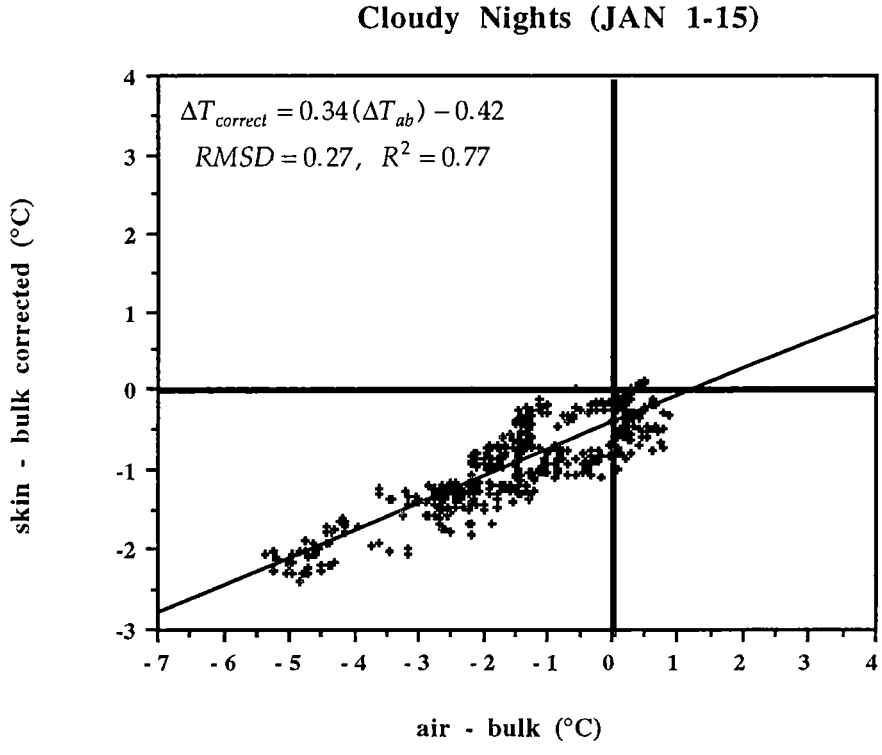
Cloudy Nights (JAN 1-15)
$\Delta T_{correct} = 0.34(\Delta T_{ab}) - 0.42$
$RMSD = 0.27,\ R^2 = 0.77$
skin - bulk corrected (°C)
air - bulk (°C)
4
3
2
1
0
-1
-2
-3
-7 -6 -5 -4 -3 -2 -1 0 1 2 3 4

C3

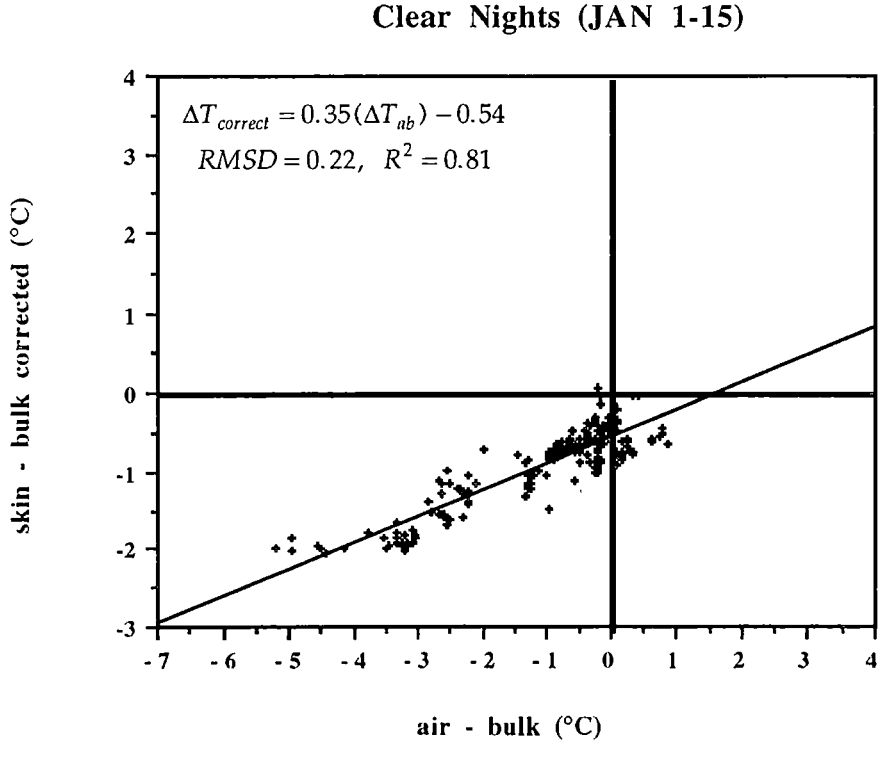
Clear Nights (JAN 1-15)
$\Delta T_{correct} = 0.35(\Delta T_{ab}) - 0.54$
$RMSD = 0.22,\ R^2 = 0.81$
skin - bulk corrected (°C)
air - bulk (°C)
4
3
2
1
0
-1
-2
-3
-7 -6 -5 -4 -3 -2 -1 0 1 2 3 4

C4

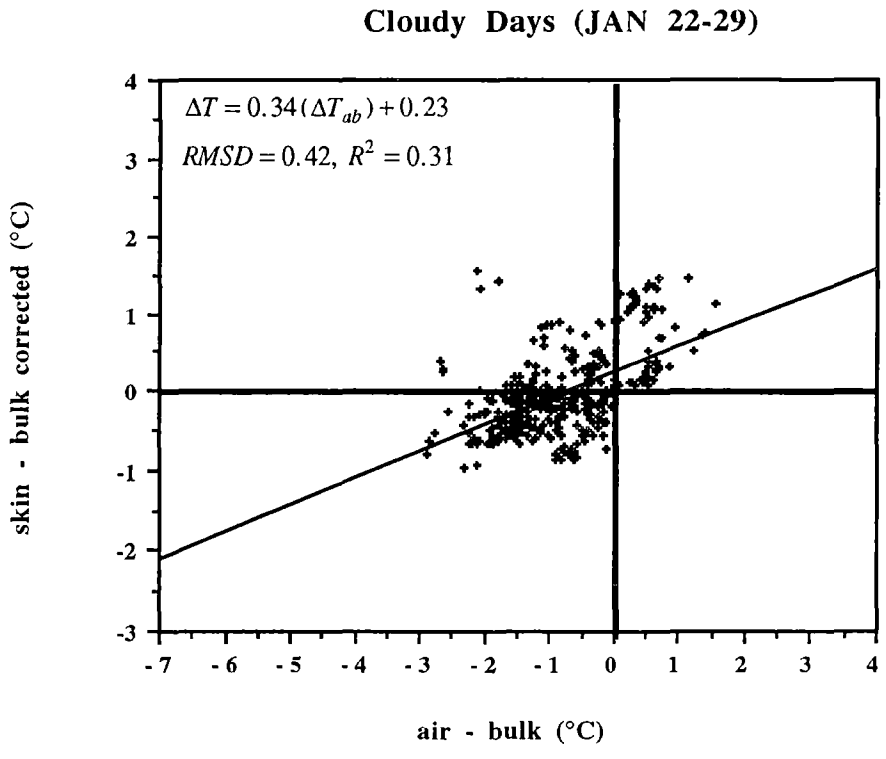
Cloudy Days (JAN 22-29)
$\Delta T = 0.34(\Delta T_{ab}) + 0.23$
$RMSD = 0.42,\ R^2 = 0.31$
skin - bulk corrected (°C)
air - bulk (°C)
4
3
2
1
0
-1
-2
-3
-7 -6 -5 -4 -3 -2 -1 0 1 2 3 4

C5

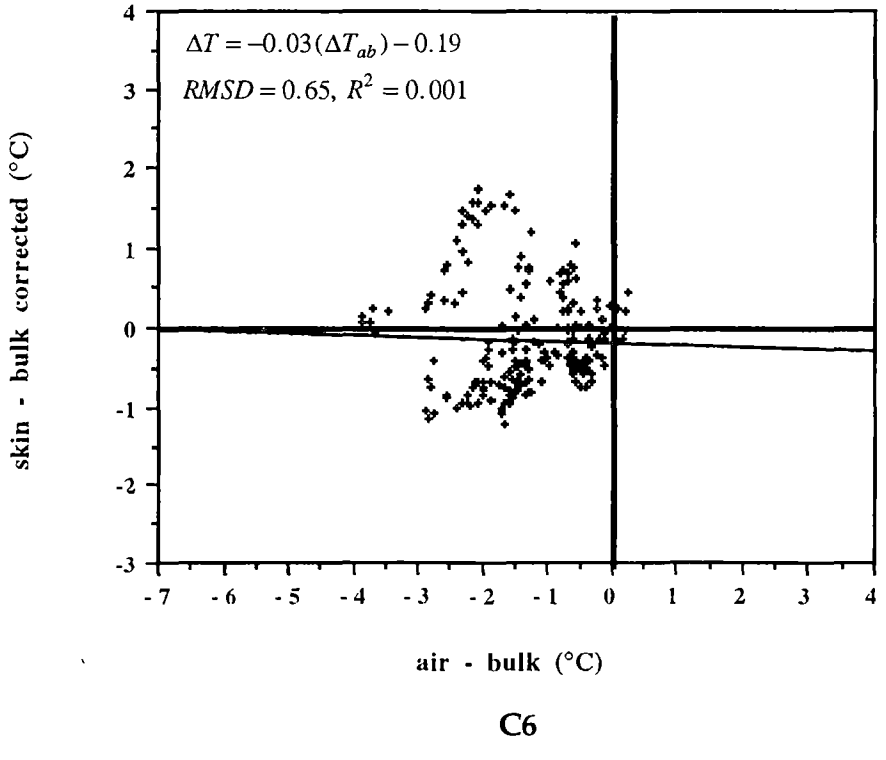
Clear Days (JAN 22-29)
$\Delta T = -0.03(\Delta T_{ab}) - 0.19$
$RMSD = 0.65,\ R^2 = 0.001$
skin - bulk corrected (°C)
air - bulk (°C)
4
3
2
1
0
-1
-2
-3
-7 -6 -5 -4 -3 -2 -1 0 1 2 3 4

C6

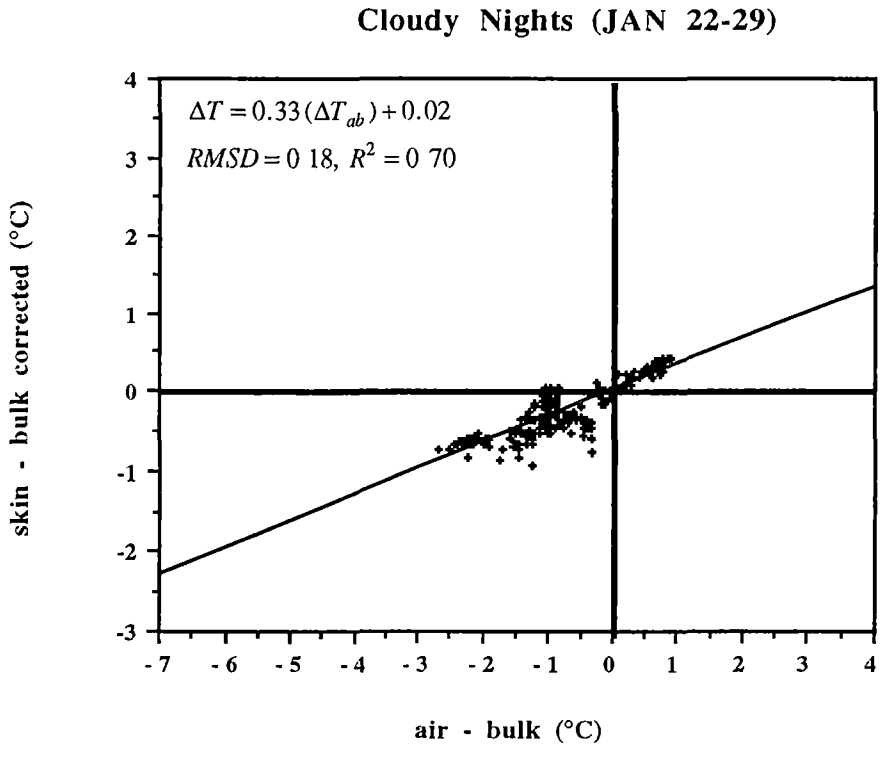
Cloudy Nights (JAN 22-29)
$\Delta T = 0.33(\Delta T_{ab}) + 0.02$
$RMSD = 0\ 18,\ R^2 = 0\ 70$
skin - bulk corrected (°C)
air - bulk (°C)
4
3
2
1
0
-1
-2
-3
-7 -6 -5 -4 -3 -2 -1 0 1 2 3 4

C7

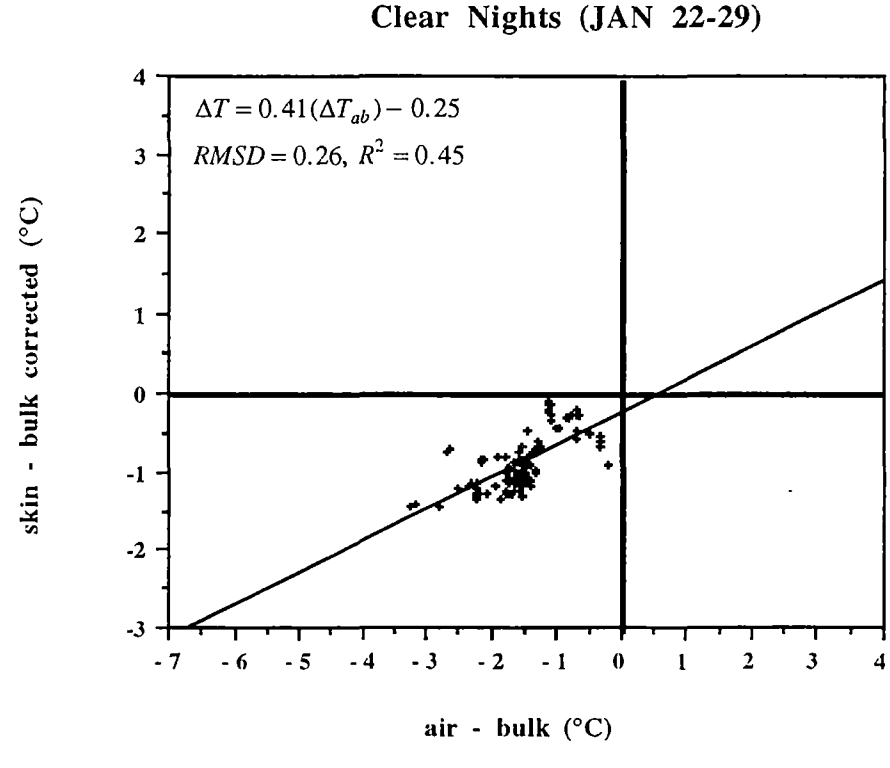
Clear Nights (JAN 22-29)
$\Delta T = 0.41(\Delta T_{ab}) - 0.25$
$RMSD = 0.26,\ R^2 = 0.45$
skin - bulk corrected (°C)
air - bulk (°C)
4
3
2
1
0
-1
-2
-3
-7 -6 -5 -4 -3 -2 -1 0 1 2 3 4

C8

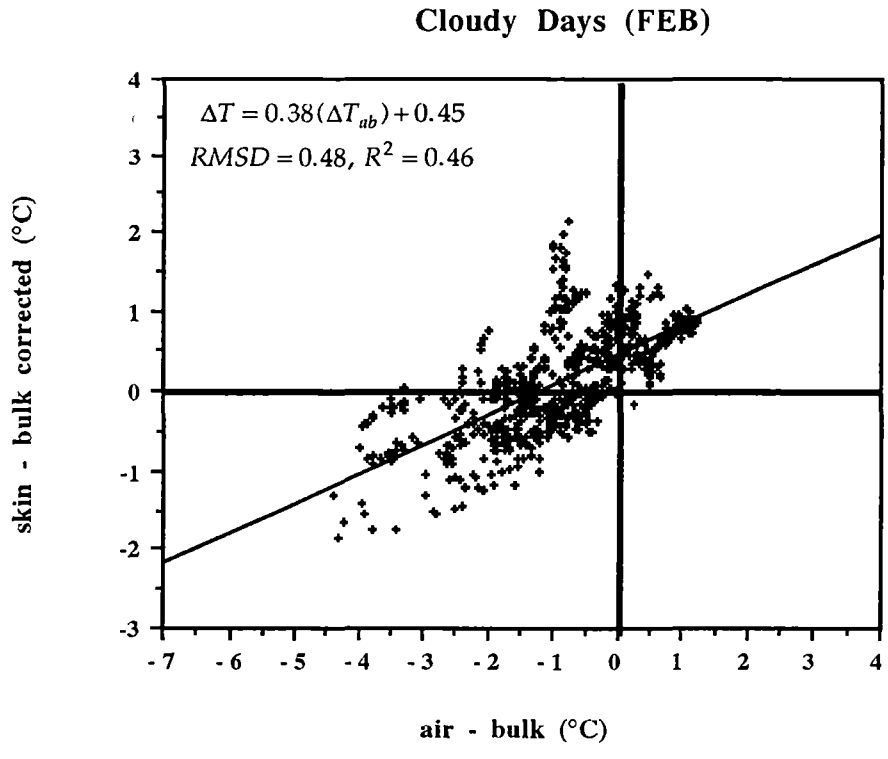
Cloudy Days (FEB)
$\Delta T = 0.38(\Delta T_{ab}) + 0.45$
$RMSD = 0.48,\ R^2 = 0.46$
skin - bulk corrected (°C)
air - bulk (°C)
4
3
2
1
0
-1
-2
-3
-7 -6 -5 -4 -3 -2 -1 0 1 2 3 4

C9

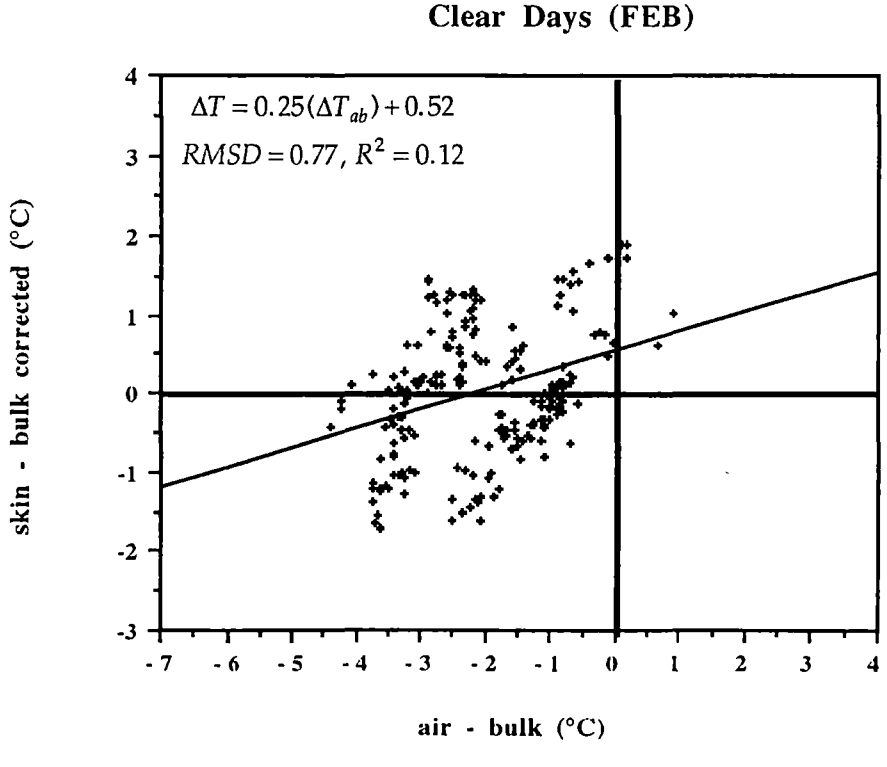
Clear Days (FEB)
$\Delta T = 0.25(\Delta T_{ab}) + 0.52$
$RMSD = 0.77,\ R^2 = 0.12$
skin - bulk corrected (°C)
air - bulk (°C)
4
3
2
1
0
-1
-2
-3
-7 -6 -5 -4 -3 -2 -1 0 1 2 3 4

C10

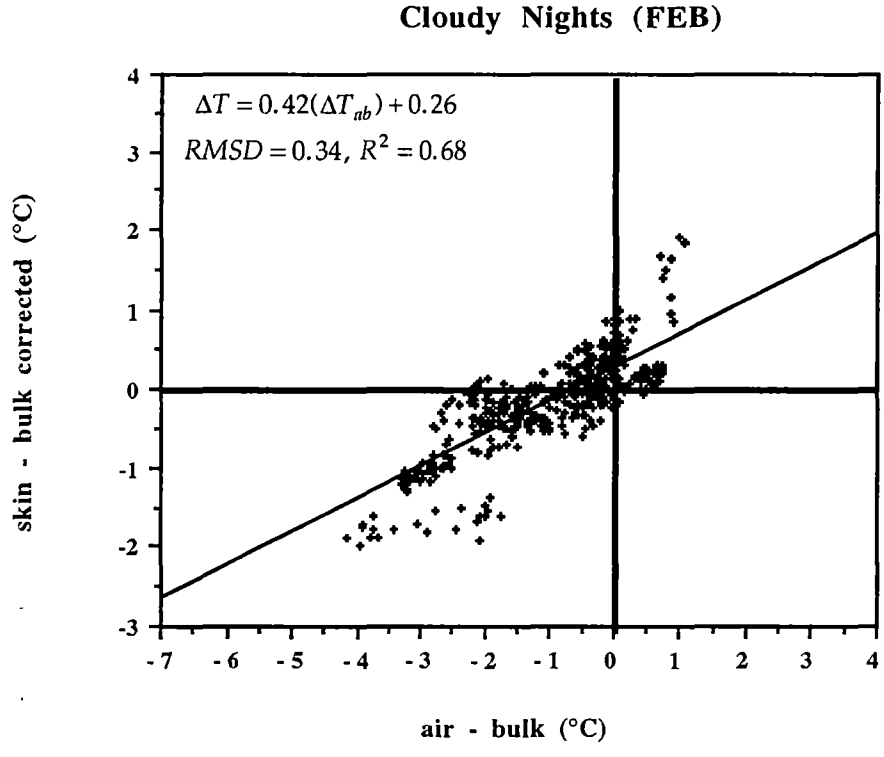
Cloudy Nights (FEB)
$\Delta T = 0.42(\Delta T_{ab}) + 0.26$
$RMSD = 0.34,\ R^2 = 0.68$
skin - bulk corrected (°C)
air - bulk (°C)
4
3
2
1
0
-1
-2
-3
-7 -6 -5 -4 -3 -2 -1 0 1 2 3 4

C11

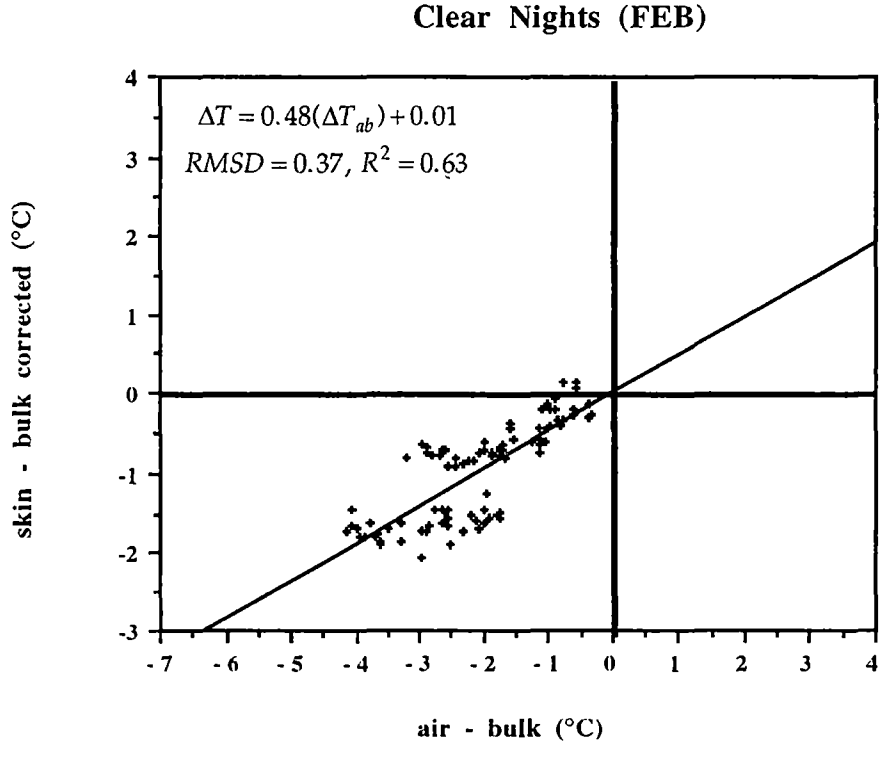
Clear Nights (FEB)
$\Delta T = 0.48(\Delta T_{ab}) + 0.01$
$RMSD = 0.37,\ R^2 = 0.63$
skin - bulk corrected (°C)
air - bulk (°C)
4
3
2
1
0
-1
-2
-3
-7 -6 -5 -4 -3 -2 -1 0 1 2 3 4

C12

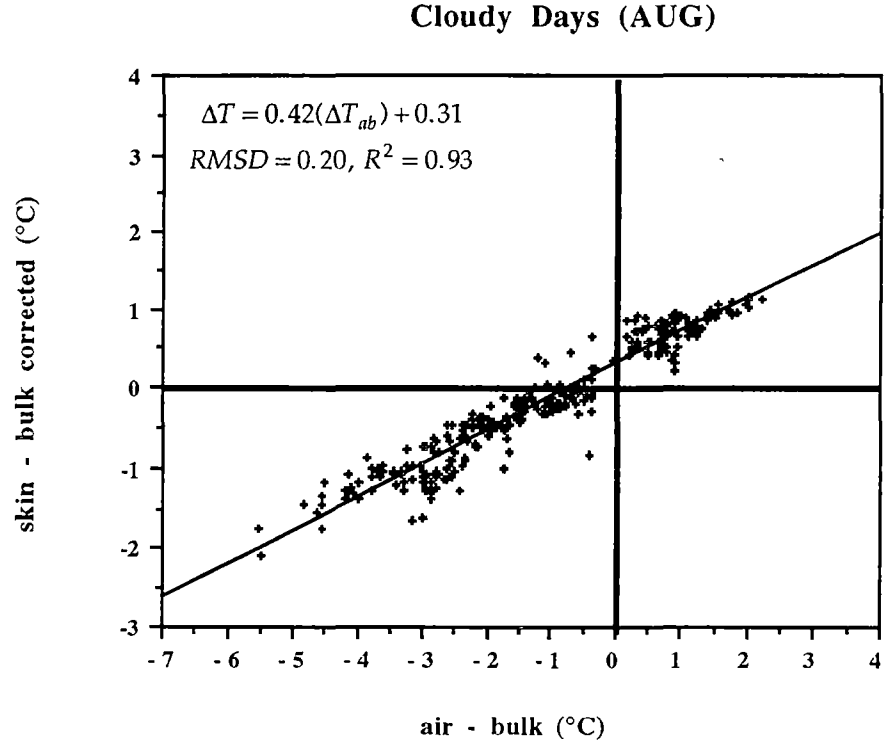
Cloudy Days (AUG)
$\Delta T = 0.42(\Delta T_{ab}) + 0.31$
$RMSD = 0.20,\ R^2 = 0.93$
skin - bulk corrected (°C)
air - bulk (°C)
4
3
2
1
0
-1
-2
-3
-7
-6
-5
-4
-3
-2
-1
0
1
2
3
4

C13

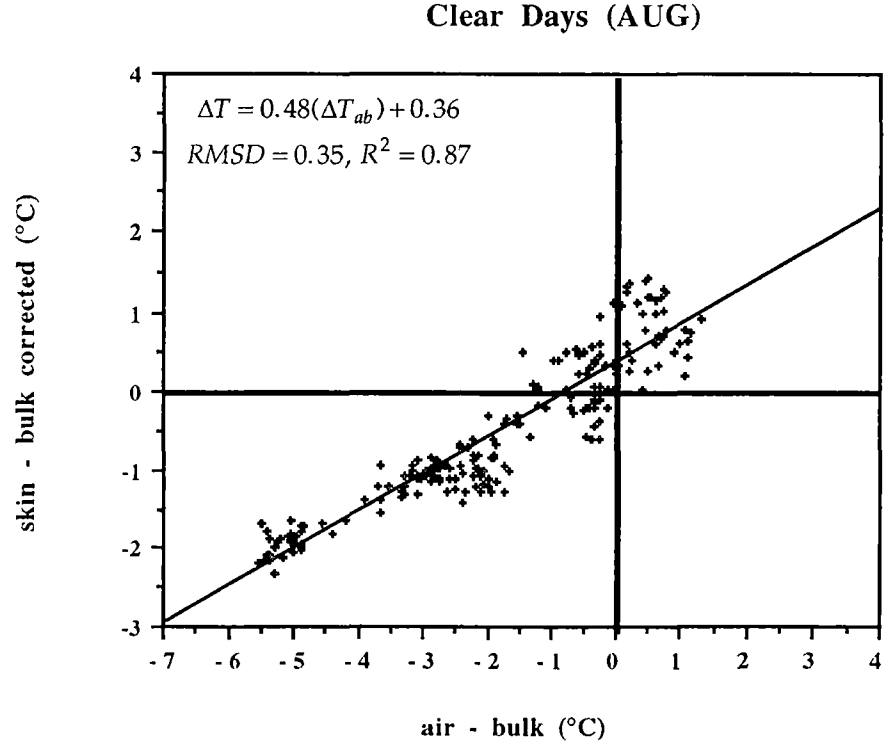
Clear Days (AUG)
$\Delta T = 0.48(\Delta T_{ab}) + 0.36$
$RMSD = 0.35,\ R^2 = 0.87$
skin - bulk corrected (°C)
air - bulk (°C)
4
3
2
1
0
-1
-2
-3
-7
-6
-5
-4
-3
-2
-1
0
1
2
3
4

C14

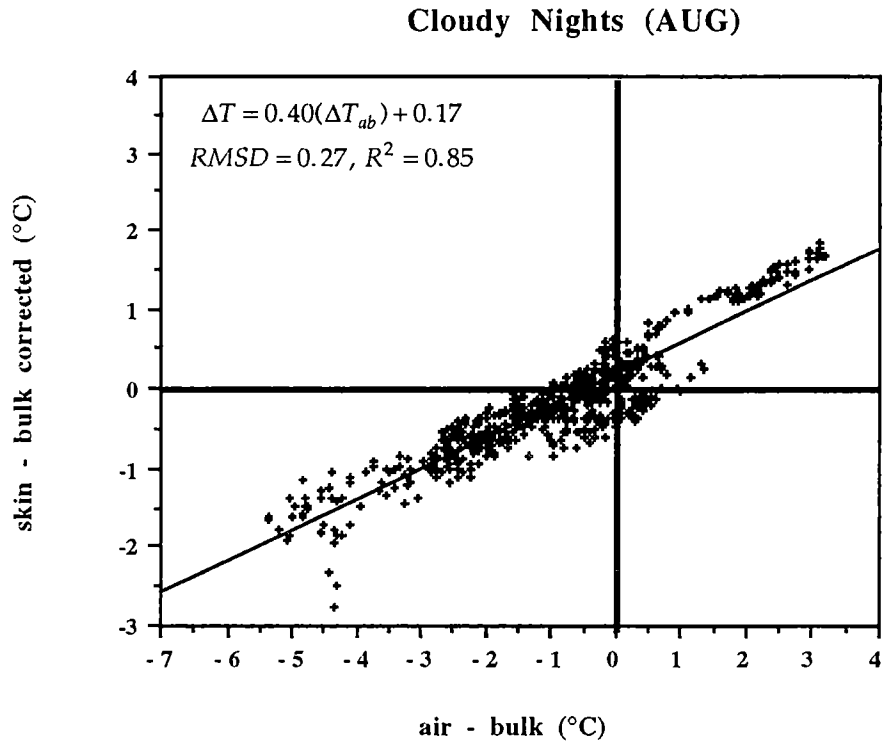
Cloudy Nights (AUG)
$\Delta T = 0.40(\Delta T_{ab}) + 0.17$
$RMSD = 0.27,\ R^2 = 0.85$
skin - bulk corrected (°C)
air - bulk (°C)
4
3
2
1
0
-1
-2
-3
-7 -6 -5 -4 -3 -2 -1 0 1 2 3 4

C15

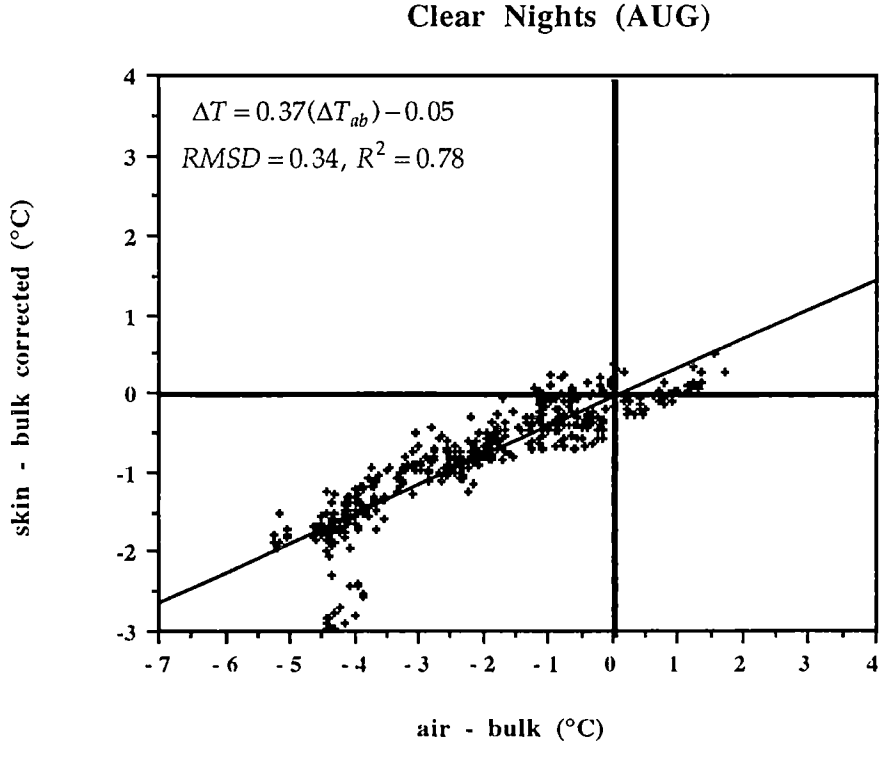
Clear Nights (AUG)
$\Delta T = 0.37(\Delta T_{ab}) - 0.05$
$RMSD = 0.34,\ R^2 = 0.78$
skin - bulk corrected (°C)
air - bulk (°C)
4
3
2
1
0
-1
-2
-3
-7 -6 -5 -4 -3 -2 -1 0 1 2 3 4

C16

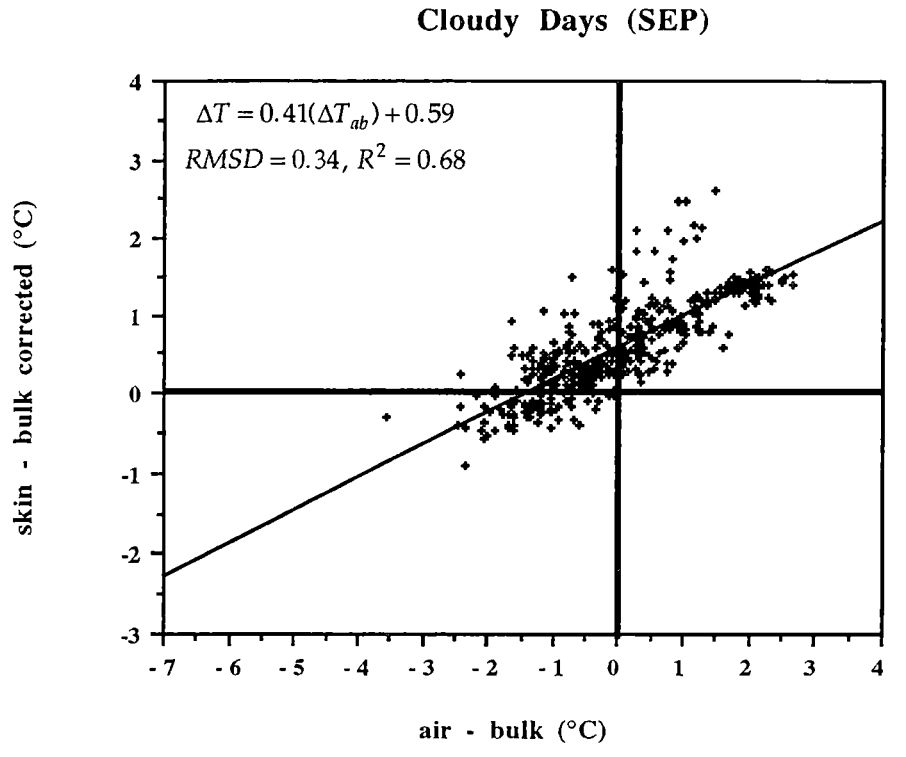
Cloudy Days (SEP)
$\Delta T = 0.41(\Delta T_{ab}) + 0.59$
$RMSD = 0.34,\ R^2 = 0.68$
skin - bulk corrected (°C)
air - bulk (°C)
4
3
2
1
0
-1
-2
-3
-7 -6 -5 -4 -3 -2 -1 0 1 2 3 4

C17

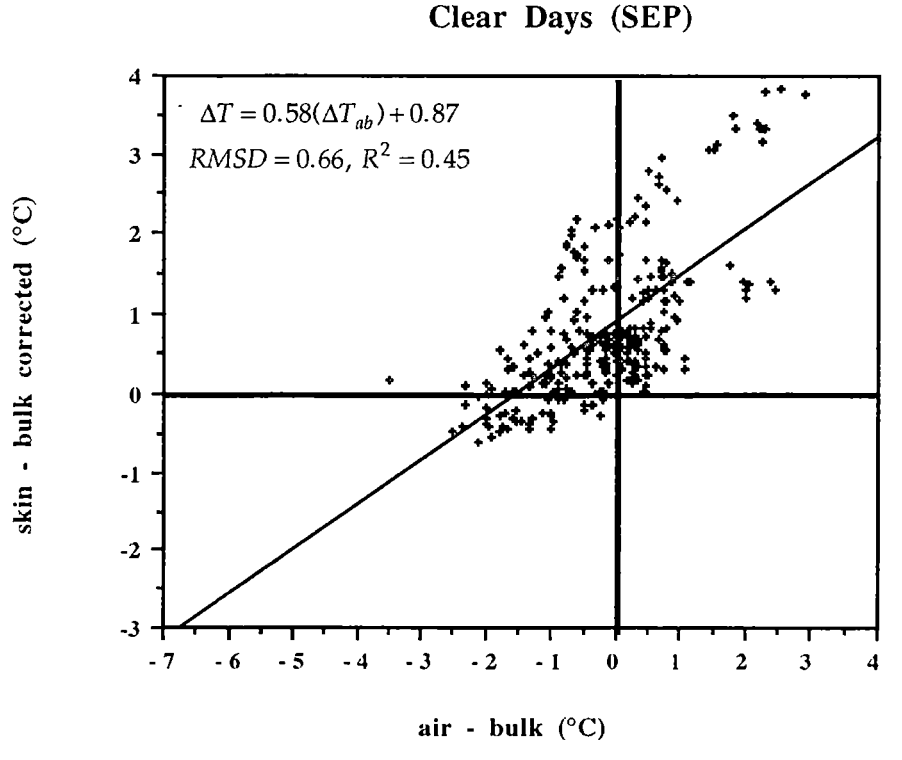
Clear Days (SEP)
$\Delta T = 0.58(\Delta T_{ab}) + 0.87$
$RMSD = 0.66,\ R^2 = 0.45$
skin - bulk corrected (°C)
air - bulk (°C)
4
3
2
1
0
-1
-2
-3
-7 -6 -5 -4 -3 -2 -1 0 1 2 3 4

C18

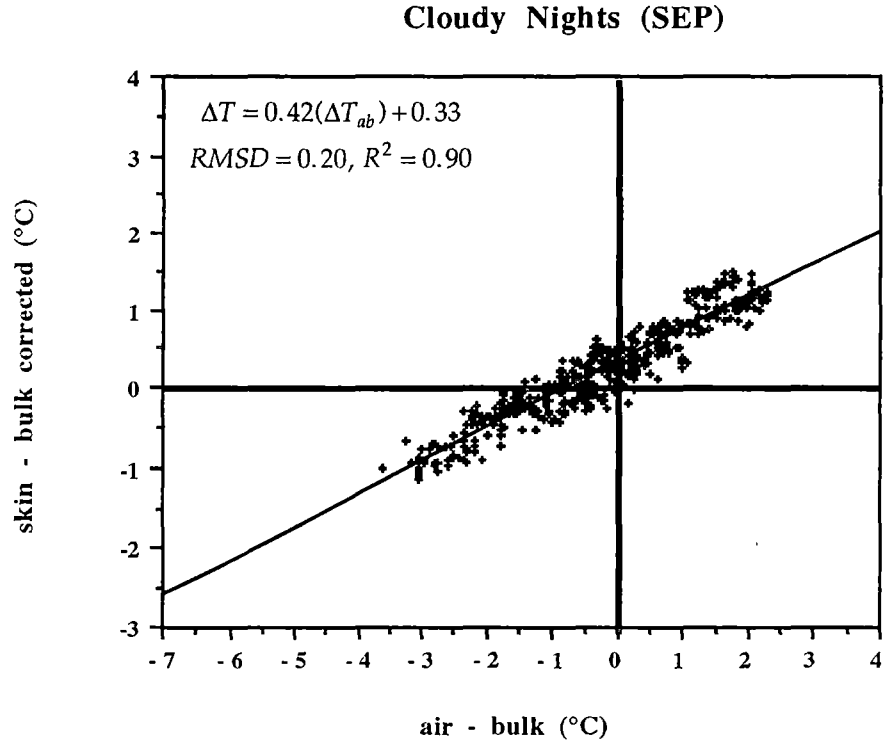
Cloudy Nights (SEP)
$\Delta T = 0.42(\Delta T_{ab}) + 0.33$
$RMSD = 0.20,\ R^2 = 0.90$
skin - bulk corrected (°C)
air - bulk (°C)
4
3
2
1
0
-1
-2
-3
-7 -6 -5 -4 -3 -2 -1 0 1 2 3 4

C19

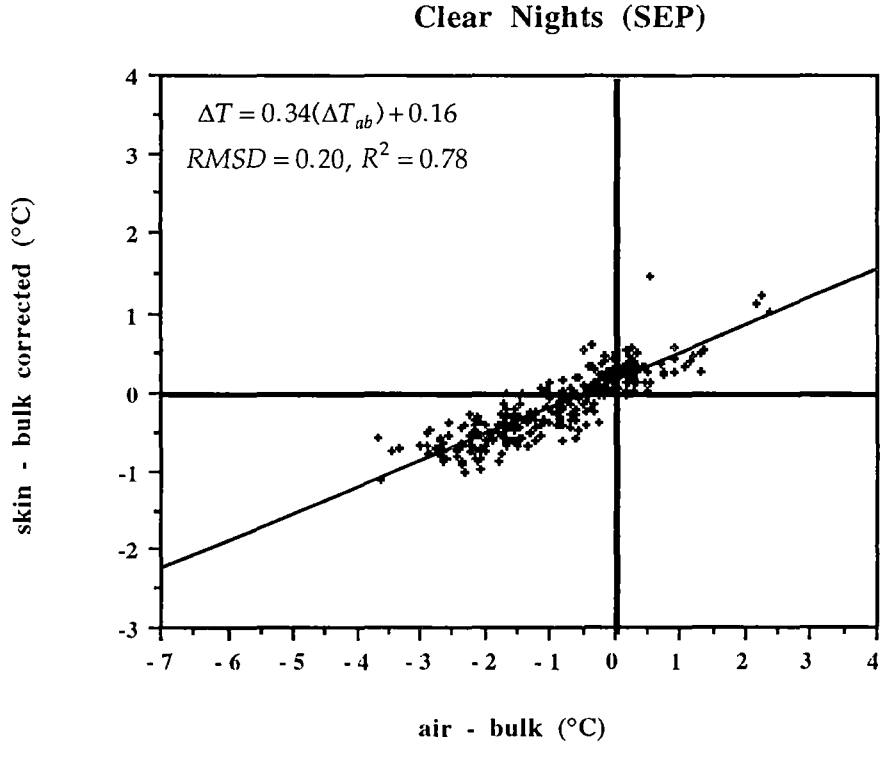
Clear Nights (SEP)
$\Delta T = 0.34(\Delta T_{ab}) + 0.16$
$RMSD = 0.20,\ R^2 = 0.78$
skin - bulk corrected (°C)
air - bulk (°C)
4
3
2
1
0
-1
-2
-3
-7 -6 -5 -4 -3 -2 -1 0 1 2 3 4

C20

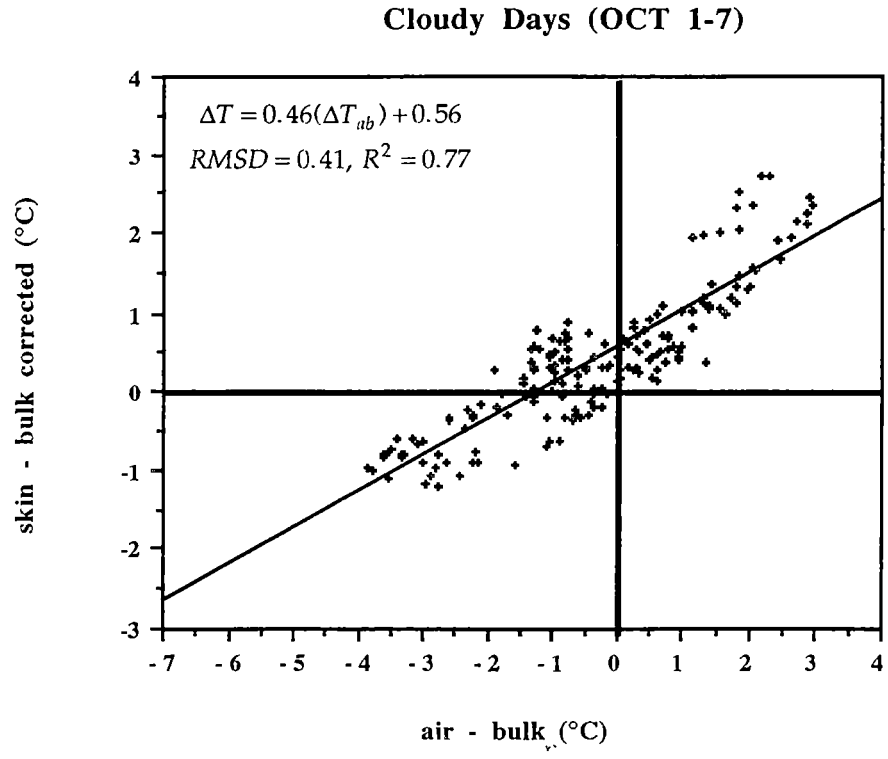
Cloudy Days (OCT 1-7)
$\Delta T = 0.46(\Delta T_{ab}) + 0.56$
$RMSD = 0.41,\ R^2 = 0.77$
skin - bulk corrected (°C)
air - bulk (°C)
4
3
2
1
0
-1
-2
-3
-7 -6 -5 -4 -3 -2 -1 0 1 2 3 4

C21

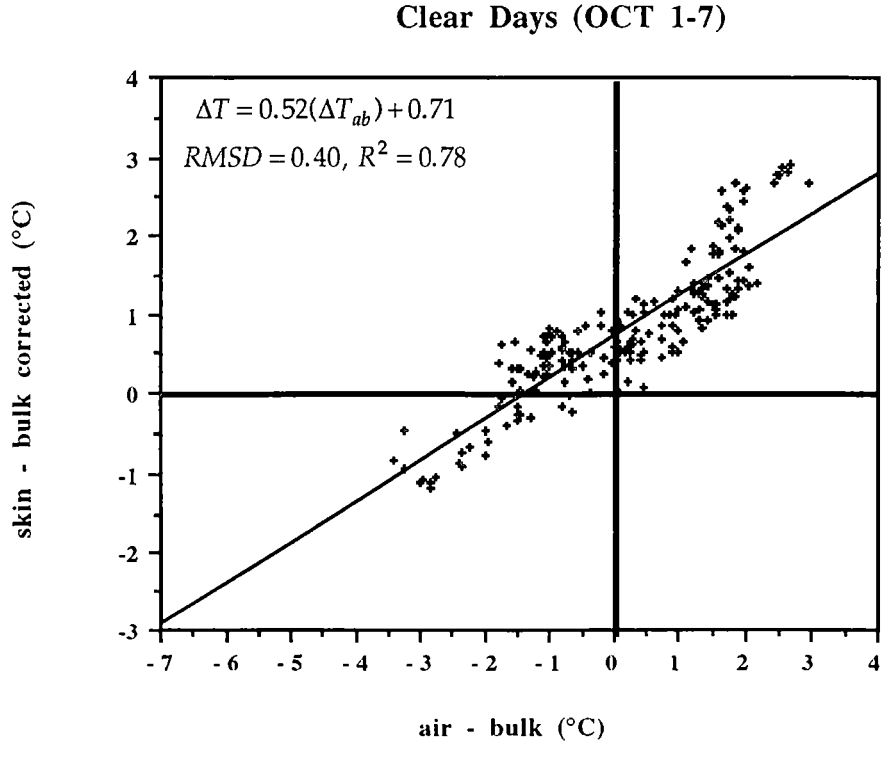
Clear Days (OCT 1-7)
$\Delta T = 0.52(\Delta T_{ab}) + 0.71$
$RMSD = 0.40,\ R^2 = 0.78$
skin - bulk corrected (°C)
air - bulk (°C)
4
3
2
1
0
-1
-2
-3
-7 -6 -5 -4 -3 -2 -1 0 1 2 3 4

C22

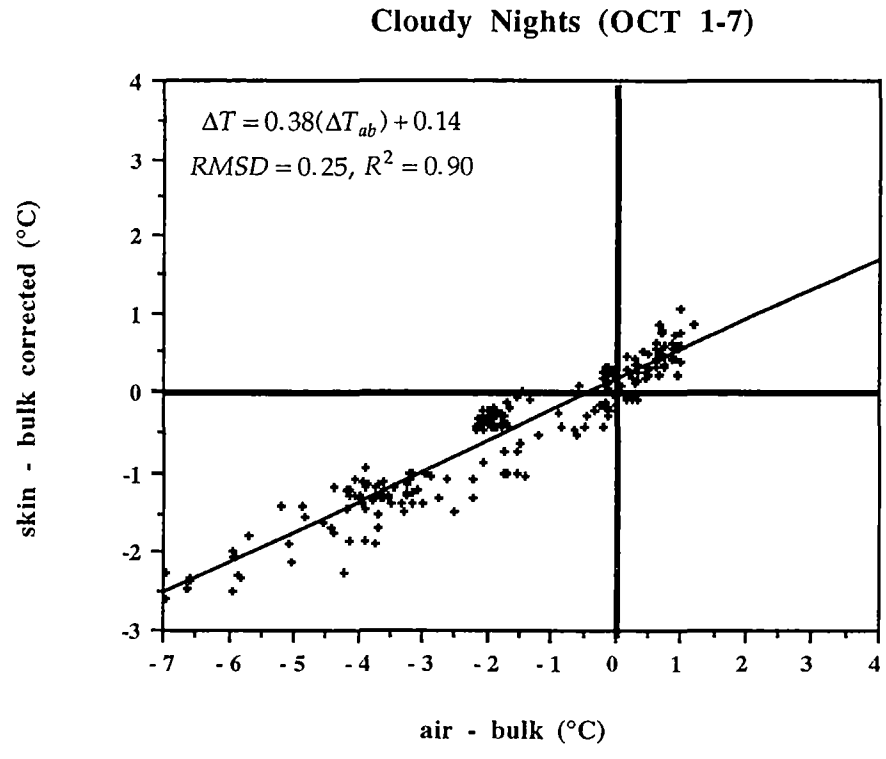
Cloudy Nights (OCT 1-7)
$\Delta T = 0.38(\Delta T_{ab}) + 0.14$
$RMSD = 0.25,\ R^2 = 0.90$
skin - bulk corrected (°C)
air - bulk (°C)

C23

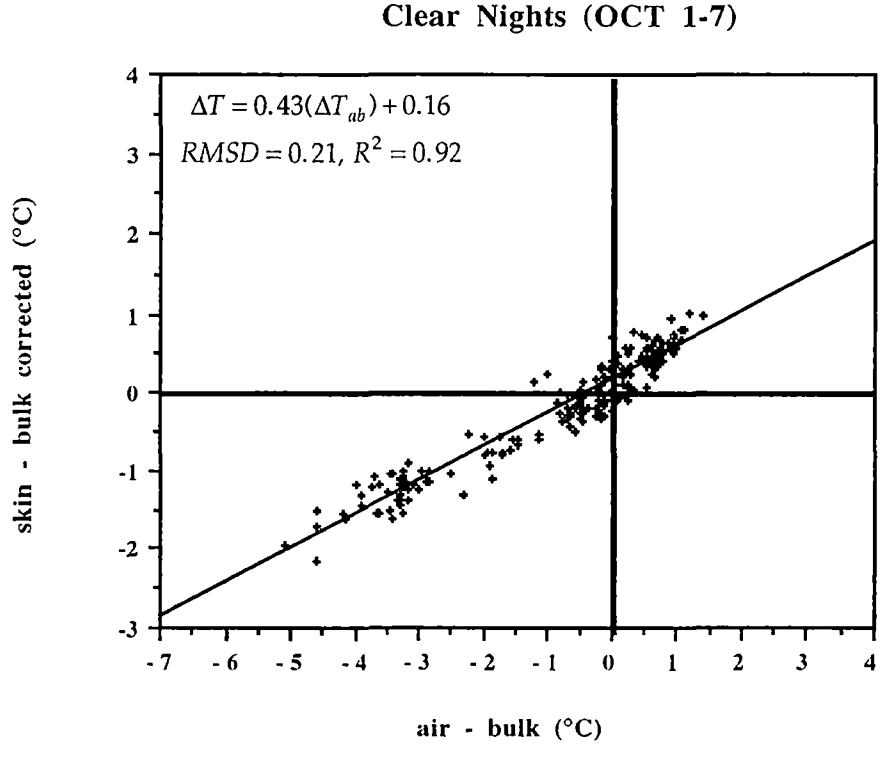
Clear Nights (OCT 1-7)
$\Delta T = 0.43(\Delta T_{ab}) + 0.16$
$RMSD = 0.21,\ R^2 = 0.92$
skin - bulk corrected (°C)
air - bulk (°C)

C24

APPENDIX D:

A Data Summary (in tabular form) for the Summer voyage (SHAM) and the Winter voyage (THIRST).

Cloudy Day (Summer)				
averaged data	Jan (SR3)	Jan (B)	Feb	mean
No. data points	657	428	708	1793
air - bulk (°C)	-1.45	-0.82	-0.93	-1.07
skin - bulk (°C)	-0.31	-0.05	0.1	-0.09
% cool skins	64	69	52	62
Standard Range	0.94	0.5	0.66	0.7
Gradient (a)	0.49	0.34	0.38	0.4
y-intercept (b)	0.41	0.23	0.45	0.36
Correlation Coeff	0.68	0.31	0.46	0.48
RMSD	0.52	0.42	0.48	0.47
Wind speed	16.6	15.2	24.2	18.7
Wind direction	194	198	165	186

D1

Clear Day (Summer)				
averaged data	Jan (SR3)	Jan (B)	Feb	mean
No. data points	352	226	214	792
air - bulk (°C)	-0.82	-1.28	-2.02	-1.37
skin - bulk (°C)	0.45	-0.16	0.01	0.1
% cool skins	42	71.5	57	57
Standard Range	0.99	0.61	0.79	0.8
Gradient (a)	0.47	-0.03	0.25	0.23
y-intercept (b)	0.84	-0.19	0.52	0.39
Correlation Coeff	0.21	0	0.12	0.11
RMSD	0.91	0.65	0.77	0.78
Wind speed	15.1	13.8	17.4	15.4
Wind direction	235	194	171	200

D2

Cloudy Night (Summer)				
averaged data	Jan (SR3)	Jan (B)	Feb	mean
No. data points	530	236	520	1286
air - bulk (°C)	-1.52	-0.72	-0.98	-1.07
skin - bulk (°C)	-0.94	-0.22	-0.15	-0.44
% cool skins	98	76	58	77
Standard Range	0.61	0.35	0.62	0.53
Gradient (a)	0.34	0.33	0.42	0.36
y-intercept (b)	-0.42	0.02	0.26	-0.05
Correlation Coeff	0.77	0.7	0.68	0.72
RMSD	0.27	0.18	0.34	0.26
Wind speed	21.6	11.5	21.4	18.17
Wind direction	182	127	152	154

D3

Clear Night (Summer)				
averaged data	Jan (SR3)	Jan (B)	Feb	mean
No. data points	213	109	96	418
air - bulk (°C)	-1.09	-1.57	-2.11	-1.59
skin - bulk (°C)	-0.92	-0.9	-1	-0.94
% cool skins	99	100	97	99
Standard Range*	0.54	0.34	0.62	0.5
Gradient (a)	0.35	0.41	0.48	0.41
y-intercept (b)	-0.54	-0.25	0.01	-0.26
Correlation Coeff	0.81	0.45	0.63	0.63
RMSD	0.22	0.26	0.37	0.28
Wind speed	17.5	10.4	21.9	16.6
Wind direction	255	199	191	215

D4

Cloudy Day (Winter) V1 THIRST				
averaged data	Aug	Sep	Oct	mean
No. data points	342	463	179	984
air - bulk (°C)	-1.05	0.07	-0.41	-0.46
skin - bulk (°C)	-0.13	0.61	0.38	0.29
% cool skins	63	18	33	38
Standard Range	0.8	0.62	0.89	0.77
Gradient (a)	0.42	0.41	0.46	0.43
y-intercept (b)	0.31	0.59	0.56	0.49
Correlation Coeff	0.93	0.68	0.77	0.79
RMSD	0.2	0.34	0.41	0.32
Wind speed	27.5	26.4	22.6	25.5
Wind direction	266	263	259	263

D5

Clear Day (Winter) V1 THIRST				
averaged data	Aug	Sep	Oct	mean
No. data points	213	294	197	704
air - bulk (°C)	-1.75	-0.17	0.16	-0.59
skin - bulk (°C)	-0.47	0.77	0.79	0.36
% cool skins	66	17.5	15	33
Standard Range	0.98	0.88	0.88	0.91
Gradient (a)	0.48	0.58	0.52	0.53
y-intercept (b)	0.36	0.87	0.71	0.65
Correlation Coeff	0.87	0.45	0.78	0.7
RMSD	0.35	0.66	0.4	0.47
Wind speed	22.8	24.4	26.5	24.6
Wind direction	261	267	292	273

D6

Cloudy Night (Winter) V1 THIRST				
averaged data	Aug	Sep	Oct	mean
No. data points	785	529	235	1549
air - bulk (°C)	-0.75	-0.16	-1.66	-0.86
skin - bulk (°C)	-0.13	0.26	-0.49	-0.12
% cool skins	63	38	68	56
Standard Range	0.74	0.64	0.87	0.75
Gradient (a)	0.4	0.42	0.38	0.4
y-intercept (b)	0.17	0.33	0.14	0.21
Correlation Coeff	0.85	0.9	0.9	0.88
RMSD	0.27	0.2	0.25	0.24
Wind speed	27	23.9	22.9	24.6
Wind direction	243	210	270	241

D7

Clear Night (Winter) V1 THIRST				
averaged data	Aug	Sep	Oct	mean
No. data points	436	320	216	972
air - bulk (°C)	-2.18	-0.94	-0.69	-1.27
skin - bulk (°C)	-0.86	-0.16	-0.14	-0.39
% cool skins	90	61	50	67
Standard Range	0.76	0.46	0.76	0.66
Gradient (a)	0.37	0.34	0.43	0.38
y-intercept (b)	-0.05	0.16	0.16	0.09
Correlation Coeff	0.78	0.78	0.92	0.83
RMSD	0.34	0.2	0.21	0.25
Wind speed	19.8	23.7	23.7	22.4
Wind direction	218	252	293	254.3

D8

APPENDIX E1: Wind Speed Histograms (SHAM and THIRST).

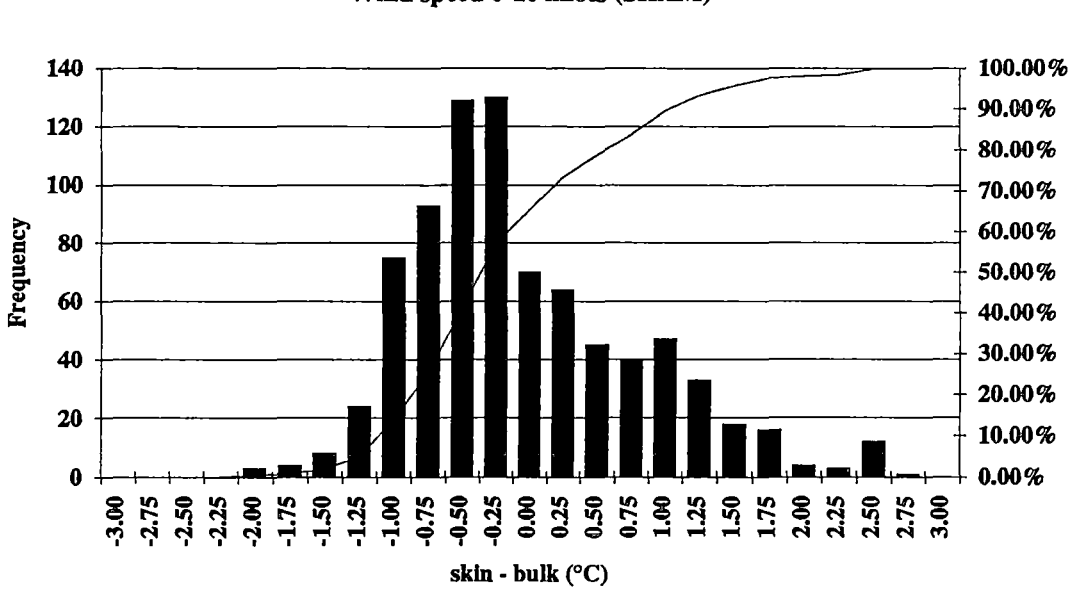

E1.1

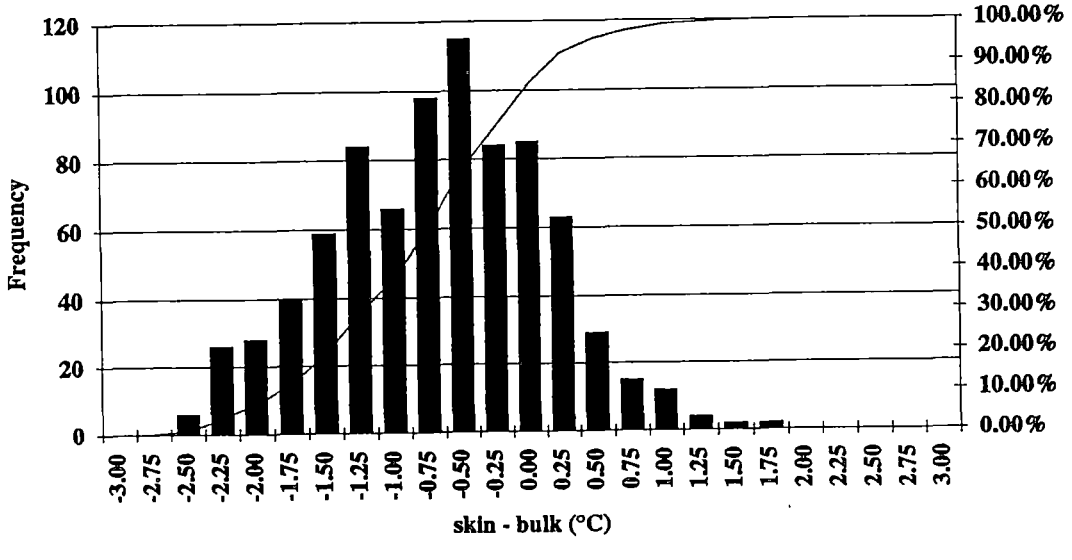

E1.2

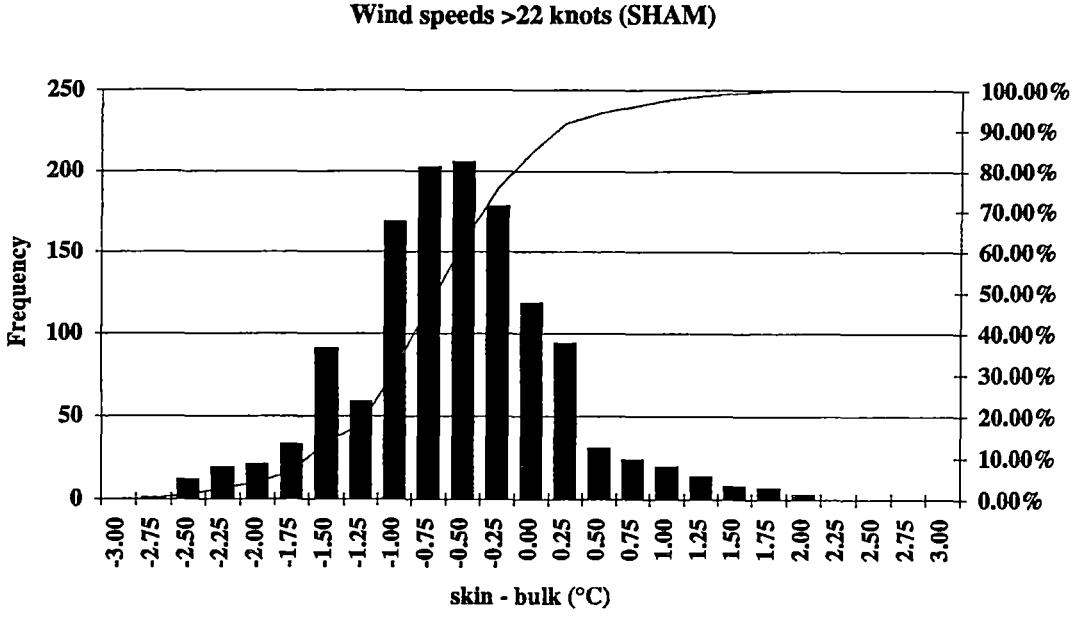
Wind speeds >22 knots (SHAM)
Frequency
250
200
150
100
50
0
100.00%
90.00%
80.00%
70.00%
60.00%
50.00%
40.00%
30.00%
20.00%
10.00%
0.00%
-3.00 -2.75 -2.50 -2.25 -2.00 -1.75 -1.50 -1.25 -1.00 -0.75 -0.50 -0.25 0.00 0.25 0.50 0.75 1.00 1.25 1.50 1.75 2.00 2.25 2.50 2.75 3.00
skin - bulk (°C)

E1.3

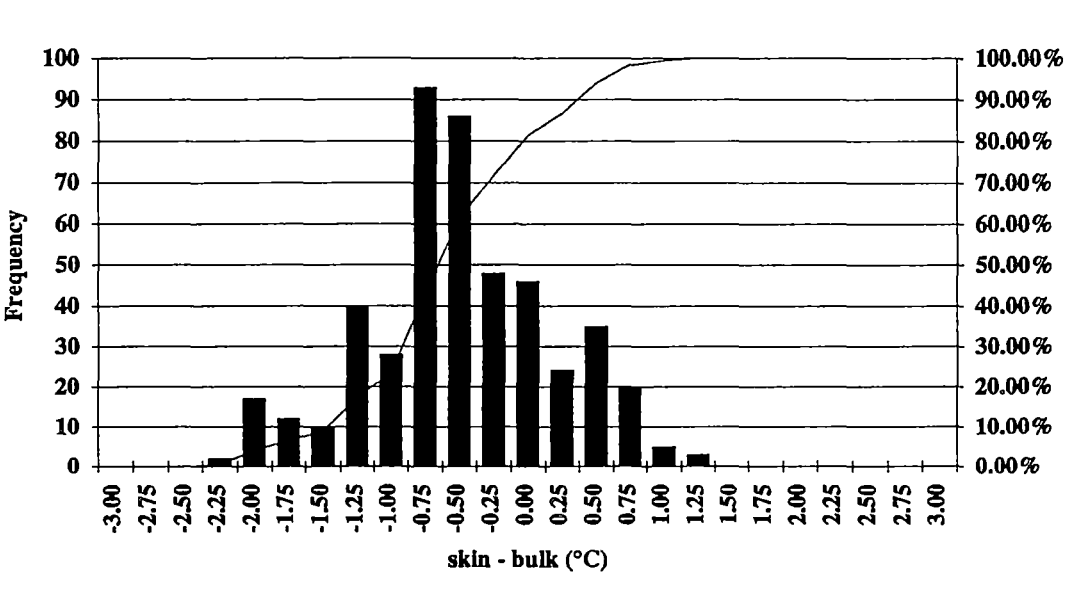
Wind speed 0-10 knots (THIRST)
Frequency
100
90
80
70
60
50
40
30
20
10
0
100.00%
90.00%
80.00%
70.00%
60.00%
50.00%
40.00%
30.00%
20.00%
10.00%
0.00%
-3.00 -2.75 -2.50 -2.25 -2.00 -1.75 -1.50 -1.25 -1.00 -0.75 -0.50 -0.25 0.00 0.25 0.50 0.75 1.00 1.25 1.50 1.75 2.00 2.25 2.50 2.75 3.00
skin - bulk (°C)

E1.4

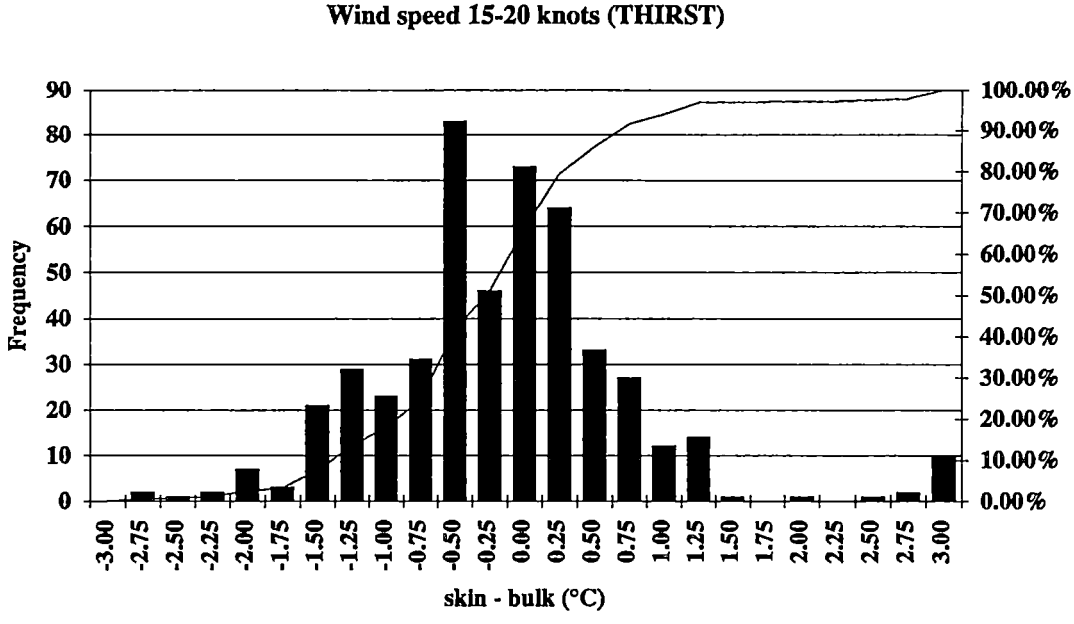
Wind speed 15-20 knots (THIRST)
Frequency
skin - bulk (°C)
0
10
20
30
40
50
60
70
80
90
0.00%
10.00%
20.00%
30.00%
40.00%
50.00%
60.00%
70.00%
80.00%
90.00%
100.00%
-3.00
-2.75
-2.50
-2.25
-2.00
-1.75
-1.50
-1.25
-1.00
-0.75
-0.50
-0.25
0.00
0.25
0.50
0.75
1.00
1.25
1.50
1.75
2.00
2.25
2.50
2.75
3.00

E1.5

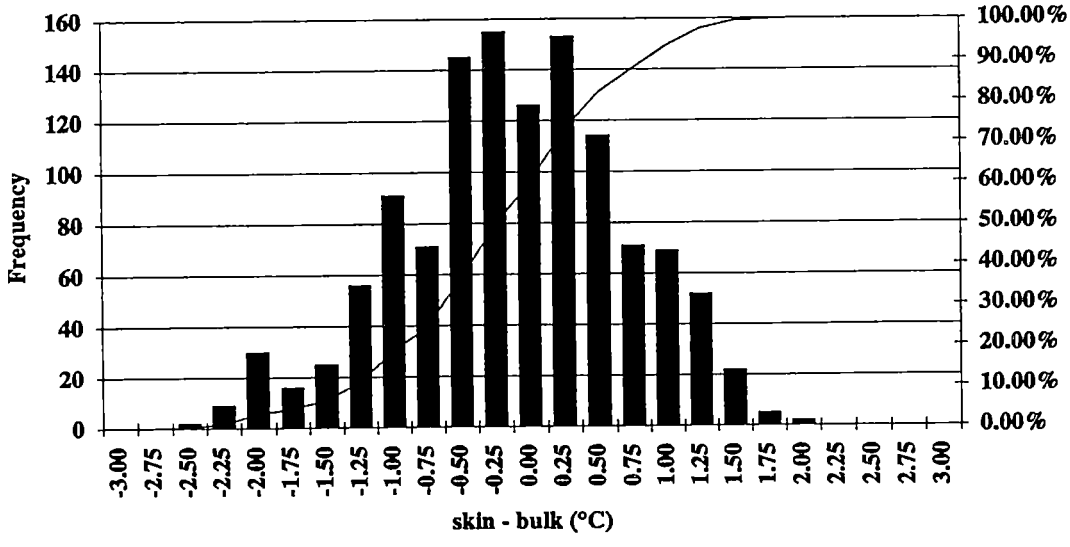
Wind speeds >30 knots (THIRST)
Frequency
skin - bulk (°C)
0
20
40
60
80
100
120
140
160
0.00%
10.00%
20.00%
30.00%
40.00%
50.00%
60.00%
70.00%
80.00%
90.00%
100.00%
-3.00
-2.75
-2.50
-2.25
-2.00
-1.75
-1.50
-1.25
-1.00
-0.75
-0.50
-0.25
0.00
0.25
0.50
0.75
1.00
1.25
1.50
1.75
2.00
2.25
2.50
2.75
3.00

E1.6

APPENDIX E2: Wind Speed Scatter Plots and Regressions (SHAM and THIRST).

Calm winds in summer (SHAM)

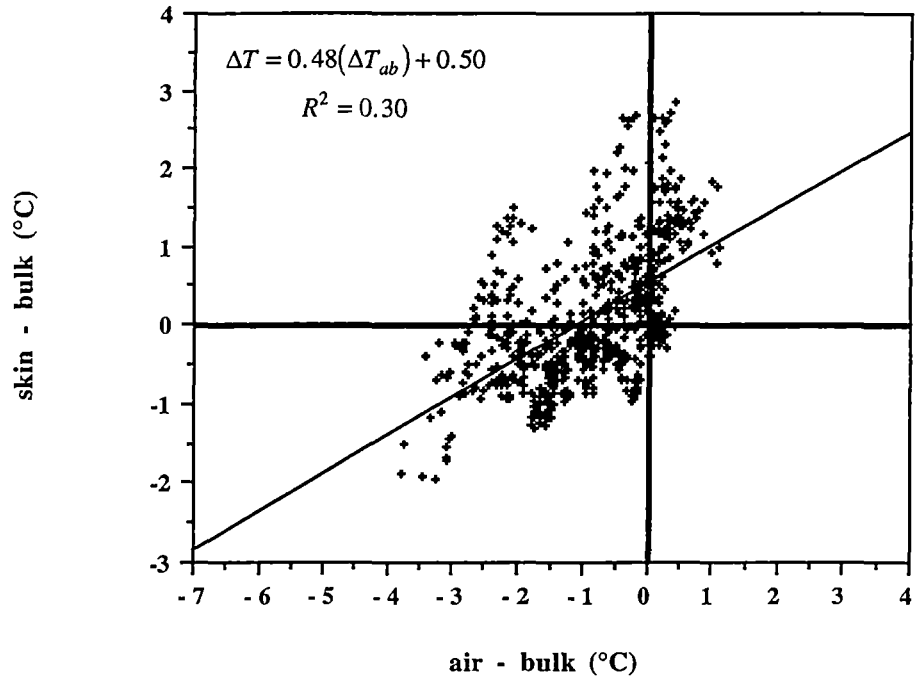

E2.1

Calm winds in winter (THIRST)

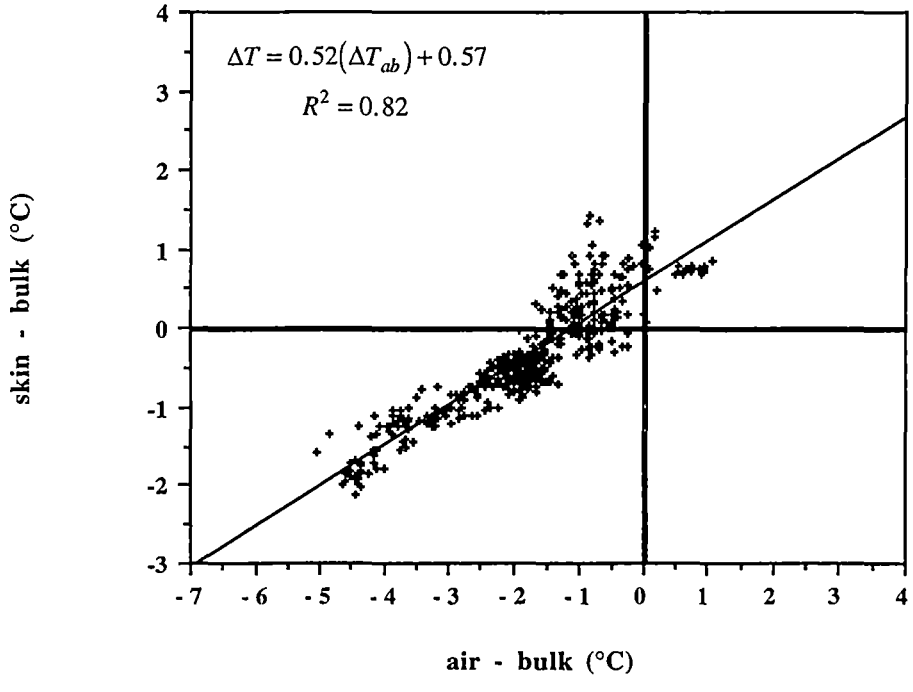

E2.2

Intermediate winds in summer (SHAM)

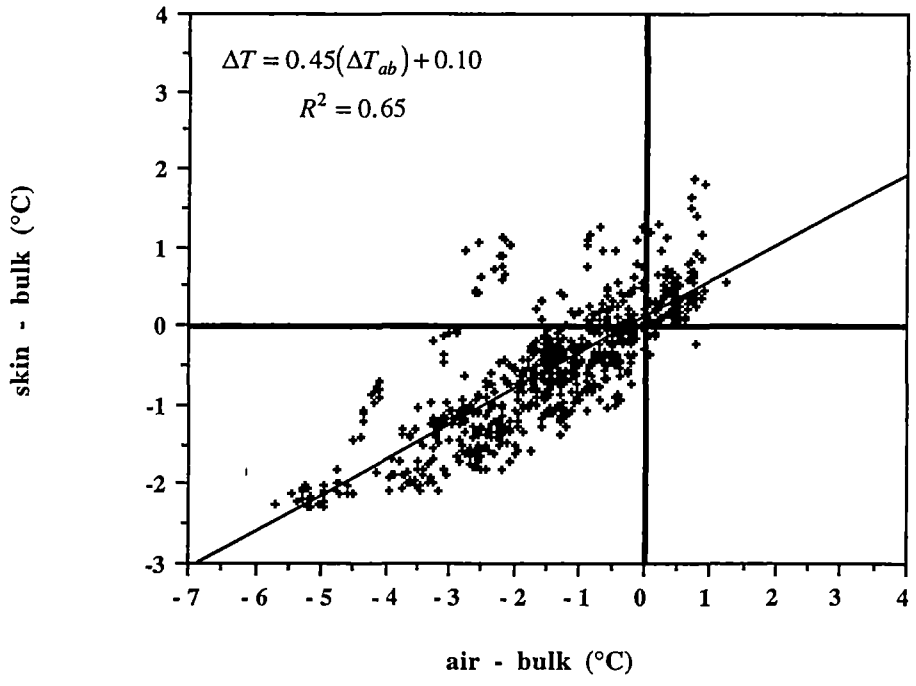

E2.3

Intermediate winds in winter (THIRST)

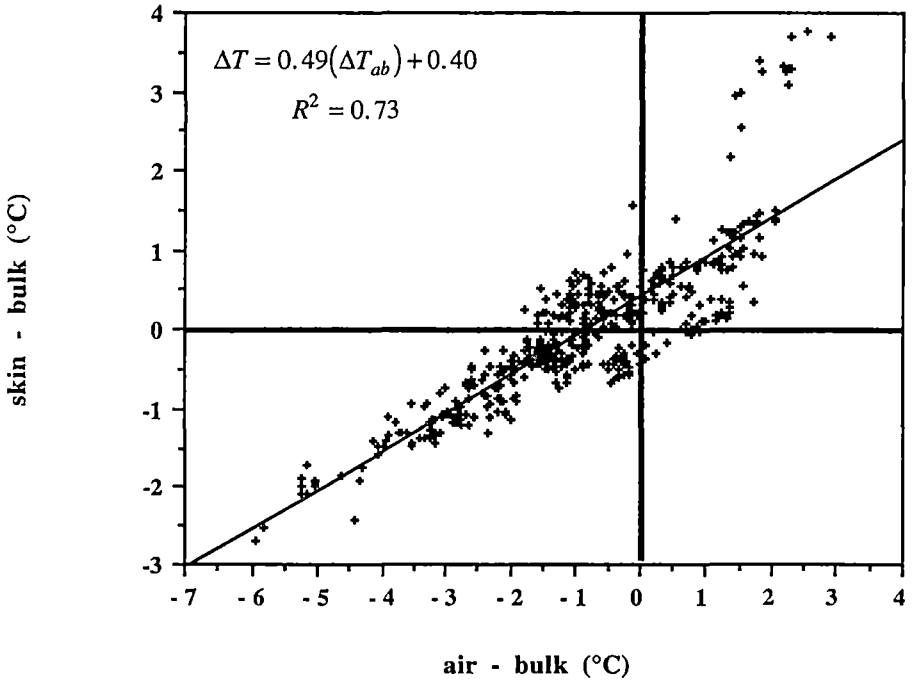

E2.4

Strong winds in summer (SHAM)

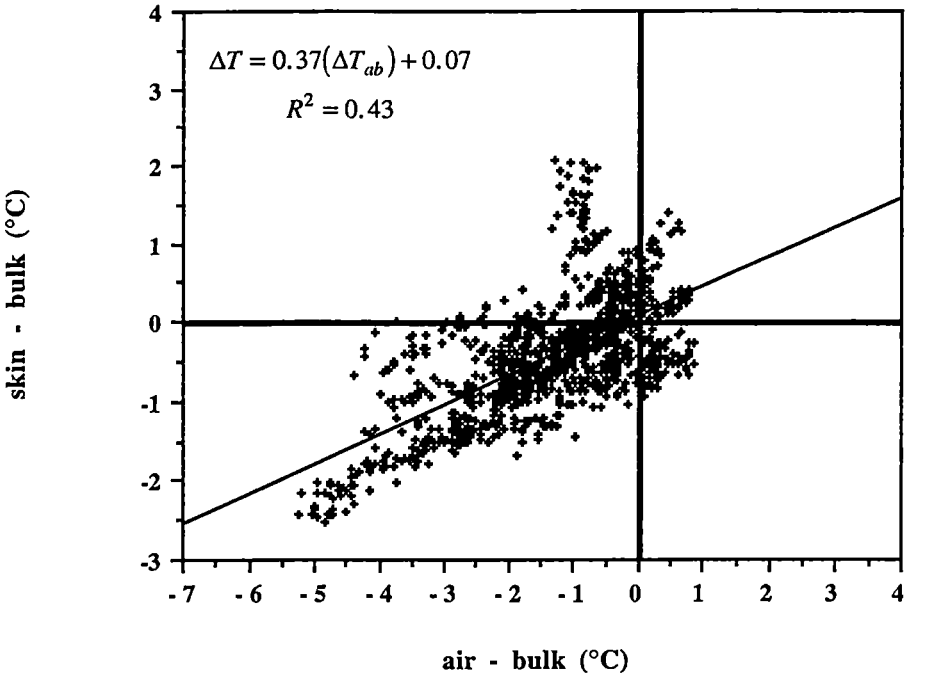

E2.5

Strong wind speeds in winter (THIRST)

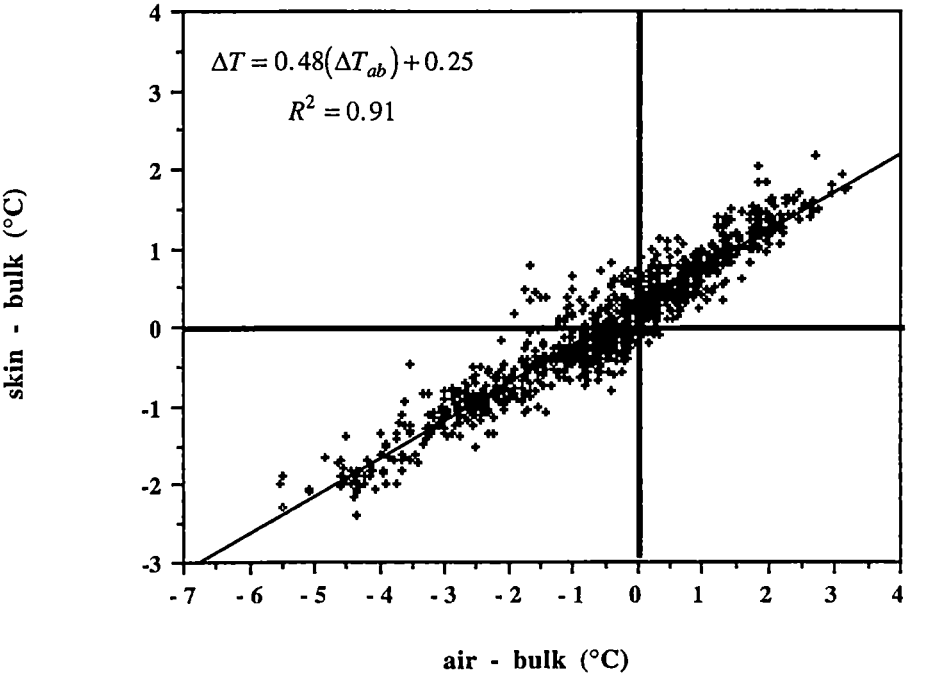

E2.6

APPENDIX: F

Signal contribution from PVC pipe

An additional experiment was carried out on the Everest radiometer to investigate the beamwidth (over a 720 mm distance). This investigation is detailed below, and it found that there is about a 5% signal contribution from the PVC pipe used to protect the radiometers. This necessitated a small adjustment to the way that the skin temperatures are calculated in the thesis, but it does not alter the overall physics of the project, nor does it change substantially the conclusions.

Experimental design

The Everest radiometer used to measure sea temperature was set up and levelled at a distance of 720 mm from the front edge of the radiometer to the tip of a soldering iron. The soldering iron was placed on an optical bench which was used to slide the soldering iron across the field of view of the radiometer at 5 mm intervals. The centre of the radiometer and the soldering iron were set at exactly the same height (see Figure F1).

Temperature measurements were taken in two orthogonal directions across the beam of the radiometer against a consistent background.

Results

Exhibit-A is a plot of the normalised radiometer temperature measurements plotted against the position of the soldering iron. Exhibit-B is the same plot but with the radiometer having been rotated through a 90° orthogonal angle.

The internal diameter of the PVC pipe is 11 cm. It can be seen from Exhibit-A that there is a 5.9 % signal contribution from outside this 11 cm diameter window. In the same graph, 94.1 % of the signal comes from inside the 11 cm window.

Similarly for Exhibit-B (orthogonal), there is a 4.9 % signal contribution from outside the 11 cm window, whilst 95.1 % of the signal comes from within the 11 cm window.

The average signal contribution from out side the 11 cm window is therefore 5.4 % and is the estimated signal contribution that comes from the PVC pipe.

A Proposed Correction

The following method was adopted to correct for the signal contribution from the pipe by assuming that the PVC pipe is at air temperature.

We can write

$$T_{skin} = 0.946\,(T_{SX}) + 0.054\,(T_{air})$$

where T_{skin} is the total temperature measurement made by the radiometer. T_{SX} is the temperature from the sea surface and where T_{air} is the (assumed) temperature of the PVC pipe.

$$\therefore T_{SX} = \frac{T_{skin} - 0.054\,T_{air}}{0.946}$$

$$\therefore T_{SX} - T_{bulk} = \frac{T_{skin} - 0.054\,T_{air}}{0.946} - T_{bulk}$$

where T_{bulk} is the ships front bow measurement of bulk sea temperature taken at 7.5 metres depth.

$$\therefore T_{SX} - T_{bulk} = 1.06\,T_{skin} - 0.06\,T_{air} - T_{bulk}$$

$$\therefore T_{SX} - T_{bulk} = T_{skin} - T_{bulk} + 0.06\,(T_{skin} - T_{air})$$

$$\therefore \Delta T_{correct} = \Delta T + 0.06(T_{skin} - T_{air})$$

The above formula does not take into account the effect of solar radiation which may cause heating of the PVC pipe during the day. This formula is more useful for correcting the night time data set. The maximum temperature difference between Tskin and Tair is 7 °C which means that the maximum correction is 0.06 x 7 = 0.4 °C.

The effect of the 5.4 % contribution from the PVC pipe on the measurement of sky temperature can be expressed as follows:

$$T_x = 0.946\ (T_{sky}) + 0.054\ (T_{air})$$

where T_x is the uncorrected sky temperature.

$$\therefore\ T_{sky} = \frac{T_x - 0.054\ T_{air}}{0.946}$$

$$\therefore\ T_{sky} = 1.06\ T_x - 0.06\ T_{air}$$

$$\therefore\ T_{sky} - T_x = 0.06\ (T_x - T_{air})$$

now if $T_{sky} - T_{air}$ is at a maximum of 50 °C, then the maximum error in T_{sky} is 3 °C. This error translates to an error of 0.05 °C in T_{skin} and is not large enough to be significant.

Figure F1

EXPERIMENTAL DESIGN

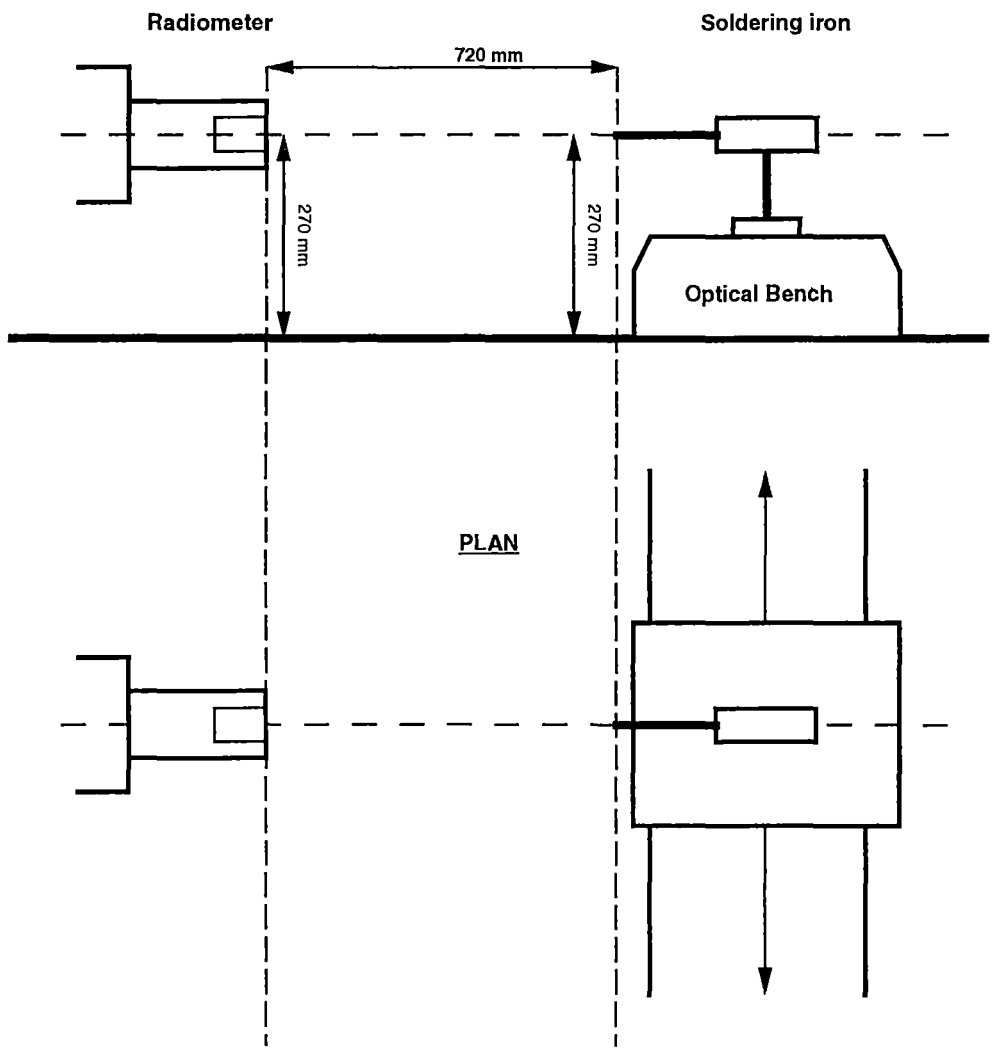

EXHIBIT-A
normalised temperature (at a distance 720 mm)

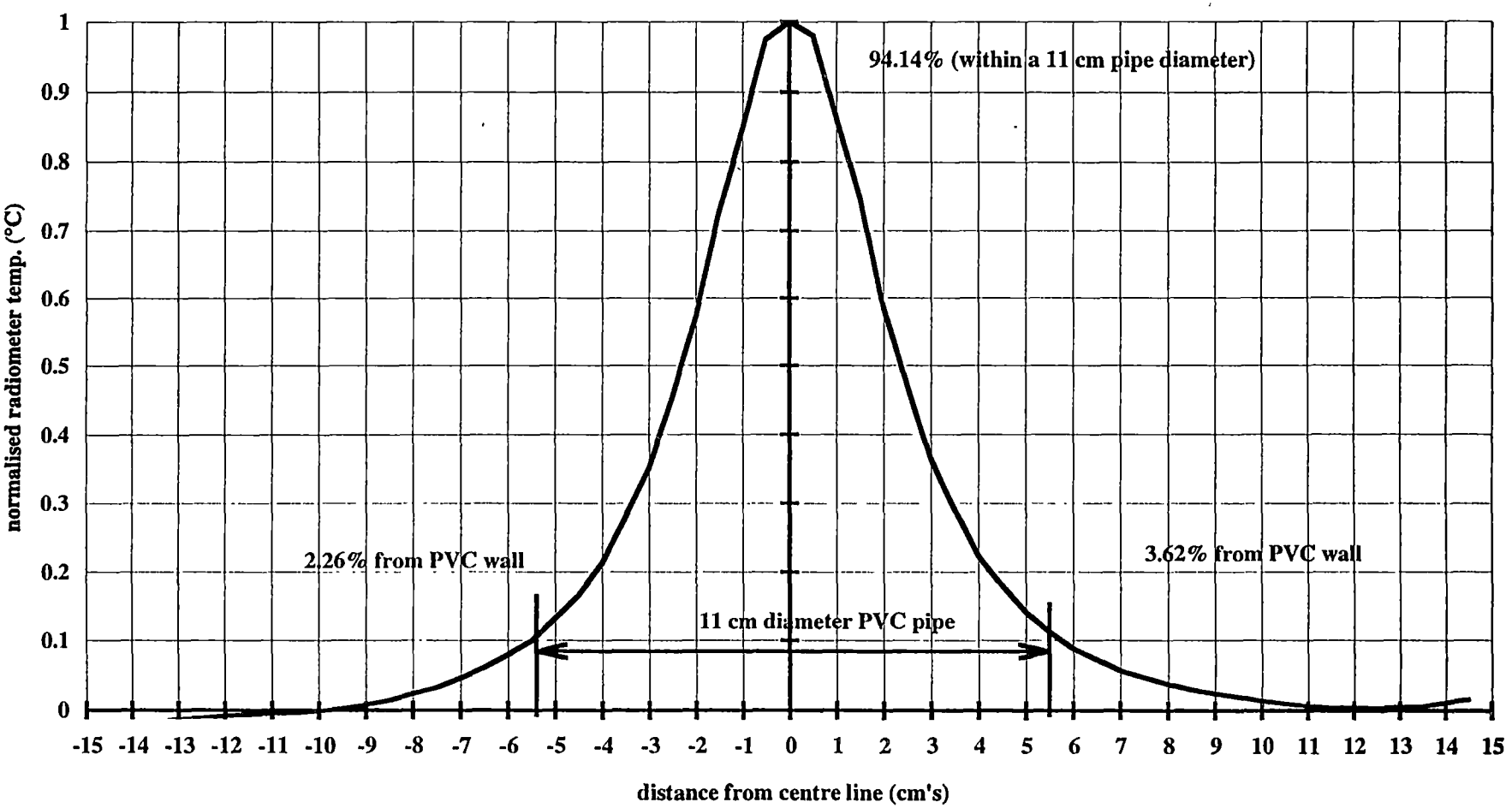

EXHIBIT-B (orthogonal)
normalised temperature (at a distance 720 mm)